

# **Boiling Water Reactor Core Analysis by means of an Improved Porous Media Two-phase Flow Approach**

Zur Erlangung des akademischen Grades eines  
**Doktors der Ingenieurwissenschaften (Dr.-Ing.)**  
von der KIT-Fakultät für Maschinenbau  
des Karlsruher Instituts für Technologie (KIT)

angenommene

**Dissertation**

von

Verónica Jáuregui Chávez

geboren in Teocaltiche, Jalisco, Mexiko

Tag der mündlichen Prüfung: 15.10.2021

Hauptreferent: Prof. Dr.-Ing. Robert Stieglitz  
Karlsruhe Institut für Technologie

Korreferent: Prof. Dr.-Ing. habil. Leo Bühler  
Karlsruhe Institut für Technologie



## Acknowledgments

I would like to thank my advisors Prof. Dr.-Ing. Robert Stieglitz and Dr. Victor Sanchez for having given me the opportunity of do my PhD at the Institute of Neutron Physics and Reactor Technology (INR) at the Karlsruhe Institute of Technology (KIT). I also would like to thank Prof. Dr. - Ing. habil. Leo Bühler for agreeing to be my supervisor. Thanks for your help and support.

Special thanks to the Mexican Comision Nacional de Ciencia y Tecnología (CONACYT) and the Deutscher Akademischer Austauschdienst (DAAD) who supported me with a scholarship to pursue my doctoral research.

I would like to thank Dr. Uwe Imke for his technical support, because without his knowledge, time, and his willingness to share his experience with me, this work would not have been possible. I would like to thank him as well for his empathy and personal support.

Thanks to all my colleagues at KIT, who with their time, support, long talks, a couple of beers and more coffees made the time at the Institute easier.

To the secretaries Birgit Zagolla and Ingeborg Schwartz for always being ready to help me with every administrative issue.

Special thanks to Petra Klug and her family, who were and are always there for me and have become “my German family.”

To all my friends in Germany and those in Mexico and all over the world who are always there no matter the distance.

Last but not least, to my parents Miguel and Blanca, my siblings Blanca, Lidia, Miguel, Antonio y Patricia for their unconditional love.





## Abstract

TWOPORFLOW is a thermal-hydraulics simulation code currently under development at the Institute of Neutron Physics and Reactor Technology (INR) of the Karlsruhe Institute of Technology (KIT). It has the capability to simulate single- and two-phase flow in a structured or unstructured porous medium using a 3-D Cartesian geometry. TWOPORFLOW calculates the transient or steady state solution of the mass, momentum, and energy conservation equations for each fluid phase with a semi-implicit numerical procedure based on the implicit continuous Eulerian (ICE) method.

TWOPORFLOW can simulate simple 1-D geometries like heated pipes, fuel assemblies resolving the sub-channel flow between rods or a whole nuclear core using a coarse mesh. Several closure correlations are implemented to model the heat transfer between solid and coolant, phase change, wall friction as well as liquid-vapor momentum coupling.

These models have been not fully evaluated. Important models such as the turbulent mixing and void dispersion were missing.

Consequently, the goal of this doctoral thesis is to extend and improve the simulating capability of TWOPORFLOW regarding the two-phase flow phenomena in Boiling Water Reactors (BWR) by implementing physical models e.g., turbulent mixing, void dispersion, and critical heat flux.

In order to evaluate the quality of the implemented models and the overall prediction capability of TWOPORFLOW, experimental data from selected experiments are used to be compared with the simulation's results.

Finally, the enhanced prediction capability of TWOPORFLOW is applied to the simulation of two BWR reactor cores, namely the one of Oskarshamn-2 (Sweden) and Laguna Verde unit 1 (Mexico) for the first time showing promising results.

Based on the performed investigations, possibilities for further development are identified in the areas of model development, numerical improvement, validation, code coupling, and parallelization.



## Kurzfassung

TWOPORFLOW ist ein thermohydraulischer Simulationscode, der derzeit am Institut für Neutronenphysik und Reaktortechnik (INR) des Karlsruher Instituts für Technologie (KIT) entwickelt wird. Er hat die Fähigkeit, ein- und zweiphasige Strömungen in einem strukturierten oder unstrukturierten porösen Medium unter Verwendung einer kartesischen 3D-Geometrie zu simulieren. TWOPORFLOW berechnet die transiente oder stationäre Lösung der Erhaltungsgleichungen von Masse, Impuls und Energie für jede Fluidphase mit einem semiimpliziten numerischen Verfahren basierend auf dem kontinuierlichen impliziten Euler-Verfahren (englisch: ICE Implicit Continuous Eulerian).

TWOPORFLOW kann einfache 1-D-Geometrien – wie beheizte Rohre oder Brennelemente – bei der Auflösung von Unter-Kanalströmung zwischen Stäben oder einen ganzen Kern mit einem Groben-Gitter simulieren. Zur Modellierung des Wärmeübergangs zwischen Feststoff und Kühlmittel, Phasenwechsel, Wandreibung sowie Flüssigkeit-Dampf-Impulskopplung werden verschiedene Schließungs-Korrelationen implementiert.

Diese Modelle wurden nicht vollständig evaluiert. Wichtige Teile wie das turbulente Mischen und die Porendispersion fehlten.

Ziel dieser Dissertation ist es daher, die Simulationsfähigkeit von TWOPORFLOW bezüglich der Zweiphasenströmungsphänomene in Siedewasserreaktoren (SWR) durch die Implementierung physikalischer Modelle wie turbulente Mischung, Porendispersion und kritischem Wärmefluss zu erweitern und zu verbessern.

Um die Qualität der implementierten Modelle und die Gesamtvorhersagefähigkeit von TWOPORFLOW zu bewerten, werden Daten aus ausgewählten Experimenten mit den Ergebnissen der Simulation verglichen.

Schließlich wird die verbesserte Vorhersagefähigkeit von TWOPORFLOW auf die Simulation von zwei SWR-Reaktorkernen (Oskarshamn-2 in Schweden und Laguna Verde-1 in Mexiko) angewendet, und zwar zum ersten Mal mit vielversprechenden Ergebnissen.

Basierend auf den durchgeführten Untersuchungen werden Weiterentwicklungsmöglichkeiten in den Bereichen Modellentwicklung, numerische Verbesserung, Validierung, Codekopplung und Parallelisierung identifiziert.



## Publications related to this thesis

1. Jauregui Chavez, Veronica; Imke, Uwe; Sanchez-Espinoza, Victor (2018). TWOPORFLOW: A two-phase flow porous media code, main features and validation with BWR-relevant bundle experiments. Nuclear Engineering and Design. Volume 338. Pages 181–188. doi: <https://doi.org/10.1016/j.nucengdes.2018.08.009>.
2. Jauregui Chavez, Veronica; Imke, Uwe; Jimenez Escalante, Javier; Sanchez-Espinoza, Victor Hugo (2017). Implementation and Validation of CHF Models in the Two - Phase Flow Porous Media Code Twoporflow. Proceedings of the 17th International Topical Meeting on Nuclear Reactor Thermal Hydraulics (NURETH-17). Paper ID:20248. Volume 5. Pages 2611–2624.
3. Jauregui Chavez, Veronica; Imke, Uwe; Jiménez Escalante, Javier; Sanchez-Espinoza Victor Hugo (2018). Further development of a thermal-hydraulics two-phase flow tool atw - International Journal for Nuclear Power Vol. 63 Issue 6/7 Pages 401-404. [https://inis.iaea.org/search/search.aspx?orig\\_q=RN:49076231](https://inis.iaea.org/search/search.aspx?orig_q=RN:49076231)
4. Jauregui Chavez, Veronica; Imke, Uwe; Sanchez-Espinoza, Victor Hugo (2022). Implementation and validation of CHF-models in the two-phase porous-media code TWOPORFLOW. Nuclear Engineering and Design. Volume 388, Number 111631 doi: <https://doi.org/10.1016/j.nucengdes.2021.111631>.



## Table of Contents

Acknowledgments .....	i
Abstract .....	iii
Kurzfassung.....	v
Publications related to this thesis .....	vii
Table of Contents .....	ix
List of Abbreviations and Acronyms .....	xiii
Nomenclature .....	xv
1 Introduction .....	1
1.1 Motivation .....	1
1.2 Challenges .....	2
1.3 Major objectives .....	3
1.4 Organization of thesis.....	3
2 General description of Boiling Water Reactors (BWRs).....	5
3 Main characteristics of thermal hydraulic core simulation tools .....	9
3.1 System thermal hydraulic codes.....	9
3.2 Sub-channel thermal hydraulic codes.....	10
3.3 Computational Fluid Dynamics (CFD) .....	10
3.4 Porous media thermal hydraulic codes.....	10
4 The porous media two-phase flow code TWOPORFLOW .....	13
4.1 Porous media approach in TWOPORFLOW .....	13
4.2 System of conservation equations .....	15
4.3 Steam-Water properties .....	17
4.4 The Heat conduction model.....	17
4.5 Constitutive models for the closure of the system of conservation equations.....	18
4.5.1 Wall heat transfer .....	20
4.5.2 Fraction of sub-cooled vapor generation .....	22
4.5.3 Liquid-vapor interface heat and mass exchange models .....	23
4.5.4 Wall friction .....	24
4.5.5 Liquid vapor momentum coupling .....	24
4.6 Numerical methods.....	24
5 Improvements of the porous media models of TWOPORFLOW .....	29
5.1 Turbulent mixing.....	29
5.1.1 Turbulent viscosity .....	29
5.1.2 Turbulent heat conductivity.....	30

5.2	Void dispersion.....	30
5.3	Critical Heat Flux (CHF).....	30
5.3.1	Biasi CHF correlation.....	32
5.3.2	Bowring correlation.....	33
5.3.3	Groeneveld look-up table .....	34
6	Validation of the pre-CHF models of TWOPORFLOW using experimental data .....	37
6.1	PSBT thermal mixing tests.....	37
6.1.1	Short test description .....	37
6.1.2	TWOPORFLOW modeling.....	41
6.1.3	Comparison of TWOPORFLOW predictions with experimental data.....	41
6.2	PSBT Sub-cooled boiling tests.....	43
6.2.1	Short test description .....	43
6.2.2	TWOPORFLOW modeling.....	46
6.2.3	Comparison TWOPORFLOW predictions with experimental data .....	47
6.3	BFBT test for steady state void dispersion.....	50
6.3.1	Short test description .....	50
6.3.2	Selected tests for code validation .....	54
6.3.3	TWOPORFLOW modeling.....	55
6.3.4	Comparison of the void fraction predicted by TWOPORFLOW with the data .....	56
6.4	Transient BFBT void tests.....	60
6.4.1	Short description of the transient void fraction tests .....	60
6.4.2	Short description of the turbine trip without by-pass tests .....	61
6.4.3	TWOPORFLOW modeling.....	61
6.4.4	Comparison the void fraction predicted by TWOPORFLOW with the measured data .....	62
6.4.5	Short description of the recirculation pump trip test .....	63
6.4.6	Comparison of the void fraction predicted by TWOPORFLOW with the measured data .....	63
6.5	General conclusions on TWOPORFLOW validation .....	65
7	Validation of Critical Heat Flux simulations in TWOPORFLOW with experimental data .....	67
7.1	Becker CHF steady-state experiments.....	67
7.1.1	Short test description .....	67
7.1.2	TWOPORFLOW modeling.....	67
7.1.3	Comparison of TWOPORFLOW predictions against experimental data.....	67
7.2	BFBT CHF steady state tests.....	69
7.2.1	Short test description .....	69
7.2.2	TWOPORFLOW modeling of the BFBT test bundle .....	71



7.2.3	Comparison of the TWOPORFLOW predictions with the experimental data .....	72
7.3	BFBT CHF transient tests .....	76
7.3.1	Short test description .....	76
7.3.2	TWOPORFLOW modeling.....	76
7.3.3	Description of the turbine trip without by-pass CHF tests .....	76
7.3.4	Comparison of the CHF predicted by TWOPORFLOW against the measured data.....	77
7.3.5	Description of the recirculation pump trip CHF tests.....	79
7.3.6	Comparison of the CHF predicted by TWOPORFLOW against the measured data.....	80
7.4	General conclusions regarding the TWOPORFLOW CHF model validation.....	82
8	Application of TWOPORFLOW for the thermal hydraulic analysis of BWR-cores .....	85
8.1	Thermal hydraulic analysis of the Oskarshamn-2 core .....	85
8.1.1	Short description of the core and thermal hydraulics parameters.....	85
8.1.2	TWOPORFLOW core model .....	87
8.1.3	TWOPORFLOW stationary core analysis: code-to data and code-to-code comparison.....	88
8.1.4	Thermal hydraulic analysis of the Oskarshamn-2 BWR stability transient.....	91
8.2	Thermal hydraulic analysis of the Laguna Verde BWR reactor core.....	93
8.2.1	Short description of the core and thermal hydraulic parameters .....	93
8.2.2	Short description of the Laguna Verde stability transient .....	95
8.2.3	Laguna Verde BWR Core Model for TWOPORFLOW .....	95
8.2.4	Steady state case simulation results and code to code comparisons.....	97
9	Summary.....	99
10	Outlook.....	101
11	References .....	103
12	Annexes.....	111
	Annex 1 Constitutive models for the closure of the conservation equations .....	111
a.	Dimensionless physical numbers .....	111
b.	Wall heat transfer .....	112
c.	Fraction of sub-cooled vapor generation.....	116
d.	Liquid-vapor interface heat and mass exchange models .....	117
e.	Wall Friction.....	123
f.	Liquid-vapor momentum coupling.....	126
	Annex 2 Boundary and experimental conditions of the steady state experiments used in the evaluations.....	129
a.	Boundary and experimental conditions of PSBT Steady state Temperature experiments	129
b.	Boundary and experimental conditions of PSBT Single sub-channel experiments ....	130

- c. Boundary and experimental conditions of BFBT Steady State Sub-channel grade tests.  
132
- d. Boundary and experimental conditions of CHF Becker tube experiments ..... 134
- e. Boundary and experimental conditions of CHF BFBT Steady State experiments..... 135

## List of Abbreviations and Acronyms

ADI	Alternating Direction Implicit solver
ANSYS-CFX	Ansys Inc. Computational Fluid Dynamics software
AOO	Anticipated Operational Occurrences
APR	Advanced Power Reactor
ATHLET	Analysis of Thermal Hydraulics of Leaks and Transient
BE	Best Estimated
BFBT	BWR Full-size Fine-mesh Bundle Test benchmark
BICGSTAB	Biconjugate Gradient Stabilized solver
BWR	Boiling Water Reactor
CFD	Computational Fluid Dynamics
CFE	Comisión Federal de Electricidad (Mexican Federal Commission of Electricity)
CHF	Critical Heat Flux
CHFR	Critical Heat Flux Ratio
CNLV	Central Nuclear Laguna Verde (Nuclear Power Plant Laguna Verde)
CNTH	Coupled Nuclear Thermal Hydraulics
COBRA-TF	Coolant Boiling in Rod Arrays-Two Fluids
CPU	Central Processing Unit
CUPID	Component Unstructured Program for Interfacial Dynamics
DNB	Departure of Nucleate Boiling
DNBR	Departure of Nucleate Boiling Ratio
DR	Decay Ratio
EPR	European Pressurized Reactor
FAVOR	Fractional Area Volume Obstacle Representation
FEBE	Forward-Euler, Backward-Euler
GRS	Gesellschaft für Anlagen- und Reaktorsicherheit (Society for Plant and Reactor Safety)
IAEA	International Atomic Energy Agency
IAPWS	International Association for the Properties of Water and Steam
ICE	Implicit Continuous Eulerian
INR	Institute for Neutron Physics and Reactor Technology
KAERI	Korea Atomic Energy Research Institute
KIT	Karlsruhe Institute of Technology
LOCA	Loss of Coolant Accident
LUT	Look Up Table
LWR	Light Water Reactor
MARS	Multi-dimensional Analysis of Reactor Safety
MASTER	Multi-purpose Analyzer for Static and Transient Effects of Reactors
MCHFR	Minimum Critical Heat Flux Ratio
MDNBR	Minimum Departure of Nucleate Boiling Ratio
MSFBT	Minimum Stable Film Boiling Temperature
NCSU	North Carolina State University
NPP	Nuclear Power Plant
NUMPS	Numerical Multi-Physics
NUPEC	Nuclear Power Engineering Corporation Japan
OECD	Organization for Economic Co-operation and Development
OpenFOAM	Open-source Field Operation and Manipulation
PA	Postulated Accidents
PAFS	Passive Auxiliary Feed Water Systems
PARCS	Purdue Advanced Reactor Core Simulation
PSBT	PWR sub-channel and Bundle Tests benchmark
PSU	Pennsylvania State University

PWR	Pressurized Water Reactor
rms	Root-mean-square
RPV	Reactor Pressure Vessel
SIMPLE	Semi-Implicit Method for Pressure Linked Equations
SOR	Successive Over Relaxation solver
TH	Thermal Hydraulics
TPF	TWOPORFLOW original empirical correlations
TPF-TRACE	TRACE correlations adapted in TWOPORFLOW
TRAC	Transient Reactor Analysis Code
TRACE	TRAC/RELAP Advanced Computational Engine
US-NRC	US Nuclear Regulatory Commission
VTT	Technical Research Center of Finland
VVER	Water-Water Energetic Reactor

## Nomenclature

$A$	Area	$[m^2]$
$A_I'''$	Interfacial area per unit volume	$[m^{-1}]$
$A_S$	Flow area of sub-channel	$[m^2]$
$A_T$	Total area of sub-channel	$[m^2]$
$C^*$	Coefficient in formula for bubbly/slug interfacial area	$[-]$
$C_D$	Drop drag coefficient	$[-]$
$C_{LM}$	Lockhart-Martinelli coefficient	$[-]$
$C_p$	Specific Heat	$[Jkg^{-1}K^{-1}]$
$D, d$	Diameter	$[m]$
$D_c$	Diameter of annular core	$[m]$
$D^*$	Diameter used in bubbly/slug flow regime	$[m]$
$D_H$	Hydraulic diameter	$[m]$
$D_{HAVE}$	Average hydraulic diameter	$[m]$
$D_H^*$	Non-dimensional hydraulic diameter	$[-]$
$E_\infty$	Droplet drag entrainment model coefficient	$[-]$
$e$	Internal energy	$[Jkg^{-1}]$
$f_f$	Friction factor	$[-]$
$\vec{F}_I$	Friction at vapor-liquid interface	$[kgm^{-2}s^{-1}]$
$F_I$	Interfacial drag coefficient	$[kgm^{-2}s^{-2}]$
$F_S$	Wall friction factor	$[kgm^{-3}s^{-1}]$
$f_{wet}$	Fraction of the surface covered by a liquid film	$[-]$
$G$	Mass flux	$[kgm^{-2}s^{-1}]$
$\vec{g}, g$	Gravity constant	$[ms^{-2}]$
$H_A$	Heat transfer area density	$[m^{-1}]$
$h$	Heat transfer coefficient	$[Wm^{-2}K^{-1}]$
$h$	Specific enthalpy (Eq. (64))	$[Jkg^{-1}]$
$K_1$	Correction factor for the hydraulic diameter in Groeneveld LUT	$[-]$
$L$	Characteristic length	$[m]$
$P$	Pressure	$[Pa]$
$P^*$	Non-dimensional pressure	$[-]$
$p_{factor}$	Pressure correction factor in Groeneveld LUT	$[-]$
$P_i$	Void dispersion term	$[Pam^{-1}]$
$P_{IS}$	Spacers' friction factor	$[kgm^{-3}s^{-1}]$
$p_r$	Reduced pressure	$[Pa]$
$P_s$	Profile slip factor	$[-]$
$Q$	Heat exchange	$[Wm^{-3}]$
$Q'''$	Volumetric heat generation rate	$[Wm^{-3}]$
$q''$	Surface heat flux	$[Wm^{-2}]$
$Q_H$	Internal heat source in porous structure	$[Wm^{-3}]$
$Q_I$	Heat exchange between phases	$[Wm^{-3}]$
$Q_{FIV}$	Heat flux in vapor	$[Wm^{-2}]$
$Q_S$	Heat transfer source between structure and fluid	$[Wm^{-3}]$
$Q_{FS}$	Heat flux between structure and fluid	$[Wm^{-2}]$
$Ra$	Surface roughness	$[m]$
$r$	Radius	$[m]$
$S$	Suppression factor	$[-]$
$T$	Temperature	$[K]$
$t$	Time	$[s]$
$\ddot{U}$	Ünal coefficient	$[-]$

$\vec{V}, V$	Velocity of fluid	$[ms^{-1}]$
$V_r$	Relative velocity	$[ms^{-1}]$
$Vn_i$	Node volume	$[m^3]$
$V_V$	Void volume in sub-channel	$[m^3]$
$V_T$	Total volume in sub-channel	$[m^3]$
$\Delta V$	Velocity difference	$[ms^{-1}]$
$\bar{v}_{gj}$	Weighted drift flux velocity	$[ms^{-1}]$
$w$	Weighting factor	$[-]$
$\vec{w}$	Darcy velocity	$[-]$
$x = \frac{G_v}{G_v + G_l}$	Quality	$[-]$
$x_e$	Equilibrium quality	$[-]$
$X_{tt}^{-1}$	Martinelli parameter	$[-]$

### *Greek letters*

$\alpha$	Volume fraction of fluid	$[-]$
$\beta$	Mixing coefficient (value between 0.02 and 0.06)	$[-]$
$\Gamma_l$	Rate of evaporation/condensation	$[kgm^{-3}s^{-1}]$
$\Gamma$	Mass transfer rate at subcooled boiling	$[-]$
$\Delta$	Change in denoting increment	$[-]$
$\nabla$	Gradient	$[m^{-1}]$
$\gamma$	Thermal expansion coefficient	$[K^{-1}]$
$\delta$	Film thickness	$[m]$
$\epsilon$	Surface roughness	$[m]$
$\epsilon_V$	Volume porosity	$[-]$
$\varepsilon$	Inverted $\Delta t$	$[s^{-1}]$
$\lambda$	Thermal conductivity	$[Wm^{-1}K^{-1}]$
$\mu$	Effective viscosity	$[Pa s]$
$\nu = \frac{\mu}{\rho}$	Kinematic viscosity	$[m^2s^{-1}]$
$\xi$	Pressure loss coefficient	$[-]$
$\rho$	Density	$[kgm^{-3}]$
$\sigma$	Surface tension	$[Nm^{-1}]$
$\theta$	Azimuthal angle	$[-]$
$\varphi$	Porosity	$[-]$

### *Dimensionless physical numbers*

$$Gr = \frac{g\gamma|T_w - T_l|D_{Have}^3}{\left(\frac{\mu_l}{\rho_{film}}\right)^2} \quad \text{Grashof number}$$

$$Nu = \frac{hL}{\lambda} \quad \text{Nusselt number}$$

$$Pe = \frac{G_l D_H C p_l}{\lambda_l} = Re Pr = \frac{Nu}{St} \quad \text{Peclet number}$$

$$Pr = \frac{\mu C p}{\lambda} \quad \text{Prandtl number}$$

$$Re = \frac{\rho V D_{HAVE}}{\mu} \quad \text{Reynolds number}$$

$$St = \frac{h}{C_p \rho V} = \frac{Nu}{Re Pr}$$

$$We = \frac{\rho_k V_k^2 L}{\sigma}$$

$$Fr = \frac{V}{\sqrt{gL}}$$

Stanton number

Weber number

Froude number

### Subscripts

<i>am</i>	Annular mist	<i>m</i>	Mixture
<i>annular</i>	Annular flow	<i>mol</i>	Molecular
<i>bs</i>	Bubble/slug	<i>msfb</i>	Minimum stable film boiling
<i>bub</i>	Bubbles	<i>nb</i>	Nucleate boiling
<i>cl</i>	Clad	<i>nc</i>	Natural convection
<i>cond</i>	Condensation	<i>onb</i>	Onset of nucleate boiling
<i>cr</i>	Critical heat flux	<i>pb</i>	Pool boiling
<i>d</i>	Direction	<i>reg</i>	Regime
<i>db</i>	Dispersed bubbly flow	<i>s</i>	Structure
<i>drop</i>	Droplets	<i>sat</i>	Saturation
<i>evap</i>	Direct evaporation from wall	<i>sing</i>	Single phase
<i>fc</i>	Forced convection	<i>sub</i>	Sub-cooled boiling
<i>film</i>	Film boiling	<i>tot</i>	Total
<i>fl</i>	Fuel	<i>tran</i>	Transition boiling
<i>i</i>	Node in lateral direction x, interface	<i>tur</i>	Turbulent
<i>j</i>	Node in lateral direction y, area boundary in fuel rod.	<i>v</i>	Vapor phase
<i>k</i>	Node in axial direction z, fluid phase	<i>w</i>	Wall surface
<i>l</i>	Liquid phase	<i>x</i>	Cartesian direction x
<i>lb</i>	Large bubbles	<i>y</i>	Cartesian direction y
<i>LUT</i>	Look-up Table	<i>z</i>	Cartesian direction z
<i>max</i>	Maximum		





# 1 Introduction

## 1.1 Motivation

Nowadays there are 451 nuclear reactors all over the world; from them 367 are Light Water Reactors and 75 of them are Boiling Water Reactors (BWR) [1]. In Mexico two BWR type GE BWR-5 Mark-II design plants are in operation and produce 6.01% of the total electric energy in the country [2]. The Fukushima severe accident highlighted the importance of reactor safety and the need for standardized safety requirements for all nuclear power plants worldwide. Moreover, it became also evident that the continuous back fitting and upgrade of the plant status is primordial to prevent accidents. For this purpose, numerical simulation tools describing the physical phenomena taking place in the whole nuclear power plant are extensively used to evaluate the plant safety status combined with probabilistic safety analysis methodologies. These numerical simulation tools must describe the core physics, thermal hydraulics, and thermo-mechanics, according to the state-of-the-art, to perform good predictions of the stationary plant conditions and later to be applied for the analysis of any kind of transients and accidents in nuclear reactors. The simulation tools cover phenomena in the core, in the primary and secondary circuit and in the containment. The focus of this doctoral thesis is the improvement of a thermal hydraulic code to describe the core phenomena of a Boiling Water Reactor using a porous-media approach.

In case of accidents in a nuclear power plant, an imbalance will occur between the heat generation inside the fuel pellets and the heat removal systems foreseen to remove the heat from the core to the heat sink. If there is a multiple failure of safety systems, an accident will progress leading to a core degradation. The local flow conditions will achieve Critical Heat Flux (CHF) conditions, where the heat transfer is non-sufficient to keep cladding material intact. Consequently, the safety barriers will fail, and the release of radioactive material will start.

A central concept in reactor safety is the Defense-in-depth concept, which is structured in five levels, and for each level goals and measures are developed to control accident events [3]:

- Prevention of abnormal operation and failures.
- Control of abnormal operation and detection of failures.
- Control of accidents within the design basis.
- Control of severe plant conditions, including prevention of accident progression and mitigation of the consequences of severe accidents.
- Mitigation of radiological consequences of significant releases of radioactive materials.

The analysis of the initiating events at each of these safety levels is done using numerical simulation tools, which must be validated using experimental data or by code-to-code comparisons.

Nowadays mainly one-dimensional system thermal hydraulic codes and sub-channel codes are being used to simulate the thermal hydraulic two-phase flow phenomena in the core of a BWR. These codes are not able to describe phenomena below the macro- and component scale. Recent work is focused on the use of improved methods such as computational fluid dynamics (CFD) or porous-media two-phase flow approaches to better describe the core thermal hydraulics of BWRs. At present, the two-phase models of CFD-codes are not yet sophisticated. Hence, the porous-media approach is a promising alternative. Codes based on this approach such as CUPID [4], and PORFLO [5], are examples for developments.

At the Karlsruhe Institute of Technology (KIT) a porous-media two-phase flow code, TWOPORFLOW, [6–10], is being developed for reactor applications. In the frame of the doctoral thesis, the TWOPORFLOW code is extended and validated for the simulation of BWR-cores. The main

challenges related to it, are described in the next subchapter. Later, the thesis objectives and the organization of the doctoral thesis is presented.

## 1.2 Challenges

In a reactor core, different mechanisms and processes that determine the integrity of the safety barriers take place e.g., two-phase flow and heat transfer along the core height. The coolant enters the lower part of the core under subcooled conditions; it is heated up reaching saturation conditions at around one third of the core height. There, steam is produced at constant temperature. The steam flow with high velocities is flowing upwards entraining water droplets, which are separated from main steam-flow by the separators located above the core. The liquid flows back to the downcomer where it is mixed with the main coolant water. To assure that only dry and hot steam is reaching the turbine, dryers are positioned in the reactor pressure vessel. Consequently, an internal recirculation loop is formed along the core, upper plenum, downcomer, and lower plenum which determines the pressure drop along the flow path and hence also along the core. Since the pressure directly affects the saturation temperature and hence the void generation inside the core, it is especially important to describe not only the heat transfer but also the pressure changes along the flow path in an accurate manner.

In addition, the geometric peculiarities of the in-vessel core components will strongly determine the flow velocity and pressure drop along the internal recirculation loop. It must be noted that the lower grid plate, the foot of the fuel assemblies, the spacer grids, the upper grid plate, and the fuel assembly head have complicated forms (see Figure 1.1). Detailed information about these components is needed to describe the flow and heat transfer inside the core and reactor pressure vessel with numerical simulation tools. Therefore, the knowledge of the thermal-hydraulic conditions in the Nuclear Power Plants (NPPs), mainly in the reactor core, is especially important. Measurements at different locations of the NPP can provide some information in this context, but important details within the fuel assemblies cannot be obtained by these methods. In order to evaluate, in detail, the thermal hydraulics phenomena inside the Reactor Pressure Vessel (RPV), it is necessary to use advanced numerical thermal-hydraulic simulation tools based on well validated physical models and numerically stable solutions.

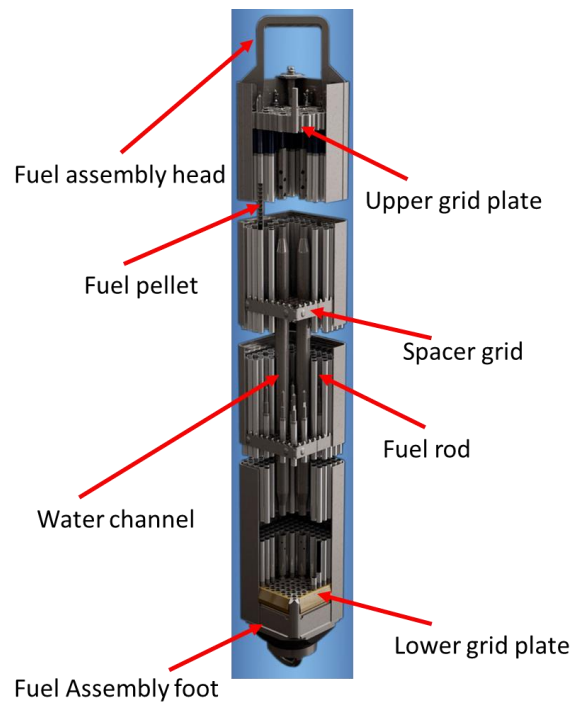


**Figure 1.1.** Main components of a BWR fuel assembly.

The main challenge of the doctoral thesis is to improve the prediction of thermal-hydraulic safety relevant phenomena occurring in the core of BWR during normal operation or under accidental conditions by using a tri-dimensional porous-media approach as implemented in the in-house code TWOPORFLOW. The code solves in 3D Cartesian geometry the mass, momentum and energy conservation equations based on the two-fluid porous-media approach to describe the thermal hydraulics of reactor cores.

The solution in TWOPORFLOW is more detailed than the one of 1D system thermal hydraulic codes, less CPU-intensive than CFD-codes and uses a full 3D approach, differing from the sub-channels codes which use a simplified momentum equation transversal to the axial direction.

Hence, the main pre-CHF heat transfer models in TWOPORFLOW are reviewed, validated, and improved in order to enhance the simulation of all safety-relevant phenomena in BWR-cores. Missing models e.g., for turbulent mixing and void dispersion are implemented and validated using appropriate test data. Furthermore, the existing Bowring CHF-correlation [11] already implemented in TWOPORFLOW as well other new correlations [12]–[14] will be implemented and extensively validated. Finally, the extended and validated TWOPORFLOW code is applied to simulate a BWR-core of a real nuclear power plant e.g., of the Mexican BWR plant Laguna Verde Unit 1. A validated 3D porous media code with a Cartesian mesh is very much appropriate to be coupled with a 3D core simulator such as PARCS [15]. This doctoral thesis will pave the way for such further developments.

### 1.3 Major objectives

Taking in to account the main challenges shortly discussed in the previous subchapter, the major goal of this thesis is to enhance the simulation of two-phase flow phenomena inside the RPV of BWRs for normal operation and transient conditions. Hence, the main thesis objectives are listed hereafter:

- Evaluation of the existing models in TWOPORFLOW, like sub-cooled boiling, transient void formation and pressure loss, using selected relevant tests.
- Improvement of the physical models of TWOPORFLOW related to safety relevant phenomena in Light Water Reactors e.g.
  - implementation of turbulent mixing in the momentum and energy conservation equations,
  - implementation of drift void dispersion in the momentum equations, and
  - improvement of Critical Heat Flux models.
- Validation of implemented models in TWOPORFLOW using selected experimental data for void fraction, pressure drop and critical power.
- Application of TWOPORFLOW to simulate a whole BWR-core at nominal and transient conditions.

### 1.4 Organization of thesis

The doctoral thesis is started with the introductory chapter, and it is followed by Chapter 2, where the general description of a Boiling Water Reactor is provided. In Chapter 3, a short description of thermal hydraulic core analysis tools is given.

In Chapter 4, a detailed description of the code, including the porous media approach, fundamental conservation equations, steam-water properties, heat conduction models, the constitutive models for conservation equations closure, and numerical method is presented.

The main work realized to achieve the objectives of this doctoral thesis is presented in the chapters 5 to 8. In Chapter 5 the improvements and implementations regarding the turbulent mixing, void dispersion and CHF are described. In Chapter 6 the validation of the models, including turbulent mixing, sub-cooled boiling, void dispersion, transient void, and pressure loss are presented, while in

Chapter 7 the validation of CHF is performed. Chapter 8 shows the application of TWOPORFLOW for the simulation of BWR reactor cores under normal and off-normal operation conditions.

The main conclusions of the doctoral thesis as well as future development possibilities are presented in Chapters 9 and 10, respectively

## 2 General description of Boiling Water Reactors (BWRs)

In Boiling Water Reactors, the steam produced in the core directly flows into the turbine. There are many manufacturers of BWR such as General Electric, ABB, former German KWU, Toshiba, etc. General Electric designed the BWR-plants of Generation 2, which are the major fraction of BWRs under operation worldwide. These plants are characterized by external recirculation loops and jet pumps located in the downcomer around the core to improve the internal recirculation of the coolant inside the reactor pressure vessel. In **Figure 1.2**, a simplified scheme of a BWR power plant of General Electric design is exhibited. The main components are the reactor building with the containment, the Reactor Pressure Vessel (RPV), the feedwater and steam line system, the turbine, condenser, and generator. The steam generated in the reactor core with entrained liquid droplets flows upwards and passes through the steam separators and dryers located above the reactor core. Afterward the steam leaves the RPV and flows through the long steam lines directly to the turbine, where it is expanded to transfer thermal energy into kinetic energy, which is utilized in the generator to produce electricity. The liquid separated from the steam in the separators flows downward in the downcomer and is mixed with the incoming main feed water. The main feed water flow is conducted to the RPV by the feedwater pumps; it passes through a pre-heater before reaching the RPV. The coolant is pumped into the lower plenum through jet pumps mounted around the core in the downcomer. The control rods are located below the core. The condenser is feed with cold water, normally taken from a natural water body like a lake, a river, or the sea.

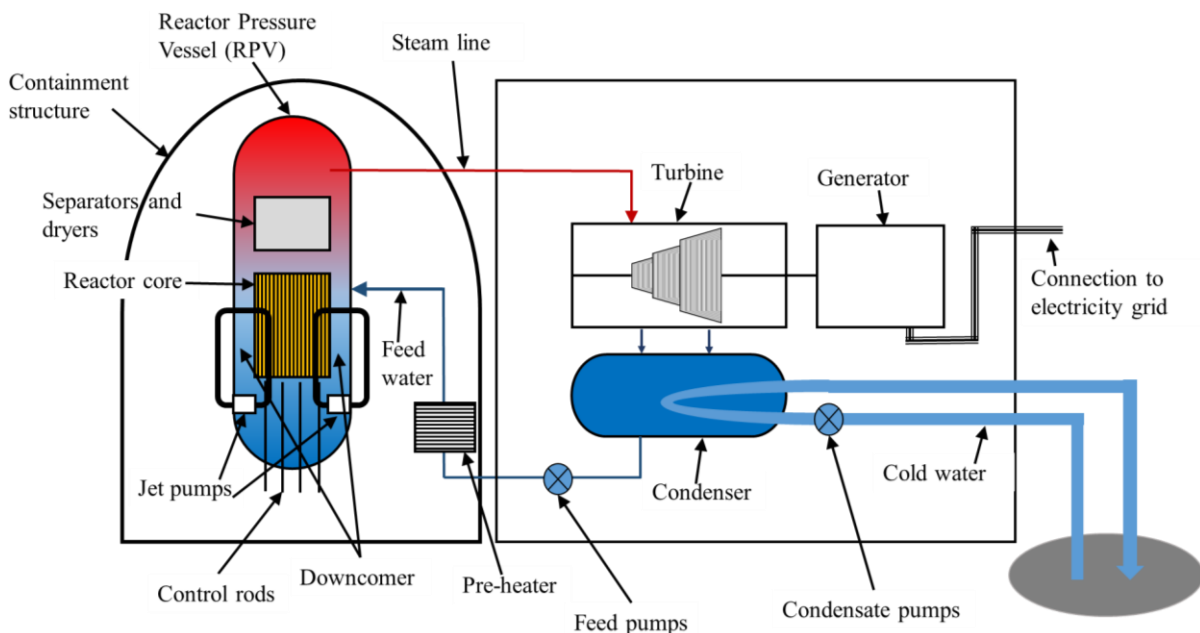


**Figure 1.2.** Simplified scheme of a BWR Nuclear Power Plant.

**Figure 1.3** shows the internals of the RPV of a BWR. The square fuel assemblies are in the core region and above the core the separators and dryers are positioned. The reactor core consists of fuel assemblies and control elements with a cross shape which can be inserted between four fuel assemblies. The fuel assemblies are composed of fuel rods cooled by light water, which serves also as the neutrons' moderator. The assemblies are arranged in simple square arrays supported by a grid plate [16]. The cylindrical fuel used in this kind of reactors is  $\text{UO}_2$  ( $^{235}\text{U}$  as fissile material and  $^{238}\text{U}$  as fertile material). The clad material is Zircaloy. Typical fuel assembly arrangements of BWR can consists of 8 x 8, or 9 x 9, 10 x 10, or 11 x 11 fuel rods. The older fuel assemblies e.g., 8x8 may not have water rods but all other new fuel assembly designs have water rods of different shapes to increase the moderation and hence the power production in the upper part of the core. The control rods are inserted from the bottom of the core and are made of boron carbide ( $\text{B}_4\text{C}$ ). They are the principal control and shutdown mechanism of the reactor power.

**Figure 1.3** shows an example of a RPV, and its main components, an example of a fuel assembly, and axial cuts of the core and an arrangement of four fuel assemblies and a control rod.

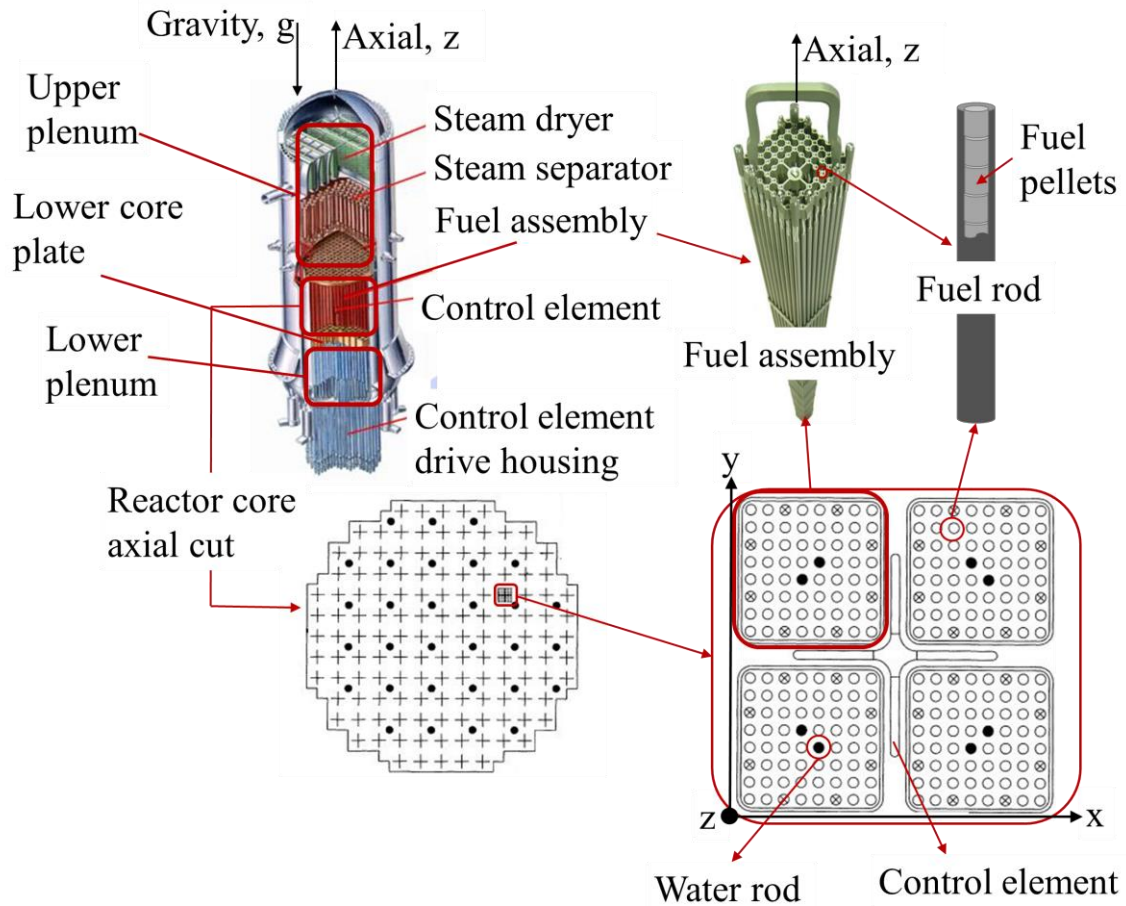


**Figure 1.3.** Scheme of a Reactor Pressure Vessel (top left) and a fuel assembly (top right), and axial cuts of both.

An example of the main thermal hydraulic BWRs data is listed in **Table 1.1**.

**Table 1.1** BWRs' thermal hydraulic typical values for cycle characteristics.

General plant data	
Gross thermal power [MW (th)]	3579
Net electrical power [MW(e)]	1178
Efficiency [%]	32.9
Thermal hydraulic parameters	
Pressure [MPa]	7.17
Inlet temperature [°C]	278
Average outlet temperature [°C]	288
Core flow rate [kg/s]	13100

The Oskarshamn-2 and the Laguna Verde unit 1 BWRs core will be simulated with TWOPRFLOW to demonstrate its improved capabilities. Both reactor cores have an arrangement of 444 assemblies and 109 control rods. Details about these reactors are given in Section 8.





### 3 Main characteristics of thermal hydraulic core simulation tools

At present, the thermal hydraulic phenomena of BWR-cores are simulated with different one-dimensional system thermal hydraulic codes e.g., TRACE, RELAP5 and quasi-three-dimensional subchannel codes such as CTF, FLICA4 or SUBCHANFLOW, which are characterized by two-phase flow models of different capability. Efforts are underway to extend the model capability of CFD codes for two-phase flow conditions like the ones of BWR-cores, which may be feasible in the medium term. A promising alternative is the porous-media approach for two-phase flow conditions as is being developed for new codes such as CUPID and PORFLO to fill the gap between the CFD and system thermal hydraulic codes.

In this chapter, the main shortcoming, and advantages of different thermal hydraulic codes to describe the BWR-core behavior are presented to emphasize the needs for alternative solutions based on the porous-media two-phase flow approach of the in-house TWOPORFLOW code.

#### 3.1 System thermal hydraulic codes

System thermal hydraulic codes are based on 1D models of two-fluids considering phase change with a coarse spatial discretization (donor-cell approach) to solve steady state or transient problems. The conservation equations of mass, momentum and energy are solved considering mechanical and thermal non-equilibrium. In the last decades, 3D models have been added to the system thermal hydraulic codes such as RELAP5, TRACE, ATHLET, CATHARE to better describe the phenomena inside the RPV and the core. The cylindrical or Cartesian meshing of the 3D models are rather coarse and, hence, phenomena taking place in smaller scales cannot be described by such codes [17]. The limitations of the system codes consist in the difficulty to simulate some phenomena at localized level e.g., turbulences, void drift, void fraction, subcooled boiling, etc.

For example, the German **ATHLET code** (Analysis of Thermal Hydraulics of Leaks and Transient) [18] is a highly modular code that consists of different modules such as: thermo-fluid-dynamic, heat transfer and heat conduction, neutron kinetics, and general control simulation modules. It solves the differential equation system using the FEBE-method (Forward-Euler, Backward-Euler). The thermo-fluid-dynamic equations are solved using either a 6-equations model (two-phase flow) or a 5-equations model (mixture momentum equation) in 1D-geometry.

The **TRACE code** (TRAC/RELAP Advanced Computational Engine) [19] is a system code developed by the United States National Regulatory Commission (US-NRC) for the analysis of loss-of-coolant accidents (LOCAs), operational transients, and other accident scenarios in PWRs and BWRs. It solves the fluid-dynamics equations in the spatial one-dimensional (1D), and three-dimensional (3D) components. TRACE takes a component-based approach to model a reactor system, including pipes, plenums, pressurizers, BWR fuel channels, jet pumps, separators, turbines, feed-water heaters, containment, valves, and vessels with associated internals. 3D (x, y, z) Cartesian- and/or (r,  $\theta$ , z) cylindrical-geometry flow calculations can be performed within the reactor vessel or other reactor components where 3D phenomena take place. Flows within a coolant loop are usually modeled in one dimension using pipes and tee components. A full two-fluid (six-equation) hydrodynamic model is used to evaluate gas-liquid flow.

Parallel to the code development, an extensive verification and validation program is conducted by the international community lead by the code developers to make sure that the codes are predicting in an accurate manner the key-phenomena of a nuclear power plant.

### **3.2 Sub-channel thermal hydraulic codes**

The sub-channel codes offer the possibility of simulating the fluid dynamics within the reactor core in more detail, i.e., at sub-channel level instead of coarse meshes used by the system thermal hydraulic codes. There are different approaches used in the sub-channel codes, depending on the problem to be simulated and the desirable detail of the simulation, going from single-phase fluid models, which have mixture liquid-vapor equations, to the multi-phase representations, which have three equations (momentum, energy, and mass) for each phase. One of the main characteristics of the sub-channel codes is the consideration that the fluid moves predominantly in axial direction, assuming the reduction of the three-dimensional equations to two equations, one for the flow in the axial direction and the other one transversal to the axial. This is a substantial simplification already, because the problem is converted mathematically from an elliptic to a parabolic type, which is for most cases justified. This approximation necessitates the introduction of cross flow, to consider the interchange of mass between neighboring channels. Two sub-channel codes are described below, CTF, which is one of the most known codes, and SUBCHANFLOW, developed at KIT.

CTF is the COBRA-TF version of the Pennsylvania State University (PSU) now the North Carolina State University (NCSU) and it originates from [20][21]. CTF extends the six conservation equations in two-fluid formulation to three fields: vapor, continuous liquid, and entrained liquid droplets, resulting in a set of nine time-averaged conservation equations. It uses coolant properties and state functions for water from the IAPWS-97 [22] (International Association for the Properties of Water and Steam) formulation. The conservation equations are solved using a semi-implicit, finite-difference numerical technique on an Eulerian mesh. CTF can solve a problem either in 3D Cartesian or sub-channel coordinates. Due to the flexible geometry definition, CTF can describe both hexagonal and square fuel assemblies and cores.

SUBCHANFLOW [23] is a sub-channel code developed at the Karlsruhe Institute of Technology (KIT) in Germany. It is based on the sub-channel COBRA-family programs. SUBCHANFLOW can manage both rectangular and hexagonal fuel bundles and core geometries built from these. It uses coolant properties and state functions for water from the IAPWS-97 [22] formulation. Thermo-physical functions for liquid metals and gases are also available. In SUBCHANFLOW, a three-mixture equation system for mass, momentum and energy balance is formulated, and corresponding constitutive equations for wall friction, wall heat transfer, slip velocity correlation, and void fraction are implemented.

### **3.3 Computational Fluid Dynamics (CFD)**

“Computational fluid dynamics (CFD) is a science that, with the help of digital computers, produces quantitative predictions of fluid-flow phenomena based on the conservation laws (conservation of mass, momentum, and energy) governing fluid motion” [24]. That gives quite a lot of freedom to simulate different geometric forms with more detail. The fundamental basis of each CFD code are the Navier-Stokes equations. The CFD codes are capable to simulate the flow behavior inside a structure with high resolution. The limitation with this kind of codes is that they need a high amount of CPU time, memory, and their two-phase flow models are still under development.

Parallel to the commercial CFD tools like, ANSYS CFX [25] open source CFD tools such as OpenFoam [26], TrioCFD [27] are gaining increasing use in different engineering areas among other also in nuclear engineering.

### **3.4 Porous media thermal hydraulic codes**

In the porous media codes, the computational domain is divided into a coarse mesh of limited volumes, each of which is characterized by volume-averaged parameters. The porous media approach is a practical method of analyzing typical geometries of interest like a fuel rod array in a nuclear reactor

core or the shell side of a steam generator in which an array of tubes carrying the primary coolant is immersed. The presence of solid objects in the flow domain has the effect of altering the pressure loss by friction and the heat transfer to the solid material, which is uniformly dispersed in the flow domain.

The porous media codes have been applied to simulate different problems, e.g. a first version of TWOPORFLOW is used to simulate micro-channel heat exchangers [7]. Other codes are used to simulate the secondary side steam generators in PWRs [28], the Passive Auxiliary Feed-water System (PAFS) [29], [30], Advanced Power Reactor 1400 (APR1400) core [31], lateral cross flow between fuel elements [32], the European Pressurized Reactor (EPR) [5], heat transfer and two-phase flow in a core debris bed [33], to name a few examples.

For example, **PORFLO** [34] is a code developed at the Technical Research Centre of Finland (VTT) . It solves a system of 5-equations in 3D porous media model using the Semi-Implicit Method for Pressure Linked Equations (SIMPLE) algorithm modified for two-phase flow. It has been coupled with the Serpent Monte Carlo reactor physics code, COSY a component/system scale thermal hydraulics solver module, and FINIX a general purpose fuel behavior module , in the framework of the project NUMPS (Numerical Multi-Physics) at VTT [35].

**CUPID** (Component Unstructured Program for Interfacial Dynamics) [36] is a code developed at the Korea Atomic Energy Research Institute (KAERI). It is a three-dimensional thermal-hydraulic code for the simulation of two-fluid, three field problems in nuclear reactor components. The governing equations are solved on an unstructured grid with a semi-implicit method. It is coupled with the system thermal hydraulic code MARS (Multi-dimensional Analysis of Reactor Safety) for the analysis of a PAFS [29] as well as with a three dimensional neutron kinetics code MASTER (Multi-purpose Analyzer for Static and Transient Effects of Reactors) [31].



## 4 The porous media two-phase flow code TWOPORFLOW

TWOPORFLOW is a porous media code developed to simulate thermal-hydraulics phenomena in single- and two-phase flow in micro-channel heat exchangers [7]. Later, it has been modified and extended to simulate the thermal hydraulics of reactor cores. TWOPORFLOW solves six governing equations for liquid and steam in 3D Cartesian geometry. More details about the equations are given in the next subchapters.

As working fluid, only steam and water are included and the state equations based on the IAWPS-formulation are implemented [22].

For fuel rods, a 2D heat conduction model is implemented for cylinder geometries where the Fourier's law equation is solved using the finite volume method considering the temperature-dependent thermo-physical material properties of the corresponding materials.

In TWOPORFLOW, a set of wall/fluid and inter-phase heat transfer correlations are implemented for a vertical flow regime covering the whole pre-CHF range to close the system of conservations equations.

### 4.1 Porous media approach in TWOPORFLOW

In the porous media approach, solid structures such as fuel rods are represented like blocking volumes and areas. TWOPORFLOW is capable to simulate a structured (calculating the porosity based on the dimensions of the regular structures) and unstructured (knowing the porosity of the medium) porous medium. **Figure 4.1** shows schematically the two types of porous medium configurations. In BWR cores, a typical configuration is the structured porous media.

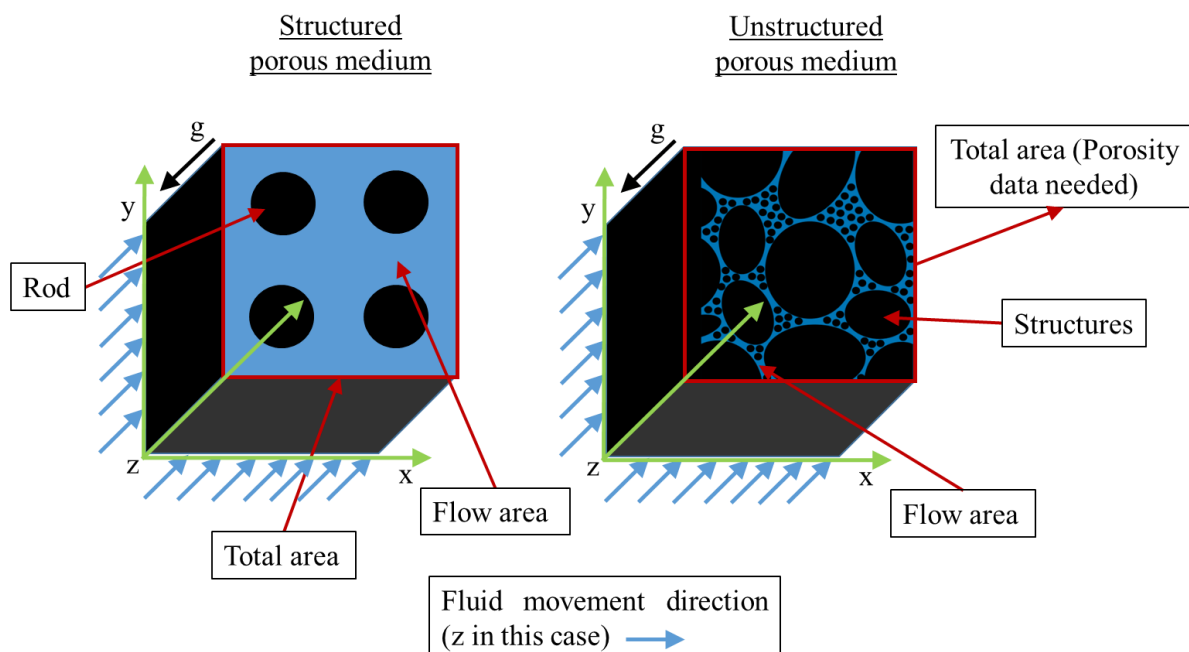


**Figure 4.1.** Scheme of structured and unstructured porosity medium.

In order to calculate the thermal hydraulics in reactor cores, TWOPORFLOW needs both the flow area fraction ( $\phi$ ) for each Cartesian coordinate ( $x, y, z$ ) and the volume porosities ( $\epsilon_V$ ) as input.

The calculation of  $\epsilon_V$  in each node is performed by dividing the volume of the fluid ( $V_V$ ) by the total volume of the node ( $V_T$ ):

$$\epsilon_V = \frac{V_V}{V_T}. \quad (1)$$

In order to calculate the flow area fraction ( $\varphi$ ) in each Cartesian coordinate, the total area ( $A_T$ ) and the flow area ( $A_w$ ) are used:

$$\varphi = \frac{A_w}{A_T}. \quad (2)$$

The hydraulic diameter ( $D_H$ ) should be given as input as well. The hydraulic diameter in each Cartesian coordinate is calculated by:

$$D_H = 4 \frac{A_w}{P_w}, \quad (3)$$

where  $P_w$  is the wetted perimeter which is the sum from the perimeters of the structures in the cross-sectional area which are in contact with the fluid.

The heat transfer area of the node is calculated from the heat transfer area density  $H_A$  (which is given as input) and the total volume of the node by the expression:

$$A = H_A V_T. \quad (4)$$

The Cartesian discretization can be done in different ways e.g., centered rod, centered coolant, or assembly wise where the whole assembly is seen as a sub-channel. These options of spatial discretization available in TWOPORFLOW are shown in **Figure 4.2**.

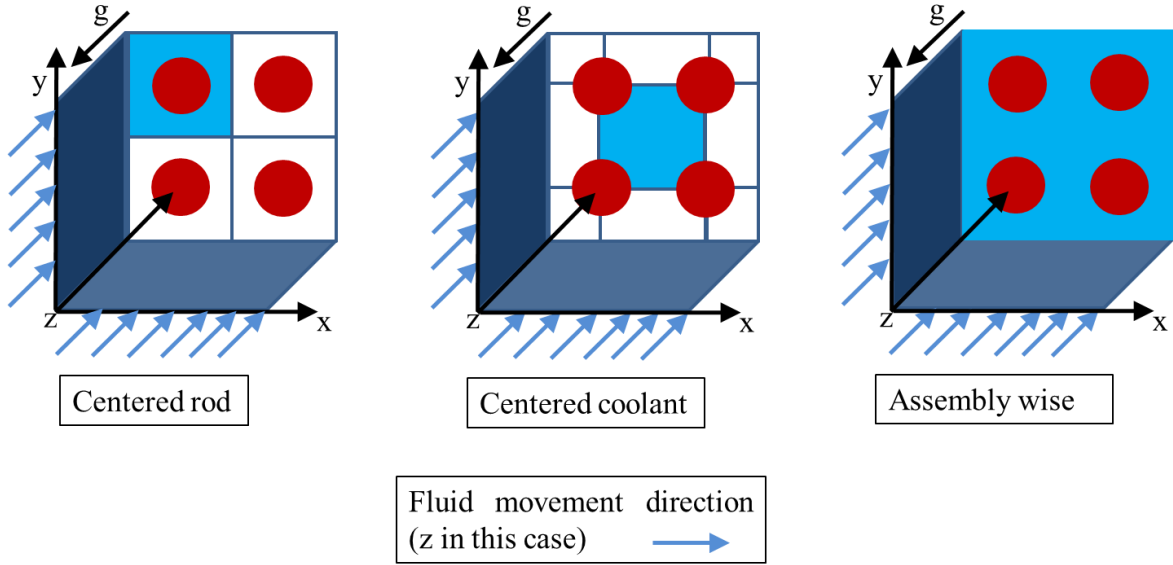


**Figure 4.2.** Different options for spatial discretization of the computational domain in TWOPORFLOW.

## 4.2 System of conservation equations

TWOPORFLOW solves a system of six conservation equations formulated according to the two-fluid model. Three conservation equations are written for both the vapor and the liquid phase. It allows a general description of the two-phase flow in three-dimensions. In this model, it is possible to calculate the velocities and temperatures of the two phases separately. Moreover, porosity is implemented by the Fractional Area Volume Obstacle Representation (FAVOR) technique [37]. According to this technique, a velocity vector related to the area porosity is defined:

$$\vec{w}_k = \begin{pmatrix} \varphi_x & V_x \\ \varphi_y & V_y \\ \varphi_z & V_z \end{pmatrix}, \quad (5)$$

where the subscripts  $x, y, z$  represent the Cartesian coordinates, and  $k$  will become the fluid ( $l$  when liquid and  $v$  when vapor).

In order to describe two-phase flow, a large number of constitutive equations are required, e.g., correlations for heat transfer, wall friction, interphase momentum coupling which will be described in section 4.5.

Hereafter, the main balance equations are shortly presented.

### *Mass balance equations*

The mass conservation equations of the liquid ( $l$ ) and vapor phase ( $v$ ) are given by the following equations:

$$\frac{\partial(\alpha_l \rho_l \epsilon v)}{\partial t} + \nabla \cdot (\alpha_l \vec{w}_l) = -\Gamma_l, \quad (6)$$

$$\frac{\partial(\alpha_v \rho_v \epsilon_v)}{\partial t} + \nabla \cdot (\alpha_v \vec{w}_v) = \Gamma_l, \quad (7)$$

where  $\alpha_v$  is the vapor volume fraction,  $\alpha_l$  is the liquid volume fraction,  $\rho$  the density of the fluid and  $\Gamma_l$  the rate of evaporation/condensation at the liquid-vapor interface, which is described in Section 4.5.3. The sum of the fluid volume fractions is:

$$\alpha_l + \alpha_v = 1. \quad (8)$$

### Momentum balance equations

The momentum conservation equations are used in a non-conservative form, and they are given hereafter for the liquid and vapor phase:

$$\alpha_l \rho_l \frac{\partial \vec{V}_l}{\partial t} + \frac{\alpha_l \vec{w}_l \nabla (\vec{V}_l)}{\epsilon_v} + \alpha_l \nabla (P) = -\vec{F}_{wl} + \vec{F}_l + \alpha_l \rho_l \vec{g} + \alpha_l \vec{D}_l, \quad (9)$$

$$\alpha_v \rho_v \frac{\partial \vec{V}_v}{\partial t} + \frac{\alpha_v \vec{w}_v \nabla (\vec{V}_v)}{\epsilon_v} + \alpha_v \nabla (P) = -\vec{F}_{wv} - \vec{F}_l + \alpha_v \rho_v \vec{g} + \alpha_v \vec{D}_v, \quad (10)$$

$\vec{V}_l$  is the velocity vector,  $P$  the pressure,  $\vec{F}_{wl}$  the structure liquid wall friction Force  $\vec{F}_{wv}$  the structure vapor wall friction Force  $\vec{F}_l$  the friction force at vapor/liquid interphase,  $\vec{g}$  the gravity vector.

The diffusion terms are defined as:

$$\vec{D}_k = \frac{1}{\epsilon_v} \begin{pmatrix} \frac{\partial}{\partial x} \phi_x \mu_k \frac{\partial V_x}{\partial x} + \frac{\partial}{\partial y} \phi_y \mu_k \frac{\partial V_x}{\partial y} + \frac{\partial}{\partial z} \phi_z \mu_k \frac{\partial V_x}{\partial z} \\ \frac{\partial}{\partial x} \phi_x \mu_k \frac{\partial V_y}{\partial x} + \frac{\partial}{\partial y} \phi_y \mu_k \frac{\partial V_y}{\partial y} + \frac{\partial}{\partial z} \phi_z \mu_k \frac{\partial V_y}{\partial z} \\ \frac{\partial}{\partial x} \phi_x \mu_k \frac{\partial V_z}{\partial x} + \frac{\partial}{\partial y} \phi_y \mu_k \frac{\partial V_z}{\partial y} + \frac{\partial}{\partial z} \phi_z \mu_k \frac{\partial V_z}{\partial z} \end{pmatrix}, \quad (11)$$

$\mu$  is the effective viscosity.

### Energy conservation equations

For energy conservation equations, the internal energy ( $e$ ) is used as the main variable:

$$\frac{\partial(\alpha_l \rho_l \epsilon_v e_l)}{\partial t} + \nabla \cdot (\alpha_l \rho_l e_l \vec{w}_l) + P \nabla \cdot (\alpha_l \vec{w}_l) + P \epsilon_v \frac{\partial \alpha_l}{\partial t} - K_l = Q_{sl} - Q_l, \quad (12)$$

$$\frac{\partial(\alpha_v \rho_v \epsilon_v e_v)}{\partial t} + \nabla \cdot (\alpha_v \rho_v e_v \vec{w}_v) + P \nabla \cdot (\alpha_v \vec{w}_v) + P \epsilon_v \frac{\partial \alpha_v}{\partial t} - K_v = Q_{sv} + Q_l, \quad (13)$$



$Q_s$  is the heat exchange between structure and fluid and  $Q_l$  is the heat exchange between the phases i.e., liquid and vapor. The thermal diffusion term ( $K_k$ ) for liquid and vapor is given by the equation:

$$K_k = \frac{\partial}{\partial x} \lambda_k \alpha_k \epsilon_x \frac{\partial}{\partial x} T_k + \frac{\partial}{\partial y} \lambda_k \alpha_k \epsilon_y \frac{\partial}{\partial y} T_k + \frac{\partial}{\partial z} \lambda_k \alpha_k \epsilon_z \frac{\partial}{\partial z} T_k, \quad (14)$$

$\lambda$  is the thermal conductivity and  $T$  the temperature.

### 4.3 Steam-Water properties

In TWOPORFLOW, water and steam are implemented as working fluid. It is possible to choose between three different methods to calculate the state properties of water/steam mixture:

- **IAPWS-97:** calculates the state dynamic properties of water according to the IAPWS-97 formulation (The International Association for the Properties of Water and Steam) [22]. The IAPWS-97 consists of a set of equations for different regions covering the range from 273.15K to 1073.15 K for a pressure  $\leq 100$  MPa and 1073.15 K to 2273.15 for a pressure  $\leq 50$  MPa.
- **Water vapor simple:** water using fits and modifications made by Bill Rivard [38] from the group t-3 “Fluid Dynamics” of the last theoretical division of IAEA (International Atomic Energy Agency), taken from code TRAC (Transient Reactor Analysis Code) and recoded to improve efficiency. The compressed liquid properties have been reprogrammed by John Kelly (Massachusetts Institute of Technology, MIT) [39].
- **Water vapor detailed:** this option calculates the properties of water according to a simplified approach of the IAPWS data, taking values from Haar, Gallagher, and Kell steam tables [40].

### 4.4 The Heat conduction model

The calculation of the temperature distribution of cylindrical solid structures with or without heat source is performed in TWOPORFLOW by solving the Fourier’s equation according to the finite volume method for given boundary conditions and considering temperature-dependent thermo-physical properties of the materials of the solid structure. For example, a fuel rod consisting of a fuel pellet, a gas gap, and a cladding, is discretized radially and axially in material zones containing a certain number of mesh-points where the temperature is predicted. In **Figure 4.3**, the radial discretization of a fuel rod is shown with subdivisions of the pellet and cladding. The gap, inner, and outer cladding points are located on the cell boundaries. Since the axial heat conduction is rather small, compared to the radial heat conduction due to the dimension of the rod, it is neglected.

The rod temperature equation is given by:

$$\rho C_p \frac{\partial T}{\partial t} = \frac{1}{r} \frac{\partial}{\partial r} \lambda r \frac{\partial T}{\partial r} + \frac{\partial}{\partial z} \lambda \frac{\partial T}{\partial z} + Q \quad (15)$$

$T$  is the Temperature,  $t$  is the time,  $r$  is the radius and  $z$  the axial position.  $\rho$  is the density,  $C_p$  is the heat capacity,  $\lambda$  the thermal conductivity and  $Q$  is the heat generated inside the fuel. The equation is integrated over the volume leading to a set of linear equations for the temperatures of each radial ring. The coupled system is solved inverting a tridiagonal matrix. Since the axial heat conduction is rather small, compared to the radial heat conduction due to the dimension of the rod, it is evaluated in an explicit manner. In **Figure 4.3**, the radial discretization of a fuel rod is shown.

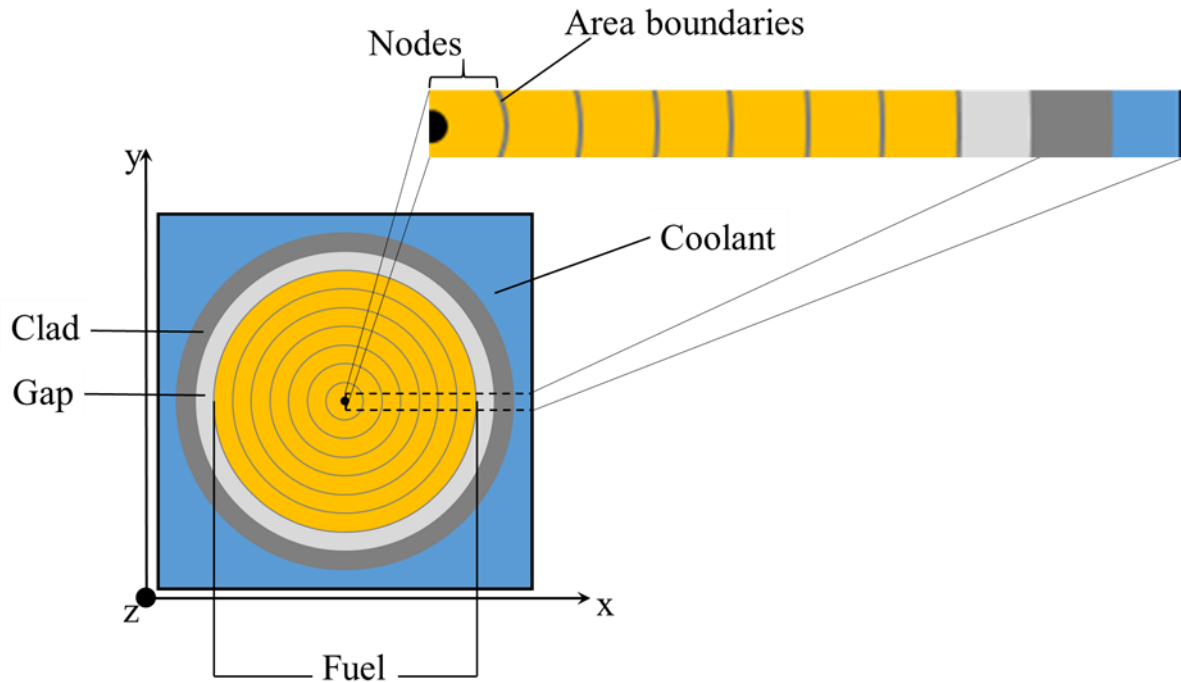


**Figure 4.3.** Schematic representation of a fuel rod with surrounding coolant and its radial discretization for the heat conduction solver.

#### 4.5 Constitutive models for the closure of the system of conservation equations

The system of conservation equations needs to be mathematically closed by the constitutive correlations. They are needed to describe the heat transfer from solid surface to coolant, liquid-vapor heat transfer including vaporization and condensation, wall friction, and liquid-vapor momentum coupling.

Non-dimensional properties are used in several empirical correlations describing physical processes like heat and momentum transfer. The non-dimensional key numbers used in TWOPORFLOW are defined in detail in Annex 1 equations (70) to (76).

In TWOPORFLOW, the following vertical flow regimes are defined based on the actual coolant temperature and saturation temperature:

##### *Sub-cooled regions ( $T_l < T_{sat}$ ):*

- **Convective heat-transfer:** the wall temperature ( $T_w$ ) and the liquid temperature ( $T_l$ ) are lower than the saturation temperature ( $T_{sat}$ ), having single-phase liquid.
- **Subcooled nucleate boiling:**  $T_w$  is higher than  $T_{sat}$ , but  $T_l$  still being lower, leading to the formation of bubbles only at the solid surface.

##### *Saturated regions ( $T_l, T_v = T_{sat}$ )*

- **Saturated nucleate boiling:** In this regime, three different flow patterns could appear: a) bubbly flow when vapor bubbles are present in a continuous liquid phase b) slug flow characterized by the presence of gas plugs separated by liquid slugs and c) annular flow characterized by the presence of a continuous core of gas surrounded by an annular liquid phase.
- **Two-phase forced convection:** Heat is transferred by convection through the thin liquid film to the vapor. Extremely high heat transfer coefficients are possible in this region.

- **Liquid deficient region:** this region is reached when  $T_w$  is higher than the critical temperature ( $T_{cr}$ ) meaning CHF is reached. A more detailed explanation of CHF is given in Chapter 5.3.

**Superheated regions ( $T_v > T_{sat}$ ):**

- **Convective heat-transfer to vapor:**  $T_v$  is higher than  $T_{sat}$  and the flow regime is single phase vapor.

In TWOPORFLOW, two different sets of models for interfacial momentum exchange, heat transfer coefficients and sub-cooled vapor generation are implemented. The first set of models consists of well-known empirical correlations characterized by their simplicity, which lead to a short computational time. The second set of models are based on correlations taken from the manual of the system code TRACE [19] and adapted to the structure and peculiarities of TWOPORFLOW. In this case, the correlations take into account additional parameters for example, the correlation of Ünal [41] to calculate the fraction of sub-cooled vapor generation, depends only on fluid velocities and temperatures, while the TRACE model [19] depends on the Peclet number, mass flow, temperatures of the fluid and the thermal conductivity, that leads the CPU time to increase. The first set of correlations are named as “TPF correlations” and the second one as “TPF-TRACE correlations.”

In **Figure 4.4**, a scheme of heat transfer and vertical flow regimes according to Collier [42] it is presented, where the areas of application of the two sets of correlations of TWOPORFLOW are indicated. The scheme shows that the heat transfer regimes are classified based on the equilibrium thermodynamic quality ( $x_e$ ) relating the flow enthalpy ( $h$ ) to the saturation liquid ( $h_{l,sat}$ ) and vapor ( $h_{v,sat}$ ) enthalpies.

$$x_e = \frac{h - h_{l,sat}}{h_{v,sat} - h_{l,sat}}. \quad (16)$$

The equilibrium quality can be used only for single-component mixtures (e.g., water with steam) and it can take values lower than zero (for sub-cooled fluids) and greater than one (for super-saturated vapors).

The flow quality ( $x$ ), which relates the vapor mass flow rate ( $G_v$ ) with the total mass flow rate (the sum of ( $G_v$ ) plus the liquid ( $G_l$ )) as:

$$x = \frac{G_v}{G_v + G_l}, \quad (17)$$

can be used to define the equilibrium quality as:

$$x_e = \frac{xh_v + (1 - x)h_l - h_{l,sat}}{h_{v,sat} - h_{l,sat}}. \quad (18)$$

Under equilibrium conditions  $h_l = h_{l,sat}$  and  $h_v = h_{v,sat}$ ; therefore  $x_e = x$ . In subsequent chapters, correlations that use the equilibrium quality, and other ones, which use the flow quality, are presented.

The TPF-TRACE set of correlations is applied only to calculate the pre-CHF flow regimes while the TPF set of correlations is applied to calculate the heat transfer along the entire boiling curve.

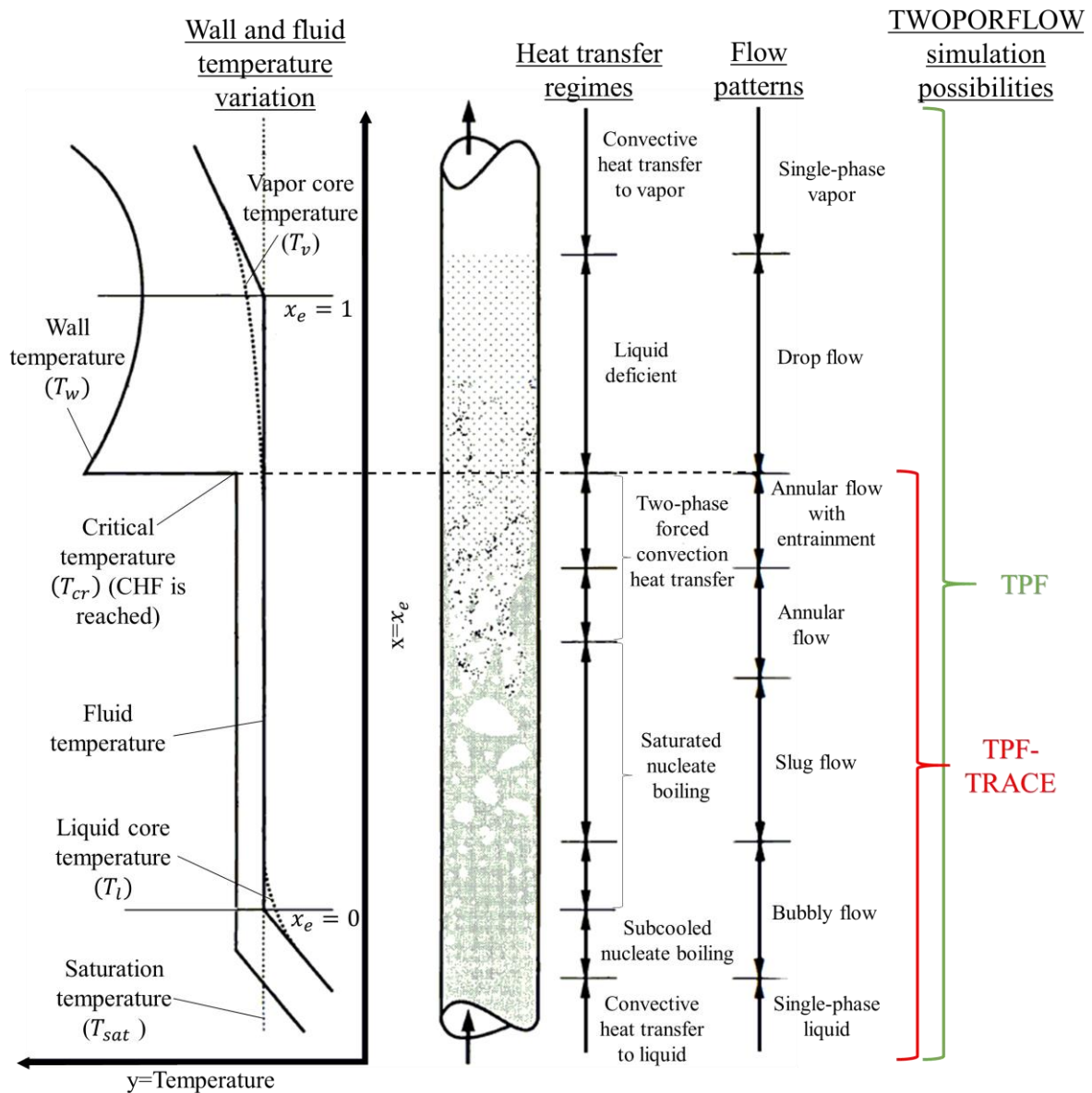


**Figure 4.4.** Heat transfer regimes description for uniform wall heat flux, and application of TWOPORFLOW (modified from [16] and [42]).

#### 4.5.1 Wall heat transfer

The boiling heat transfer plays a key role in reactor cores of BWR, in steam generators of PWR under normal conditions and in the core of PWR under accidental conditions. Hence, the modeling of such safety-relevant phenomena in simulation tools such as TWOPORFLOW is important. In TWOPORFLOW, correlations to calculate the heat transfer in all the pre-CHF regimes, single phase gas, condensation, and the film boiling - by interpolation between CHF and the MSFBT (Minimum Stable Film Boiling Temperature) or Minimal Heat Flux (lower limit for the heat flux in the film boiling regime)- are implemented.

Since the CHF-prediction in TWOPORFLOW is done using the Bowring [11] correlation and this correlation has not yet been validated, a goal of this dissertation is to implement and validate other models, in order to have a wider range of applicability in the code (different boundary conditions and

geometries). For each flow regime, the heat transfer coefficient is computed based on a specific correlation considering the local void fraction and the wall surface temperature.

The wall heat transfer area and the hydraulic diameter are provided by input. The hydraulic diameter is given at the cell interfaces for each direction of the flow (x, y, z). However, the hydraulic diameter must be calculated at the center of the cell for the TWOPORFLOW heat transfer models. Hence, the averaged hydraulic diameter at the cell center is determined by the following relation:

$$D_{Have} = \frac{\sum_{i=1}^3 D_{Hi} G_i}{\sum_{i=1}^3 G_i}. \quad (19)$$

$D_{Hi}$  represents the hydraulic diameter in direction  $i$  and  $G_i$  is mass flow rate and it is given by the subsequent equation:

$$G_i = \alpha_v \rho_v |V_{v,i}| + \alpha_l \rho_l |V_{l,i}|. \quad (20)$$

In general, the heat transfer from the fuel rod surface to the coolant is computed by using the heat transfer coefficients ( $h$ ) to the liquid and vapor phase. The vapor power density generated by the heated rod surface is calculated by the following relation:

$$Q_{sv} = \frac{A h_{v,fc} (T_w - T_v)}{V}, \quad (21)$$

$A$  is the area of the rod surface and  $V$  the cell volume. The liquid power density generated by the heated rod surface is expressed by the relation:

$$Q_{sl} = \frac{A (h_{l,fc} (T_w - T_l) + h_{l,nb} (T_w - T_{sat}))}{V}. \quad (22)$$

$h_{l,fc}$  is the liquid heat transfer coefficient for forced convection and  $h_{l,nb}$  is the liquid heat transfer coefficient for nucleate boiling.

The constitutive models used to calculate the wall heat transfer in TWOPORFLOW by means of the TPF and the TPF-TRACE groups of correlations, in the different flow regimes are listed in **Table 4.1**. The details of the correlations are given in the Annex 1.

**Table 4.1.** Wall heat transfer constitutive models in TWOPORFLOW

Flow regime	Models (Detailed equations in Annex 1 section 1.a)	
	TPF	TPF-TRACE [19]
<b>Single-phase liquid/vapor convective heat transfer</b>	[43] Eq. (78) and (79) Annex 1	[44] [45] Eq. (97) to (99) Annex 1
<b>Subcooled/nucleate/saturated boiling</b>	[46] [47] Eq. (80) to (85) Annex 1	<b>Onset of nucleate boiling</b> [48] Eq. (100) Annex 1
		<b>Subcooled/nucleate boiling</b> [49] Eq. (105) to (107) Annex 1
<b>Transition boiling</b>	[50] [51] Eq. (86) to (89) Annex 1	
<b>Film boiling</b>	[52] [53] Eq. (90) to (94) Annex 1	
<b>Condensation</b>	[54] [51] Eq. (95) and (96) Annex 1	[55][43] Eq. (101) to (104) Annex 1

#### 4.5.2 Fraction of sub-cooled vapor generation

The sub-cooled boiling is a transition regime between convection and saturated boiling. Vapor bubbles are generated at the wall due to nucleate boiling. Some of them collapse immediately due to condensation while others detach and become part of the bulk two-phase flow. Other bubbles slide along the heated surface before either condensing or detach. The mass transfer rate due to subcooled boiling is necessary to calculate the heat exchange for direct evaporation from the wall, which at the same time is necessary to calculate the heat exchange between phases.

The correlations used in TWOPORFLOW to calculate the sub-cooled vapor generation in both groups of correlations are listed in **Table 4.2.** .

**Table 4.2.** Fraction of sub-cooled vapor generation correlations in TWOPORFLOW

TPF	TPF-TRACE [19]
[56] Eq. (108) to (110) Annex 1	[57] Eq. (111) and (112) Annex 1

### 4.5.3 Liquid-vapor interface heat and mass exchange models

The interfacial heat and mass exchange are defined at the vapor interface by the expression:

$$Q_{Iv} + \Gamma_I h_{v,sat} = Q_I, \quad (23)$$

and at the liquid interface as:

$$Q_{Il} - \Gamma_I h_{l,sat} = -Q_I. \quad (24)$$

The interfacial heat mass transfer rate is given by the combination of the equations (23) and (24):

$$\Gamma_I = - \left( \frac{Q_{Iv} + Q_{Il}}{h_{v,sat} - h_{l,sat}} \right). \quad (25)$$

The models used in TWOPORFLOW to calculate the interfacial heat and mass exchange and the heat mass transfer rate in the different regimes are listed in **Table 4.3**. The TPF group of correlations use, in this case, the same model for all the two-phase flow regimes.

**Table 4.3.** Liquid-vapor interface heat and mass exchange models in TWOPORFLOW

Regime	TPF	TPF-TRACE[19]
Dispersed bubbly flow	[58] [51]Eq. (113) to (134) Annex 1	[59] [60] [61] [62] Eq. (135) to (141) Annex 1
Bubble/Slug		[63] [60] [64]
Annular/Mist		[55] [65] [66] [67] [68] [69] Eq. (153) to (166) Annex 1
Interpolation Dispersed/cap slug bubble and annular mist		Eq. (167) Annex 1

#### 4.5.4 Wall friction

The wall shear forces need to be calculated to solve the momentum conservation equations. It is necessary to calculate first a dimensionless friction factor  $f_f$ . The models used in TWOPORFLOW to calculate the wall friction are listed in the **Table 4.4**.

<b>Table 4.4. Wall frictions models in TWOPORFLOW</b>		
Regime	TPF	TPF-TRACE
Bubbly Slug	[16] [47] [70] Eq. (168) to (177) Annex 1	[71] [72] Eq. (179) to (182) Annex 1
Annular flow		[73] Eq. (183) to (187) Annex 1
Transition bubbly/slug to annular/mist		Eq. (188) and (189) Annex 1

#### 4.5.5 Liquid vapor momentum coupling

As well as the wall friction, the friction forces between phases are necessary to solve the momentum conservation equations. In TWOPORFLOW the velocities of the two phases are coupled by the interfacial drag force that arises from shear between the phases and is defined by:

$$\vec{F}_I = F_I V_r |\vec{V}|. \quad (26)$$

The models used in TWOPORFLOW to calculate the interfacial friction forces are listed in the **Table 4.5**.

<b>Table 4.5. Liquid vapor momentum coupling models in TWOPORFLOW</b>		
Regime	TPF	TPF-TRACE
Bubbly/slug	[16] Eq. (190) Annex 1	Eq. (191) to (193) Annex 1
Annular/Mist		[74] Eq. (194) to (204) Annex 1

#### 4.6 Numerical methods

In TWOPORFLOW a semi implicit transient numerical procedure based on the implicit continuous Eulerian (ICE) method [75] [76] is used to solve the basic conservation equations, based on a finite volume method with a staggered grid configuration in three dimensional Cartesian coordinates. The scalar variables are cell centered, whereas the velocity components are located on cell faces (see **Figure 4.5**).



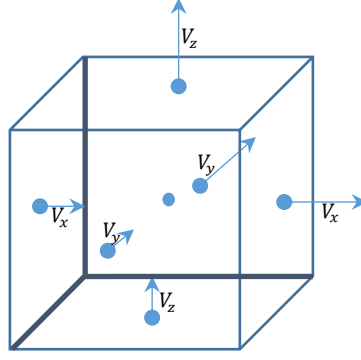


**Figure 4.5.** Typical mesh cell.

In TWOPORFLOW a steady state solution is calculated by a pseudo-transient. The criteria used to determine the steady state are the residuum of liquid and vapor velocities, void fraction, as well as the vapor, liquid, and surface temperatures:

$$\frac{dT_v}{dt} = \frac{T_v - T_{v,t-\Delta t}}{\Delta t}, \quad (27)$$

$$\frac{dT_l}{dt} = \frac{T_l - T_{l,t-\Delta t}}{\Delta t}, \quad (28)$$

$$\frac{dT_s}{dt} = \frac{T_s - T_{s,t-\Delta t}}{\Delta t}, \quad (29)$$

$$\frac{d\alpha_v}{dt} = \frac{\alpha_v - \alpha_{v,t-\Delta t}}{\Delta t}, \quad (30)$$

$$\frac{d|\vec{V}_v|}{dt} = \frac{|\vec{V}_v| - |\vec{V}_{v,t-\Delta t}|}{\Delta t}, \quad (31)$$

and:

$$\frac{d|\vec{V}_l|}{dt} = \frac{|\vec{V}_l| - |\vec{V}_{l,t-\Delta t}|}{\Delta t}. \quad (32)$$

The limits to reach steady state are given in the input. The simulations presented in this work are done using the values:

- For the temperature's residuum=  $1 \times 10^{-4} \frac{K}{s}$ ,
- Void residuum=  $1 \times 10^{-4} \frac{1}{s}$ ,
- Velocities residuum =  $1 \times 10^{-4} \frac{m}{s^2}$ .

The momentum convective terms are treated explicitly, and the momentum equations are written as finite-difference equations rearranged in a way that the new time step velocities are rewritten as a linear function of the local and adjacent cell implicit pressures.

The set of conservative continuity and energy equations is cell volume integrated in consideration of the volume and area porosities given by input. For each time step the velocity components in the cell boundary flux terms are eliminated by the momentum equations. Mass and energy equations are linearized in order to reduce the whole system to a pressure Poisson equation [77]. This can be solved using a Direct, SOR, ADI, or BICGSTAB solver. Pressure, temperature, and void fraction are obtained to calculate the fluid properties and the velocities are set up from the pressure gradients.

The heat conduction equation of the rods is solved with a finite-volume method and is calculated implicitly.

Stationary solutions are found by performing a transient calculation starting with appropriate initial and boundary conditions. The program stops at the end of the maximum time previously given as an input (for the transient) or when the steady state is reached. The enlargement of the time step is limited to 10%. In each computational cell the local time step is calculated by:

$$\Delta t = \frac{1}{\varepsilon} , \quad (33)$$

where:

$$\varepsilon = \left[ \frac{V_x}{\Delta x} + \frac{V_y}{\Delta y} + \frac{V_z}{\Delta z} \right] + 2 \left[ \frac{1}{\Delta x^2} + \frac{1}{\Delta y^2} + \frac{1}{\Delta z^2} \right] \left[ \frac{\alpha_l \mu_l}{\rho_l} + \frac{\alpha_v \mu_v}{\rho_v} + \frac{\alpha_l \lambda_l}{\rho_l C p_l} + \frac{\alpha_v \lambda_v}{\rho_v C p_v} \right]. \quad (34)$$

The time step is limited by the Courant condition (first term of equation (34)), the viscous diffusion time scale, and the thermal inertia of the fluids (second term of equation (34)). The solution of the energy equation inside the fuel rods uses an implicit method, so the properties of the fuel rods do not appear in the time step limitation. The global time step is taken as the minimum of all local time steps. A flow chart of the solution procedure is presented in **Figure 4.6**.

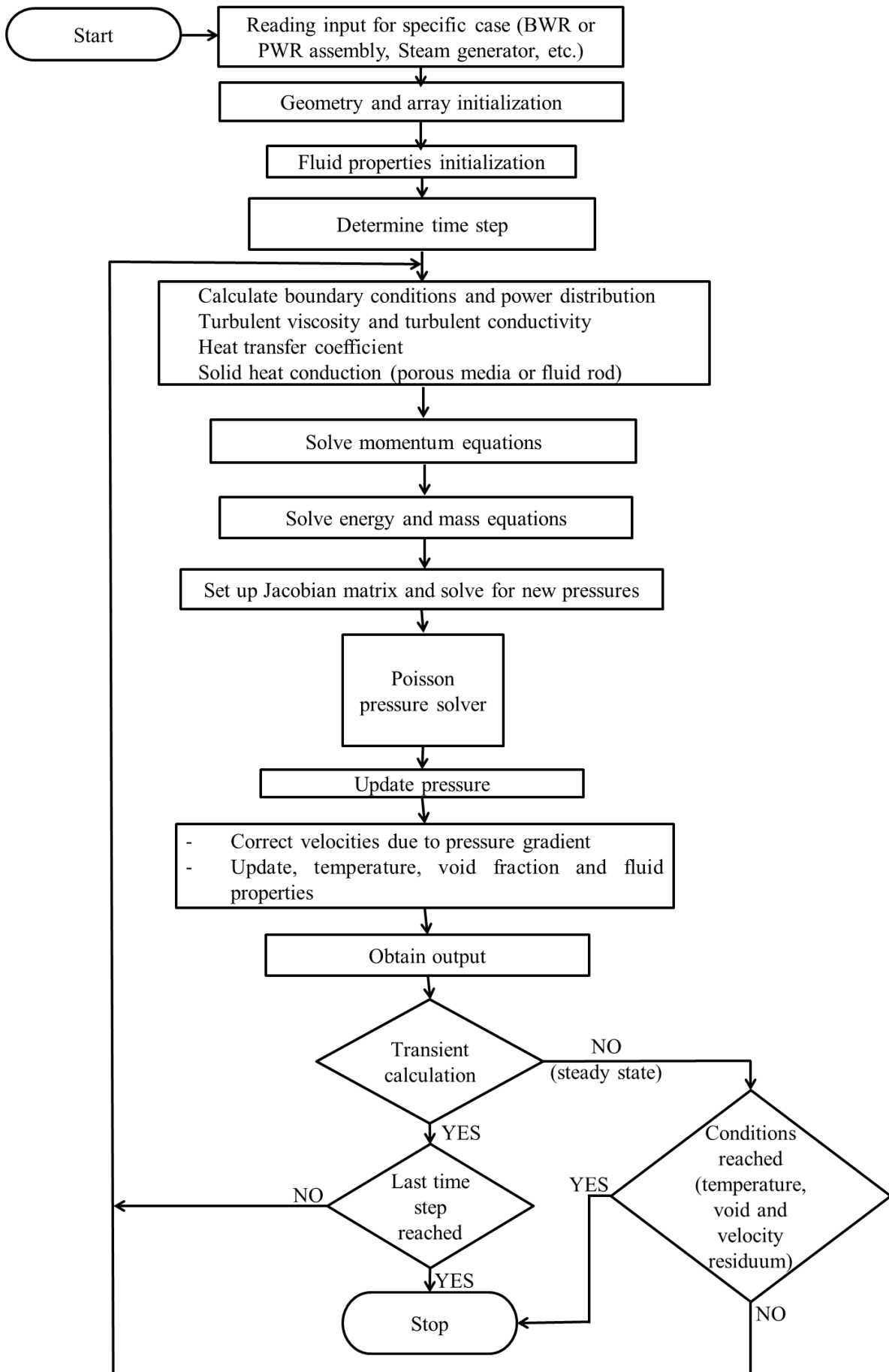


Figure 4.6. Flow chart of TWOPORFLOW.



## 5 Improvements of the porous media models of TWOPORFLOW

Simulation tools for design or safety evaluation of reactor cores must have reliable and validated models to describe safety-relevant phenomena e.g., pressure drop, heat transfer for flow regimes in the pre- and post-CHF region.

Hence, the models describing the natural mixing between sub-channels as well as the forced mixing due to constructive peculiarities e.g., mixing grids, and dry-out and departure from nucleate boiling will be revised and if necessary, implemented in the code.

Mixing models were not present in TWOPORFLOW, and for CHF only the Bowring correlation was implemented. The code was only capable of simulating correctly the phenomena that occurred in the pre-CHF regime.

In this section, the implementations of the single-phase thermal mixing, void drift and CHF are described. One of the basic ideas of this code is to maintain the straightforwardness and fast convergence. For this reasons, simple algebraic equations are used to calculate the thermal mixing and void dispersion.

### 5.1 Turbulent mixing

TWOPORFLOW is a code based on empirical correlations using a coarse mesh. A very detailed modelling of mixing effects as usually used in CFD codes does not fit into this concept. The mixing of momentum and energy is based on simple, but experimentally proven correlations in the area of thermal hydraulics of reactor cores.

#### 5.1.1 Turbulent viscosity

Turbulence models are based on the turbulent-viscosity hypothesis introduced by Boussinesq in 1877 [78]. As a result, the eddy viscosity can be specified as a function of a characteristic velocity and a characteristic length. Although the eddy viscosity hypothesis is not completely correct, it can provide an adequate estimate of turbulent flows. The effect of the turbulent viscosity of the flow between sub-channels in the momentum equations is described by a simple algebraic equation approach. According to it, the turbulent flow can be simulated as a pseudo fluid having an effective viscosity ( $\mu$ ), which is the result of the sum of the molecular and the turbulent viscosities. This extension is based on a mixing coefficient ( $\beta$ ) determined by fitting to experimental results [79]. According to it, the total viscosity is expressed by the following equation:

$$\mu_k = \mu_{mol,k} + \mu_{tur,k}, \quad (35)$$

where  $\mu_{tur}$  is the turbulent viscosity and  $\mu_{mol}$  the molecular viscosity. The subscript  $k$  indicates that it is applied for liquid  $l$  and vapor  $v$  phases. The turbulent viscosity is calculated as:

$$\mu_{tur,k} = \beta \rho_k V_k L, \quad (36)$$

where  $\rho$  is the viscosity,  $V$  the velocity of the fluid and  $L$  the characteristic length between sub-channels, which is defined by the sub-channel width.

### 5.1.2 Turbulent heat conductivity

In order to describe the effect of the turbulent flow between channels in the energy equation, the turbulent heat conductivity ( $\lambda_{tur}$ ) between adjacent sub-channels is calculated using the Prandtl number [80]. The Prandtl number is defined as the ratio between the momentum eddy diffusivity and the energy eddy diffusivity. In detailed turbulence analysis, the Prandtl number is a variable on a local scale. In the simplified view of TPF a constant value of 0.9 for the turbulent Prandtl number is used [81]. The turbulent heat conductivity is defined by the ratio of turbulent viscosity multiplied by the heat capacity and divided by the turbulent Prandtl number:

$$\lambda_{tur,k} = \frac{\mu_{tur,k} C_{p,k}}{Pr_{tur,k}}. \quad (37)$$

The turbulent heat conductivity is added to the molecular thermal conductivity of the fluid and it directly affects the conductivity terms in equations (12) and (13):

$$\lambda_k = \lambda_{mol,k} + \lambda_{tur,k}. \quad (38)$$

## 5.2 Void dispersion

The void distribution in the reactor core has a great influence on the neutron physics of the system. In strong axial dominated flow, vapor volume is transported in lateral direction. A simple model to describe void dispersion is added by the void dispersion term ( $P_i$ ) to the vapor momentum equation for bubbly flow. It is calculated from an assessment of the turbulent kinetic energy using the next equation [82]:

$$P_i = 0.4 \mu_{tur,l} \frac{V_l}{D_H}. \quad (39)$$

This implementation directly affects the equation (10) adding a term, and thus gives the following equation:

$$\alpha_v \rho_v \frac{\partial \vec{V}_v}{\partial t} + \frac{\alpha_v \vec{w}_v \nabla (\vec{V}_v)}{\epsilon_v} + \alpha_v \nabla (P) = -F_{wv} \vec{V}_v - \vec{F}_l + \alpha_v \rho_v \vec{g} + \alpha_v \vec{D}_v - P_i \nabla \alpha_v. \quad (40)$$

## 5.3 Critical Heat Flux (CHF)

The CHF is a physical phenomenon which leads to the substantial deterioration of the heat-transfer coefficient of the two-phase flow [16]. Two different kinds of CHF conditions are important. In PWRs, the Departure of Nucleate Boiling (DNB) phenomenon occurs when the liquid in contact with the cladding disappears (due to a local increase of the heat flux) and instead it is in contact with a vapor film which strongly decreases the heat transfer coefficient since the heat capacity of vapor is quite small, compared to the one of water. Dry-out takes place when the liquid film of annular flow in a BWRs is evaporated at some location along the core height. In **Figure 5.1** both phenomena are shown graphically.

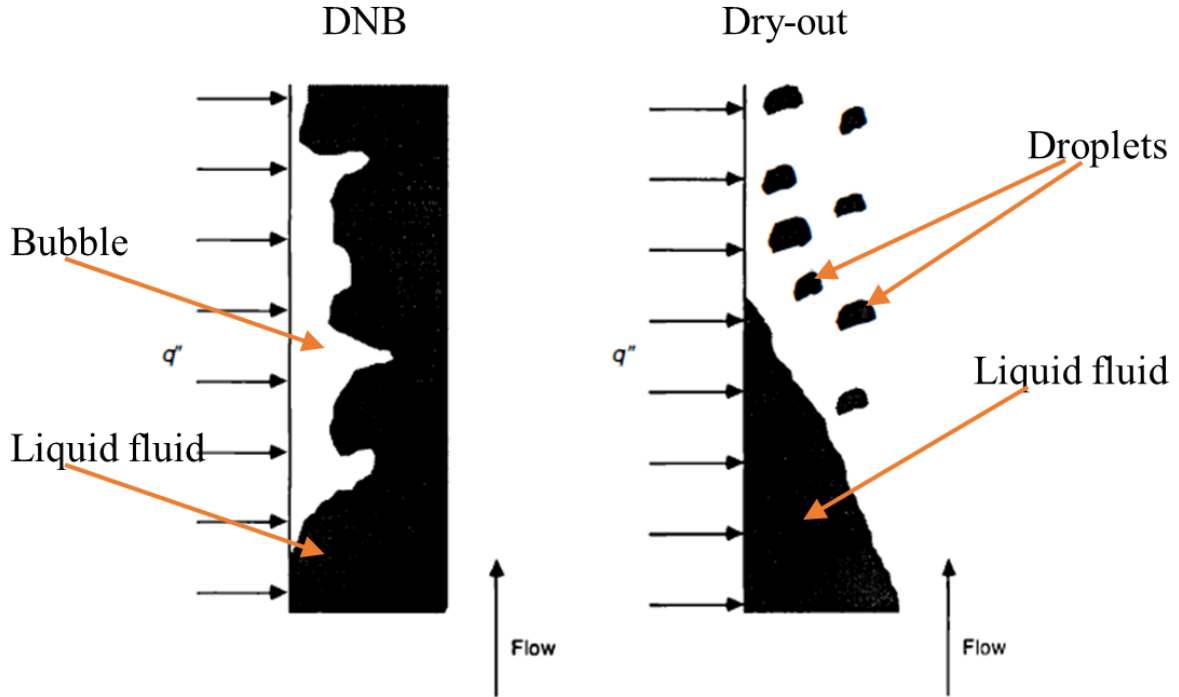


**Figure 5.1.** Departure of Nuclear Boiling and Dry-out.

The CHF is used to calculate the CHF Ratio (CHFR) known as well like DNB Ratio (DNBR). This is one of the most important safety margins in nuclear reactors. The CHFR is calculated as follows [16]:

$$CHFR = \frac{q''_{cr}}{q''}. \quad (41)$$

In this equation,  $q''$  is the actual critical heat flux predicted for a fuel assembly and  $q''_{cr}$  is the experimentally measured heat flux at which the CHF conditions occur.

This safety criterion establishes that the minimum value of CHFR (MCHFR or MDNBR) should not be less than 1.3.

In order to extend the models of TWOPORFLOW beyond the pre-CHF point, Bowring CHF model is revised, and new models have been added. In this connection, the iterative calculation of critical surface temperature considering the numerical stability is implemented. The new models are two correlations, (Biasi and Bowring) and the Groeneveld Look-up table.

The application ranges of key-parameters of the models are shown in **Table 5.1**.

**Table 5.1.** Limits of application from the CHF models implemented in TWOPORFLOW.

Correlation	Limits of application
Biasi	$D = 0.0030 - 0.0375 \text{ m}$
	$L = 0.2 - 6.0 \text{ m}$
	$P = 0.27 - 14 \text{ MPa}$
	$G = 100 - 6000 \text{ kg/m}^2\text{s}$
	$x = 1/(1 + \rho_l/\rho_v) \text{ to } 1$
Bowring	$D = 0.002 - 0.045 \text{ m}$
	$L = 0.15 - 3.7 \text{ m}$
	$P = 0.2 - 19 \text{ MPa}$
	$G = 136 - 18600 \text{ kg/m}^2\text{s}$
Groeneveld LUT	$D = 0.003 - 0.025 \text{ m}$
	$P = 0.1 - 21.0 \text{ MPa}$
	$G = 0.0 - 8000 \text{ kg/m}^2\text{s}$
	$x_e = -0.5 \text{ to } 0.9$

### 5.3.1 Biasi CHF correlation

The CHF Biasi correlation [12] has been developed for round ducts, and uniform heating with a root-mean-square (rms) error of 7.26% in 4551 data points, and 85.5% of the points are within +/- 10% absolute deviation. It is a function of pressure, mass flux, flow quality, and tube diameter. This correlation has been used in different thermal hydraulic simulation programs for nuclear applications, [20] and [19]. For high-quality conditions and a specific mass flow rate of  $G < 300 \text{ kg/m}^2\text{s}$ , the following equation is used:

$$q''_{cr} = (15.048 \times 10^7)(100D_H)^{-n}G^{-0.6}H(P)(1 - x), \quad (42)$$

For the low-quality region ( $G > 300 \text{ kg/m}^2\text{s}$ ), Biasi proposed:

$$q''_{cr} = (2.764 \times 10^7)(100D_H)^{-n}G^{-\frac{1}{6}}\left(1.468F(P)G^{-\frac{1}{6}} - x\right). \quad (43)$$

Where  $D_H$  is the hydraulic diameter,  $x$  is the quality defined as the ratio of the mass flow rate of vapor and the total mass flow rate:

$$x = \frac{G_v}{G_v + G_l} \quad (44)$$

and  $F(P)$  and  $H(P)$  are analytical functions of the pressure ( $P$ ), introduced to extend the validity range of the latter:

$$H(P) = -1.159 + 0.149P_{bar}e^{-0.019P_{bar}} + 9P_{bar}(10 + P_{bar}^2)^{-1}. \quad (45)$$



$$F(P) = 0.7249 + 0.099P_{bar}e^{-0.032P}. \quad (46)$$

Where  $P_{bar} = 10P$ , being  $P$  the pressure in MPa. For those expressions, the value of  $n$  is a constant dependent of  $D_H$  equal to:

$$n = \begin{cases} 0.4, D_H \geq 0.01 \text{ m} \\ 0.6, D_H < 0.01 \text{ m} \end{cases} \quad (47)$$

### 5.3.2 Bowring correlation

The Bowring correlation [11] is developed for round tubes with a uniform axial heat flux. The root mean square (rms) error in this correlation is 7% with 3800 data points. This correlation is a function of mass flow, pressure, flow quality, tube diameter, and inlet sub-cooling; and has probably the widest range of applicability in terms of pressure and mass flux [16]. The correlation is described by the following equations:

$$q''_{cr} = \frac{A - Bh_{fg}x}{C}, \quad (48)$$

being  $A, B$  and  $C$  functions of  $G, D, P$ :

$$A = \frac{2.317 \left( \frac{h_{fg}D_H G}{4} \right) F_1}{1 + 0.0143F_2 D_H^{1/2} G}, \quad (49)$$

$$B = \frac{D_H G}{4}, \quad (50)$$

and:

$$C = \frac{0.077F_3 D_H G}{1 + 0.347F_4 \left( \frac{G}{1356} \right)^n}. \quad (51)$$

Where  $n$  is calculated as:

$$n = 2 - 5p_r, \quad (52)$$

being a function of the reduced pressure ( $p_r$ ) as well as  $F_1$  to  $F_4$ :

$$p_r = 0.45P, \quad (53)$$

and the pressure ( $P$ ) is given in MPa.

For  $p_r < 1\text{MPa}$ :

$$F_1 = \frac{p_r^{18.942} \exp[20.89(1 - p_r)] + 0.917}{1.917}, \quad (54)$$

$$F_2 = \frac{F_1}{\left( \frac{p_r^{1.316} \exp[2.444(1 - p_r)] + 0.309}{1.309} \right)}, \quad (55)$$

$$F_3 = \frac{p_r^{17.023} \exp[16.658(1 - p_r)] + 0.667}{1.667}, \quad (56)$$

and:

$$F_4 = F_3 p_r^{1.649}. \quad (57)$$

For  $p_r > 1\text{MPa}$ :

$$F_1 = p_r^{-0.368} \exp[0.648(1 - p_r)], \quad (58)$$

$$F_2 = \frac{F_1}{p_r^{-0.448} \exp[0.245(1 - p_r)]}, \quad (59)$$

$$F_3 = p_r^{0.219}, \quad (60)$$

and:

$$F_4 = F_3 p_r^{1.649}. \quad (61)$$

### 5.3.3 Groeneveld look-up table

The 2006 Groeneveld Look-Up Table (LUT) [13] is a normalized database that predicts the CHF as a function of the coolant pressure, mass flow, and thermodynamic quality. It contains around 25000 data points taken from different correlations. The rms error at constant inlet flow conditions is 5.86%. The Groeneveld CHF used in TWOPORFLOW can be expressed as follows:

$$q''_{cr} = q''_{LUT} K_1 p_{factor}. \quad (62)$$

For a mass flow larger than the upper limit of  $G = 8,000 \text{ kg/m}^2 \text{ s}$  this value is used and for values of equilibrium quality below -0.5 a linear extrapolation is made:

$$q''_{cr} = \frac{q_{0.5} + (q_{0.4} - q_{0.5})(x_e + 0.5)}{0.1} K_1 p_{factor}. \quad (63)$$

The equilibrium quality is defined as:

$$x_e = \frac{h - h_{l,sat}}{h_{v,sat} - h_{l,sat}}, \quad (64)$$

where  $h$  is the local specific enthalpy of the fluid (single phase or two-phase),  $h_{l,sat}$  the liquid and  $h_{v,sat}$  the vapor saturated enthalpies, respectively. Thus, in the two-phase saturated region,  $0 \leq x_e \leq 1$ , in the subcooled region  $x_e < 0$  and in the superheated region  $x_e > 1$ .

In the last two expressions  $K_1$  is a correction factor for the hydraulic diameter taken from [14] and is expressed as:

$$K_1 = \begin{cases} \left[ \frac{0.008}{D_h} \right]^{1/2}, & D_H < 0.025 \text{ m} \\ K_1 = 0.57, & D_H > 0.025 \text{ m} \end{cases} \quad (65)$$

The  $p_{factor}$  is an approach used in case the pressure is outside the given ranges (if the pressure is inside the ranges  $p_{factor} = 1$ ). Then, the following equation is used for extrapolation [83]:

$$q''_{cr} = CHF(P_i, G_0, x_{e,0}) \frac{\rho_v^{1/2} h_{fg} [\sigma(\rho_l - \rho_v)]^{1/4} \Big|_{P_0}}{\rho_v^{1/2} h_{fg} [\sigma(\rho_l - \rho_v)]^{1/4} \Big|_{P_k}}. \quad (66)$$

Where  $P_k$  is either 100 kPa (if  $P_0 < 100$  kPa) or 21,000 kPa (if  $P_0 > 21,000$  kPa). In this particular case, the subscript  $k$  represents the pressure values of application ( $P_k, k = 100 - 21000$  kPa). In order to avoid the extra computational burden related to the calls at the fluid properties subroutine, it is necessary to evaluate the last term in Eq. (66) where a curve-fit is used [19]:

$$p_{factor} = \frac{q''_{CHF}(P, G, x_e)}{q''_{CHF}(P_k, G, x_e)} = 1.546P^* - 1.6108P^{*2} + 1.7818P^{*3} - 0.7199P^{*4}, \quad (67)$$

where the non-dimensional pressure is defined as:

$$P^* = \frac{P_{cr} - P}{P_{cr} - P_k}. \quad (68)$$

## 6 Validation of the pre-CHF models of TWOPORFLOW using experimental data

One of the main objectives of this work is the validation of both, the recently implemented and the already existing physical models in TWOPORFLOW. The physical phenomena investigated are turbulent mixing, sub-cooled boiling, void dispersion, transient void, and pressure loss using the already described groups of correlations TPF and TPF-TRACE (section 4.5). The validation of these phenomena is presented in chapters 6.1 through 6.4, making a general conclusion of the validation in section 6.5.

A brief description of the experiments is provided at the begin of each sub-chapter. It is necessary to mention that in TWOPORFLOW the axial mesh is relatively coarse compared to standard CFD simulations for single-phase flow. As usual in two-phase flow codes using interpenetrating fluids, the cell size cannot be smaller than the bubble or slug size. In addition, the axial nodalisation is oriented at the axial power distributions of the tests and the spatial resolution of the measurements.

Further details of the experiments and their boundary conditions in steady state are shown in the Annexes.

### 6.1 PSBT thermal mixing tests

By turbulent mixing, momentum, and energy transfer take place, but no net mass transfer between sub-channels. In order to describe the effect of the turbulent flow between sub-channels in the momentum equations a simple algebraic equation approach is implemented (Section 5.1).

The subchannel analysis of bundles is sensitive to the mixing coefficient ( $\beta$ ) (see section 5.1). According to [84], for assemblies containing mixing vane spacers, a constant value of ( $\beta$ ) is determined by single-phase flow experiments measuring the exit sub-channel temperature, which is valid for the geometry under consideration. In order to validate the thermal mixing model in TWOPORFLOW, steady-state liquid fluid temperature tests are simulated to obtain the value of ( $\beta$ ) which gives the best prediction of the experimental temperatures. The obtained results are compared with the ones obtained by another works, Section 6.1.3. By analogy, the liquid mixing coefficient is used for the vapor as well. In bubbly and slug flow regimes the vapor mixing coefficient is not as important as the liquid one, because the flow is mainly determined by the liquid flow due to the strong drag effects. The void dispersion term in the momentum equation gives the important contribution to vapor mixing effects between sub-channels.

#### 6.1.1 Short test description

The Nuclear Power Engineering Corporation (NUPEC) has developed and performed a series of tests, which are summarized in the NUPEC PWR sub-channel and Bundle Tests (PSBT) benchmark. It consists of two phases of measurements, in a representative PWR fuel assembly: Phase I.- Void distribution and Phase II.- departure from nucleate boiling (DNB) [85]. The latter is as well divided in three exercises: steady-state fluid temperature benchmark, steady-state DNB benchmark, and transient DNB benchmark. In order to validate the implementation of the turbulent-viscosity and conductivity in TWOPORFLOW (equations (36) and (37) in section 5.1), nine tests of the steady state fluid temperature benchmark have been used. These single-phase flow tests use a special lateral power distribution as given in **Figure 6.1**.

The assembly has a 5 x 5 rod array containing two non-mixing vane spacers, 8 simple spacers and 7 mixing vane spacers with pressure loss coefficients ( $\xi$  defined in Eq. (171), Annex 1) of 0.7, 0.4, and 1.0 correspondingly. The assembly has a constant axial power distribution. The boundary conditions are varying between the following ranges (details of the boundary conditions and geometric dimensions are given in Annex 2, **Tables 12.1 and 12.2**):

- Outlet pressure: 4.92 – 16.58 MPa,
- Inlet mass flow: 540 – 4722 kg/m<sup>2</sup>s,

- Inlet temperature: 86 – 289.2 °C,
- Bundle power: 0.4 – 3.44 MW.

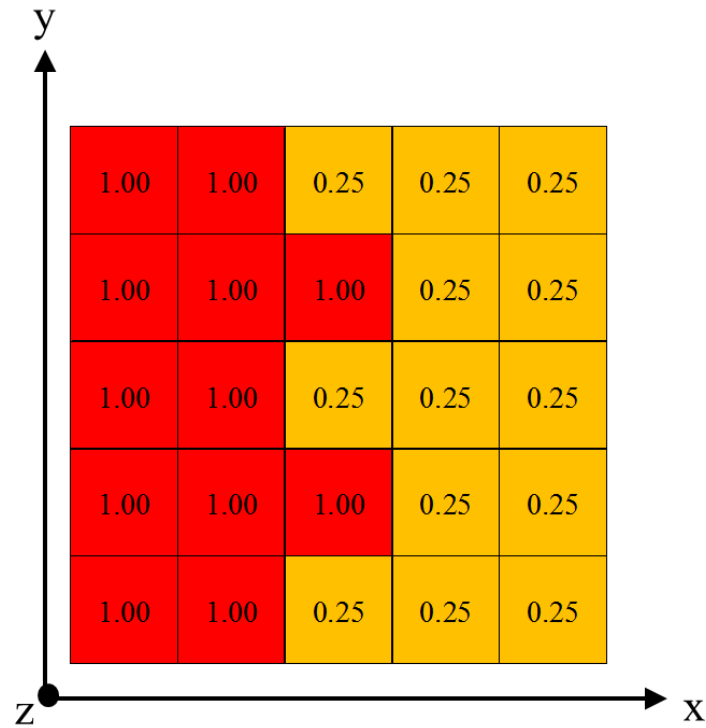


**Figure 6.1.** Normalized lateral power distribution of PSBT steady state fluid temperature bundle tests.

**Figure 6.2** shows the layout of the NUPEC PSBT test. The heated section has a length of 3658 mm and is shown in detail in **Figure 6.3**.

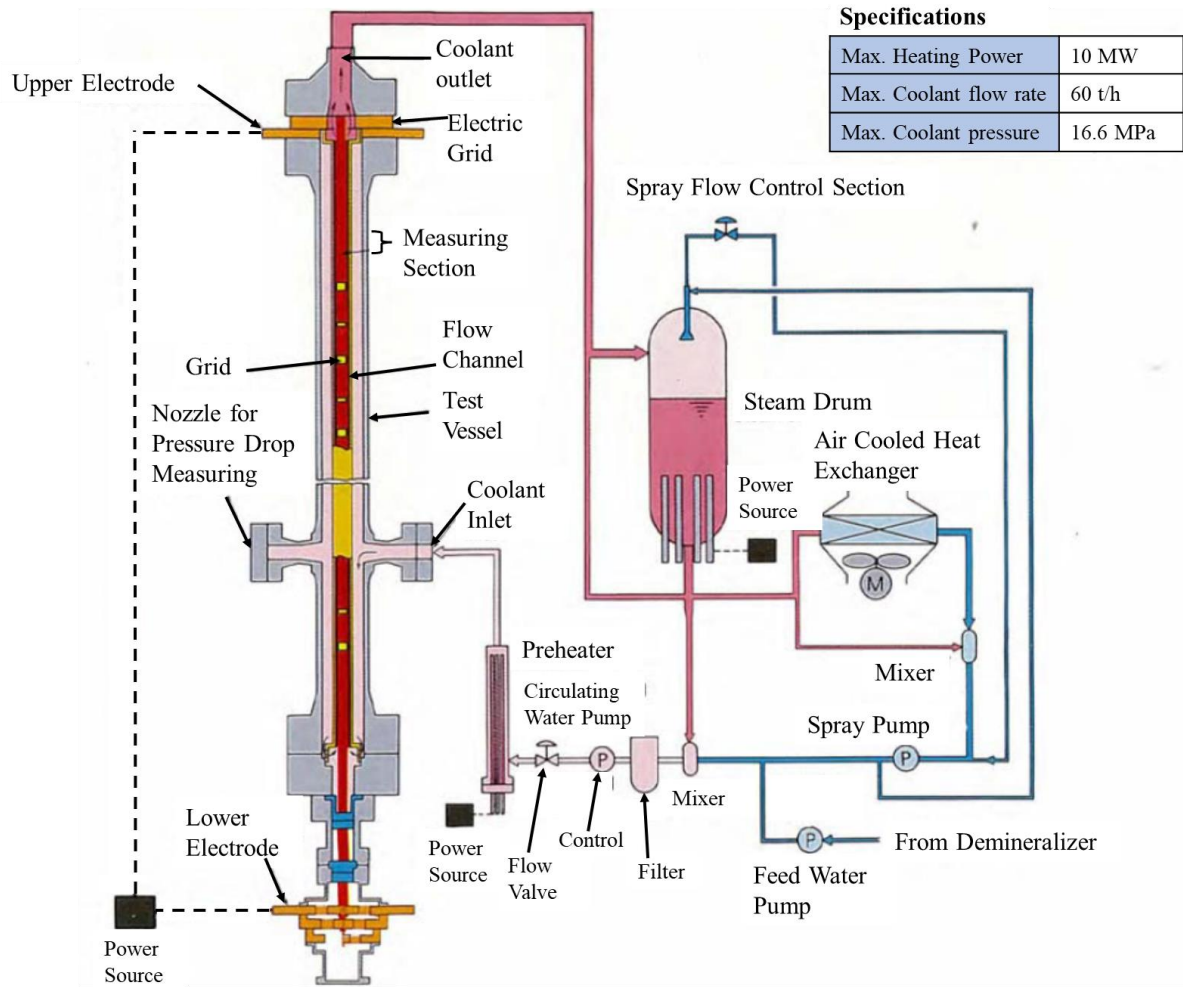


Figure 6.2. System diagram of NUPEC PSBT facility [85].

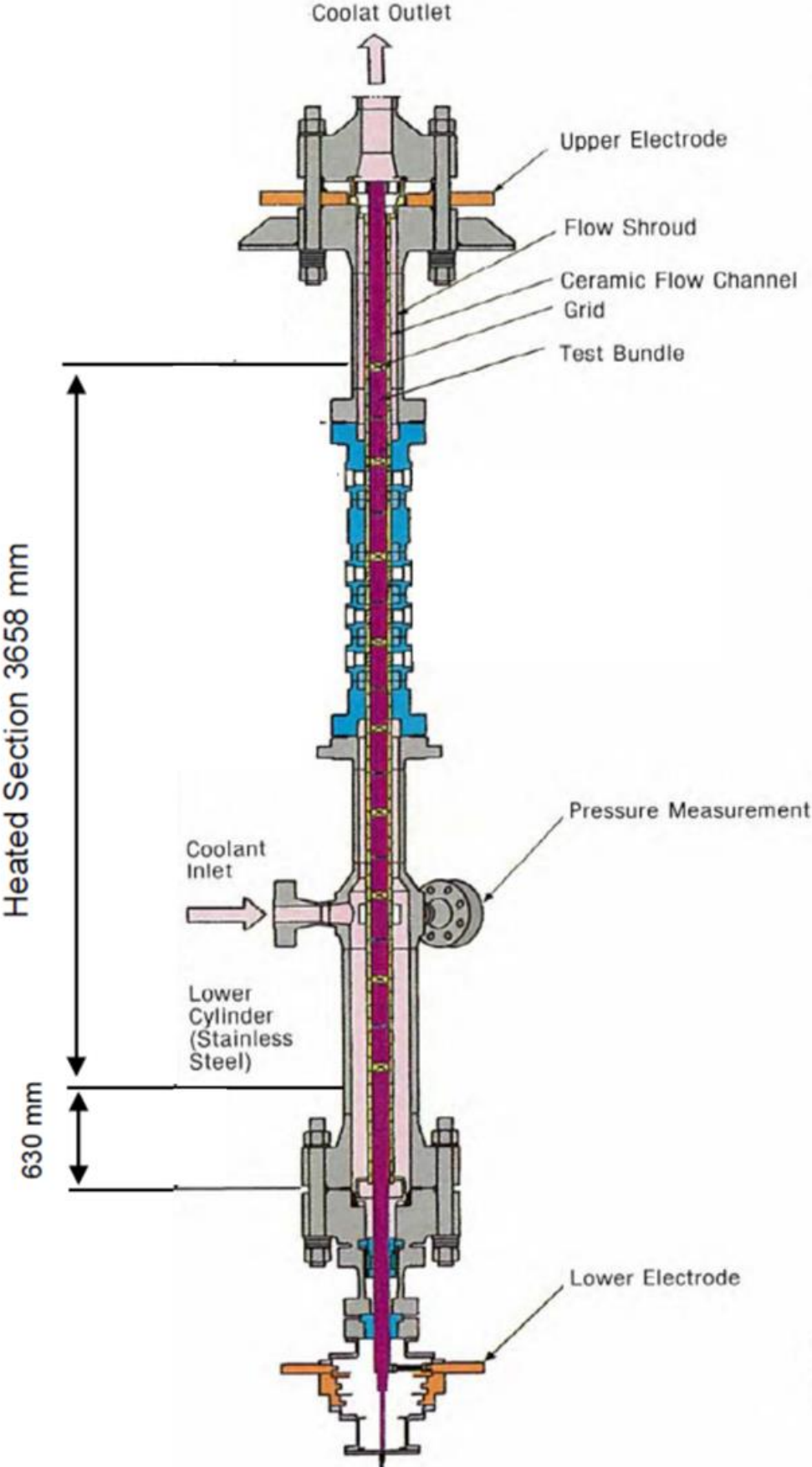


Figure 6.3. Test section thermal mixing tests of NUPEC PSBT facility [85].



The reported measurement error of the thermocouples in the experiments is about 1°C.

### 6.1.2 TWOPORFLOW modeling

In TWOPORFLOW, the mesh is constructed by a coolant centered sub-channel approach, resulting in an arrangement of 6x6 sub-channels in directions X and Y, respectively. The axial length has been divided in 27 equidistant nodes of 137.2 mm. The hydraulic diameters in axial direction are 11.7 mm (central channels), 8.13 (wall channels) and 6.35 (corner channels).

The number of rods per channel is  $\frac{1}{4}$ ,  $\frac{1}{2}$ , or one depending on the location of the sub-channel. In the centered coolant approach, the normalized power distribution of the sub-channel must be calculated considering all the rod parts that are inside the sub-channel (**Figure 6.4**).

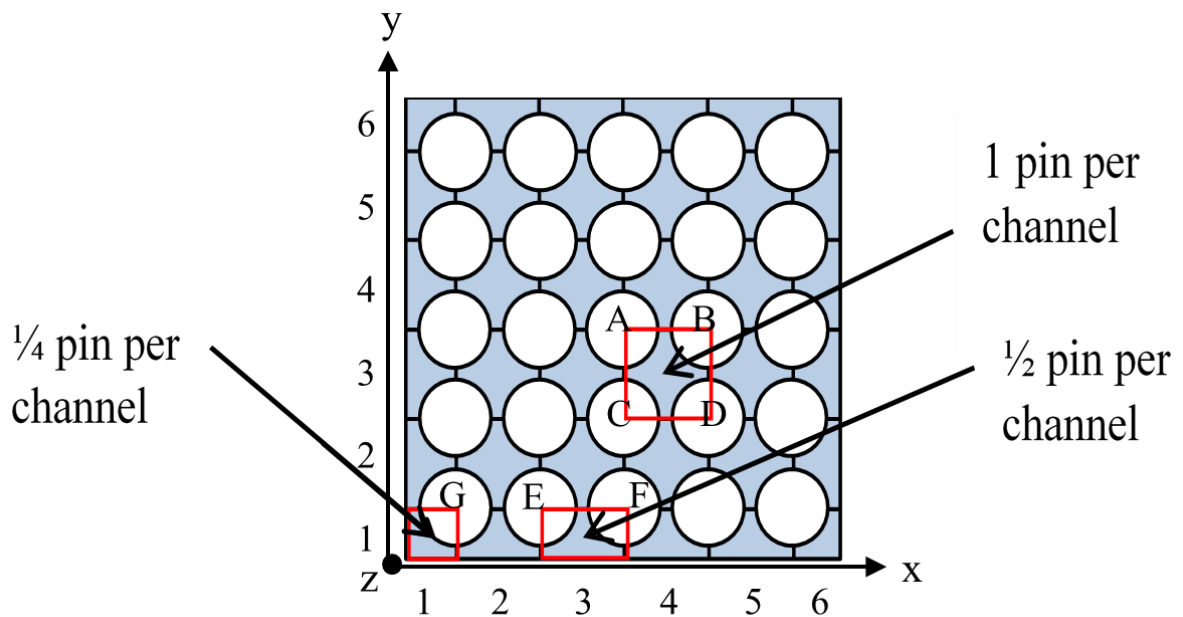


**Figure 6.4.** View from the top of the 6x6 sub-channel TWOPORFLOW's model of PSBT steady state fluid temperature bundle tests.

In the porous media description, the subchannel like flow is simulated by using a partial free flow area in the main flow direction giving the appropriate porosity. In the two lateral directions, the small gap between the heater rods defines the porosity. The heat transfer along the circumference of the rods is described by a surface area density in each volume cell. The boundary conditions sufficient to solve the equations inside the bundle are the flow rate and temperature at the bottom (inlet) and the pressure at the top (outlet).

### 6.1.3 Comparison of TWOPORFLOW predictions with experimental data

In both TPF and TPF-TRACE group of correlations six different values for the mixing coefficients ( $\beta$ ), namely 0.03, 0.04, 0.05, 0.06, 0.07 and 0.08 have been used. It is worth to note that in [23] and [86] is found out that mixing coefficient ( $\beta$ ) of 0.06 and 0.05 are the most appropriate values in order to predict the outlet temperature close to the measured values.

The outlet temperatures of each sub-channel predicted by TWOPORFLOW are compared with the measured ones. Then, the standard deviation of the predictions from the experimental values are calculated by the relation:

$$s = \sqrt{\frac{\sum_{i=1}^N (T_{exp,i} - T_{sim,i})^2}{N - 1}}, \quad (69)$$

where  $\{T_{exp,1}, T_{exp,2}, \dots, T_{exp,N}\}$  are the experimental values of the outlet temperatures,  $\{T_{sim,1}, T_{sim,2}, \dots, T_{sim,N}\}$  are the predicted outlet temperatures, and  $N$  is the number of simulation results. The standard deviation of the bundle outlet temperature calculated with Eq. 70 is shown in **Figure 6.5** for the different mixing coefficients considered in the simulations. It can be observed that the mixing coefficients 0.05 and 0.06 have the smaller standard deviations for both sets of correlations (TPF, TPF-TRCAE).

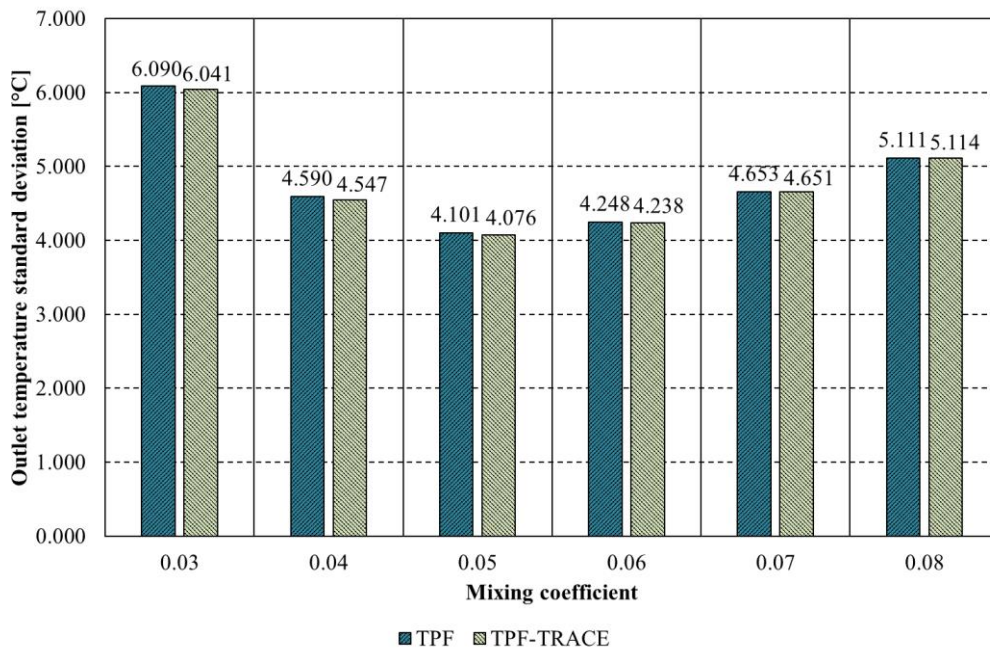


**Figure 6.5.** Comparison of standard deviations of the outlet temperature predicted using the TPF and TPF-TRACE set of correlations for six different mixing coefficients of PSBT steady state fluid temperature bundle tests.

In addition, a more detailed comparison of the predicted outlet temperatures using  $\beta = 0.05$  as mixing coefficient and the data follows.

The values of the experimental data, against the difference between the experimental and the simulated data for both correlations is shown in **Figure 6.6**. The graphic shows the 36 outlet channels of 9 different simulation cases which are in total 324 comparison points for every group of correlations.

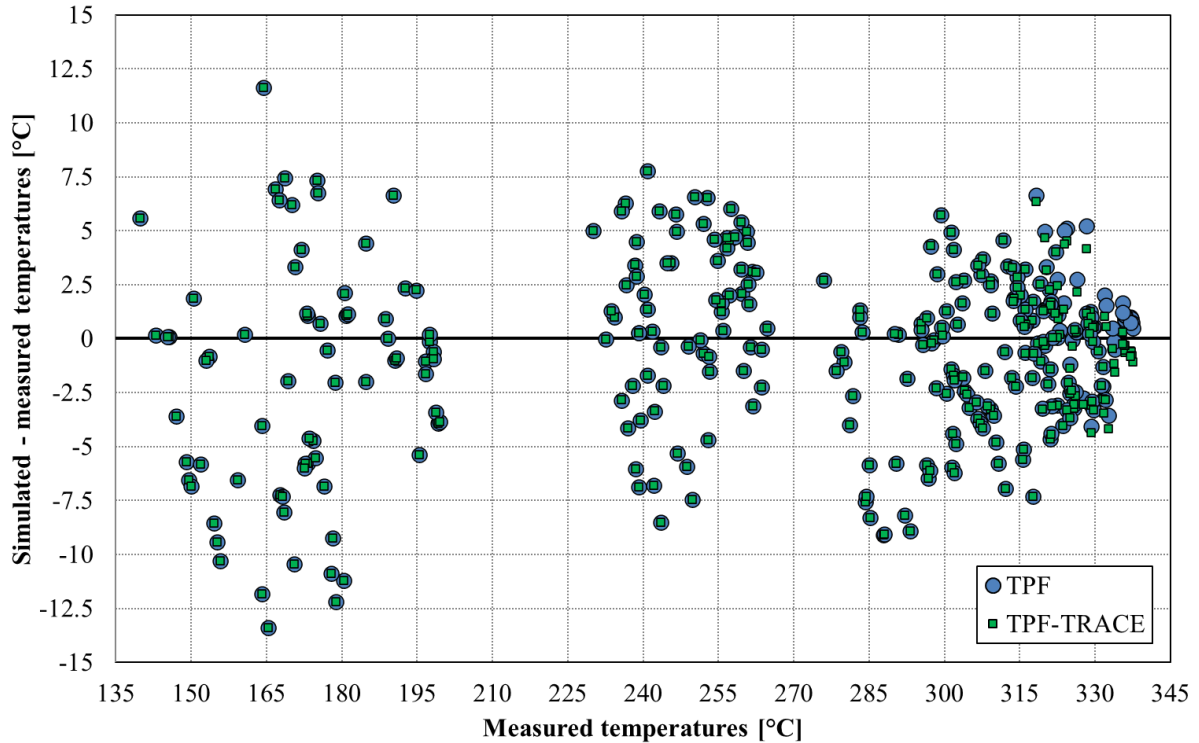


**Figure 6.6.** Difference between measured and simulated outlet temperature of predicted coolant temperature at the outlet of the 36 channels of the PSBT steady state fluid temperature tests obtained with TPF and TPF-TRACE set of correlations.

The average difference of the outlet temperature compared with the experimental with TPF is  $3.19^{\circ}\text{C}$  while with TPF-TRACE correlations is  $3.17^{\circ}\text{C}$ .

The maximal difference is around  $13.39^{\circ}\text{C}$  for both correlation sets. This corresponds to the channels located near the canister wall (channel (4, 6) in **Figure 6.4**), and where the largest power difference of the connected rods exists. These tests have also the highest mass flux of  $4722.31 \text{ kg}/(\text{m}^2\text{s})$ .

However, more than 80% of the deviations are under  $4^{\circ}\text{C}$ .

All predictions using the TPF set of correlations are nearer to the experimental data than the ones using TPF-TRACE correlation set. However, comparing the sub-channel temperatures obtained with both correlations, the average difference between them is  $0.094^{\circ}\text{C}$ .

Based on this analysis it can be concluded that both set of correlations predicts the bundle behavior with similar quality using the mixing coefficient of 0.05.

## 6.2 PSBT Sub-cooled boiling tests

### 6.2.1 Short test description

The validation of the subcooled boiling models of TWOPORFLOW is performed using the data of 43 tests of Single sub-channel test performed in the frame of the PSBT benchmark [85].

The single channel tests consist of four different geometrical types of sub-channels, which are described below (see **Figure 6.7**):

- Case S1. Center channels surrounded by four rods (16 selected cases are simulated).
- Case S2. Center channels surrounded by 3 fuel rods and a guide tube (12 cases).
- Case S3. Side channels surrounded by two rods and a part of the assembly wall (8 cases).
- Case S4. Corner channel surrounded by one rod and two wall parts (7 cases).

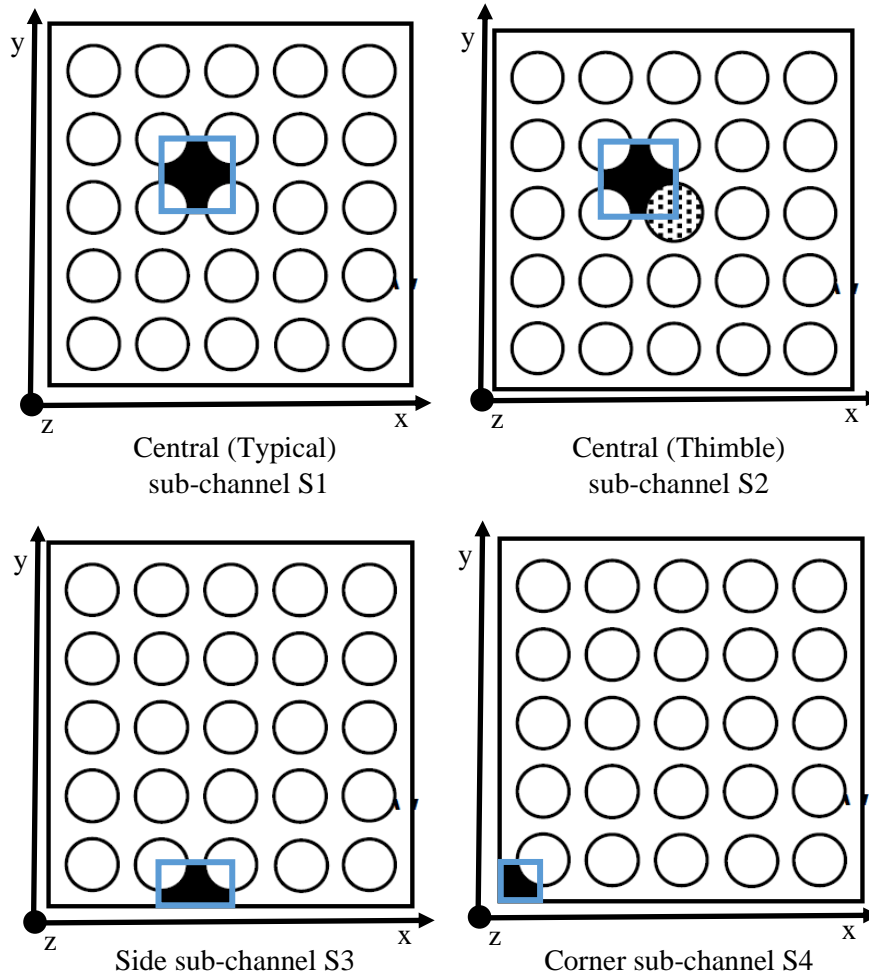


**Figure 6.7.** Different types of sub-channels simulated, the areas delimited by blue lines, are the equivalent to the different sub-channels' simulations of PSBT Single sub-channel tests.

The single sub-channel test section is uniformly heated along 1555 mm and the void measurement is done at 1400 mm elevation from the bottom of the heated section (see **Figure 6.8**). The loop used for this test is the same shown in **Figure 6.2**.

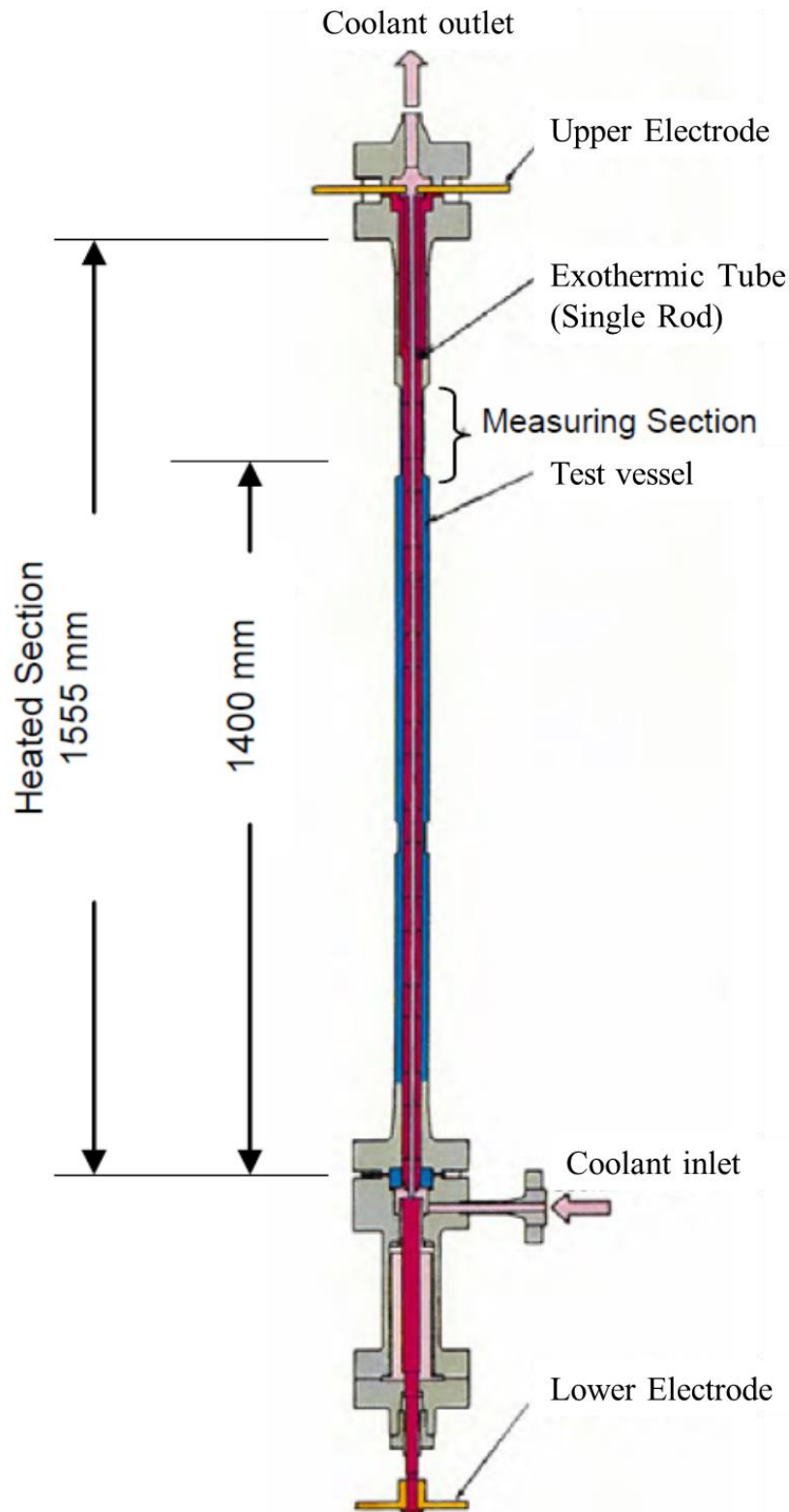


**Figure 6.8.** Test section sub-cooled boiling tests of NUPEC PSBT facility [85].

The void measurements are done using a narrow gamma-ray beam CT scanner to measure the subchannel averaged void fraction and a wide gamma-ray beam to measure the chordal averaged void fraction. For each subchannel type (corner, side, or center) a relationship between the subchannel averaged and the chordal averaged void fractions was individually derived. These relationships were then used to correct the subchannel averaged void fraction measured with the wide beam in the bundle tests. The system was operated by translate/rotate method. At each translation/rotation location, the

intensity of gamma-ray attenuated by the object, the so-called “projection data,” was detected. An image reconstruction was then performed by a filtered back-projection algorithm to obtain the distribution of the linear attenuation coefficient. The void fraction measurement procedure is shown in **Figure 6.9**. The estimated accuracy of the tests corresponds to a standard deviation of 0.03 absolute void fraction [85].

### CT Measurement

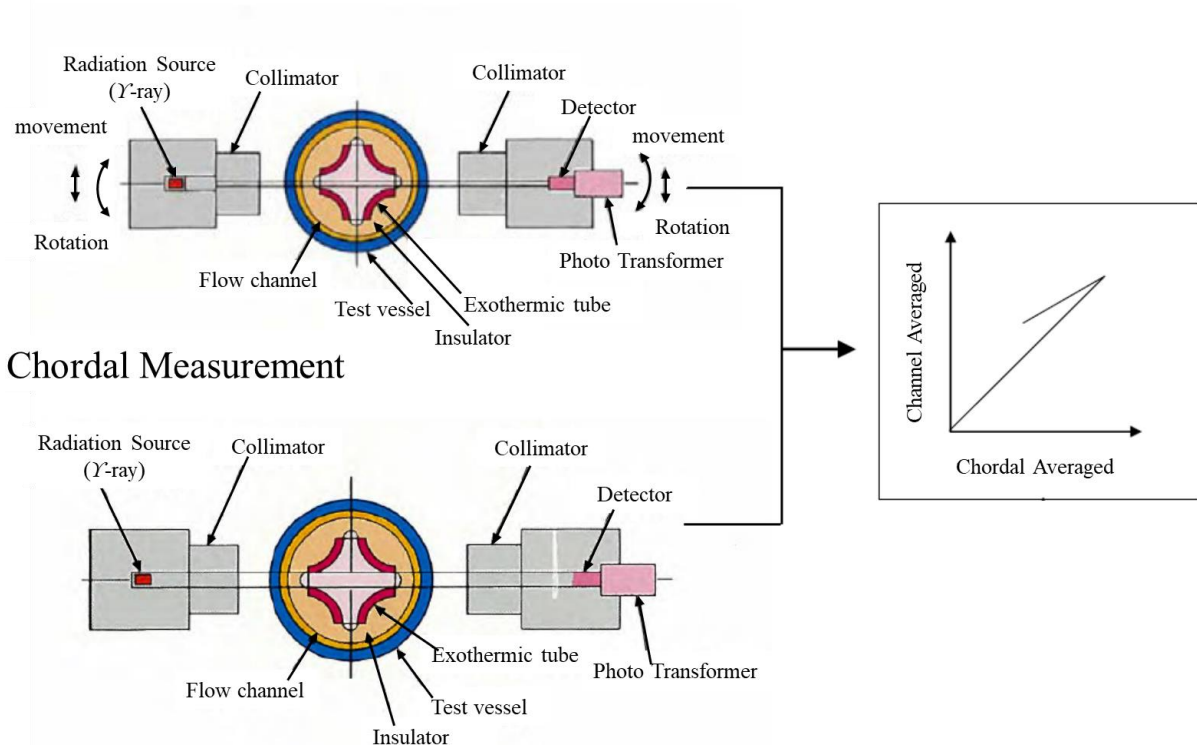


**Figure 6.9.** Void fraction measurement procedure in NUPEC PSBT facility [85].

Until this point, we will refer to the tests as S1, S2, S3 and S4 or typical, thimble, side, and corner sub-channel correspondingly.

The boundary conditions of the tests are described in **Table 6.1** (for more details, see Annex 2, **Tables 12.3** and **12.4**):

**Table 6.1.** Boundary conditions value ranges of Single sub-channel PSBT tests.

Sub-Channel type	Pressure [MPa]	Power [MW]	Inlet temperature [°C]	Mass flow [kg/m <sup>2</sup> s]
S1 Typical	4.9 - 16.6	0.0499 - 0.0799	189.2 - 339.7	1369.44 - 3055.56
S2 Thimble	4.95 - 16.6	0.015 - 0.0601	209.2 - 345	494.44 - 3058.33
S3 Side	4.94 - 14.8	0.0252 - 0.0405	189 - 314.5	1369.44 - 3027.78
S4 Corner	4.96 - 14.7	0.0125 - 0.0152	214 - 334.5	1394.44 - 3088.89

### 6.2.2 TWOPORFLOW modeling

The different subchannels are represented in TWOPORFLOW by one 1D cell (coolant centered sub-channel approach) subdivided axially in one cell with a length of 50 mm, 14 cells using 100 mm and one cell with 105 mm. This nodalization assures that the predicted values correspond to the location of the measured data i.e., 1400 mm (calculated in TWOPORFLOW at the center of the cell). The number of rods per channel is  $\frac{1}{4}$ ,  $\frac{1}{2}$ ,  $\frac{3}{4}$  or one depending on the type of sub-channel. In order to represent the



different pin and coolant areas in axial direction, different porosities are given depending on the case. For the cases S1 and S2 the porosity value is 0.1332, for S3 0.0851 and for S4 0.0530.

The physical models selected for these tests are the ones described in section 4.5 for the groups of correlations TPF and TPF-TRACE.

The boundary conditions are already being described in section 6.2.1 Short test description.

### 6.2.3 Comparison TWOPORFLOW predictions with experimental data

As mentioned, the tests have been analyzed using TWOPORFLOW with two sets of correlations (TPF and TPF-TRACE). In **Figures 6.10** through **6.13** the absolute difference of the predicted and measured void fraction is plotted in dependence of the measured one at the axial elevation of 1400 mm.

It is worth to note that although the void fraction measurement error given by the benchmark amounts 0.03, participants in the benchmark considered a value of 0.05 acceptable, because of the uncertainties implied by the experimental methods [23].

For the sub-channel S1, TWOPORFLOW with the TPF correlation sets tends to slightly under-predict the void fraction, while with TPF-TRACE correlation sets tends to over/under-predict the measured data for void fractions between 0.05 and 0.6 (**Figure 6.10**).

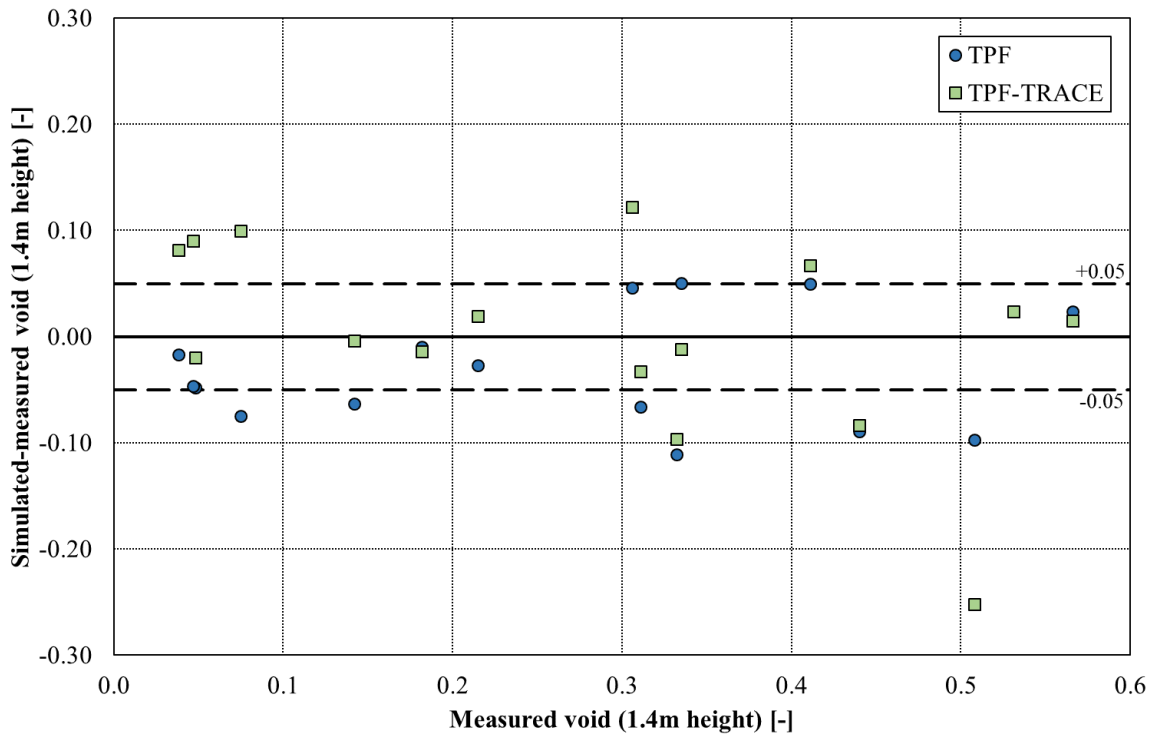


**Figure 6.10.** Comparison of the absolute difference of the void fraction with respect to the measurements at 1.4 m height of both groups of correlations TPF and TPF-TRACE sub-channel type S1 (typical sub-channel) of Single sub-channel PSBT tests.

For the sub-channel S2, the simulations with both type of correlations tend to under-predict the void data from 0.08 to 0.35, where the under-prediction is more pronounced than for S1.

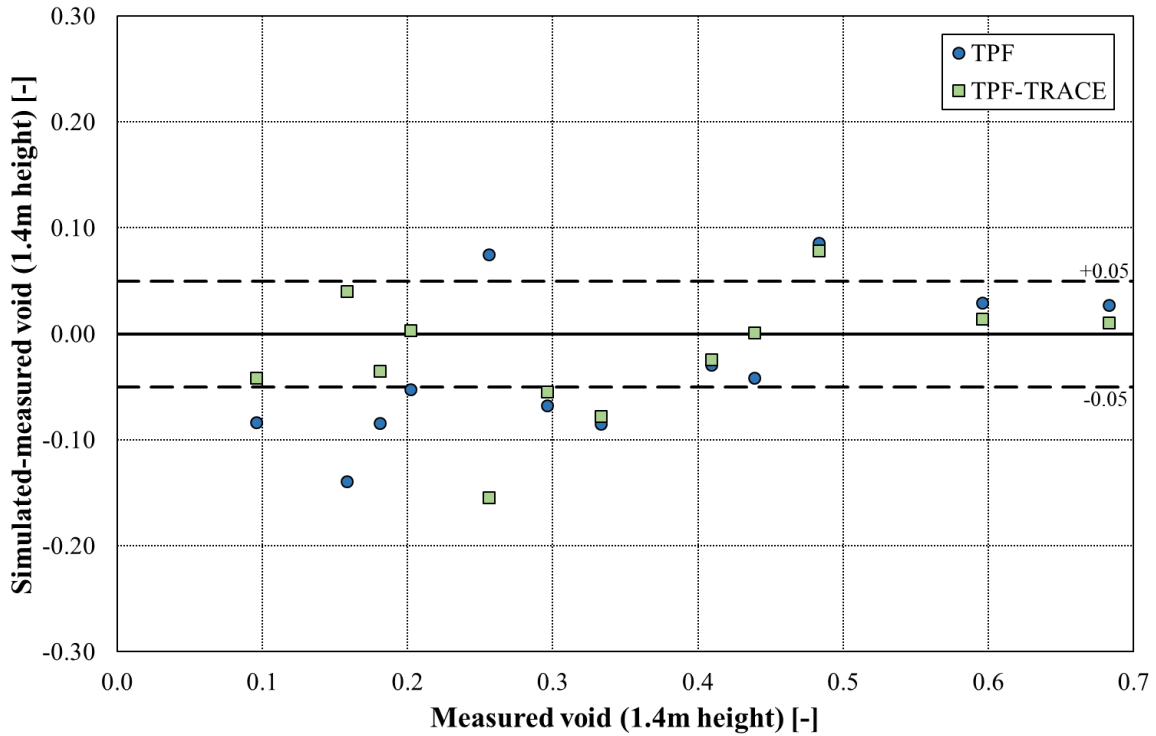


**Figure 6.11.** Comparison of the absolute void fraction differences with respect to the measurements at 1.4 m height of both groups of correlations TPF and TPF-TRACE sub-channel type S2 (thimble sub-channel) of Single sub-channel PSBT tests.

For sub-channel S3, the simulations of the eight tests with TPF-TRACE mainly over-predicts the data for void fractions below 0.42 and underpredicts it for values larger than 0.45. Specially for small void fractions the over-estimations are high. For a void fraction of around 0.48, a large underestimation is calculated. The predicted void fraction with the TPF-correlation set is mainly within the error band of  $\pm 0.05$ , except for one value of 0.82.

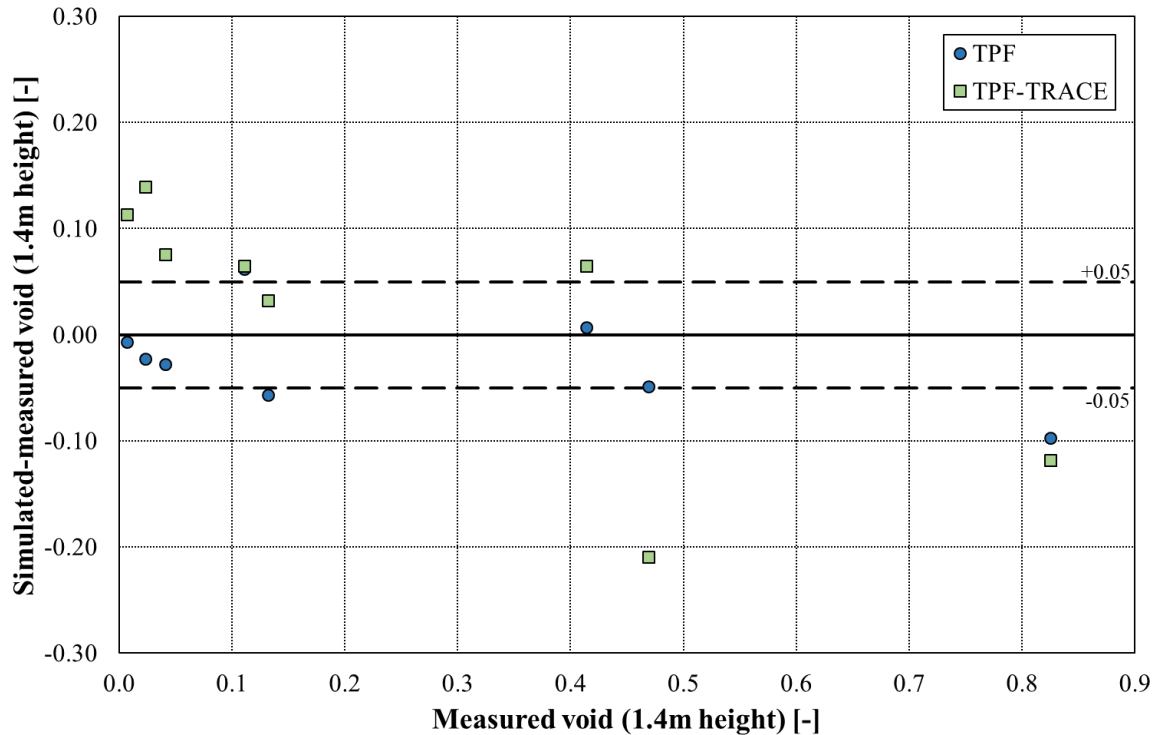


**Figure 6.12.** Comparison of the absolute void fraction differences with respect on the measurements at 1.4 m height of both groups of correlations TPF and TPF-TRACE sub-channel type S3 (side sub-channel) of Single sub-channel PSBT tests.



For the subchannel S4 **Figure 6.13**, both correlation sets slightly under-predict the measured data for low void fractions around 0.001. There are two simulations using the TPF-TRACE correlations, in which the measured data are similar, but a large difference between the simulated and the measured void fraction is found. In the test with less difference, the boundary conditions are a pressure of 14.7 MPa, an inlet temperature of 318.4 °C and a mass flow rate of 0.13 kg/s. The boundary conditions for the case with the larger difference are 4.9 MPa, 214 °C and 0.06 kg/s. The TPF-TRACE correlations for sub-cooled boiling are dependent on the Peclet number, saturation temperature and mass flow (equations (104) and (105) Annex 1). This dependence on these three parameters leads to the large differences in the simulations, because the void fraction in the measurement is similar, but the boundary conditions differ. Those differences are not present in the TPF correlations, because there are only dependent on the temperature (equations (101) to (103) Annex 1). The simple correlations seem to be more robust using less parameters.

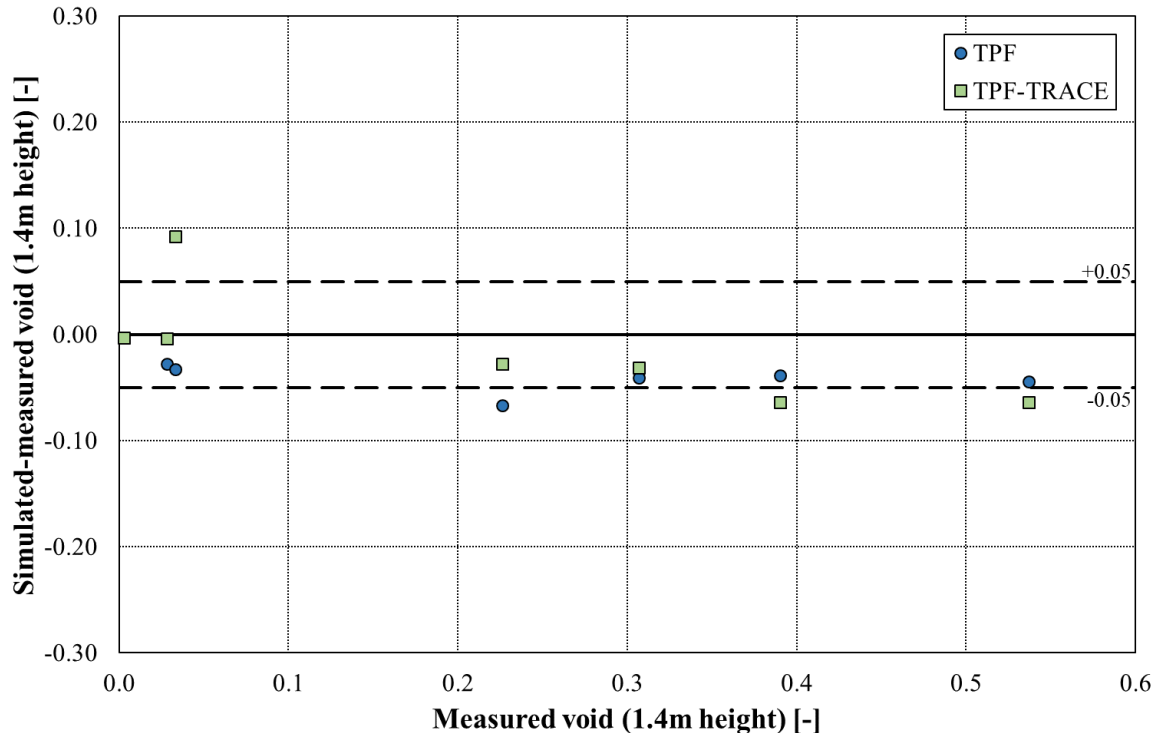


**Figure 6.13.** Comparison of the absolute void fraction differences with respect to the measurements at 1.4 m height of both groups of correlations TPF and TPF-TRACE sub-channel type S4 (corner sub-channel) of Single sub-channel PSBT tests.

In general, it can be stated that TWOPORFLOW tends to under-predict the measured void data specially for the subchannel of type S2, S3 and S4, where a cold structure is connected to the subchannel (S2: thimble, S3 and S4: wall of the test). In addition, it can be observed that for low void fractions, the TPF-TRACE correlation sets tend to overestimate the data. One reason for it is the fact that the sub-cooled boiling is dominated by evaporation-condensation effects, which in both cases are simulated by simplified models.

Furthermore, the TWOPORFLOW results are compared with the ones of the subchannel code named Subchanflow [23] in **Table 6.2**. There, it can be observed that the results obtained with TPF correlations are nearer to the results obtained with Subchanflow. With the exception for using the TPF correlations in assembly S3, the standard deviation in Subchanflow is lower in all cases (**Table 6.2**).

<b>Table 6.2.</b> Comparison of the void fraction standard deviations of both groups of correlations TPF and TPF-TRACE of Single sub-channel PSBT tests.			
	TPF	TPF-TRACE	Subchanflow
S1	0.05	0.09	0.05
S2	0.07	0.06	0.04
S3	0.05	0.12	0.08
S4	0.02	0.05	0.03

Based on these investigations, it is recommended to use the TPF correlations to simulate sub-cooled boiling.

## **6.3 BFBT test for steady state void dispersion**

### **6.3.1 Short test description**

The validation of the TWOPORFLOW groups of correlations (TPF and TPF-TRACE) is performed using the NUPEC BWR Full-size Fine-mesh Bundle Test (BFBT) benchmark [87] data. It provides good-quality experimental data for the validation of different thermal hydraulic codes. Both static void distribution and Critical Power tests are considered. **Figure 6.14** shows the layout and a cross-sectional view of the NUPEC BFBT facility. The test section is shown in **Figure 6.15**, where the heated section has a length of 3708 mm. An X-ray CT scanner has been used to measure fine mesh void test distributions. The scanner has been located 50 mm above the heated length (assembly exit). The scanning section consists of a pressure vessel made of titanium (Ti), the channel wall and the cladding of the heater rods at this location are made of beryllium (Be) to minimize X-ray attenuation in the structure. The system consists of an X-ray tube and 512 detectors. To obtain a measurement of every sub-channel, a rotation technic is used (**Figure 6.16**).

The reported sub-channel void fraction accuracy is 3% (0.03) and the measurements have been taken at assembly exit.

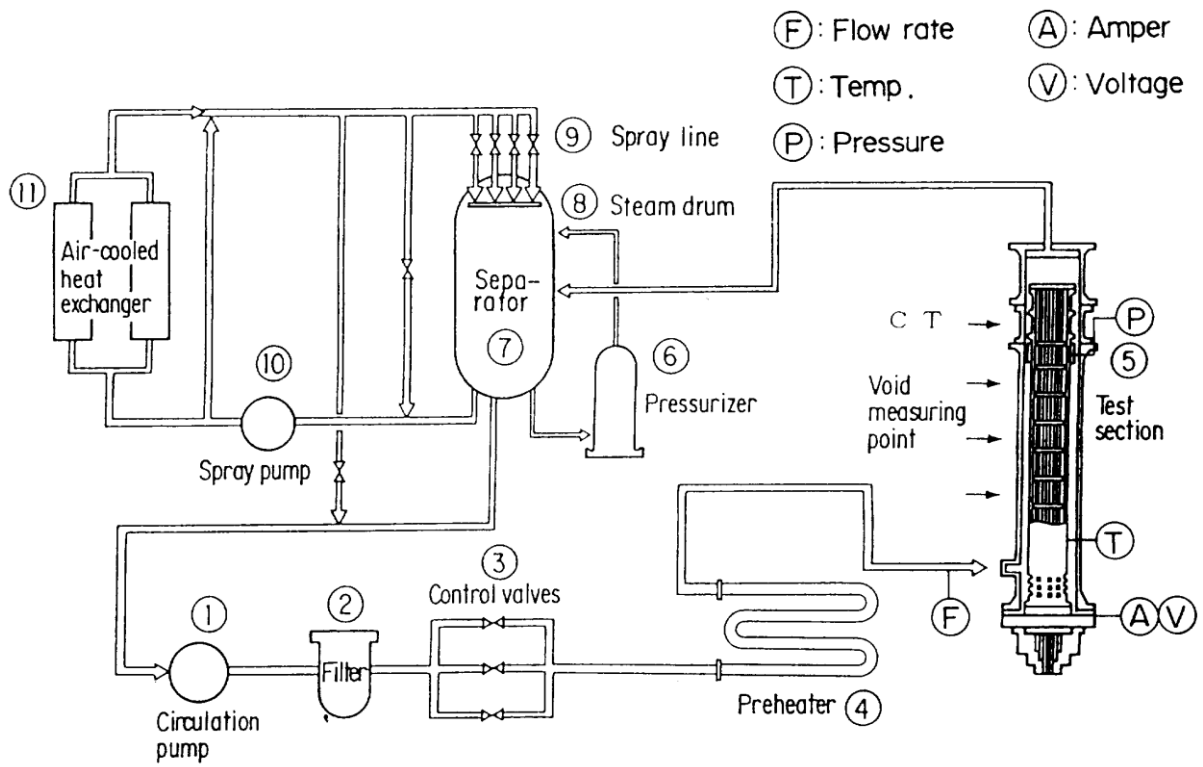


Figure 6.14. Layout of NUPEC BFBT facility [87].

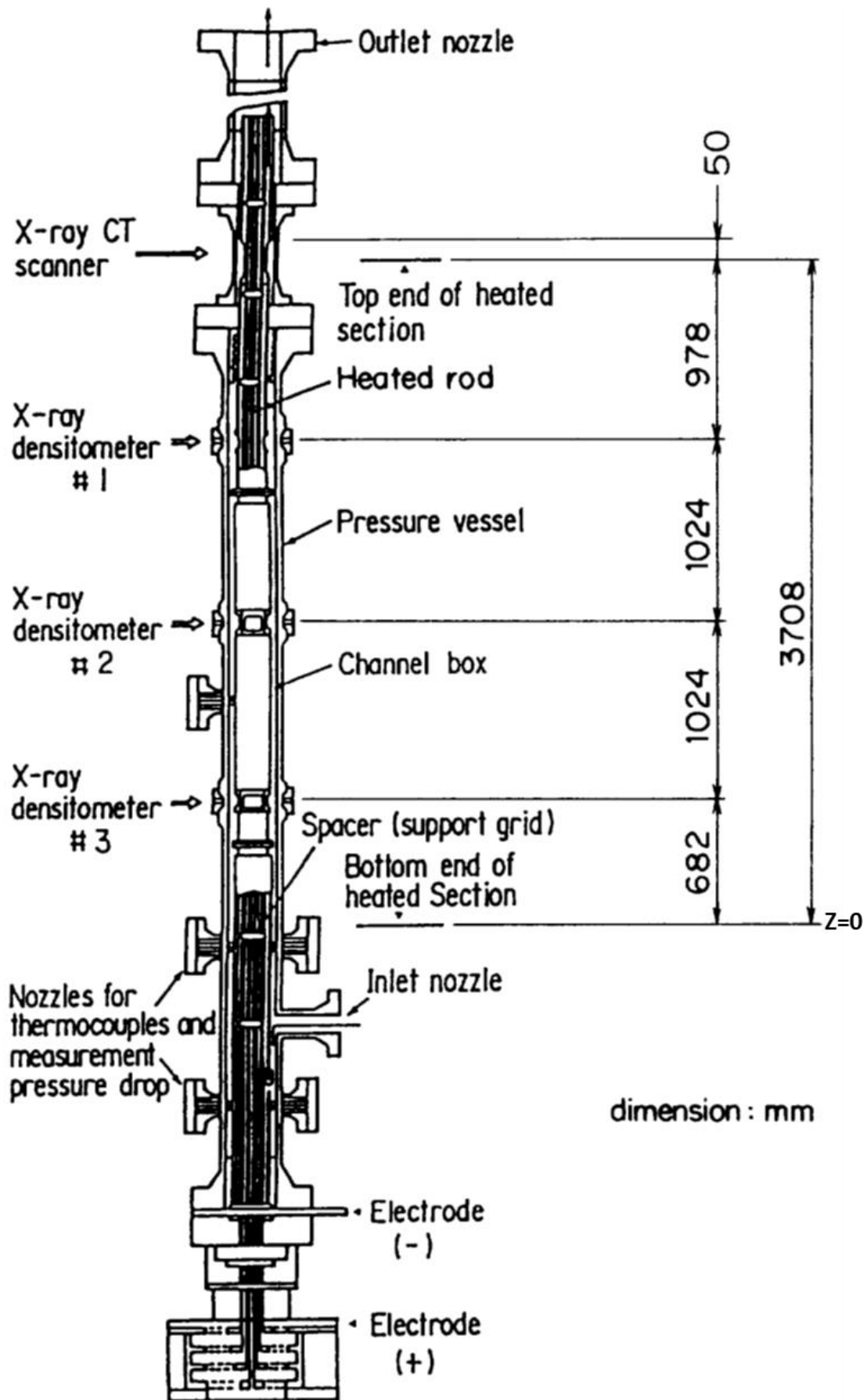


Figure 6.15. Cross-sectional view of test section of the BFBT test section [87].

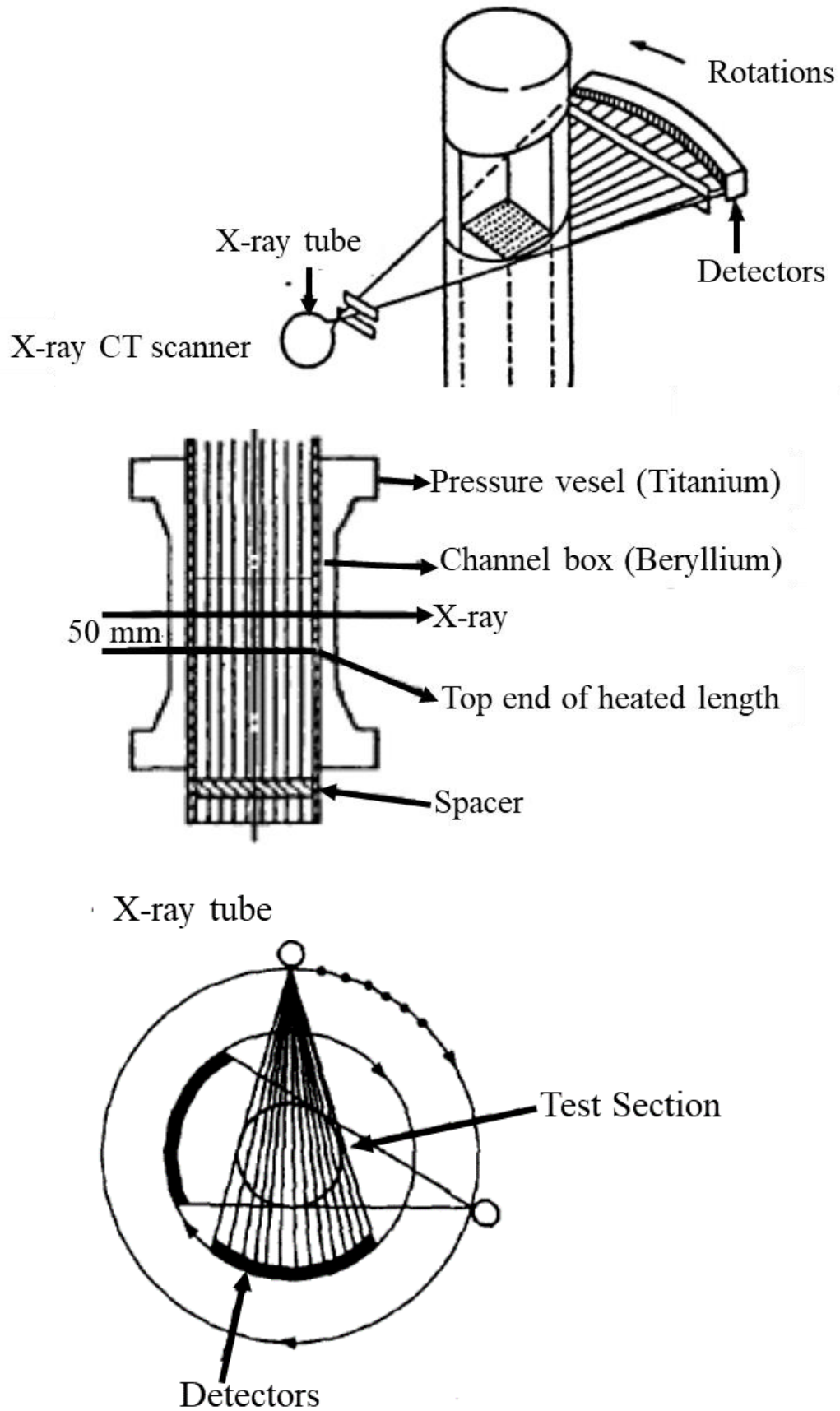


Figure 6.16. Void fraction measurement system BFBT steady state tests [87].

### 6.3.2 Selected tests for code validation

In order to obtain a correct simulation of bundle average void fractions, it is necessary to work with appropriate wall friction, interfacial friction, turbulent mixing, and void dispersion models. For the validation of the void dispersion models in TWOPORFLOW, fifteen tests of the Exercise 1 Phase I “steady-state sub-channel grade benchmark” are used. The tests have an 8x8 pin assembly geometry (Figure 6.17), a width of 1325 mm, an axial heated length of 3708 mm and a total length of 3758 mm.

The assemblies have seven non-mixing spacers with pressure loss coefficient ( $\xi$ ) of 1.2, different lateral power distributions, (uniform for assembly 1; Figure 6.18-A for assemblies 01, 02, 03; and Figure 6.18-B for assembly 4), and different axial power distributions (constant for assemblies 01, 02, 03, and 4; and cosine for assembly 1).

Three types of experiments, related to the void fraction, have been performed for every assembly. Experiments with a low (0.4 to 0.5), middle (0.6 to 0.7) and high (0.7 to 0.8) assembly averaged void fraction, making a total of fifteen tests. Further details of the experiment are shown in Annex 2 Tables 12.5 and 12.6 and Figure 12.1 ( there, the axial power distributions are shown).

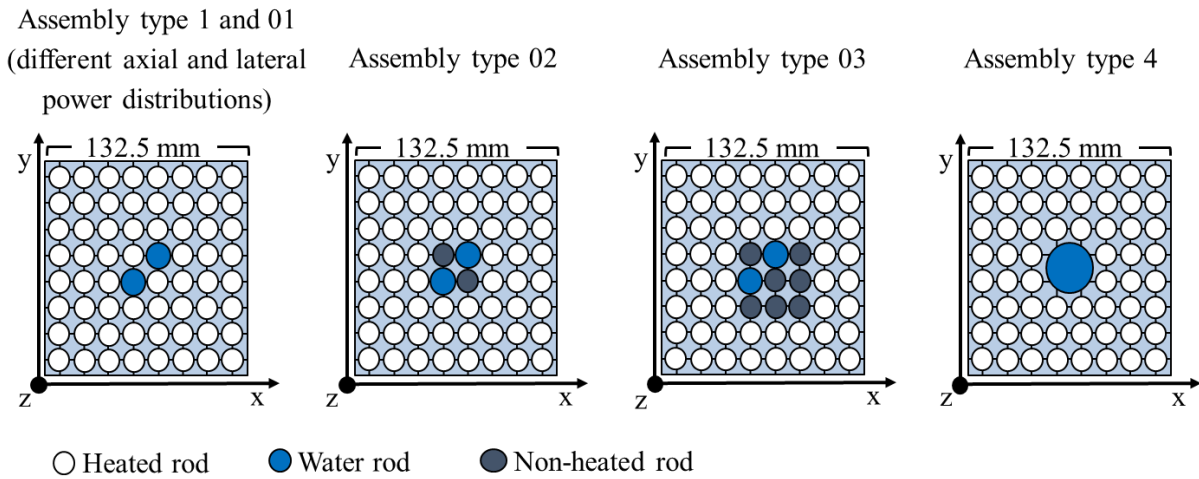


Figure 6.17. Top view of test Assemblies 1, 01, 02, 03 and 04 of BFBT steady state tests [87].

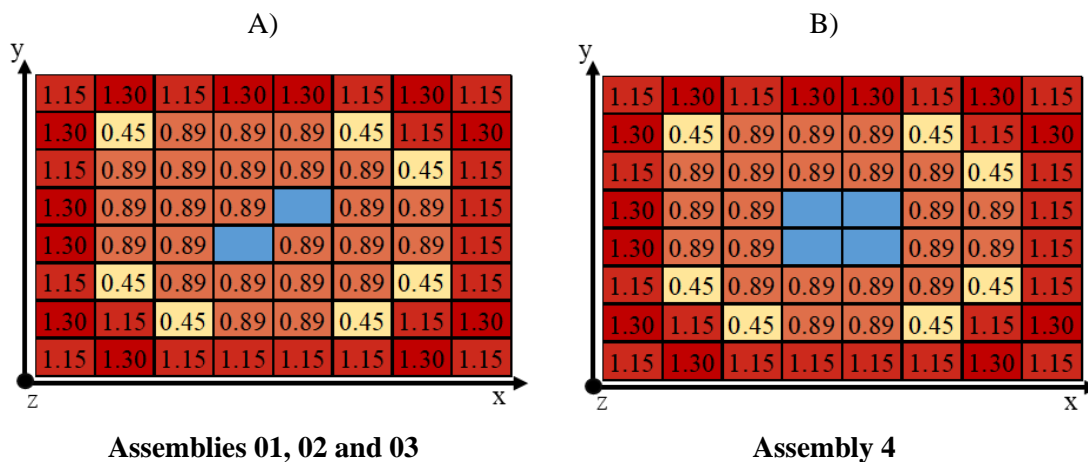


Figure 6.18. Lateral power distribution BFBT.

The boundary conditions of the tests are shown in **Table 6.1**:

<b>Table 6.3.</b> Boundary conditions value ranges of steady-state sub-channel grade benchmark BFBT tests.				
Assembly type	Pressure [MPa]	Flow[kg/m <sup>2</sup> s]	Power [MW]	Inlet temperature [°C]
01	7.17 - 7.21	733.05 - 737.14	1.9 - 6.44	277.66 - 278.28
02	7.17 - 7.19	733.05 - 735.1	1.91 - 6.45	276.19 - 277.88
03	7.17 - 7.18	733.05 - 734.08	1.92 - 6.45	277.7 - 278.19
04	7.15 - 7.159	755.57 - 760.86	1.92 - 3.52	277.68 - 277.77
1	7.16 - 7.2	732.03 - 736.12	1.92 - 6.48	277.73 - 278.01

### 6.3.3 TWOPORFLOW modeling

The heated length of the test section is modeled in TWOPORFLOW using a coolant centered sub-channel approach resulting in 9x9 sub-channel and 24 axial cells. The axial mesh has been chosen to have the same number of cells as number of power axial distribution values are given in the benchmark (24 axial cells of 154.5 mm length).

The number of rods per channel is  $\frac{1}{4}$ ,  $\frac{1}{2}$ ,  $\frac{3}{4}$  or one depending on the location of the sub-channel. In the centered coolant approach, the normalized power distribution of the sub-channel must be calculated considering all the rod parts that are inside the sub-channel (**Figure 6.19**).

In addition to it, the mixing coefficient of 0.007 is also provided to TWOPORFLOW for this bundle (a this small value is used because the assemblies do not have mixing vane spacers as is the case in PSBT and taking into account the values for sub-cooled boiling given by [79]). Porosities and heat transfer area densities are deduced from the different channel geometries inside the bundle. Channels at the outer boundary and the corners have different values than the inner ones.

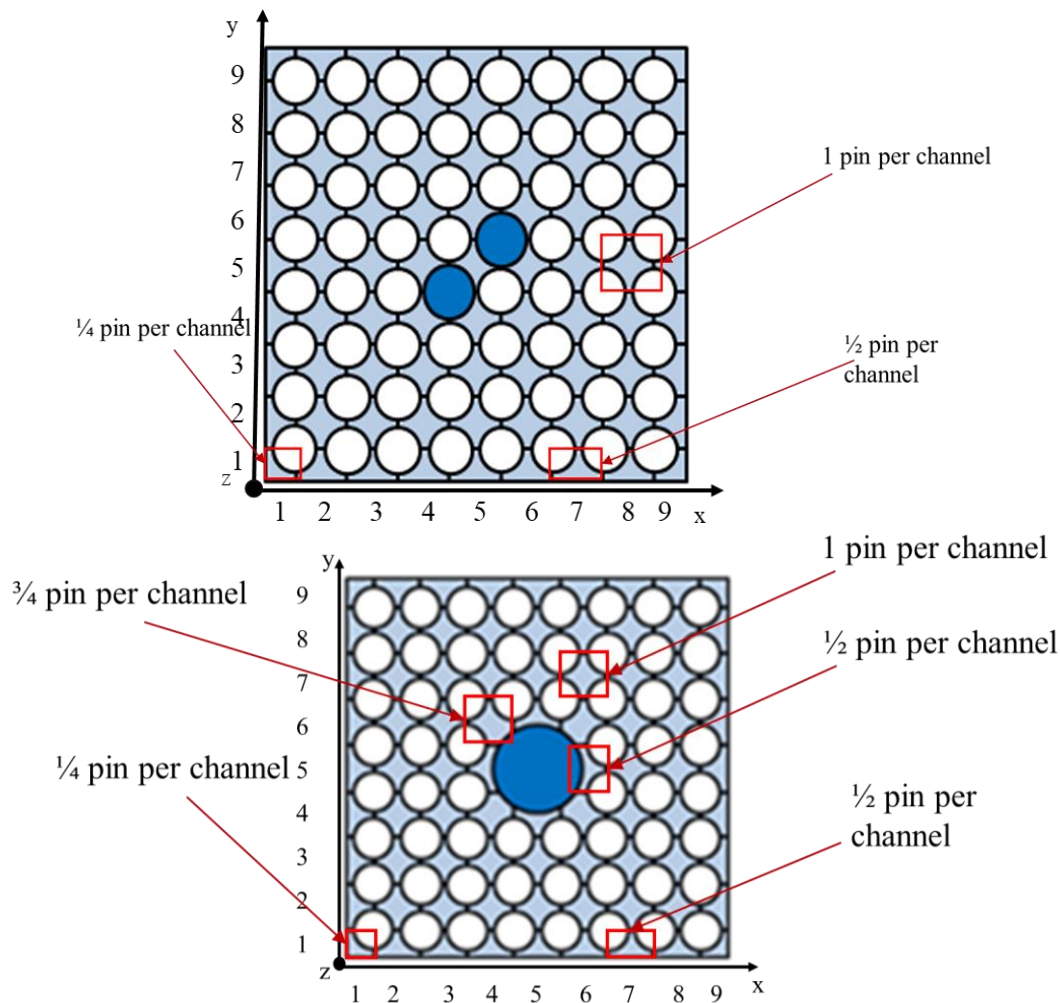


**Figure 6.19.** View from the top of the TWOPORFLOW's model of NUPEC BFBT steady-state sub-channel grade benchmark with two water channels (top) and a central water channel (bottom).

Finally, the boundary conditions at the bundle inlet (mass flow rate and coolant temperature) and at the bundle outlet (pressure) as well as the bundle power summarized in **Table 6.3** are given to this model.

### 6.3.4 Comparison of the void fraction predicted by TWOPORFLOW with the data

In **Figures 6.20** to **6.24**, a comparison of the void fraction predicted using the two correlation sets (TPF and TPF-TRACE) at the bundle outlet with the measured data of the five fuel assembly types is given. In these figures three different tests for each fuel assembly are presented. One test with void fraction of 0.4, the second 0.6 and the third 0.8, meaning 243 points for TPF and TPF-TRACE groups of correlations for every fuel assembly type.

According to a COBRA-TF analysis [88] big uncertainties of the measured data have been found and discussed during the benchmark exercise. Based on it, it is agreed that deviations of  $\pm 0.2$  in the void fraction are acceptable.

It can be seen there that for void fractions below 0.4 TWOPORFLOW tends to over-predict while for values above 0.8 the tendency is to underestimate the measure valued by more than 10 %.



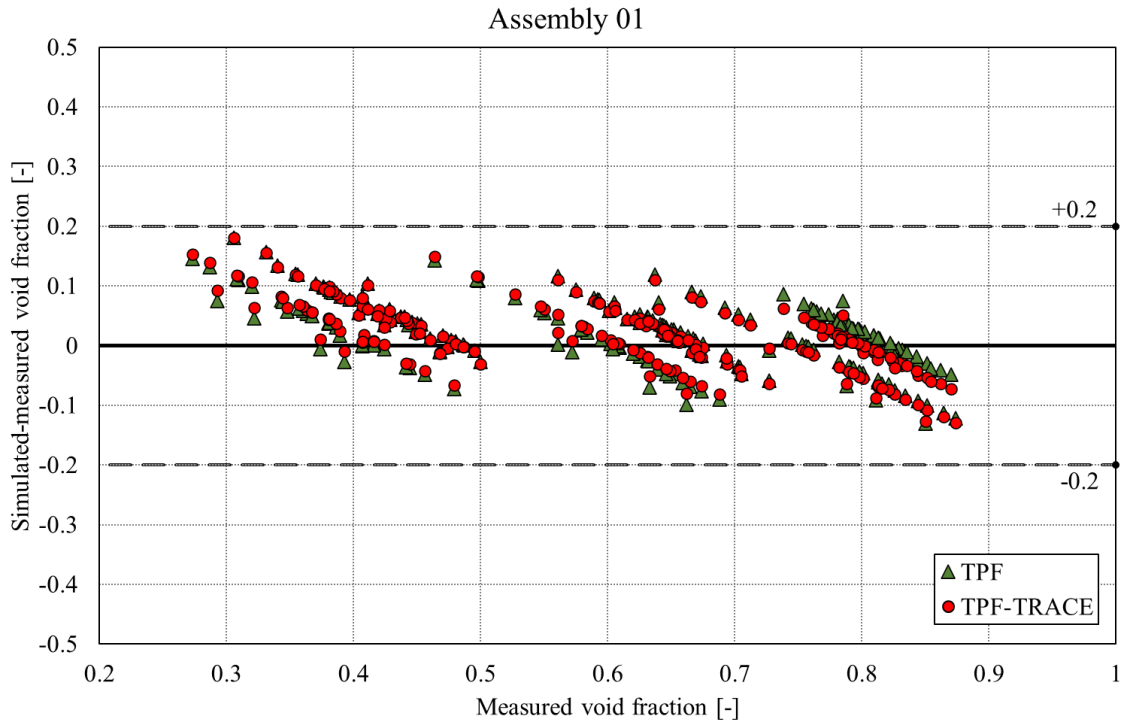


**Figure 6.20.** Difference between measured and simulated average void fraction for assembly type 01 at the CT position (3758 mm) for BFBT steady-state sub-channel grade benchmark with TPF and TPF-TRACE groups of correlations

For the Assembly 02, the absolute difference of the calculated and predicted void fraction as function of the measured average void is within the  $\pm 0.2$  range, where the measured values are mainly overpredicted for void fractions below 0.6 and under-predicted above it using both correlation sets.

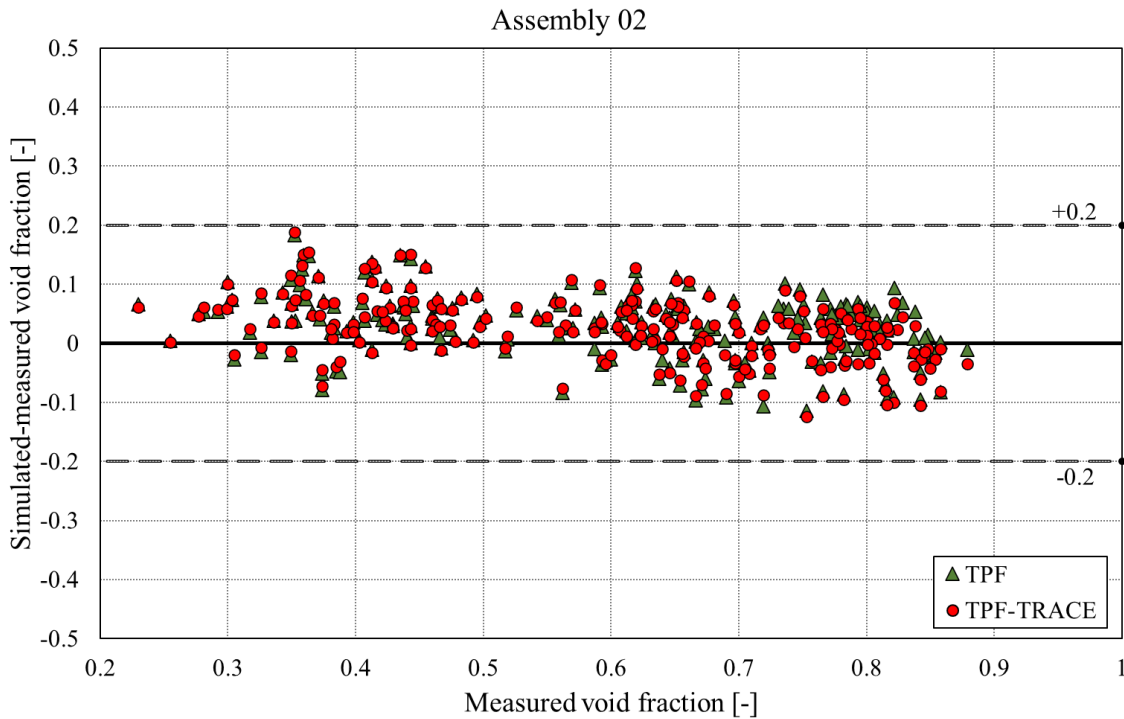


**Figure 6.21.** Difference between measured and simulated average void fraction for assembly type 02 at the CT position (3758 mm) for BFBT steady-state sub-channel grade benchmark with TPF and TPF-TRACE groups of correlations

For the Assembly 03, the absolute difference of the void fraction predicted by the two correlation sets of TWOPORFLOW mainly over-predicts and under-predicts the data in the entire range of void

fractions. A larger over-prediction/under-prediction larger than 0.20 is observed for few simulations around 0.3 and 0.67, respectively, **Figure 6.22**.

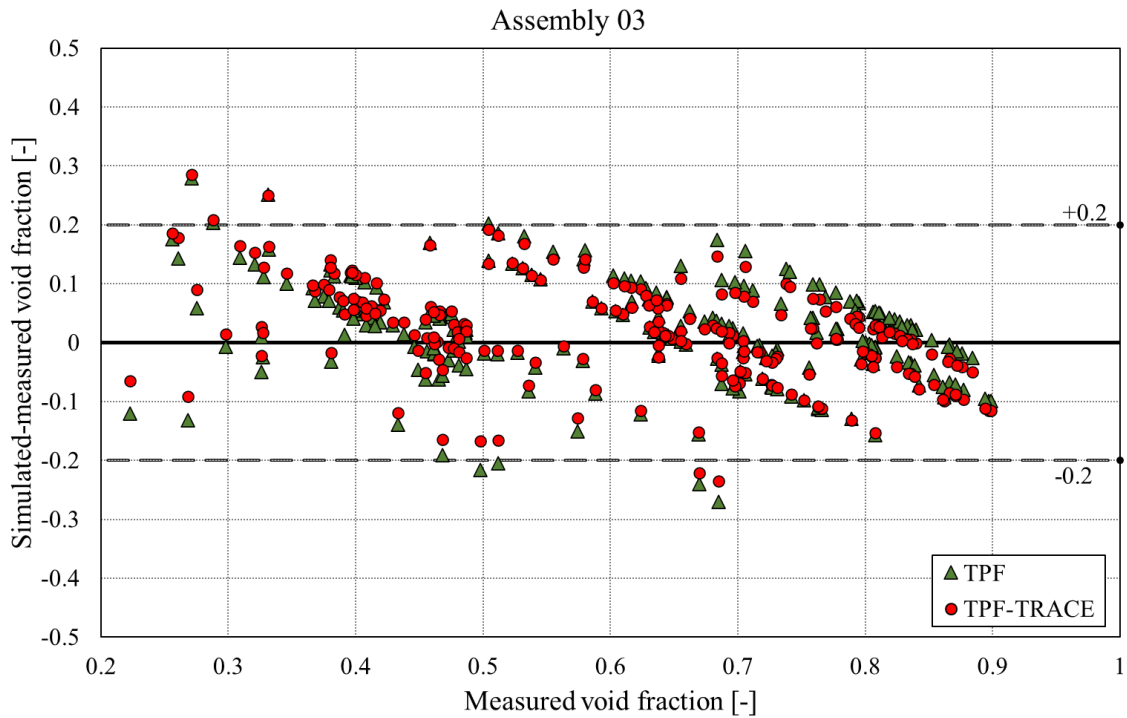


**Figure 6.22.** Difference between measured and simulated average void fraction for assembly type 03 at the CT position (3758 mm) for BFBT steady-state sub-channel grade benchmark with TPF and TPF-TRACE groups of correlations

In case of the Assembly type 04, where the water rods are quite large (area of four subchannels), it can be observed that an over-prediction of the measured data by more than 0.2 is observed for the full range of void fractions, **Figure 6.23**.

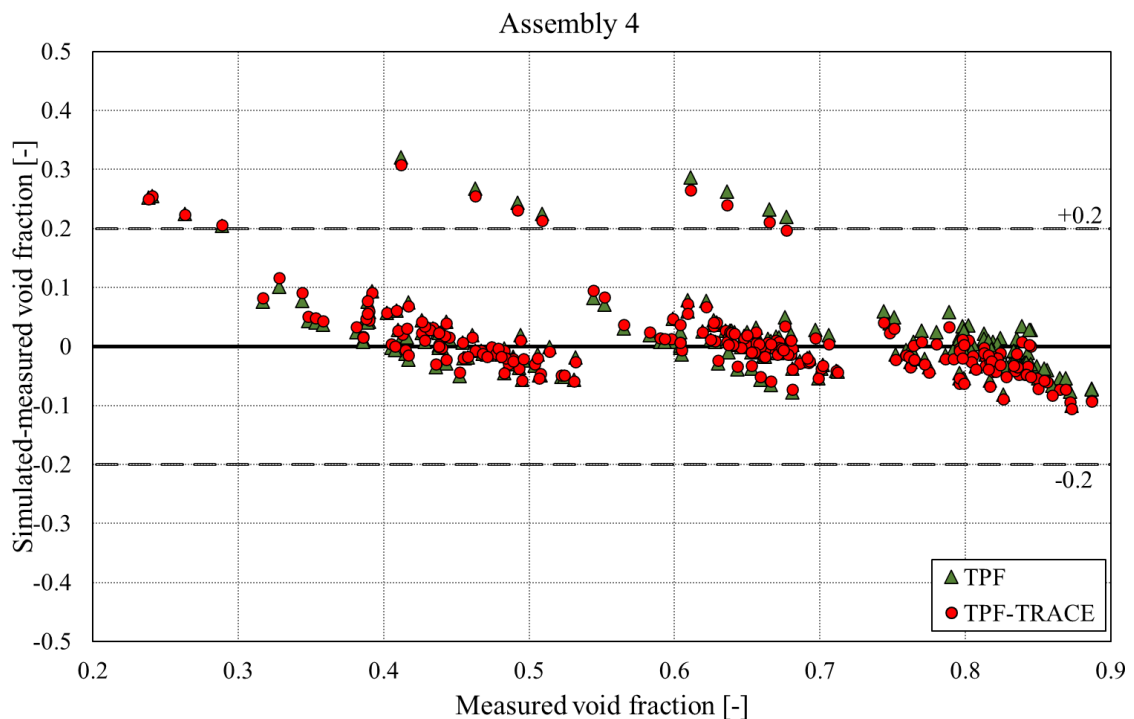


**Figure 6.23.** Difference between measured and simulated average void fraction for assembly type 04 at the CT position (3758 mm) for BFBT steady-state sub-channel grade benchmark with TPF and TPF-TRACE groups of correlations

For the Assembly type 1, which is characterized by having a cosine axial power fraction it can be stated that the absolute difference of the predicted and measured data is mainly below  $\pm 0.1$  with a tendency to an over-prediction of the measured data above 0.1 for void fractions below 0.55, as shown in **Figure 6.24**.

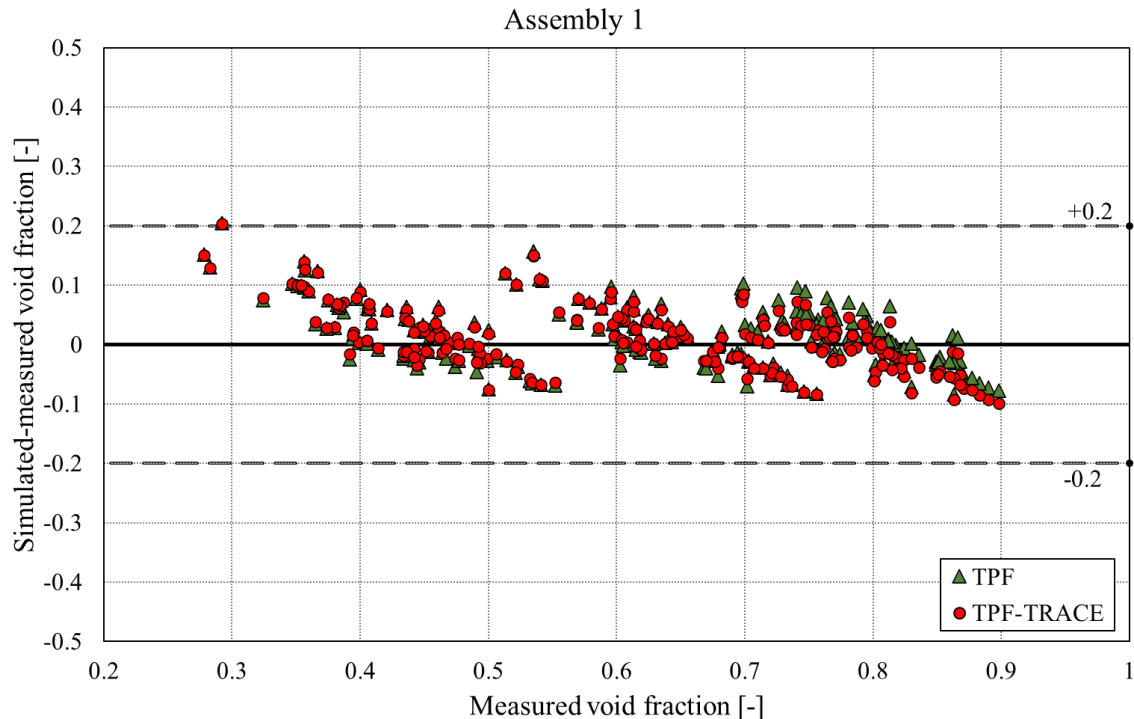


**Figure 6.24.** Difference between measured and simulated average void fraction for assembly type 1 at the CT position (3758 mm) for BFBT steady-state sub-channel grade benchmark with TPF and TPF-TRACE groups of correlations

Summarizing it can be stated that from 1215 predictions of the void fraction at the outlet of the sub-channels only 24 for TPF and 20 for TPF-TRACE are outside the range of 0.2. The values outside the range correspond to those sub-channels with non-heated rods and surrounding the water rod in the Assembly 03 and 4, respectively.

Sub-cooled boiling is dominated by local evaporation at the wall and condensation at the bulk. These mechanisms are described in TWOPORFLOW using simplified models, which is the reason for the observed deviations of the predictions from the experimental data, especially in regions with unheated structures.

In general, it can be stated that both sets of correlations predict similar bundle behavior. In all the cases, the larger differences are located either near the non-heated rods, water rods or at the edge of the assembly. These local effects cannot be resolved in detail due to the porous media approach, which does not account for the large gradients in void fraction inside of a computational cell. All the results of the simulations are in the sub-cooled boiling/nucleate boiling flow regime.

In order to evaluate the accuracy and precision of the code predictions, the absolute error of the predictions is compared to the experimental data.

**Figure 6.25** shows the comparison of the absolute error of the TWOPORFLOW predictions using the two set of correlations for the five Assembly types and three different void fraction values (low, middle, high). It can be observed that apart from assembly 4, in all the cases, low void fractions have the larger deviation: for a void fraction of 0.4, the absolute error is the largest. Assembly type 4 has the lowest absolute error while Assembly type 03 the largest.

On the other hand, it can be observed that both correlation sets predict similar deviations from the experimental data, which are not larger than 0.03 void fraction.

Finally, it is worth to note that near unheated water rods in BWR assemblies, large temperature gradients appear due to the heat flux coming from the neighboring fuel rods. Channel-centered subchannel modelling averages the heat fluxes from the different surfaces, so it cannot describe in detail the behavior of such configuration. Local condensation in the cold region plays a key role. The averaging inherent in the present modelling cannot be corrected by any parameters of the empirical correlations. This would lead to deterioration in the regions without strong temperature gradients. To simulate the behavior around unheated rods high-resolution CFD calculation are essential to get some insight.

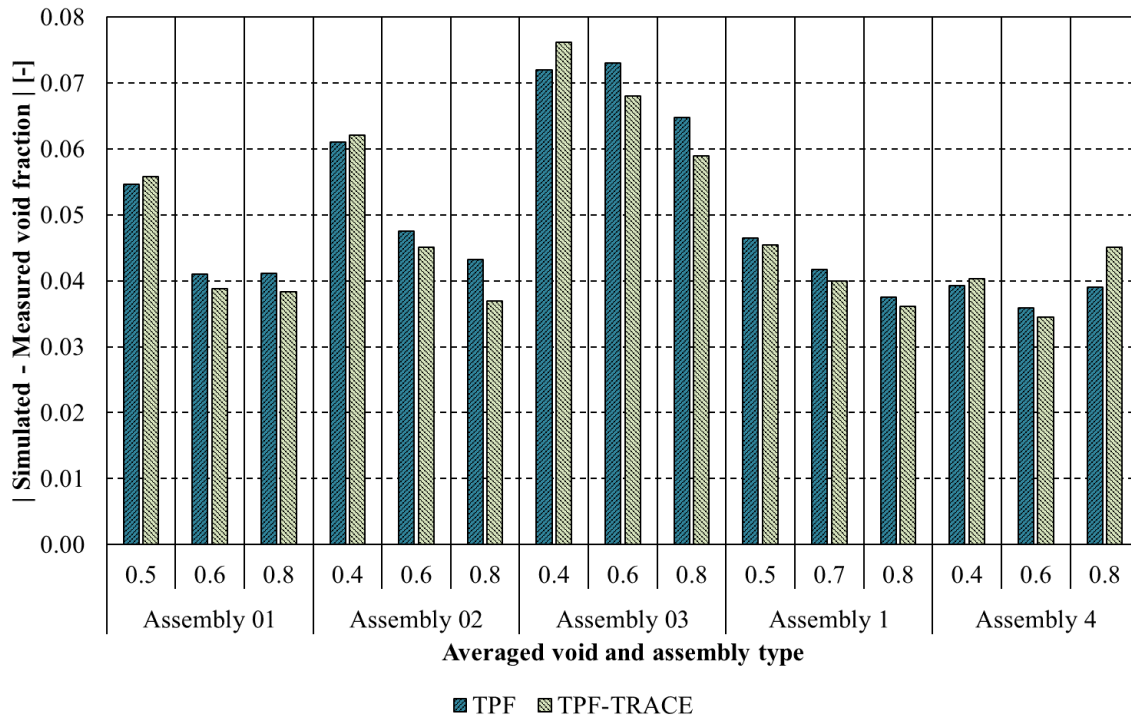


**Figure 6.25.** Comparison of the void fraction accuracy of both groups of correlations TPF and TPF-TRACE with respect to the experimental data of BFBT steady-state sub-channel grade benchmark by assembly and void fractions 0.4, 0.6, 0.8.

## 6.4 Transient BFBT void tests

### 6.4.1 Short description of the transient void fraction tests

For the development of transient calculations, not only appropriate wall friction, interfacial friction, turbulent mixing, and void drift models, but also a detailed heat conduction model is necessary. In order to evaluate the quality of typical transient simulations using TWOPORFLOW, the turbine trip without by-pass and the recirculation pump trip tests that belongs to the transient macroscopic grade benchmark are selected [87]. These tests are performed using an assembly type 4 (see **Figure 6.17**) equipped with 7 non-mixing spacers (pressure loss coefficient ( $\xi$ ) of 1.2). The initial boundary conditions of the tests are:

- Outlet pressure: 7.2 MPa,
- Inlet mass flow: 55T/h,
- Inlet temperature: 279 °C,
- Bundle power: 4.5 MW.

### 6.4.2 Short description of the turbine trip without by-pass tests

A turbine trip is an event in which a malfunction of a turbine or reactor system causes abrupt stop of the steam flow to the turbine by closing the steam inlet valves. In **Figure 6.26**, the typical evolution of thermal hydraulic parameters in case of a turbine trip event without by-pass is shown. There the boundary conditions are normalized to 1 i.e., divided by the conditions at initial time.

The power, pressure at outlet, temperature and flow rate remain constant for the first 10 seconds. Afterwards, a fast power peak and a moderate pressure increase occur. It is caused by the void collapsing in the core due to the propagation of a pressure wave from the main steam line to the core after the turbine isolation valve closure. After 45 seconds, the speed of the recirculation pumps is increased to achieve nominal conditions.

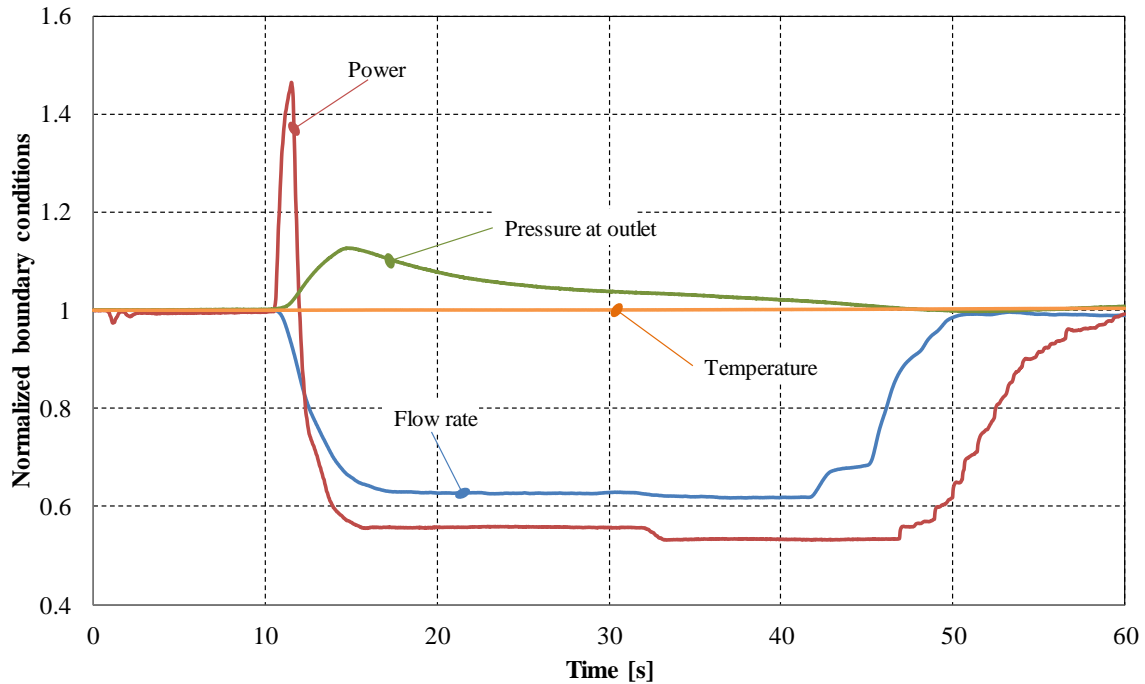


**Figure 6.26.** Normalized to one boundary conditions in the turbine trip without by-pass BFBT transient tests.

The bundle averaged void fractions have been measured using X-ray densitometers at three different heights 683, 1706, and 2730 mm. It is worth mentioning that the measurements data needed to be corrected due to a systematic overestimation of void fraction (see [88] for details) leading to an uncertainty of more than 2% for the measured values. In both scenarios the transient test last for 60 seconds.

### 6.4.3 TWOPORFLOW modeling

The tests are modeled in TWOPORFLOW using the same discretization described in section 6.3.3 **Figure 6.19** for a fuel assembly type 4 (**Figure 6.17**) meaning a coolant centered approach with 9x9 sub-channels in lateral and 24 channels in axial direction. The thermal inertia is determined by the thermal conductivity and heat capacity of the heaters simulating the fuel rods. These are directly implemented as subroutines in TPF using the data of the benchmark specification. The boundary conditions (flow rate, temperature, pressure) are provided by timetables, which are used as interpolation tables inside the code.

#### 6.4.4 Comparison the void fraction predicted by TWOPORFLOW with the measured data

The void fraction evolution as predicted by TWOPORFLOW using both correlation sets (TPF and TPF-TRACE) during the 60 seconds transient is compared with the experimental data in **Figure 6.27**. There, it can be observed that in general TWOPORFLOW is able to predict qualitatively the time evolution of the void fraction measured at the three elevations. The predictions using the TPF-TRACE correlations is similar to the ones obtained using the TPF-correlations, except for the low void fractions ( $< 0.21$ ). For low void fractions, the predicted void fraction using the TPF-correlations is in good agreement with the data. For void fractions higher than 0.5, the simulations tend to under-predict the data during the first 15 sec and the last 6 sec while the code over-predicts the measured data between 15 and 54 sec.

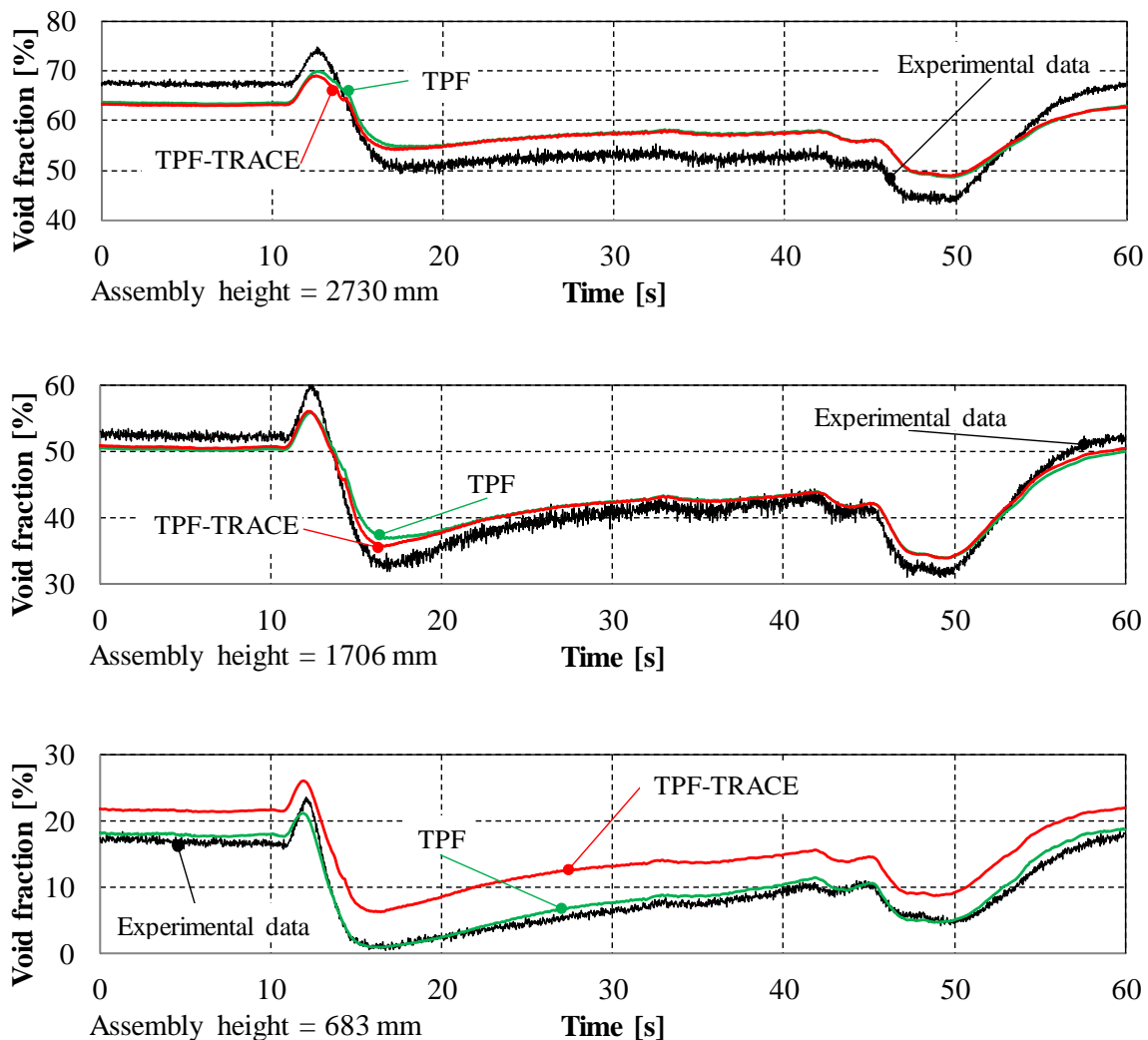


**Figure 6.27.** Comparison of measured and simulated with TWOPORFLOW percentage of void fraction variation related to the time in turbine trip without bypass transient BFBT test at 683, 1706 and 2730mm assembly height.

In **Table 6.4** the time averaged (mean) absolute error at 683, 1706 and 2730mm assembly height is presented. TPF correlations show a better agreement with the experimental data at low quality regions ( $\pm 0.87\%$  void fraction) and the discrepancies increase with the steam quality ( $\pm 1.86\%$  at 1706mm and  $\pm 4\%$  at 2730mm). The TPF-TRACE correlations present significant deviations in both low- and high-quality regions, having a better agreement at 1706mm between 30 and 60% void fraction.



<b>Table 6.4.</b> % Void fraction Mean Absolute Error (MAE) in turbine trip without by-pass BFBT transient test $\left( Error_{avg} = \frac{\sum_{i=1}^n  \alpha_{sim} - \alpha_{exp} }{n} * 100 \right).$			
Correlations	Measurement height [mm]		
	683	1706	2730
TPF	0.87	1.86	4.00
TPF-TRACE	5.34	1.55	3.96

#### 6.4.5 Short description of the recirculation pump trip test

A recirculation pump trip is an event in which the recirculation pump fails and results in a reduction in recirculation flow, which reduces the core coolant flow rate. The BFBT test is performed using the Assembly type 4 and the boundary conditions of a typical recirculation pump trip of a BWR. In **Figure 6.28**, the time evolution of the power, pressure, mass flow rate and coolant temperature (normalized to the conditions at the test start) for the recirculation pump trip are shown.

In case of a recirculation pump trip event, a decrease of the mass flow rate happens within few seconds. That leads to increasing the void fraction and, consequently, a decreasing in the neutron moderation in the core leading to a power decrease. During the next 30 seconds, the mass flow rate stabilizes at 1/3 of the nominal value. After 40 seconds the pumps start to operate again increasing the flow rate to the steady state value [89].

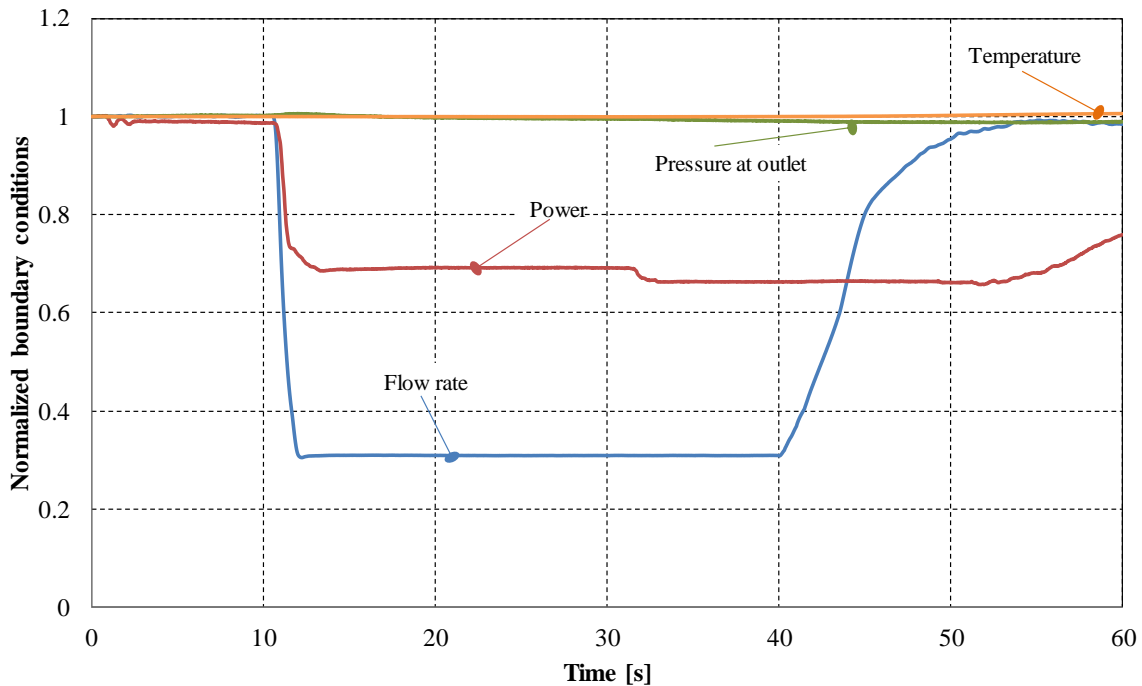


**Figure 6.28.** Normalized boundary conditions in the recirculation pump trip BFBT transient test.

#### 6.4.6 Comparison of the void fraction predicted by TWOPORFLOW with the measured data

The predicted void fraction using the TPF, and TPF-TRACE correlation sets at three axial locations is compared to the measured data in **Figure 6.29**.

The predictions using the TPF-correlations show excellent agreement with the data except for a two short time windows (0 to 12 and 42 to 60 sec) at the elevation of 2730 mm, where the code tends to

under-predict the data. The predictions with TPF-TRACE-correlation set in general under-predicts the measured void fractions and this under-prediction increases with increasing elevation. Only at the lowest elevation i.e., for low void fractions, this correlation sets tend to over-predict the void fraction at two-time windows (0-11 and 48-53 sec).

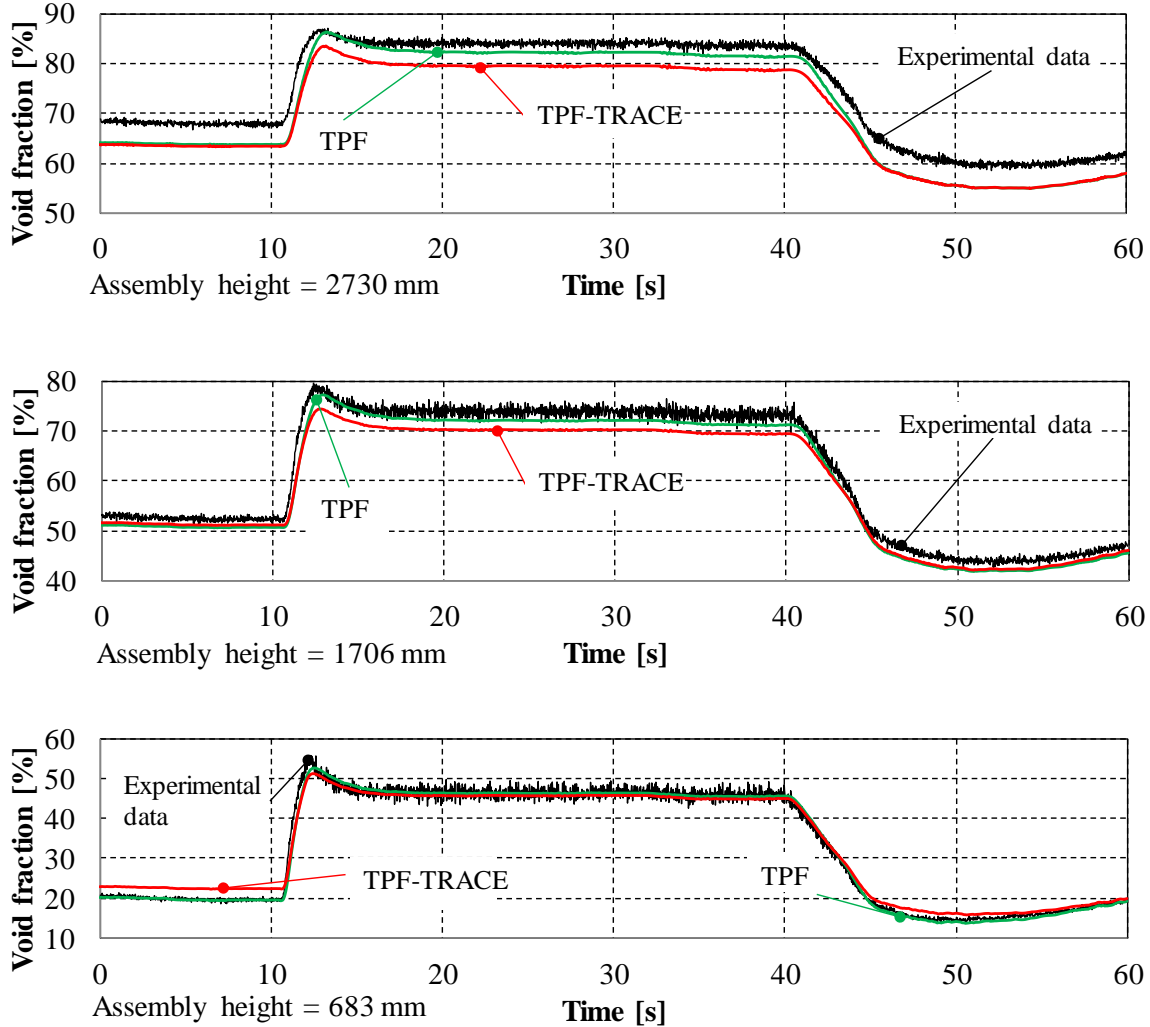


**Figure 6.29.** Comparison of measured and simulated with TWOPORFLOW percentage of void fraction variation related to the time in recirculation pump trip BFBT transient test at 683, 1706 and 2730mm assembly height.

In **Table 6.5**, the time averaged (mean) absolute error at  $z = 683, 1706$  and  $2730\text{mm}$  assembly height is presented. The results show the same behavior as the comparisons with the turbine trip without by-pass transient measurements, meaning that TPF correlations show a better agreement with the experimental data at low quality regions ( $\pm 0.86\%$  void fraction) and the discrepancies increase with the steam quality ( $\pm 1.87\%$  at  $1706\text{mm}$  and  $\pm 3.09\%$  at  $2730\text{mm}$ ). The TPF-TRACE correlations present significant deviations in both low- and high-quality regions, having a better agreement at  $1706\text{mm}$  between 30 and 60% void fraction.



<b>Table 6.5.</b> % Void fraction Mean Absolute Error (MAE) in recirculation pump trip BFBT transient test			
$\left( Error_{avg} = \frac{\sum_{i=1}^n  \alpha_{sim} - \alpha_{exp} }{n} * 100 \right).$			
	Measurement height [mm]		
Correlations	683	1706	2730
TPF	0.86	1.87	3.09
TPF-TRACE	1.43	2.73	4.56

The TPF correlations are considered as validated having an error, which goes from  $\pm 0.8\%$  void fraction in low quality regions to  $\pm 5\%$  in high quality regions.

These results are similar as the results obtained with another codes as the studies of [88], [89] and [90] confirm. The TPF-TRACE correlations need to be reviewed and are not recommended for these types of simulations. They are constructed by many detailed physical descriptions of the interaction of vapor and liquid leading to several theoretical or empirically determined parameters, which are difficult to deduce from global experimental values. The original TPF approach uses less complicated models with less parameters leading to a better validation procedure. Void fraction calculations are very sensitive to the models describing momentum coupling, evaporation, and condensation. The non-linear behavior makes it difficult to find the single model being responsible for deviations from the experimental behavior.

## 6.5 General conclusions on TWOPORFLOW validation

In sections 6.1 through 6.4 the validation of pre-CHF phenomena in TWOPORFLOW using two different groups of correlations (TPF and TPF-TRACE) has been analyzed using two PSBT and two BFBT groups of tests. The calculation of thermal mixing in section 6.1 demonstrates that comparing the sub-channel temperatures obtained with both groups of correlations, the averaged difference is about  $0.094^{\circ}\text{C}$ . Both families of correlations give nearly the same quality of results for turbulent mixing and TWOPORFLOW uses a similar mixing coefficient  $\beta$  (0.05) as other validated codes.

In section 6.2 for the validation of sub-cooled boiling, the obtained results reveal that neither TPF nor TPF-TRACE correlations are capable to obtain results inside the reported experimental void fraction accuracy (0.03 absolute void fraction). However, the results nearer to the experimental data are obtained with TPF correlations and it is recommended to use this group of correlations for sub-cooled boiling.

The validation of steady state void dispersion is performed in section 6.3, in which the deviations between both groups of correlations are not larger than 0.03 void fraction having the larger deviations near the unheated rods. That is because the simple global modelling of turbulence by mixing coefficients is not enough to describe the large temperature gradients between channels with heated and unheated rods. In addition, considering two-phase flow, local condensation in the cold region plays an important role. To simulate the behavior around unheated rods CFD calculations are essential to get some insight.

Finally, in section 6.4 the simulation of transient void is investigated concluding that the TPF correlations present the experimental data better in all quality regions while the TPF-TRACE correlations show high discrepancies at low and high steam quality regions.

Considering all these conclusions, the TPF-TRACE correlations do not give any improvement compared to the simpler empirical correlations. The recommendation is to use TPF correlations.



## 7 Validation of Critical Heat Flux simulations in TWOPORFLOW with experimental data

In this section, the TWOPORFLOW capability to simulate Critical Heat Flux is validated using different experimental data performed under steady state or transient thermal hydraulic conditions and geometries like tubes and fuel assemblies. Three different CHF-methods implemented in TWOPORFLOW are validated: Biasi, Bowring, and Groeneveld LUT (described in section 5.3).

### 7.1 Becker CHF steady-state experiments

#### 7.1.1 Short test description

The Becker CHF tests have been performed at the Department of Nuclear Reactor Energy at the Royal Institute of Technology (KTH) [91] in Stockholm. The tests consist of a tube with a heated length of 7000 mm uniformly heated. The temperature is measured with thermocouples positioned every 20cm between the bottom and 3m height, at higher z levels the measurements have been made every 10 cm. The boundary conditions of the tests are:

- Outlet pressure: 6.85 MPa,
- Inlet mass flow: 496 – 3034 kg/m<sup>2</sup>s,
- Inlet temperature: 274 – 278 °C,
- Bundle power: 0.06 – 0.18 MW.

Further details of the tests are given in Annex 2 **Tables 12.7** and **12.8**. The reported experimental error in the heat flux measurement is 1% and in the location of CHF is  $\pm 5$  cm.

#### 7.1.2 TWOPORFLOW modeling

In TWOPORFLOW one dimensional pipe flow is described by distributing the wall structure material and the fluid flow area in one cell located in the x-y-plane. The flow takes place in z-direction build up by several Cartesian volume cells. Key input parameters for the code are the hydraulic diameter, the flow area and the heat exchange area of the wall structure calculated from the heated perimeter. Flow in a tube is a special case of the porous media construction explained in section 4.1, where the rod is replaced by the tube wall structure. The location of the coolant relative to the structure (inside, outside) does not play a role in the porous media description.

The different boundary conditions of the tests are defined in TWOPORFLOW as time-dependent boundary conditions at the core inlet (mass flow rate and inlet temperature) and outlet (pressure).

#### 7.1.3 Comparison of TWOPORFLOW predictions against experimental data

The TWOPORFLOW simulations have been performed for the developed model of the 14 Becker tests using three different implemented CHF models, namely the ones of Bowring, Biasi, and Groeneveld.

**Figure 7.1** shows the comparison of the CHF predicted by the code with three different correlations and the measured data as function of the mass flux for the tests is shown.

The CHF predicted with the correlations of Bowring and Groeneveld are close to the experimental ones for all mass flow rate ranges. In case of the CHF predicted by the Biasi correlation, there is a clear dependency from the mass flux, where the over-prediction increases with increasing mass fluxes (lower qualities) in most cases. Biasi shows a CHF standard deviation from the experimental data

of 9.19%, Bowring 1.30% and Groeneveld 1.43%. Biasi, which presents the larger deviations, was developed for cylindrical ducts. However, the reported deviation of this correlation is 7.26% in 4551 measured data points, and 85.5% of the points are within +/- 10% absolute deviation, which agrees with the 9.19% deviation presented in this work.

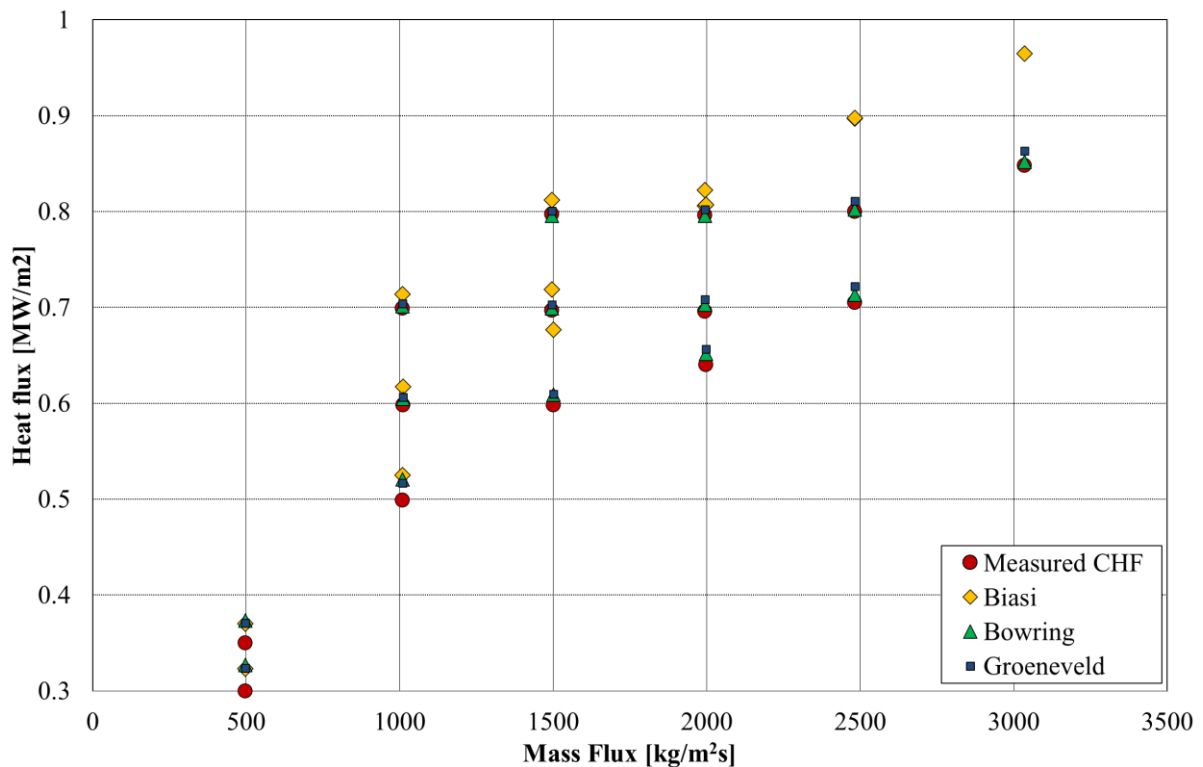


**Figure 7.1.** Comparison of measured and predicted CHF as function of the mass flux for the Becker CHF Steady State experiments.

In **Figure 7.2**, the absolute difference of the predicted and measured location of CHF-appearance is shown for all tests performed.

It can be observed that the CHF predicted by Groeneveld over-predicts the measured CHF axial location for low mass flux ( $\sim 500 \text{ kg/m}^2\text{s}$ ) and for mass fluxes higher than  $2500 \text{ kg/m}^2\text{s}$  in 4 of 6 experiments, the other 2 appear almost at the same axial height than the experimental data being under-predicted by about 0.01 m. For mass fluxes larger than  $500 \text{ kg/m}^2\text{s}$  and lower than  $2500 \text{ kg/m}^2\text{s}$  TWOPORFLOW under-predicts the CHF-location using Groeneveld LUT.

The CHF-predicted by Bowring correlation shows similar behavior than the one of Groeneveld. This correlation over-predicts the measured CHF-location for low mass flux ( $\sim 500 \text{ kg/m}^2\text{s}$ ) and for mass fluxes larger than  $2500 \text{ kg/m}^2\text{s}$  in 3 of 6 experiments, the other 3 appear almost at the same axial height compared to the experimental data being under-predicted in about 0.05 m for mass fluxes  $\sim 2000 \text{ kg/m}^2\text{s}$  and 0.01 m for mass fluxes  $\sim 2500 \text{ kg/m}^2\text{s}$ . In mass fluxes larger than  $500 \text{ kg/m}^2\text{s}$  and lower than  $2500 \text{ kg/m}^2\text{s}$  TWOPORFLOW under-predicts the CHF-location using Groeneveld LUT.

On the contrary, the CHF-location calculated by Biasi is over-predicted for mass fluxes  $\sim 500 \text{ kg/m}^2\text{s}$  and largely under-predicted in larger mass fluxes. The averaged absolute differences for Biasi, Bowring and Groeneveld methods are 0.20, 0.10 and 0.13 m, correspondingly.

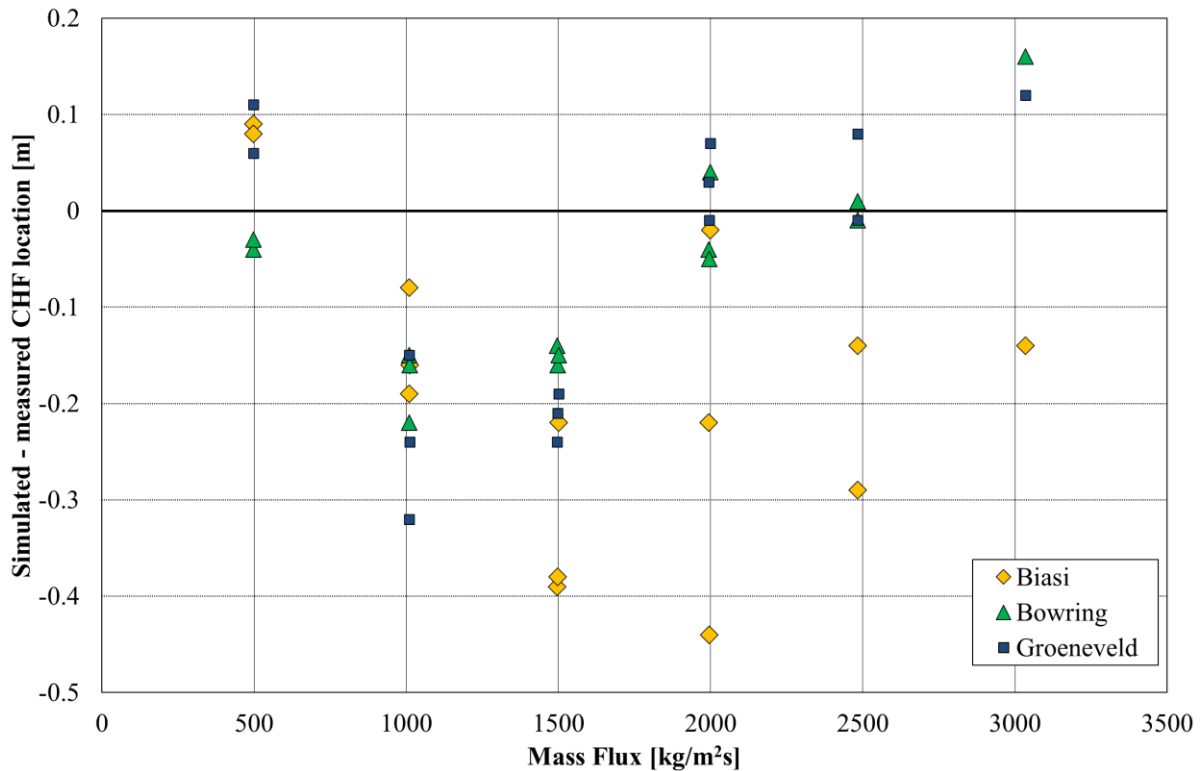


**Figure 7.2.** Difference between the appearance of CHF in simulated and experimental data as function of the mass flux for the Becker CHF Steady State experiments.

Generally, the Biasi correlations predicts the CHF-value and the axial location with the largest deviations, 9.19% for CHF and  $\pm 0.20$  m for CHF axial appearance. The higher deviations are in lower steam qualities. The Bowring correlation, on the other hand, presents the most accurate results with deviations of 1.30% for CHF and  $\pm 0.10$  m for CHF axial appearance. Groeneveld LUT shows similar results than the Bowring correlation with a deviation of 1.43% for CHF and  $\pm 0.13$  m for CHF axial appearance.

## 7.2 BFBT CHF steady state tests

### 7.2.1 Short test description

In order to validate the prediction capability of TWOPORFLOW regarding safety-relevant phenomena in the core of BWR, the BFBT-test data is used. For this purpose, 111 steady-state critical power BFBT-experiments of the Exercise 1 of the Phase II of the BFBT benchmark are simulated. The assemblies used in this benchmark are of type 4 as described in **Figure 6.17** of section 6.3.1, having an 8 x 8 pin arrangement with a single central water rod (60 fuel rods) and an axial heated length of 3708 mm.

Three different variations of assembly type 4 are used, C2A, C2B and C3. Assemblies C2A and C3 have lateral power distribution as described in **Figure 7.3-A** corresponding to an assembly at the beginning of the cycle with a cosine axial power shape and an inlet peak power shape. Assembly C2B has a lateral power distribution corresponding to the middle of the cycle as presented in **Figure 7.3-B** with cosine axial power shape. The assemblies have seven spacers along the height with  $\xi = 1.2$ .

A summary of the boundary conditions is presented in **Table 7.1**.

Table 7.1. Boundary conditions value ranges of steady-state Critical Power benchmark BFBT tests.				
Assembly	Pressure [MPa]	Flow [kg/m <sup>2</sup> s]	Power [MW]	Inlet temperature [°C]
C2A	7.2	292.95-1929.15	3.20-10.0	261.59-283.16
C2B	7.2	291.49-1903.61	3.45-10.7	262.42-283.42
C3	7.2	291.49-1908.6	3.31-10.2	263.01-283.13

Further details of the boundary conditions and axial power shapes are to be found in Annex 2 Tables 12.9 through 12.12 and Figure 12.2.

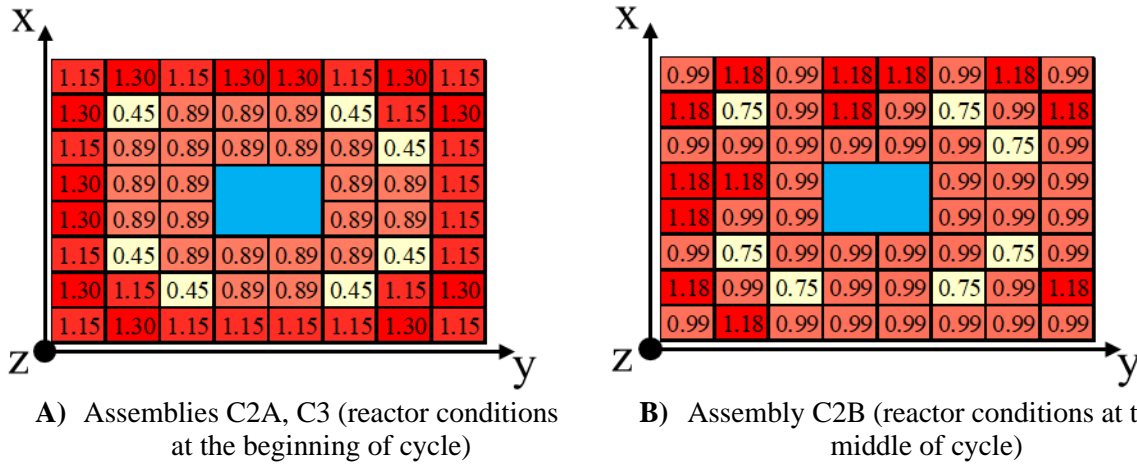
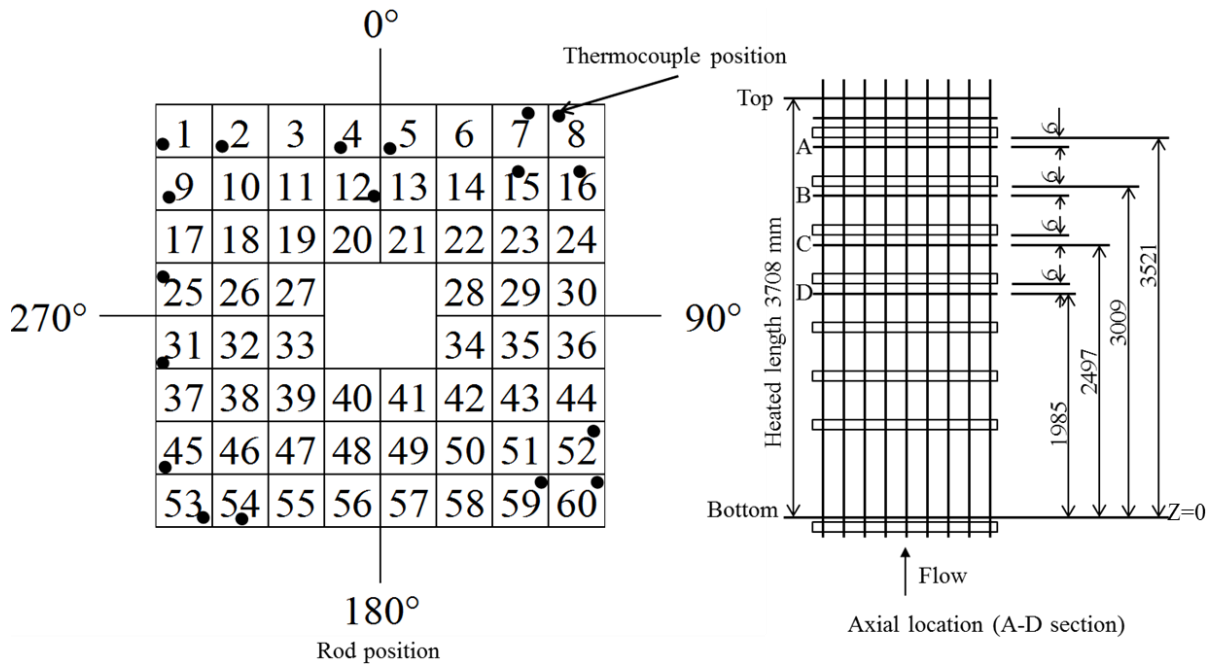


Figure 7.3. Lateral normalized power distribution BFBT.

The critical power is measured by slowly increasing the bundle power while monitoring the individual heater rod thermocouple signals, measuring the local cladding temperature with an accuracy of 1.5°C. The power measurement has an accuracy of 1.5%. The critical power is defined when the peak rod surface temperature became 14°C higher than the steady-state cladding temperature level. Dry-out is observed in the peak power rod located at the peripheral row adjacent to the channel box. The boiling transition is always observed just upstream of the spacers.

Figure 7.4 shows a summary of the radial and axial thermocouple positions (further details of the thermocouples positions are to be found in Annex 2, Figures 12.3 through 12.5). The thermocouples are located at different circumferential angles in a rod, some rods have more than one thermocouple attached. In TWOPORFLOW it is not possible to calculate the circumferential position of CHF. Due to the porous medium approach, such details cannot be resolved. For that reason, in this study the experimental temperatures are compared with the averaged rod temperatures in the sub-channel, where the CHF appears. Measurements are in the rods 1, 2, 4, 8, 12, 25, 31, 45, 53, 59, and 60, at different axial locations A (3521 mm), B (3009 mm), C (2497 mm), D (1985 mm), and at different circumferential angles.



**Figure 7.4.** Definition of thermocouple radial and axial position with the radial location of the TC (black dots) for the BFBT CHF Steady State Tests.

### 7.2.2 TWOPORFLOW modeling of the BFBT test bundle

The BFBT-test section is modeled using a pin-centered approach. Hence, the test section is represented by of 8x8 Cartesian cells, where in each cell a rod is considered, except for the four central cells, where each cell includes a quarter of the water rod, **Figure 7.5**. In axial direction, the model consists of 24 equidistant cells of 154.5 mm. The axial and radial power distribution as used in the tests are also given as input in TWOPORFLOW, see Section 7.2.1.

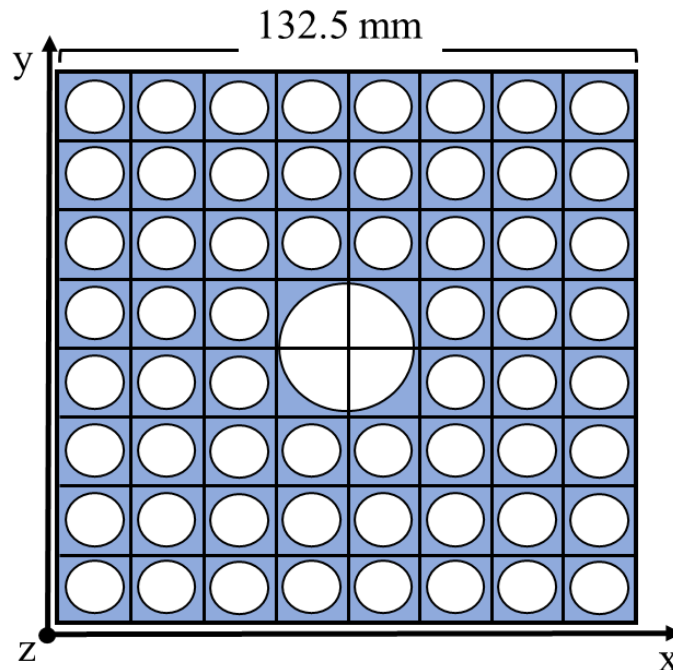


**Figure 7.5.** View from the top of the TWOPORFLOW's model of NUPEC BFBT phase II, Critical Power, exercise 1 steady state benchmark.

### 7.2.3 Comparison of the TWOPORFLOW predictions with the experimental data

Using the BFBT-experiments, the steady state CHF tests have been simulated with TWOPORFLOW using the boundary conditions given in **Table 7.1** and three different CHF-correlations i.e., Biasi, Bowring and Groeneveld.

In **Figures 7.6, 7.7, and 7.8** the absolute error i.e. the difference of the predicted and measured CHF-value (*Simulated – Experimental CHF*) is plotted versus the mass flux for the assembly C2A, C2B and C3. Each point represents the CHF value for a test.

In **Figure 7.6**, it can be observed that the Bowring correlation over-predicts the CHF in all the cases. The over-prediction for mass fluxes lower than 600 kg/m<sup>2</sup>s are not higher than 0.02 MW/m<sup>2</sup>. For mass fluxes from 880 to 1930 kg/m<sup>2</sup>s the over-predictions are in a range of 0.05 to 0.1 MW/m<sup>2</sup>. Biasi and Groeneveld LUT present similar behavior. Both correlations under-predict most of the cases for fluxes lower than 600 kg/m<sup>2</sup>s presenting the results in a range of 0 to 0.041 and 0 to 0.39 MW/m<sup>2</sup> CHF difference. For mass fluxes from 880 to 1930 kg/m<sup>2</sup>s Biasi over-predicts the CHF in a range of 0.01 to 0.06 MW/m<sup>2</sup> and Groeneveld in a range of 0.011 to 0.11 MW/m<sup>2</sup>. The averaged CHF deviations are 0.03, 0.06 and 0.05 MW/m<sup>2</sup> for Biasi, Bowring and Groeneveld correspondingly.

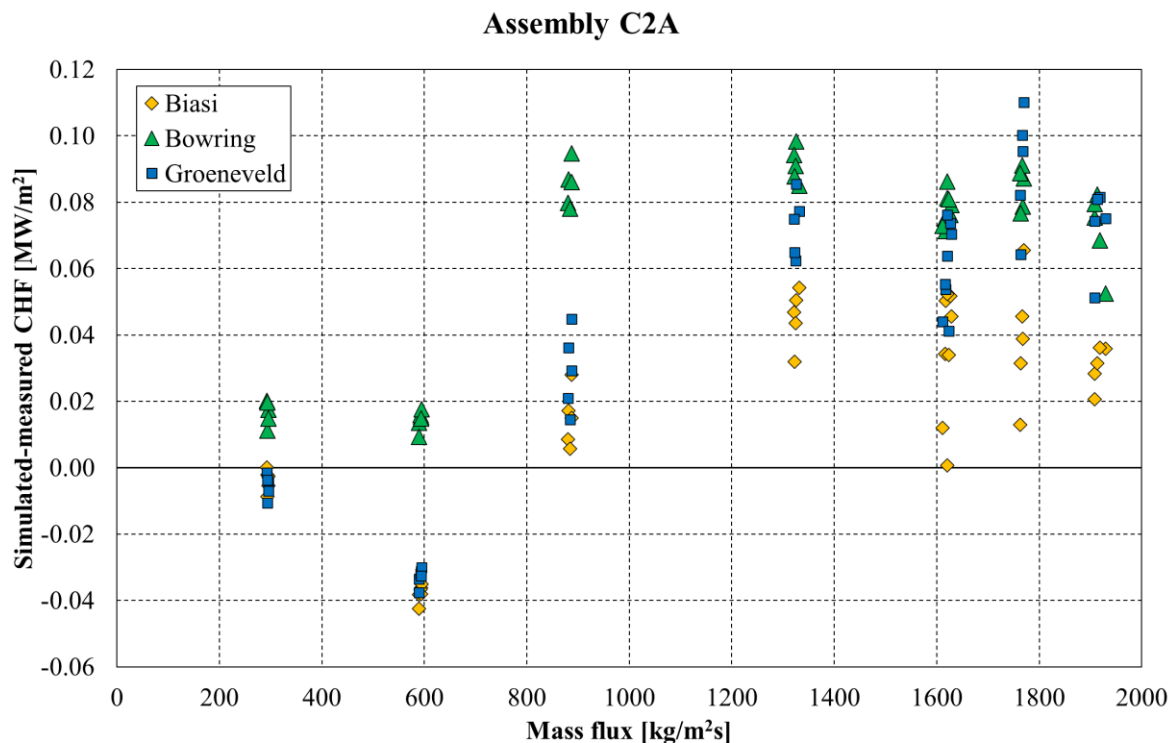


**Figure 7.6.** The absolute error of the CHF-predictions (simulated-experimental CHF) with respect to the mass flux using Biasi, Bowring, and Groeneveld LUT in assembly C2A for the BFBT CHF Steady State Tests.

In **Figure 7.7**, it can be observed that the Biasi correlation over-predicts the CHF in all the cases with mass fluxes from 580 to 1930 kg/m<sup>2</sup>s in a range of 0.01 and 0.09 MW/m<sup>2</sup> and for mass fluxes ~300 kg/m<sup>2</sup>s the differences are in a range of 0 to an under-prediction of 0.005 MW/m<sup>2</sup>. Bowring over-predicts all the cases from 300 to 1320 kg/m<sup>2</sup>s in a range of 0.02 to 0.15 MW/m<sup>2</sup>. The cases with mass flux ~1610 kg/m<sup>2</sup>s have differences in a range of ±0.01 MW/m<sup>2</sup> and for higher mass fluxes the under-predictions are in a range of 0.01 to 0.07 MW/m<sup>2</sup>. Groeneveld LUT has a similar behavior as Bowring with over-prediction in all the cases from 580 to 1320 kg/m<sup>2</sup>s. For mass fluxes ~300 kg/m<sup>2</sup>s the differences are in a range of 0 to an under-prediction of 0.005 MW/m<sup>2</sup>. The cases with mass flux ~1610 kg/m<sup>2</sup>s have differences in a range of ±0.02 MW/m<sup>2</sup> and for higher mass fluxes the under-predictions are in a range of 0.01 to 0.07 MW/m<sup>2</sup>. All three correlation show an increase in CHF difference from 290 to 890 kg/m<sup>2</sup>s



and a decrease for higher mass fluxes. The averaged CHF deviations are 0.04, 0.05 and 0.04 MW/m<sup>2</sup> for Biasi, Bowring and Groeneveld correspondingly.

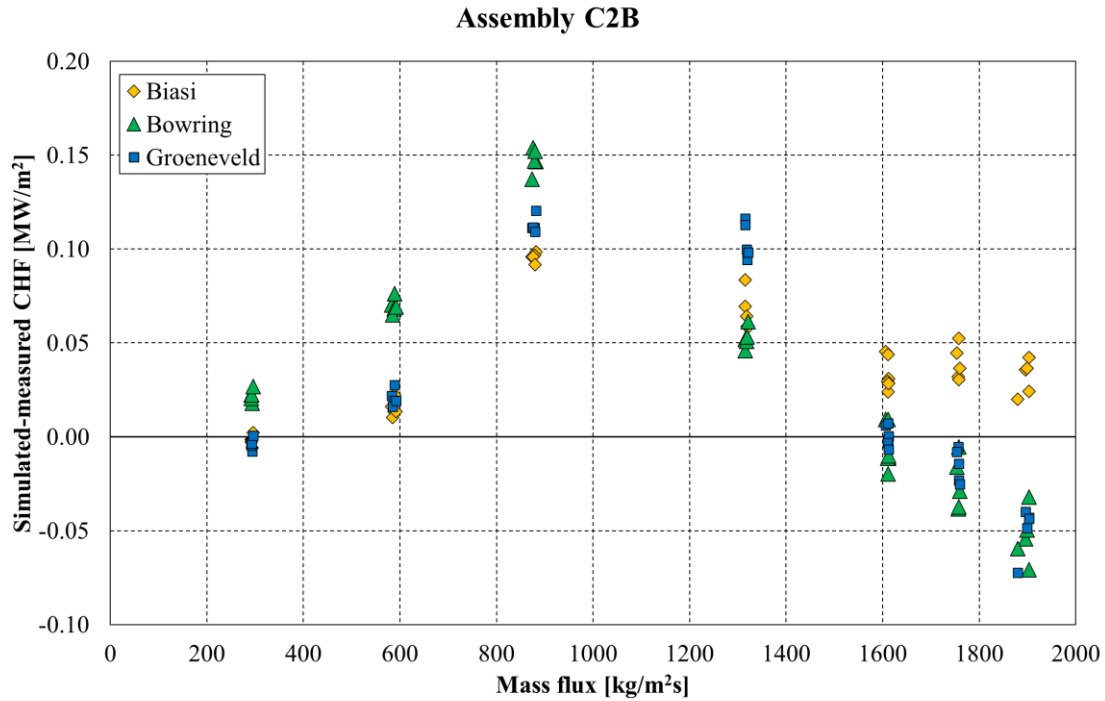


**Figure 7.7.** Variation of the CHF error (simulated-experimental CHF) with respect to the mass flux using Biasi, Bowring, and Groeneveld LUT in assembly C2B for the BFBT CHF Steady State Tests.

In **Figure 7.8** it can be observed that all the methods over-predict the CHF from mass fluxes from 870 to 1910 kg/m<sup>2</sup>s, Biasi in the range of 0.01 to 0.11 MW/m<sup>2</sup>, Bowring in the range of 0.06 to 0.14 MW/m<sup>2</sup>, and Groeneveld in the range of 0.04 to 0.15 MW/m<sup>2</sup>. For lower fluxes Biasi presents a range from 0 to an under-prediction of 0.05 MW/m<sup>2</sup>, Bowring from 0 to an under-prediction of 0.004 MW/m<sup>2</sup>, and Groeneveld from 0 to 0.04 MW/m<sup>2</sup>. The averaged CHF deviations are 0.07, 0.08 and 0.09 MW/m<sup>2</sup> for Biasi, Bowring and Groeneveld correspondingly.

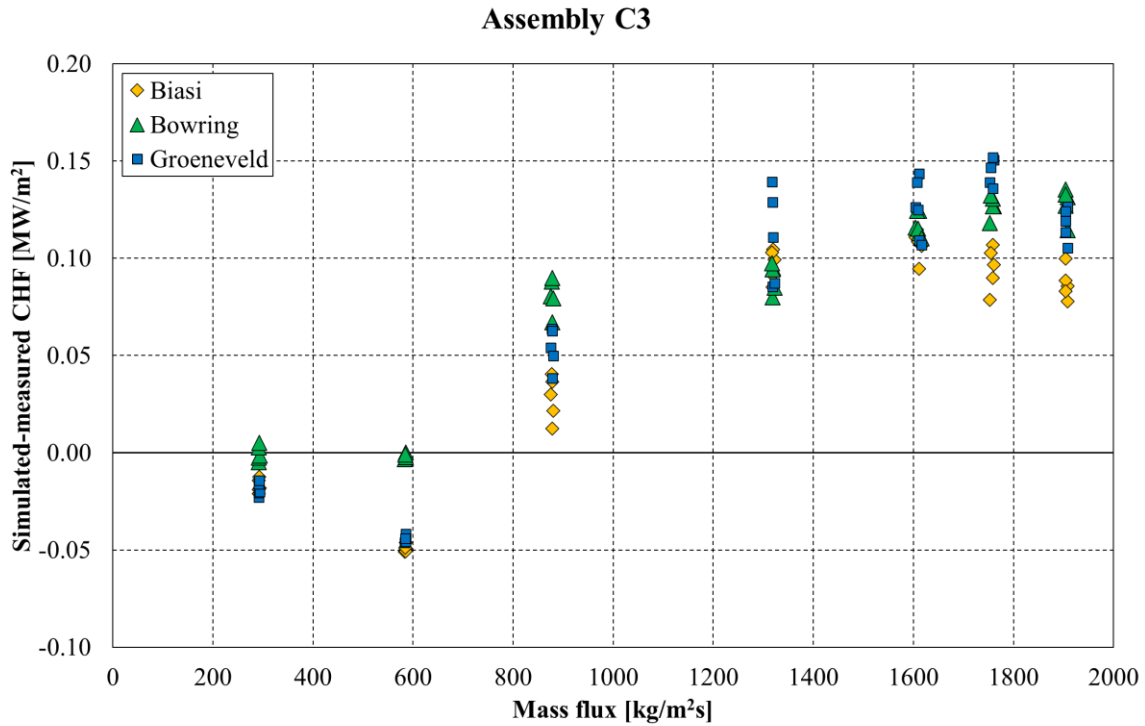


**Figure 7.8.** Variation of the CHF error (simulated-experimental CHF) with respect to the mass flux using Biasi, Bowring, and Groeneveld LUT in assembly C3 for the BFBT CHF Steady State Tests.

In order to investigate the correct prediction of the lateral CHF location occurrence, the BFBT-assembly is divided into three regions: 1, 2, and 3, see **Figure 7.9**. In the experimental data CHF appears 91 times in region one, 20 times in region two and there are no cases in region three. The Biasi correlation shows exactly the same number of appearances per region, Bowring 82 times in region one, 29 times in region two and no cases in region three, Groeneveld show 84 appearances in region one, 27 appearances in region two and no cases in region three.

1	1	1	1	1	1	1	1
1	2	2	2	2	2	2	1
1	2	3	3	3	3	2	1
1	2	3	0	0	3	2	1
1	2	3	0	0	3	2	1
1	2	3	3	3	3	2	1
1	2	2	2	2	2	2	1
1	1	1	1	1	1	1	1
	Experimental	Biasi	Bowring	Groeneveld			
Region 1	91	91	82	84			
Region 2	20	20	29	27			
Region 3	0	0	0	0			

**Figure 7.9.** Radial location of CHF in experimental data and simulated data for the BFBT CHF Steady State Tests.

Moreover, the axial appearance of CHF as predicted by TWOPORFLOW is compared against the experimental data. In the benchmark documentation it is mentioned that the dry-out is observed

upstream the spacers, but an exact axial position is not mentioned. The thermocouples are located only at four positions downstream the spacers A (3521 mm), B (3009 mm), C (2497 mm) and D (1985 mm) as shown in **Figure 7.4**.

Additionally, and possibly because of the axial power distribution of the assemblies, in type C2A and C2B (cosine power distribution) just in the upper 3 (A, B, C) and 2 (A, B) spacers, correspondingly, measurements have been taken. In assembly C3 the measurements have been done at all the mentioned spacers. Due to these inconsistencies in the measurements, it is not possible to know the exact height at which CHF appears in the different experiments.

However, a comparison between the axial CHF appearance obtained with TWOPORFLOW and the measured data is done, taking as reference the location of the thermocouples.

The mentioned inconsistencies in the measurements could lead to an apparent under-prediction of the data in TWOPORFLOW, mostly in the assemblies C2A and C2B.

The deviation of simulation results compared to the experiments is considered to be  $\pm 0.512$  m which is the distance between the spacers. In **Figure 7.10** it is shown that all the correlations present values inside the given deviation, but Bowring in assembly C3. The behavior of Bowring dependent on the axial power shape is remarkable because no power shape correction factor is included in all correlations.

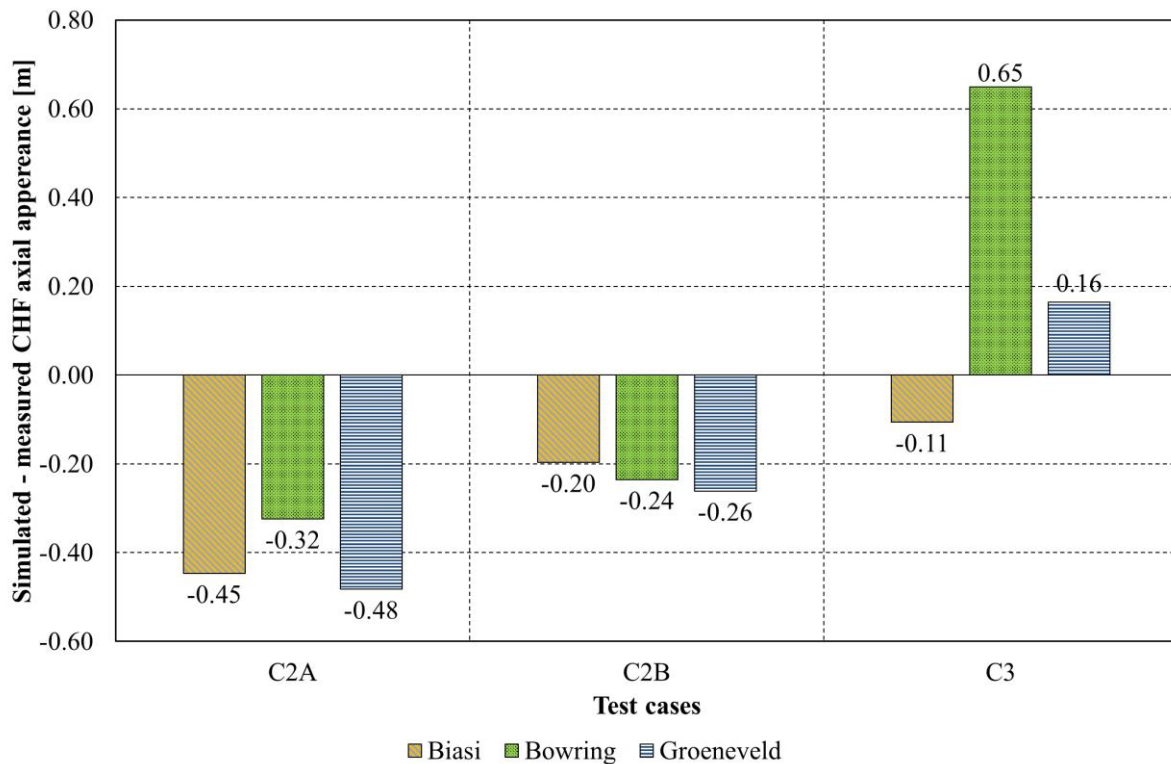


**Figure 7.10.** Difference of simulated minus measured CHF axial appearance in fuel assemblies' type C2A, C2B and C3 for the BFBT CHF Steady State Tests.

Summarizing, the Biasi correlation gives the better CHF values related to the investigated experiments, but in general the results of the three correlations are similar.

In addition, the Biasi correlation is the most accurate to predict the lateral CHF appearances.

For the axial location of CHF all correlations present values inside the given deviation, with the exception of Bowring in assembly C3.

## **7.3 BFBT CHF transient tests**

### **7.3.1 Short test description**

Transient BFBT-tests have been performed for each assembly arrangement C2A and C3, where the CHF is measured. The thermal hydraulic conditions of these tests are representative of two BWR-transients, namely a turbine trip with bypass and for a recirculation pump trip. In the post-boiling transition test series, the rod surface temperature is measured under the quasi-steady-state condition beyond the boiling transition. The main purpose of this test series is the quantification of the post-dry-out heat transfer coefficient.

### **7.3.2 TWOPORFLOW modeling**

The TWOPORFLOW model of the assemblies C2A and C3 is the same as the one developed to analyze the steady-state CHF test, Section 7.2.2. It is worth to mention that the C3 assembly has an inlet-peak axial power distribution (**Annex 2, Figure 12.2**) and the radial power distribution of both assemblies corresponds to the beginning of the cycle (**Figure 7.3-A**).

The tests have been modeled in TWOPORFLOW using a pin centered sub-channel approach of 8x8 sub-channels with a central water rod and 24 axial cells as presented in **Figure 7.5**. The axial mesh is chosen to have the same number of cells as number of power axial distribution values given in the benchmark, in which 24 axial cells with a length of 154.5 mm are given. The measurements of these tests have been made with the same arrangement described in section 7.2.1.

### **7.3.3 Description of the turbine trip without by-pass CHF tests**

In the turbine trip without by-pass, the power, pressure at outlet, temperature, and flow rate remain constant for the first 22 seconds. Afterwards they change dramatically: the fast closure of the turbine isolation valve leads to the propagation of a pressure wave from the main steam line to the core, and this in turn leads to the collapse of the void, a higher coolant density and, in consequence, a better moderation of the neutrons leading to a power rise. In **Figure 7.11** the boundary conditions normalized to one (divided by the conditions at initial time) for this test are shown which are used in TWOPORFLOW for the simulation.

The initial boundary conditions of the tests are:

- Outlet pressure: 7.1 MPa,
- Inlet mass flow: 42 t/h,
- Inlet temperature: 276.7°C assembly C2A and 275.5 °C assembly C3,
- Bundle power: 8.5 MW.

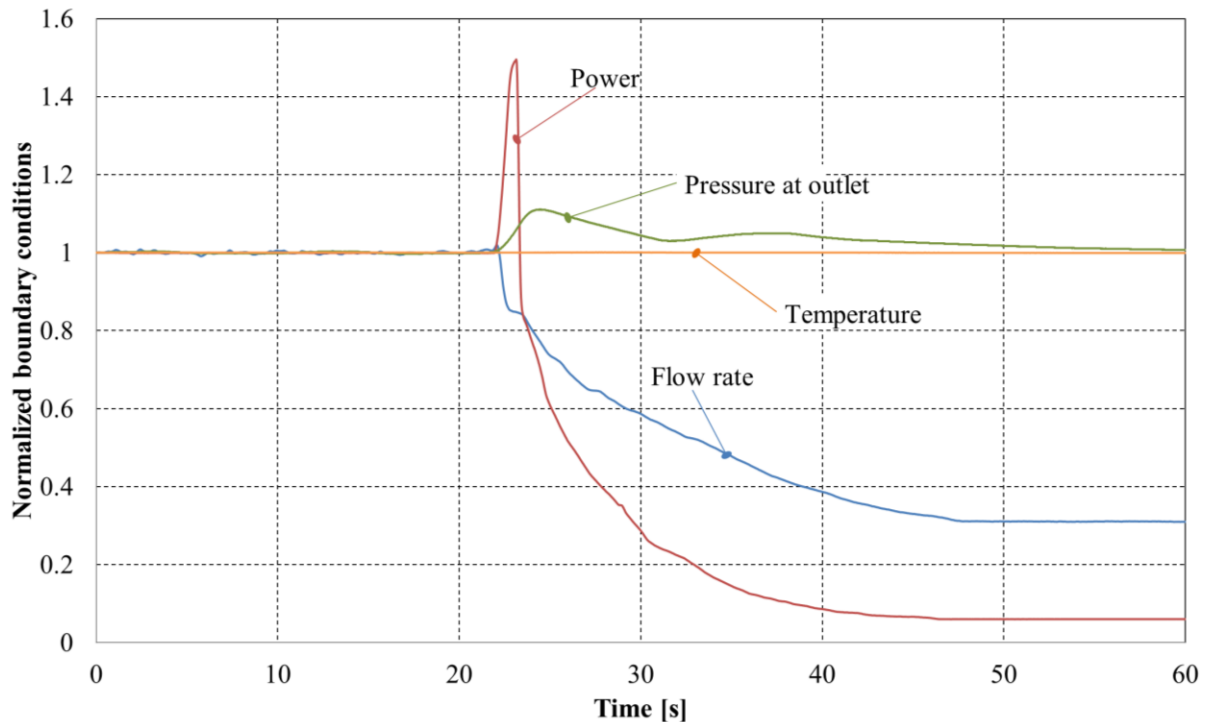


**Figure 7.11.** Normalized boundary conditions for the BFBT turbine trip without bypass transient CHF test (transient starts at 22s).

### 7.3.4 Comparison of the CHF predicted by TWOPORFLOW against the measured data

The transient CHF-test have been simulated with TWOPORFLOW using three correlations: Biasi, Bowring and Groeneveld. In the test, CHF is reached at 23s, at the top of the spacers.

In **Table 7.2**, a comparison of the CHF predicted by TWOPORFLOW with the three CHF-correlations and the experimental value for the two assembly arrangements is shown. There is also the time for the appearance of CHF included.

Assembly	Experimental		Biasi		Bowring		Groeneveld	
	CHF [MW/m <sup>2</sup> ]	Time [s]	CHF [MW/m <sup>2</sup> ]	Time [s]	CHF [MW/m <sup>2</sup> ]	Time [s]	CHF [MW/m <sup>2</sup> ]	Time [s]
C2A	1.19	23	1.21	23.06	1.23	23.26	1.20	23.02
C3	1.23	23	1.24	22.96	1.25	23.16	1.24	22.94

In general, the predicted CHF and the time values are close to the measured ones. The CHF appears less than a second later than in the tests. In **Figure 7.12**, the differences between the CHF predicted by TWOPORFLOW with different correlations and the experimental results is exhibited. The best predictions of the CHF are performed by TWOPORFLOW with the Groeneveld correlation.

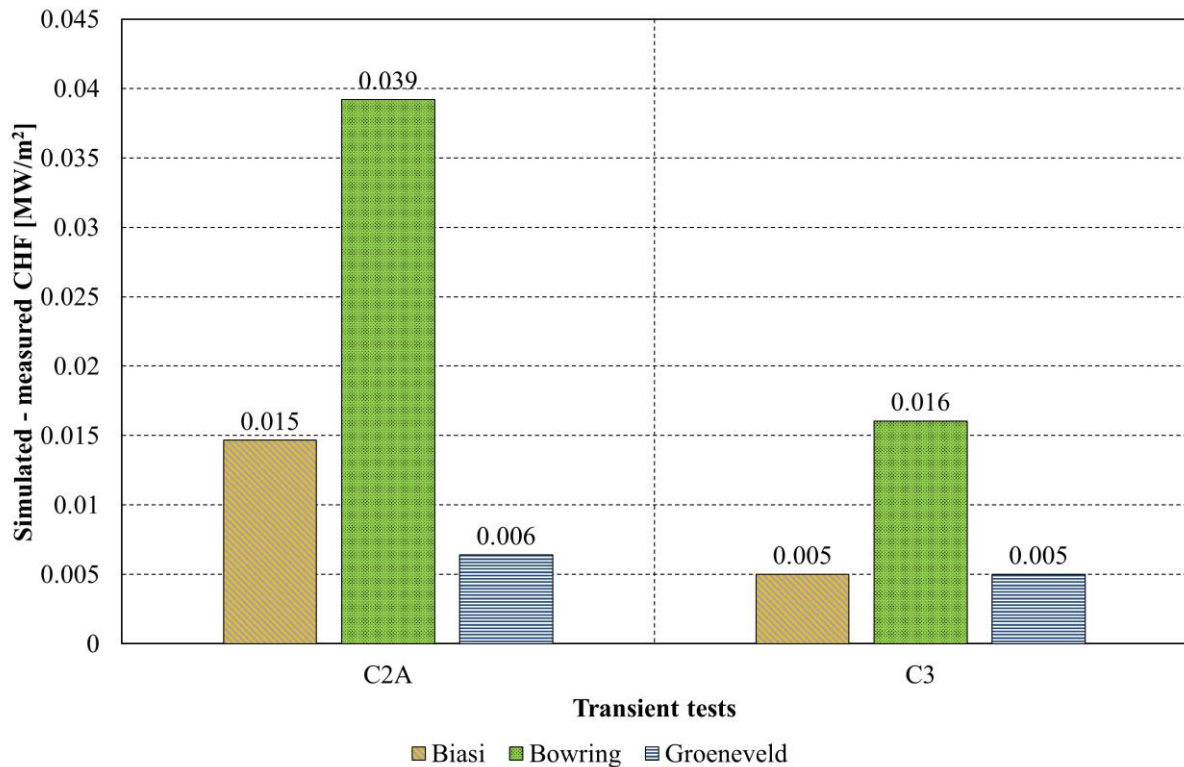


**Figure 7.12.** TWOPORFLOW simulation results minus measured CHF data in turbine trip without by-pass BFBT critical power transient benchmark using Biasi and Bowring correlations and Groeneveld LUT for assembly types C2A and C3.

In addition, the axial location of the CHF-appearance predicted by TWOPORFLOW is compared against the experimental data. As described in section 7.2.3, there is not an exact measured axial position, but the position of the thermocouples, considering the measurements to have a deviation of  $\pm 0.512$  m which is the distance between the spacers. The measurements have been done in the same way than in the steady state tests at the spacers A, B and C in assembly C2A and A, B, C, and D in assembly C3 (**Figure 7.4**).

In the experiments, the CHF is being detected first at spacer B (3009 mm) in both assemblies.

**Figure 7.13** shows that the CHF-appearance for the assembly C2A predicted the Biasi and Bowring correlations are located upstream the spacer B, while the one predicted by using the Groeneveld correlation is located below this spacer, all the cases are inside the given deviation. For the C3 assembly -with an inlet peak power distribution-, the CHF predicted with TWOPORFLOW using the Biasi correlation appears a little downwards the spacer while the CHF predicted with TWOPORFLOW using the Bowring correlation is located just 0.081 m upwards of the spacer. Only the application of the Groeneveld correlation appears outside the given deviation at a height near the spacer D.

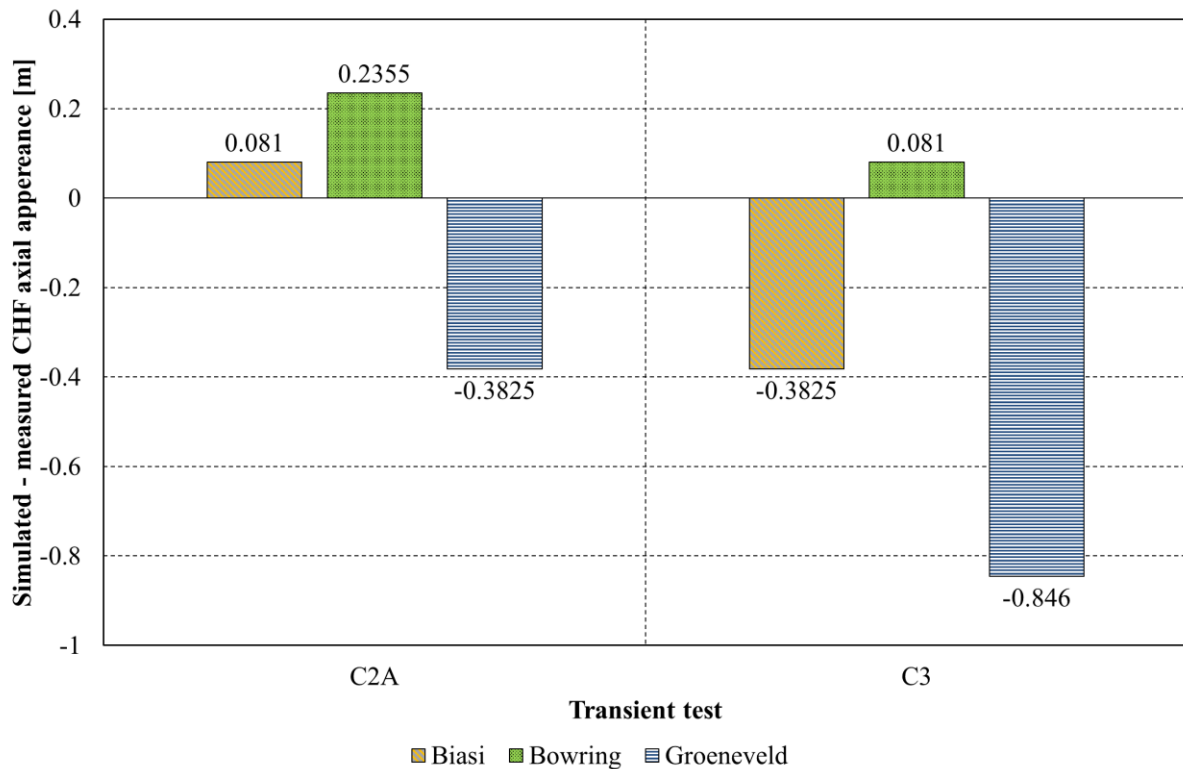


**Figure 7.13.** Deviation of the CHF predicted by TWOPORFLOW with different correlations from the measured axial location for the turbine trip without by-pass BFBT critical power transient benchmark using Biasi and Bowring correlations and Groeneveld LUT for assembly types C2A and C3.

### 7.3.5 Description of the recirculation pump trip CHF tests

Due to the recirculation pump trip, the mass flow rate starts to decrease after 22 seconds leading to an increase of the void fraction and hence to a decrease of the neutron moderation and associated with it of the fission power. During the next 30 seconds, the mass flow stabilizes at 1/3rd of the nominal value. **Figure 7.14** shows the evolution of the boundary conditions normalized to one (divided by the conditions at initial time) for this test.

The initial boundary conditions of the tests are:

- Outlet pressure: 7.2 MPa,
- Inlet mass flow: 46.2 t/h,
- Inlet temperature: 278.1 °C assembly C2A and 277.4 °C assembly C3,
- Bundle power: 8.5 MW.

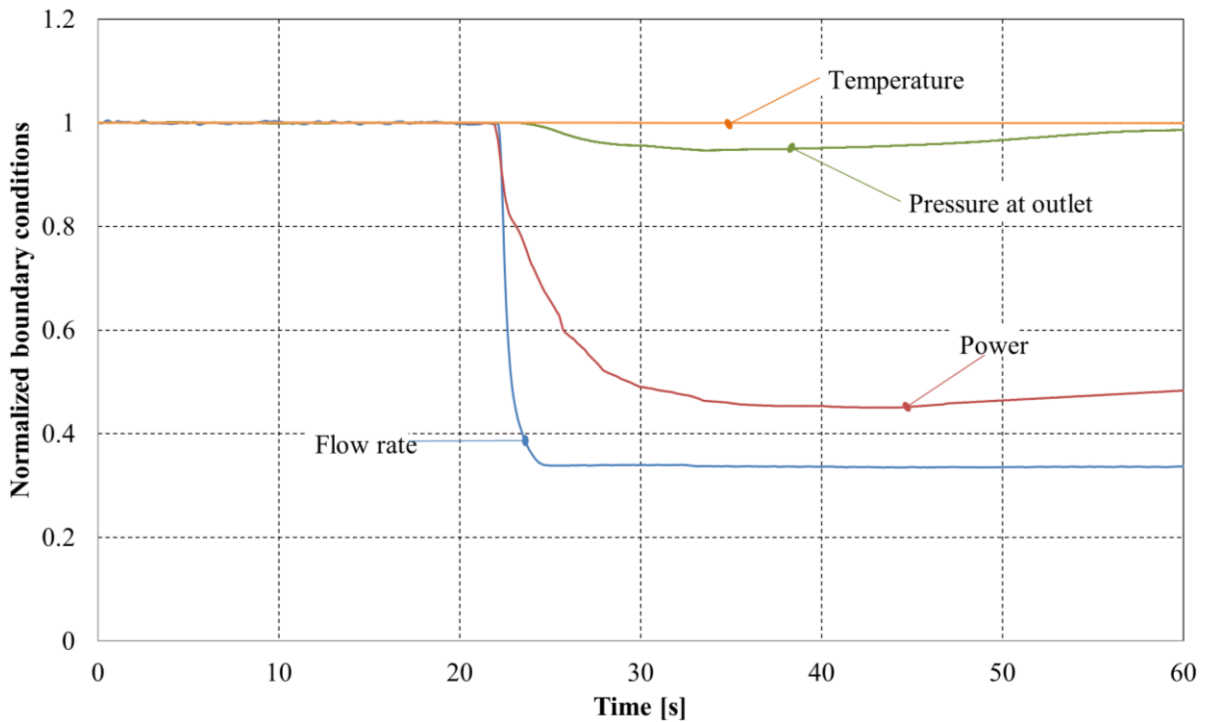


**Figure 7.14.** Evolution of the normalized BFBT transient boundary conditions of the recirculation pump trip CHF test.

### 7.3.6 Comparison of the CHF predicted by TWOPORFLOW against the measured data

As mentioned, the steady state is maintained until 22s, CHF is reached at 23s.

In **Table 7.3**, a comparison of the CHF measured in the two assemblies C2A and C3 with the CHF predicted by TWOPORFLOW with different CHF-correlations is presented. Considering that the time measured for the appearance of CHF amounts 23 s, it can be stated that the predicted CHF values are close to the measured ones.

**Table 7.3.** Comparison of CHF and the time of appearance predicted by TWOPORFLOW with different correlations with experimental data.

Assembly	Experimental		Biasi		Bowring		Groeneveld	
	CHF [MW/m <sup>2</sup> ]	Time [s]	CHF [MW/m <sup>2</sup> ]	Time [s]	CHF [MW/m <sup>2</sup> ]	Time [s]	CHF [MW/m <sup>2</sup> ]	Time [s]
C2A	0.75	23	0.74	23.16	0.73	23.74	0.74	23.18
C3	0.67	23	0.64	23.58	0.61	23.98	0.63	23.60

In **Figure 7.15**, the absolute difference between the CHF simulated with different correlations and the experimental is shown. There it can be observed that the TWOPORFLOW -predictions always under-predict the measured CHF. Consider that the steam quality increases suddenly in the tests, Again, TWOPORFLOW with the correlations of Biasi and Groeneveld predicts the smallest deviations from the data.



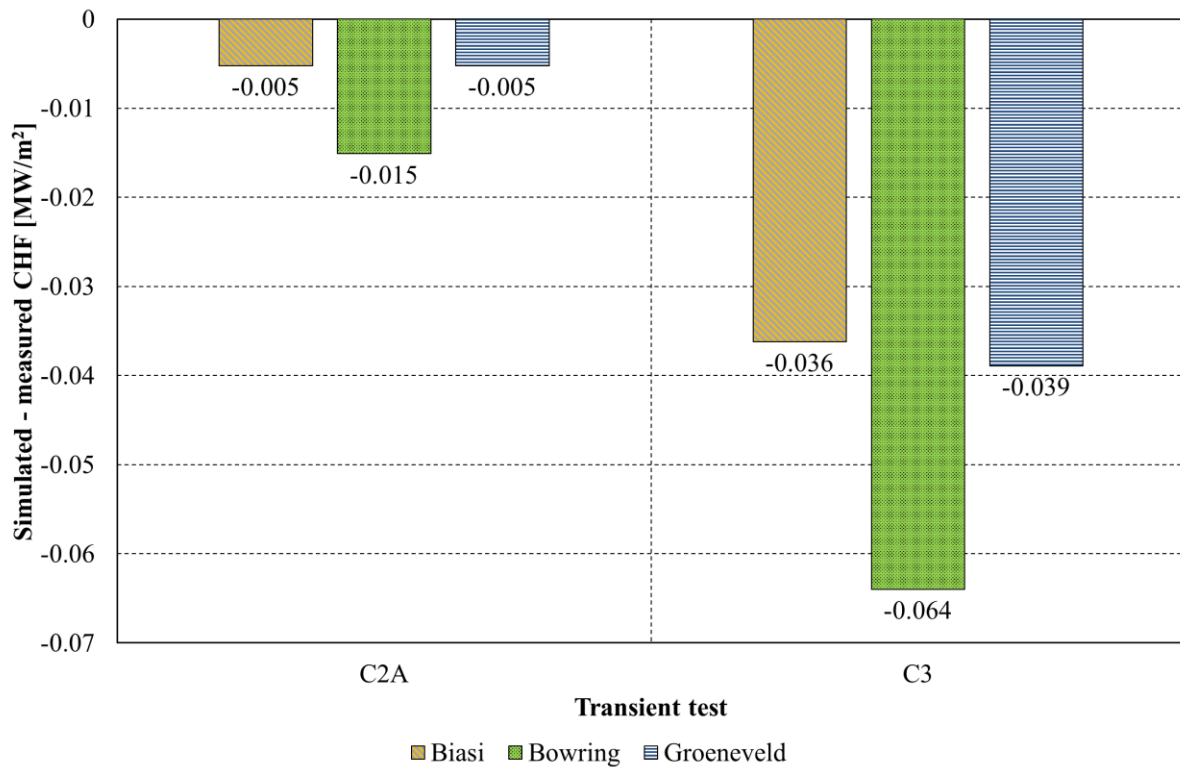


**Figure 7.15.** Deviation of the TWOPORFLOW CHF-simulations from the measured data using Biasi and Bowring correlations and Groeneveld LUT in case of the recirculation pump trip BFBT critical power transient benchmark for assembly types C2A and C3.

According to the tests, the CHF appears at spacer B (3009 mm) in assembly type C2A and at spacer C in assembly type C3. Applying again the  $\pm 0.512$  m criterion explained in section 7.2.3, it can be observed in **Figure 7.16** that the CHF predictions with Biasi and Bowring are upstream the thermocouple at position B, while the ones using the Groeneveld correlation appear below this spacer. For the assembly C3 the CHF predicted by TWOPORFLOW with the Biasi and Bowring correlations are a little downwards spacer C and one predicted with the Groeneveld correlation is upwards of this spacer. All the cases are inside the given deviation.

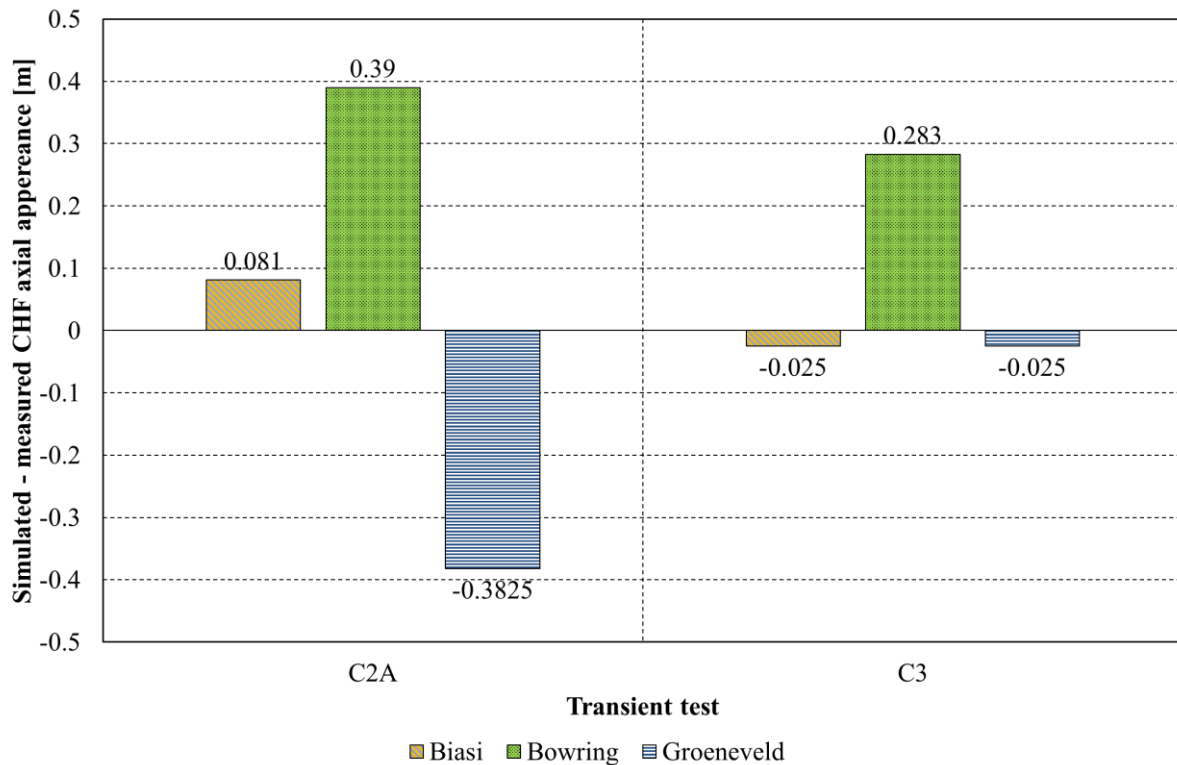


**Figure 7.16.** Deviation of the location of the CHF appearance predicted by TWOPORFLOW from the measured data using Biasi and Bowring correlations and Groeneveld LUT in case of the recirculation pump trip BFBT critical power transient benchmark for assembly types C2A and C3.

#### 7.4 General conclusions regarding the TWOPORFLOW CHF model validation

The prediction capability of TWOPORFLOW using three CHF-correlations is validated based on the BFBT CHF data provided by the benchmark.

For the Becker CHF steady state experiments (tubes) TWOPORFLOW shows the larger deviations using the Biasi correlation 9.19% for CHF and  $\pm 0.20$  m for CHF axial appearance. However, the correlation reports a deviation of 7.26% in 4551 data points, and 85.5% of the points are within  $\pm 10\%$  absolute deviation, which agrees with the 9.19% deviation presented in this work. The Bowring correlation, on the other hand, presented the most accurate results with deviations of 1.30% for CHF and  $\pm 0.10$  m for CHF axial appearance. Groeneveld LUT shows similar results than the Bowring correlation with deviation of 1.43% for CHF and  $\pm 0.13$  m for CHF axial appearance.

In the case of the BFBT CHF steady state tests, for assembly C2A the correlations present CHF deviations of 0.03, 0.06 and 0.05 MW/m<sup>2</sup> for Biasi, Bowring and Groeneveld correspondingly. In the case of assembly C2B the averaged CHF deviations are 0.04, 0.05 and 0.04 MW/m<sup>2</sup> for Biasi, Bowring and Groeneveld correspondingly. For assembly C3 the averaged CHF deviations are 0.07, 0.08 and 0.09 MW/m<sup>2</sup> for Biasi, Bowring and Groeneveld correspondingly.

The lateral and axial appearance of CHF was studied for BFBT CHF steady states as well. For the lateral appearance, the assembly was divided in 3 regions. In the experimental data, 91 times CHF appears in region one, 20 times in region two and there are no cases in region three. The Biasi correlation shows exactly the same number of appearances per region, Bowring 82 times in region one, 29 times in region two and no cases in region three, Groeneveld show 84 appearances in region one, 27 appearances in region two and no cases in region three.

For the axial CHF appearance in BFBT steady state tests, the deviation of the experiments is inside the deviation of  $\pm 0.512$  m which is the distance between the spacers and all the correlations present values inside the given deviation, but Bowring in assembly C3.

In the case of BFBT transient tests, the deviation from the measured data observed with Biasi correlation is  $-0.005 \text{ MW/m}^2$  and  $-0.036 \text{ MW/m}^2$ , for assemblies C2A and C3 correspondingly. For Bowring  $-0.015 \text{ MW/m}^2$  and  $-0.064 \text{ MW/m}^2$  for assemblies C2A and C3 correspondingly. For Groeneveld  $-0.005 \text{ MW/m}^2$  and  $-0.039 \text{ MW/m}^2$  C2A and C3 for assemblies C2A and C3 correspondingly. The axial appearance is inside the given deviation in all the cases.



## 8 Application of TWOPORFLOW for the thermal hydraulic analysis of BWR-cores

To demonstrate the prediction capability of the extended and validated TWOPORFLOW code versions, two different BWR-cores have been selected:

- The core of the Nuclear Power Plant Oskarshamn-2, and
- The core of the Laguna Verde Nuclear Power Plant Unit 1.

For the core analysis, only the TPF-correlation sets with the Groeneveld LUT for CHF calculation will be used.

### 8.1 Thermal hydraulic analysis of the Oskarshamn-2 core

#### 8.1.1 Short description of the core and thermal hydraulics parameters

The Oskarshamn-2 core has an active diameter of 3.672 m, a thermal power of 1800 MW. and an active length of 3.712 m [92]. It consists of 444 fuel assemblies of 4 different types and 109 control elements of cross-type.

The four different types of assemblies are:

- Type 1 has 64 fuel rods and 6 spacers with  $\xi = 0.598$ . There are 232 type 1 assemblies in the core. The control rods enter through this kind of assembly (**Figure 8.1**).
- Types 2 and 3 have 72 fuel rods, a central water channel and 6 spacers with  $\xi = 0.877$  for type 2 and  $\xi = 0.812$  for type 3. There are 186 of these assemblies in the core (**Figure 8.2**).
- Type 4 has 91 fuel rods, 8 of them are just partial length rods with a length of 2.310 m, where 2.0945 m is the heated section and 0.2155 m is the unheated plenum. Partial length rods are rods which begin at the lower part of the active length and terminate at an intermediate level below the end of the active length reducing the amount of fuel in the upper core region. Assemblies type 4 have a central water channel and 6 spacers with a  $\xi = 0.834$  the first 4 (from down to top) and  $\xi = 0.681$  the last two. There are 26 of these assemblies in the core (**Figure 8.3**).

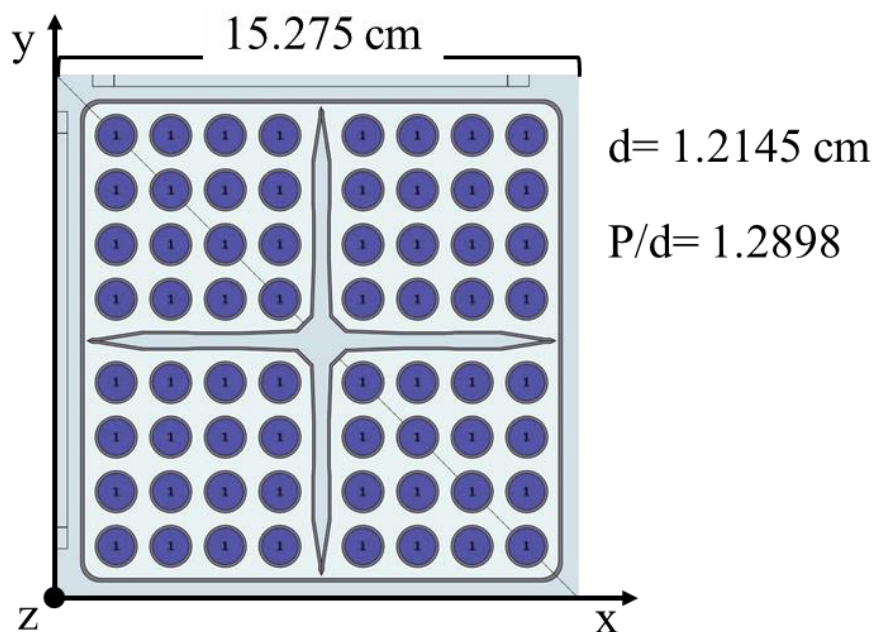


**Figure 8.1.** Fuel assembly type 1, the circles represent the fuel rods, P is the pin pitch, d the pin diameter and the cruciform area the passing region for the control rods of Oskarshamn-2.

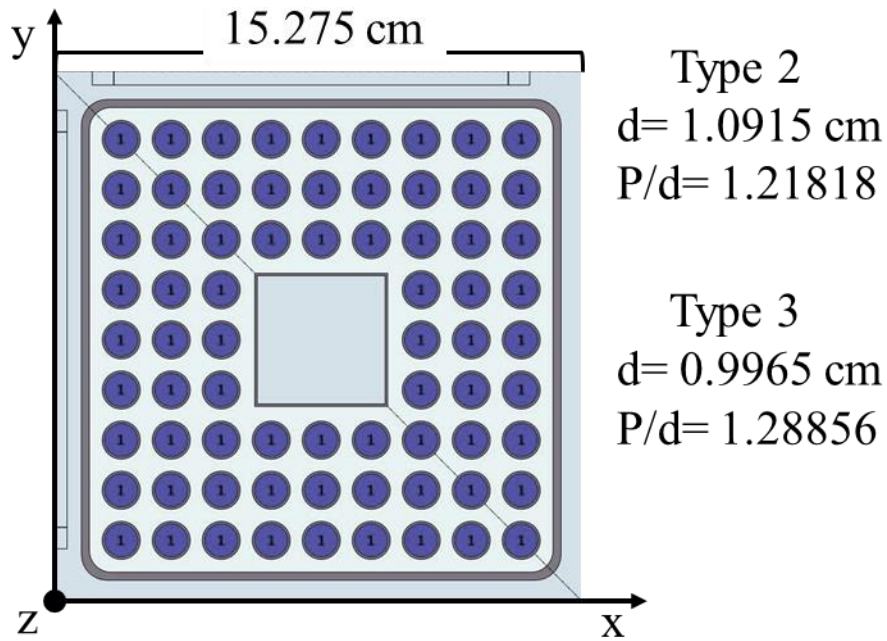


**Figure 8.2.** Fuel assemblies' type 2 and 3, the circles represent the fuel rods, P is the pin pitch, d the pin diameter and the square the water channel of Oskarshamn-2.

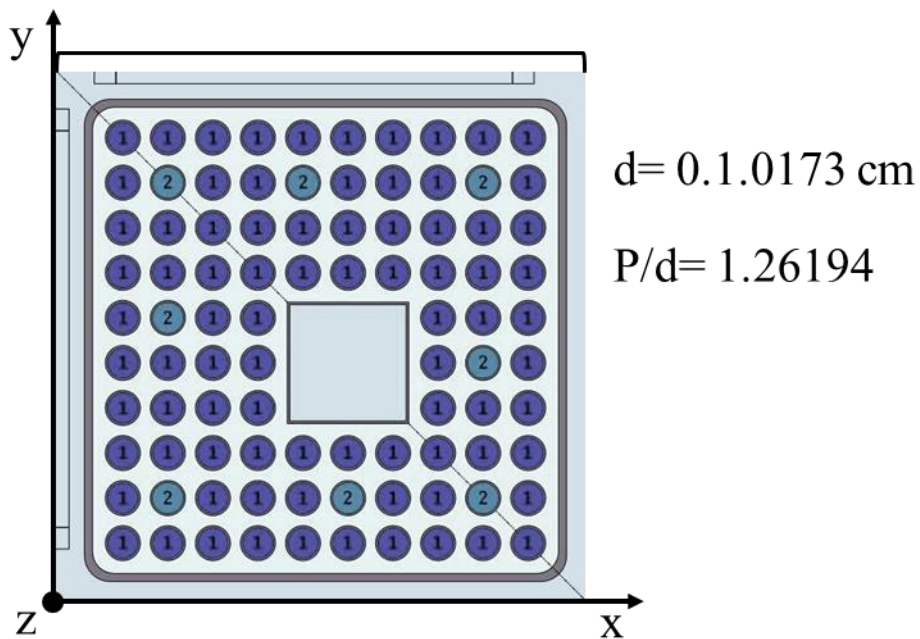


**Figure 8.3.** Fuel assembly type 4, the circles with the number 1 represent the full-length fuel rods, the ones with the number two the partial length fuel rods, P is the pin pitch, d the pin diameter and the square the water channel of Oskarshamn-2.

In **Figure 8.4** a cut of Oskarshamn-2 and the different fuel assembly types is shown. A lateral arrangement of 24 x 24 channels is presented, in which every channel represents an assembly or a reactor pressure vessel part. The distribution of the different type of assemblies in the core is shown, where 0 corresponds to the reactor pressure vessel (reflectors) the number 1 to the assembly Type 1, number 2 to assembly Type 2, number 3 to assembly Type 3 and number 4 to assembly Type 4. The coolant flows from bottom to top in axial direction z.

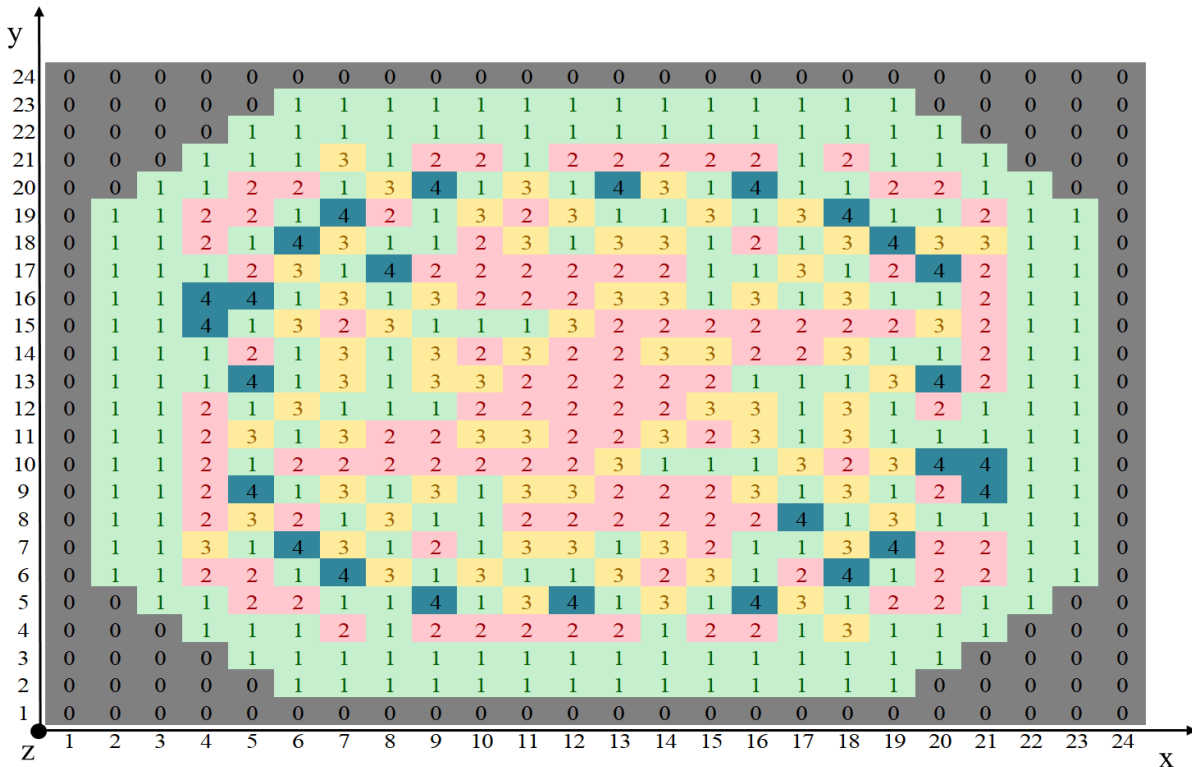


Figure 8.4. Radial distribution of the different fuel assembly types within the Oskarshamn-2 core

### 8.1.2 TWOPORFLOW core model

A three-dimensional core model has been developed to represent the core of the Oskarshamn reactor in TWOPORFLOW. It consists of a 24 x 24 Cartesian grid with 60 axial cells. The first ten equidistant spaced axial cells represent the 0.7424 m lower plenum, and the last 50 equidistant cells correspond to the 3.712 m high active core. In this model, the lower core plate and the spacers are modeled merely by pressure losses at the corresponding axial positions. For each 3D Cartesian cell, the volume and area porosities, the heat transfer area density the power released to the rods and at specific locations, the pressure loss coefficients are provided as input. In addition, the mass flow rate and coolant temperature at the inlet and the pressure at the outlet are provided as boundary conditions.

In Figures 8.5 and 8.6, the relative radial power distribution and the axial power distribution as predicted by the coupled code TRACE/PARCS are given, which are used as input in TWOPORFLOW.



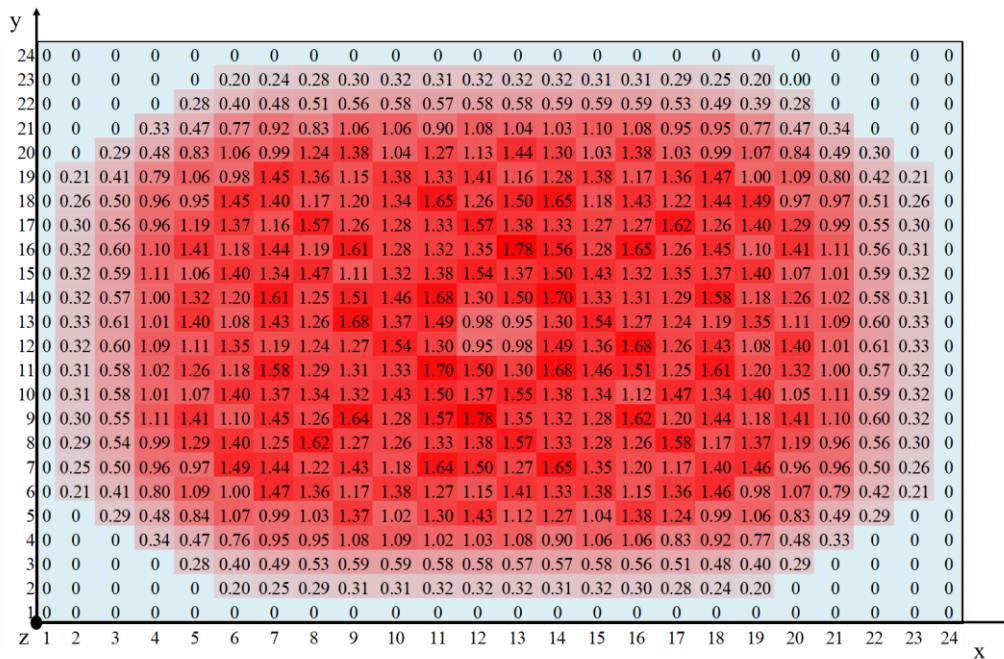


**Figure 8.5.** Relative normalized radial power distribution of the Oskarshamn-2 reactor core calculated by TRACE/PARCS [93] for the stationary plant conditions.

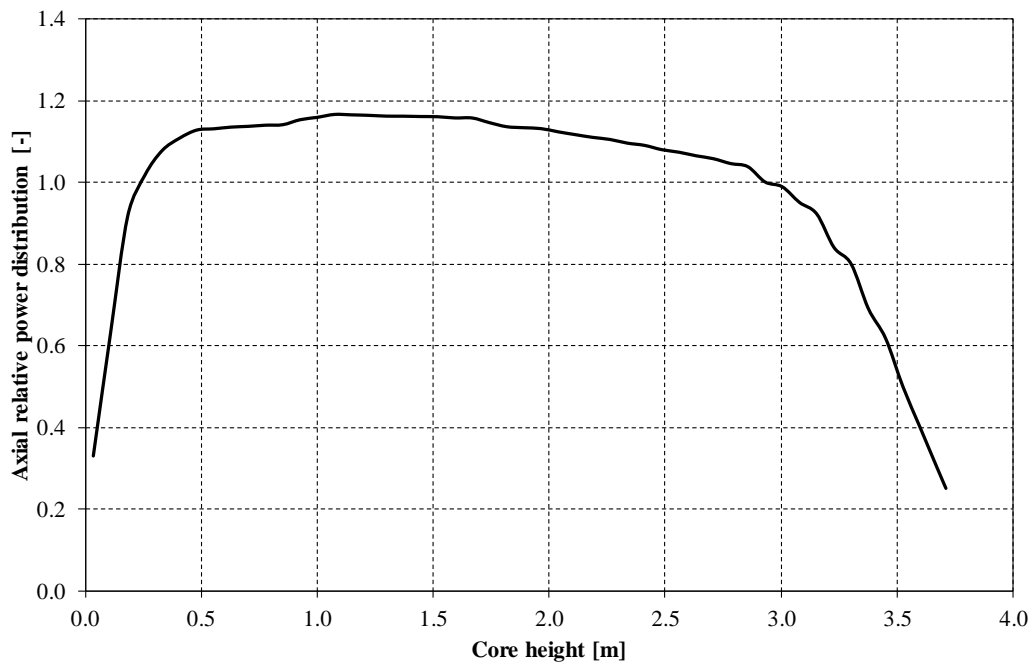


**Figure 8.6.** Axial relative normalized power distribution in the Oskarshamn-2 reactor core calculated by [93] with a TRACE/PARCS coupling for the 1999 Feed-water Transient.

### 8.1.3 TWOPORFLOW stationary core analysis: code-to data and code-to-code comparison

The Oskarshamn core stationary conditions are analyzed with TOWPORFLOW using the model described above and the initial and boundary conditions listed hereafter.

- Outlet pressure: 7 MPa,
- Inlet mass flow: 4.6911 t/s,



- Inlet temperature: 270.42 °C,
- Bundle power: 1802 MW.

The main core parameters predicted by TWOPORFLOW are compared to the ones calculated by a subchannel code (COBRA-TF) and a system thermal hydraulic code (ATHLET) as part of the international O2-Benchmark [93].

In **Table 8.1**, selected parameters e.g., the pressure loss, and the core average void fraction, and their corresponding absolute errors predicted by TWOPORFLOW are compared to results of COBRA-TF and ATHLET; including the benchmark data.

There can be observed that TWOPORFLOW shows a good agreement with the benchmark data, and the TWOPORFLOW predicted parameters are similar to the ones of COBRA-TF and ATHLET, having the smallest absolute error in pressure loss of the three codes with -0.0103 MPa and the second smallest in average void with -0.018.

<b>Table 8.1.</b> Comparison of the Oskarshamn-2 benchmark's results with the TWOPORFLOW simulation in Steady State.				
	Benchmark	TWOPORFLOW	COBRA-TF	ATHLET
Pressure loss [MPa]	0.1162	0.1059	0.1603	0.131
Pressure loss absolute error [MPa]	-	-0.0103	-0.0441	0.0148
Core Averaged Void [-]	0.42	0.402	0.425	0.399
Average void absolute error [-]	-	-0.018	0.005	-0.021

A comparison of the axial averaged core void fractions predicted by TWOPORFLOW, and the other codes is presented in **Figure 8.7**. Since no void fraction measurements from the reactor core are available, code to code comparison is only possible. The three codes predict a similar void fraction evolution along the core height, having the largest difference in the sub-cooled boiling area i.e., at the core bottom. That could be due to the different approaches (ATHLET is a system code, COBRA-TF a sub-channel code and TWOPORFLOW a porous media code). In the ATHLET model, the local pressure loss effect caused by the spacer grids are not being presented, that is the reason why it is not possible to see the local pressure loss effect caused by the spacer grids; for TWOPORFLOW and COBRA-TF these effects are observed, but the height at which they appear is not always the same. That is due to differences in locations in which the spacers are modeled.

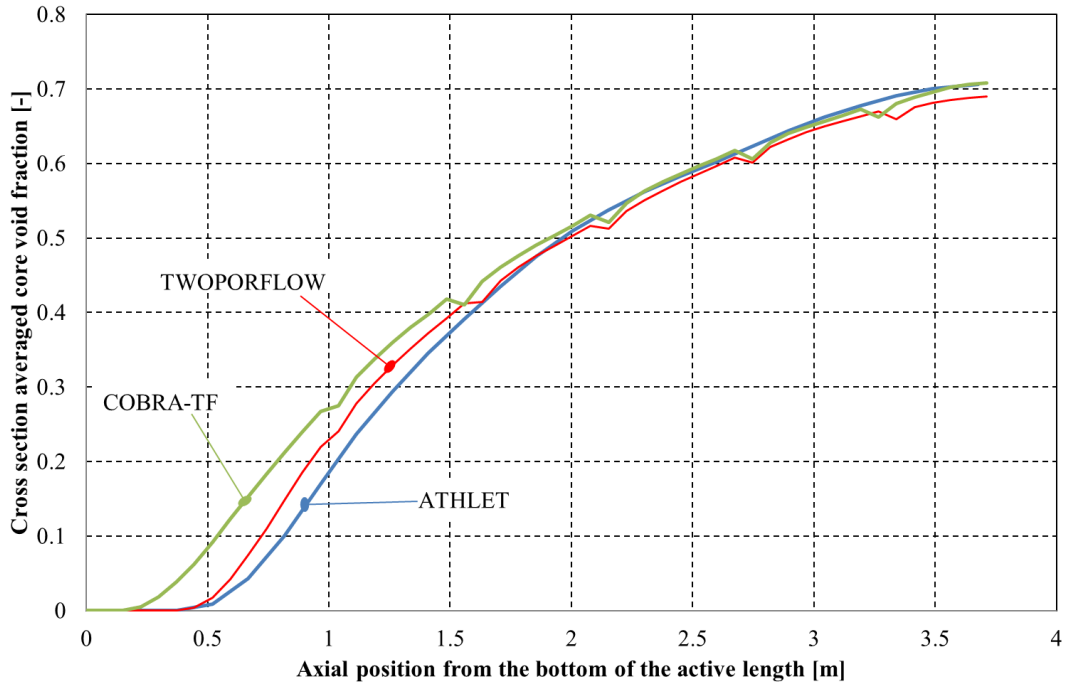


**Figure 8.7.** Comparison between the average void fractions dependent on the axial position calculated with TWOPORFLOW, COBRA-TF and ATHLET for the Oskarshamn-2 Nuclear Power Plant at steady state.

In **Figure 8.8**, the axial void fraction distribution of the core predicted by TWOPORFLOW and COBRA-TF are compared to each other for the hottest fuel assembly with the coordinates (12,9) in **Figure 8.5**. It seems that the reactor model in COBRA-TF has a slightly larger active length, and there are slight differences in the spacer grid positions as well. However, the results with both codes are similar, having the largest differences again in the subcooled boiling region (approximately the first 50 cm of axial height).

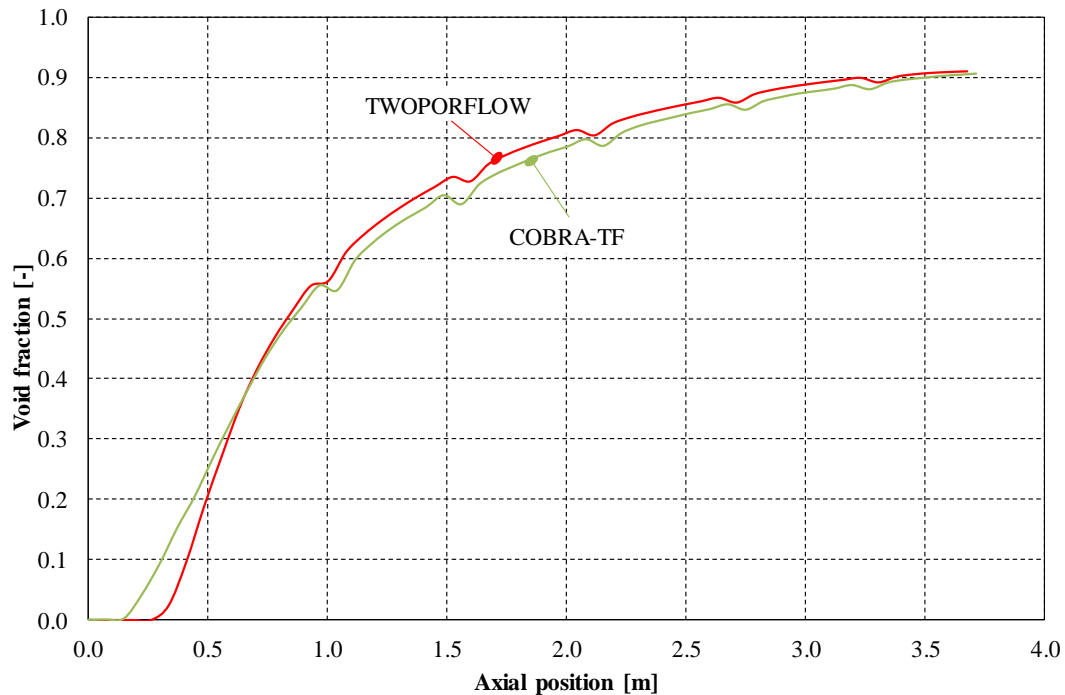


**Figure 8.8.** Comparison between the average void fractions in the hottest channel dependent on the axial position calculated with TWOPORFLOW and COBRA-TF for the Oskarshamn-2 Nuclear Power Plant at steady state.

### 8.1.4 Thermal hydraulic analysis of the Oskarshamn-2 BWR stability transient

On February 25, 1999, a stability transient event took place in the Oskarshamn-2 reactor, which was later documented by [94] [95] as the O2 OECD/NEA benchmark.

A maintenance work outside the Unit 2 lead to a control system logic failure in the loss of feedwater pre- heaters. The failure signal was transmitted to the turbine, causing a turbine trip, but, due to a failure in the relay circuit, the load reject (sudden reduction in the electric power demanded by the grid) signal was never transmitted to the reactor. Consequently, the power level of the generator was reduced from 625 MWe to 585 MWe and steam line bypass valves opened to allow the excess steam into the main condenser while maintaining full reactor power. As the reactor never received the load rejection signal, the expected automatic controls, such as automatic insertion of control rods (SCRAM) and main recirculation pump trips, never occurred. Because of the turbine trip and opening of the steam line bypass valves, the feed water preheater system was no longer functional, and the feed water temperature decreased by 75°C over a period of 150 seconds. The feed water temperature decrease resulted in colder water entering the reactor vessel, which created a positive reactivity feedback and increased the core power level.

A pump controller reduced the main re-circulation flow when the reactor power increased more than 2% above the nominal power, thereby reducing the power. Cold feed water continued entering the vessel, which caused the power level to increase and activated the pump controller.

The operators partially scrammed the reactor by fully inserting 7 predefined control rods and reducing flow to the minimum at about two minutes after the initiation of the event. After the partial SCRAM, the power was reduced to 65% and the flow to 3200 kg/sec.

However, the flow of cold feed water continued, which caused the reactor power to increase and enter the unstable region of the power. The reactor power started to oscillate with successively increasing amplitudes over a period of 20 seconds.

The reactor scrammed due to high power at 3 minutes and 6 seconds after the initial load rejection event, when the power exceeded 132 % at 2500 kg/s recirculation flow. The scram proceeded according to the design, opening the generator breaker two seconds after the scram, disconnecting it from the main grid and moving the reactor into a hot shutdown state.

**Figure 8.9** illustrates the normalized qualities of (divided by the initial steady state conditions) the 300 seconds of the transient.

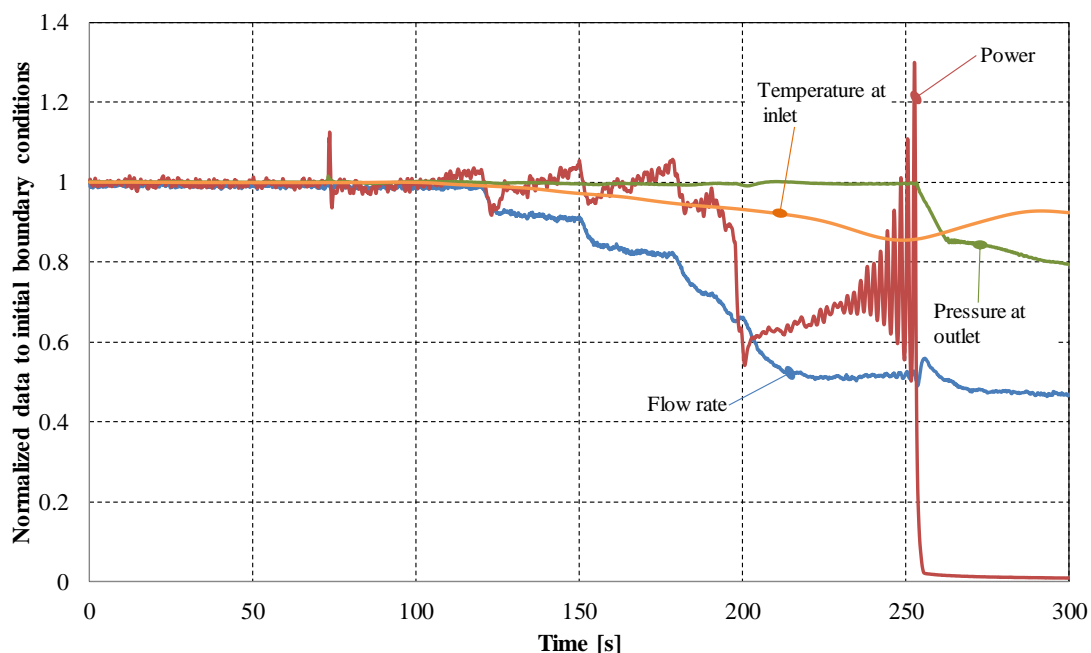


**Figure 8.9.** Normalized to one boundary conditions during the 300 seconds of the Oskarshamn-2 instability transient.

A BWR stability problem is normally evaluated with a coupled system thermal hydraulic code and a 3D kinetics code such as TRACE/PARCS, RELAP5/PARCS, etc. Since TWOPORFLOW is not yet coupled with a 3D neutron kinetics code, and a TRACE/PARCS solution of the O2-Stability problem is available at KIT, a thermal hydraulic analysis of the O2-core has been performed with TWOPORFLOW using time-dependent boundary conditions (power, mass flow rate, pressure, inlet core temperature) obtained from the O2-benchmark with TRACE/PARCS [96]. The results obtained by TWOPORFLOW are compared to the ones of other codes e.g. COBRA-TF and ATHLET [93] in **Figures 8.10** and **8.11**.

From the result at the beginning of the transient i.e., for the first 250 seconds, we can conclude that the COBRA-TF simulation is performed using different initial boundary conditions compared to ATHLET and TWOPORFLOW.

The first significant power oscillation in the core takes place around second 72, what is reflected in both temperature and density results. While the temperature and the flow rate decrease (around second 150) in the core, the temperature decreases, and the coolant density increases (**Figure 8.9**). The coolant temperature simulated with ATHLET has a more significant decrease compared to TWOPORFLOW, while the densities are similar in both codes. The highest differences between the codes are shown between 220 and the 260 seconds, which is the range of time showing the largest instabilities in the core power (**Figures 8.10** and **8.11**).

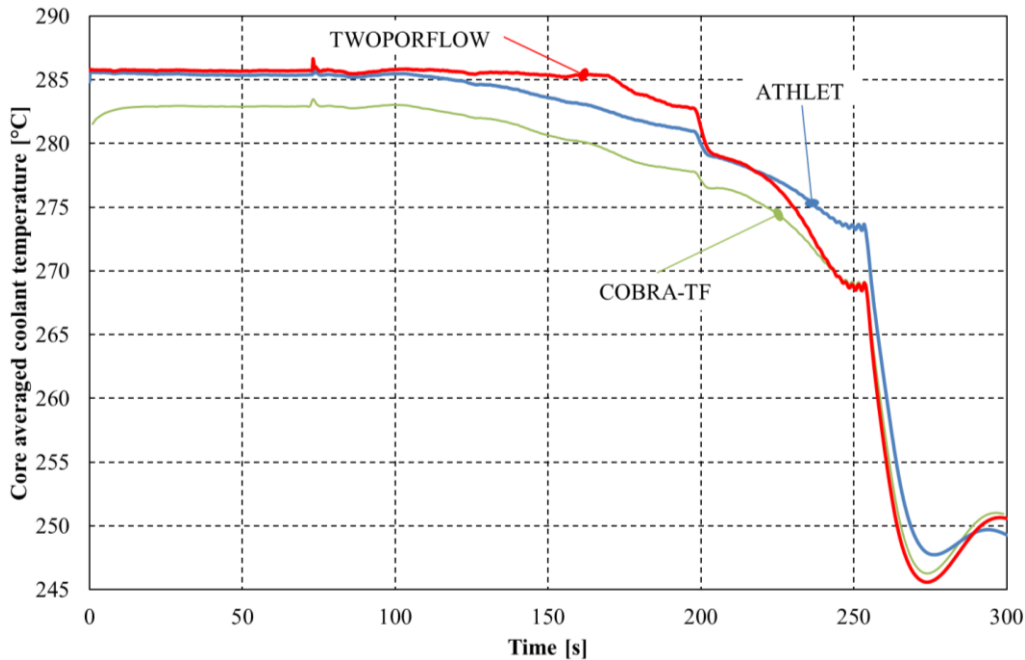


**Figure 8.10.** Comparison of core averaged coolant temperature between the TWOPORFLOW, ATHLET and COBRA-TF simulations of the Oskarshamn-2 instability transient [94] [95].

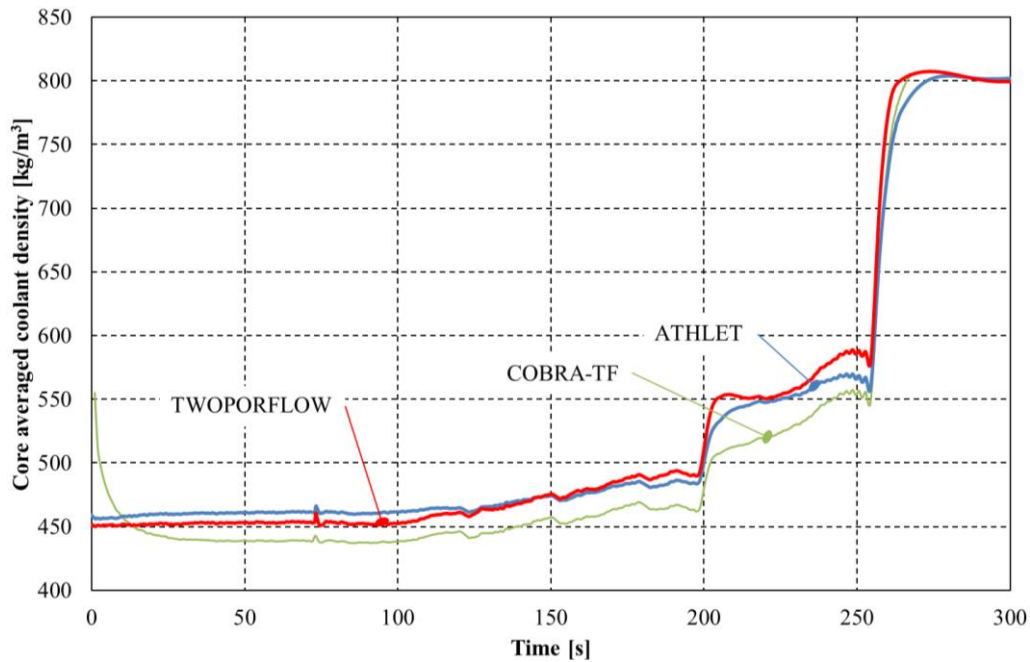


**Figure 8.11.** Comparison of core averaged coolant density between the TWOPORFLOW, ATHLET and COBRA-TF simulations of the Oskarshamn-2 instability transient [94] [95].

## 8.2 Thermal hydraulic analysis of the Laguna Verde BWR reactor core

### 8.2.1 Short description of the core and thermal hydraulic parameters

The core of the Laguna Verde Unit 1 consists of 444 fuel assemblies and has a thermal power of 2027 MW [97].

The core loading includes two fuel assembly types and 109 control elements (cross-type). It has an active height of 3.81 m. The two different types of assemblies are:

- Type 1 has 62 fuel and 2 water rods with 7 spacers with  $\xi = 1.191$ . There are 312 type 1 assemblies in the core (**Figure 8.12**).
- Type 2 has 60 fuel rods with a central water channel and 7 spacers with  $\xi = 1.069$ . There are 132 of these assemblies in the core (**Figure 8.13**).

The assembly distribution inside LVNPP reactor core is shown in **Figure 8.14**.

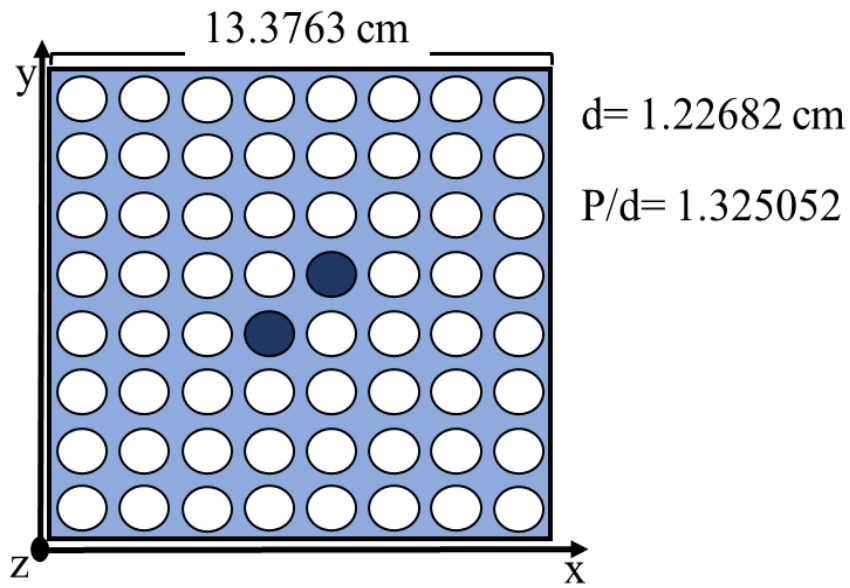


**Figure 8.12.** Fuel assembly type 1, P is the pin pitch, d the pin diameter, the un-colored circles represent the fuel rods and the two-colored circles the water rods of Laguna Verde Unit 1.

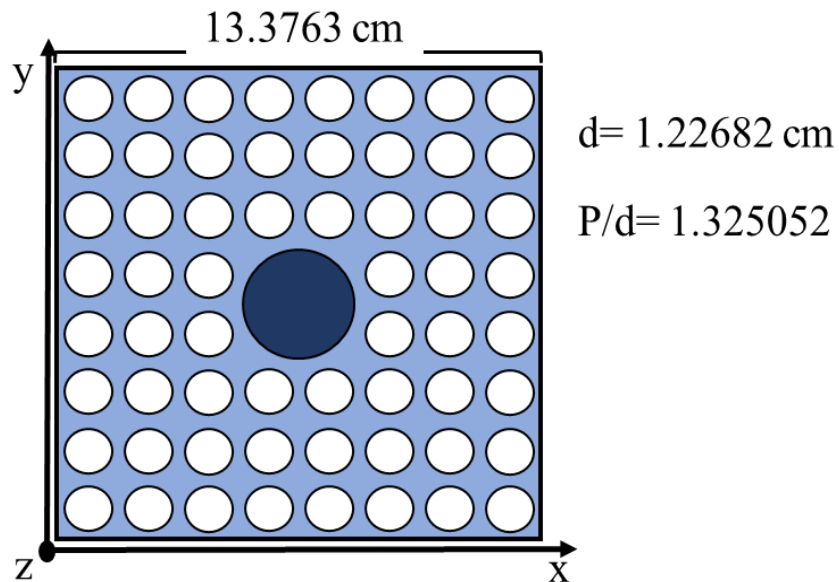


**Figure 8.13.** Fuel assembly type 2, P is the pin pitch, d the pin diameter, the un-colored circles represent the fuel rods and the colored circle the water rod of Laguna Verde Unit 1.

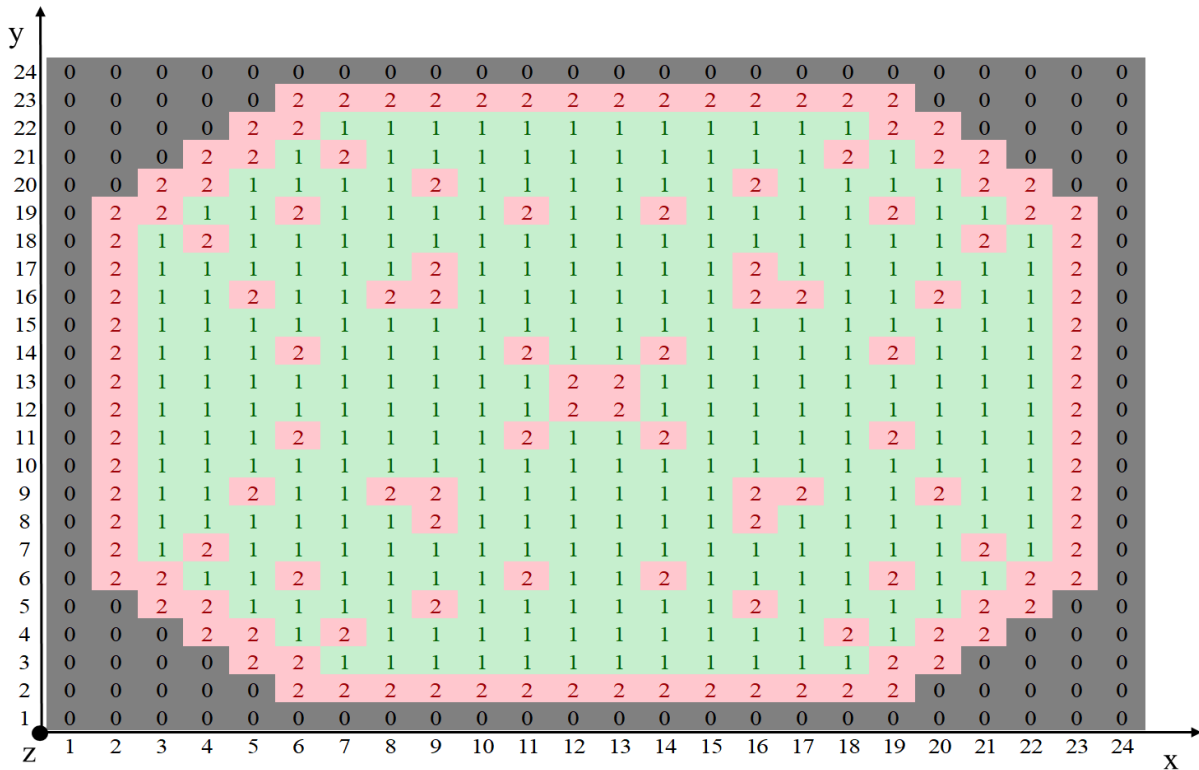


**Figure 8.14.** Distribution of the different assembly types inside the Laguna Verde Unit 1 reactor core, 0 corresponds to the reflectors, 1 to assembly Type 1 and 2 to assembly Type 2.

### 8.2.2 Short description of the Laguna Verde stability transient

On January 24th, 1995, during the fourth operation cycle, the Nuclear Power Plant Laguna Verde Unit 1 (LVNPP) experienced power oscillations throughout the transition to high speed of the re-circulation pumps. With the reactor operating conditions of 34.9% power and 37.8% flow through the core, the re-circulation valves started to close up to reach the minimum positions, leading to power oscillations in the reactor [98].

This transient is evaluated with the core simulator SIMULATE-3K which consist of a 3D diffusion solver and an internal thermal hydraulic module [99]. The key-parameter of the LV core predicted with SIMULATE-3K are used as initial and boundary conditions for the thermal hydraulic analysis to be performed with TWOPORFLOW.

### 8.2.3 Laguna Verde BWR Core Model for TWOPORFLOW

A three-dimensional core model is developed to represent the core of the Laguna Verde reactor in TWOPORFLOW. It consists of a 24 x 24 Cartesian grid with 35 equidistant axial cells. The first five axial cells represent the 0.762 m high lower plenum, and the 30 last cells correspond to the 3.81 m high active core. In this model, the lower core plate and the spacers are modeled by pressure losses at the corresponding axial positions.

The relative radial and axial power distributions predicted in [98] and shown in **Figures 8.15** and **8.16** are used as initial conditions for the TWOPORFLOW analysis together with the time dependent boundary conditions .

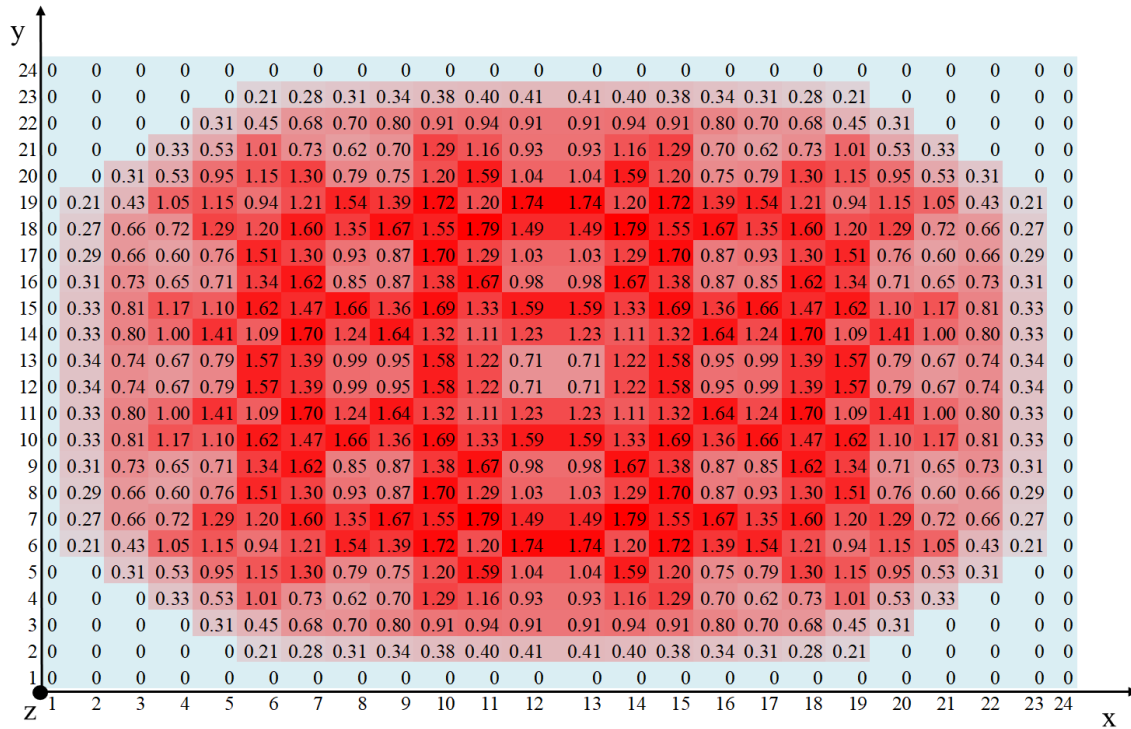


Figure 8.15. Relative normalized radial power distribution in the Laguna Verde Nuclear Power Plant reactor core [98].

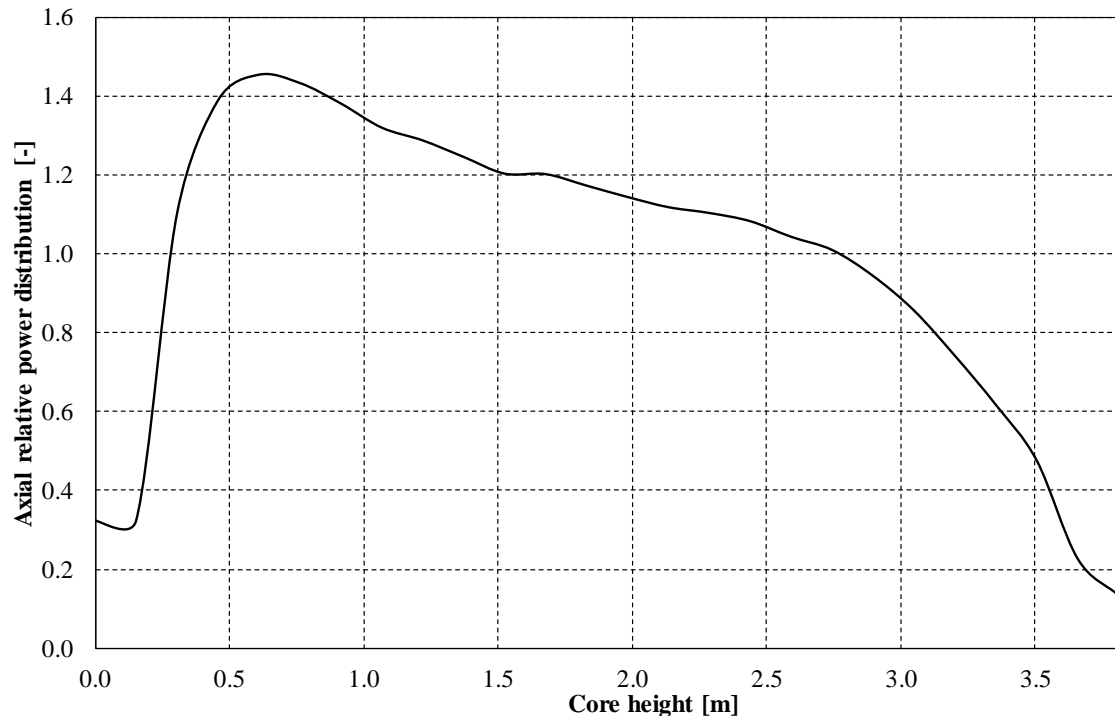


Figure 8.16. Relative normalized axial power distribution in the Laguna Verde Nuclear Power Plant reactor core [98].



### 8.2.4 Steady state case simulation results and code to code comparisons

A TWOPORFLOW simulation of the stationary core conditions using the model described before and the following boundary conditions:

- Outlet pressure: 6.51 MPa,
- Inlet mass flow: 2.92889 t/s,
- Inlet temperature: 268.66 °C,
- Bundle power: 714.8 MW.

The results obtained with TWOPORFLOW are compared against the results of SIMULATE-3K [98] and a TRACE simulation performed by [96]. The TRACE model is not detailed i.e., the 444 assemblies are not simulated individually but grouped in 29 fuel assemblies' subtypes with different neutronic characteristics, in which the hottest channel is grouped in the assembly number 27 (cell located in (11, 7) **Figure 8.15**.

The comparison of the results obtained with TWOPORFLOW with the ones obtained by SIMULATE-3 and TRACE reference model, as well as with the are presented in **Table 8.2**. It can be observed that the key-parameters predicted by TWOPORFLOW are in good agreement with the ones of SIMULATE-3 and TRACE

<b>Table 8.2.</b> Comparison of the SIMULATE-3, and TRACE results with the TWOPORFLOW simulated data in Steady State.			
	SIMULATE-3	TRACE	TWOPORFLOW
Pressure loss [MPa]	0.04	0.037	0.0363
Pressure loss absolute deviation [MPa]	-	-0.003	-0.0037
Core average void [-]	0.366	0.412	0.335
Average void absolute deviation [-]	-	0.046	-0.031

In **Figure 8.17**, the average core void fraction along the core height is shown. The void fraction predicted with TWOPORFLOW is in very good agreement with the one calculated by SIMULATE-3 in the sub-cooled boiling region i.e., in the bottom part of the core (up to 1.75 m). But at higher core elevations the discrepancies increase up to 0.059 at the top of the reactor core. The differences of the void fraction predicted by TRACE and TWOPORFLOW are more pronounced and in general TWOPORFLOW underpredicts the void fraction along the whole core elevation. The simplified core model of TRACE i.e., grouping the fuel assembly in a reduced number of channels (only 29 instead of 444 in TWOPORFLOW) may be the reason to these differences.

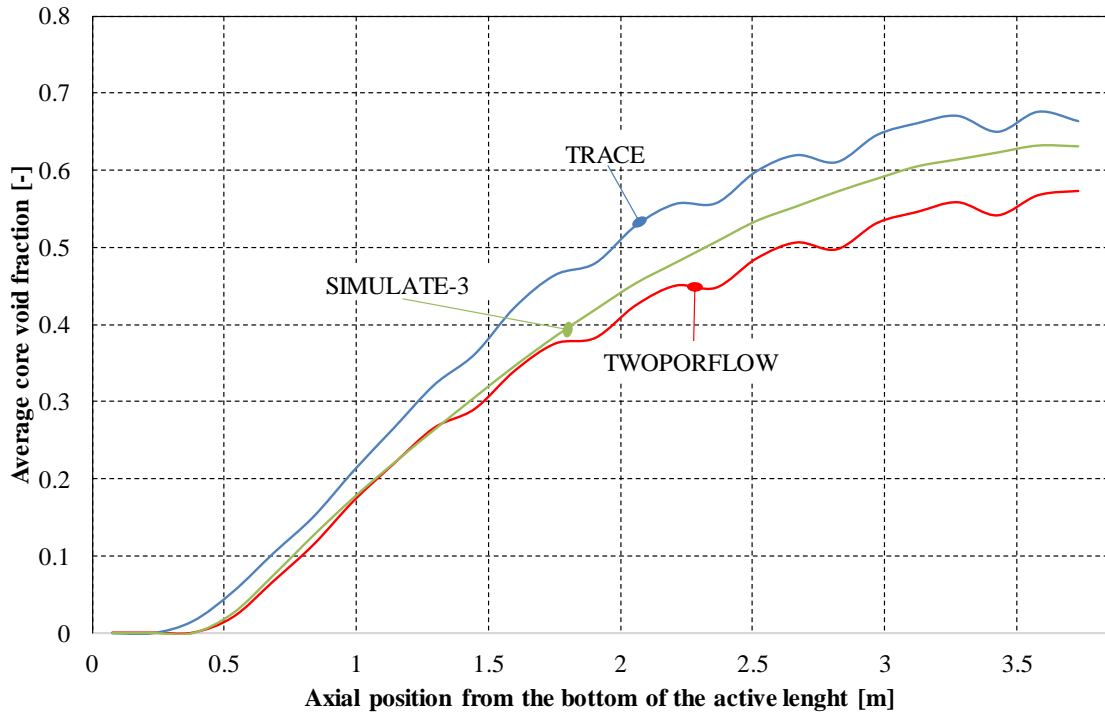


**Figure 8.17.** Comparison between the core averaged void fractions dependent on the axial position calculated with SIMULATE-3, TWOPORFLOW and TRACE for the Laguna Verde Nuclear Power Plant.

Finally, the axial void fraction distribution predicted by TWOPORFLOW and TRACE for the hottest channel in the cell (11,7) and in the channel 27, respectively, is compared in **Figure 8.18**. In this case, the agreement of the predicted void fraction in the lower part of the core by both codes is good while the discrepancies increase at higher elevations.

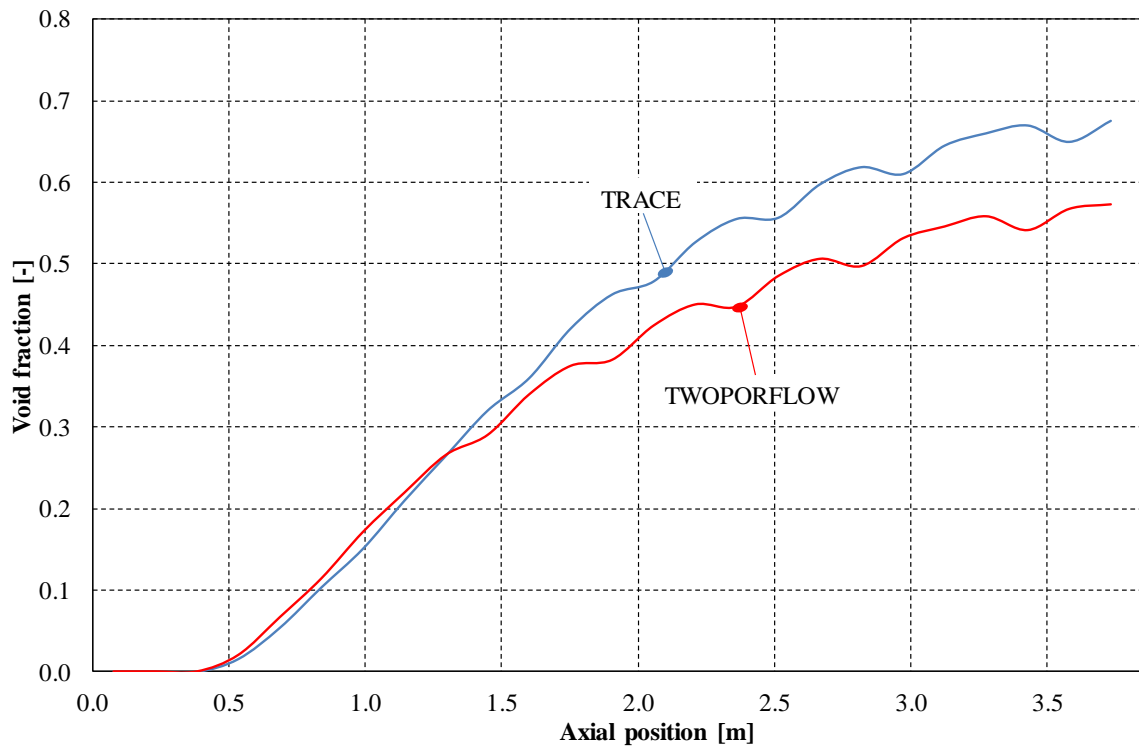


**Figure 8.18.** Comparison between the void fractions in the hottest channel dependent on the axial position calculated with TWOPORFLOW and TRACE for the Laguna Verde Nuclear Power Plant.

## 9 Summary

The goals of this thesis are, first, to analyze 2 different groups of two-phase flow correlations models with respect of their simulation capabilities and their limitations. Then, to identify the major sources of deviations and to implement improved models for turbulent mixing, void dispersion, and CHF. An extended validation process is performed to enable their use in steady state and transient reactor core simulations.

### Improvements in physical models.

- ***Turbulent mixing in the momentum and energy conservations equations.*** It is calculated by a simple zero equation turbulence model using a mixing coefficient given as input to in order to calculate the turbulent viscosity which is added to the molecular viscosity and at the same time affects the turbulent thermal conductivity.
- ***Void dispersion in the momentum equations.*** It is calculated by an empirical correlation added to the vapor momentum equation for bubbly flow.
- ***Improvements in CHF.*** The revision of the Bowring correlation and the implementation of the Biasi correlation and the Groeneveld Look-Up Table method have been realized.

### Evaluation of TPF and TPF-TRACE groups of correlations.

- ***Turbulent mixing in the momentum and energy conservations equations.*** This evaluation has been made using the PSBT steady state fluid temperature benchmark. The simulation of thermal mixing demonstrates that, comparing the sub-channel temperatures, the average difference between the correlation groups is 0.09°C. Both families of correlations give nearly the same quality of results for turbulent mixing. TWOPORFLOW shows qualified results in single phase flow using a similar value of the mixing coefficient as used by other validated codes.
- ***Sub-cooled boiling*** has been investigated using the PSBT Single sub-channel benchmark. The obtained results reveal that neither TPF nor TPF-TRACE correlations are capable to obtain results less or equal the reported experimental void fraction accuracy (0.03 absolute void fraction) and it is recommended to perform further investigations in the sub-cooled boiling region using another benchmark or experimental data.
- ***Void dispersion in the momentum equations*** has been evaluated using the BFBT steady-state sub-channel grade benchmark. It is concluded that the deviations between both groups of correlations are not larger than 3% having both the higher deviations near the unheated rods.
- ***Transient void.*** In order to make these evaluations, two transient scenarios have been selected from the BFBT transient macroscopic grade benchmark. The TPF correlations present better results compared to the experimental data in all quality regions while the TPF-TRACE correlations show high discrepancies at low and high steam quality regions.

The TPF-TRACE correlations have been implemented in the code with the purpose to obtain an improvement in the simulation of physical phenomena. This purpose has been not met. The results of both types of correlations are, in most of the cases, similar and even in transient conditions the TPF correlations show better results. The recommendation is, to eliminate the TPF-TRACE group of correlations in TWOPORFLOW and focus the effort on the improvement of TPF correlations.

### Evaluation of CHF models.

- ***Tube geometries*** have been analyzed using the Becker experiments. The Biasi correlation presents the less accurate results. The largest deviation appears at lower steam qualities. The Bowring correlation gives the most accurate results and the Groeneveld LUT shows similar results. For tube simulations, the Groeneveld LUT and the Bowring correlation are recommended to be used.

- ***Assembly geometries under normal operating conditions*** have been analyzed using the BFBT steady state benchmark. The Biasi correlation presents the most accurate results for all the different pressures and assembly types. The Biasi and the Groeneveld correlation results give both an acceptable accuracy in all the conditions, while Bowring is more inaccurate in the predictions. The Biasi correlation or the Groeneveld LUT are recommended for the simulation of fuel assemblies in steady state conditions.
- ***Assembly geometries under transient conditions*** have been analyzed using two exercises (recirculation pump trip and turbine trip without bypass) from the BFBT transient benchmark. The TWOPORFLOW code gives accurate results using the Biasi correlation and the Groeneveld LUT.

It is important to remark that the most consistent method in the simulation of CHF is the Groeneveld LUT, having similar accuracies in almost all the geometries and conditions.

#### **Application to simulate BWR reactor cores.**

TWOPORFLOW is applied to simulate BWR reactor cores. In this context, only TPF correlations models have been used, because they give the best results for the validation calculations.

- ***Oskarshamn-2 nuclear reactor simulation under steady state conditions.*** The steady state simulations have been compared against data generated with COBRA-TF and ATHLET. The compared parameters are core averaged void fraction, core averaged void fractions dependent on the axial positions and core averaged pressure loss. The simulations show similar results compared to COBRA-TF and ATHLET having the largest difference in the sub-cooled area.
- ***Oskarshamn-2 nuclear reactor simulation under transient conditions.*** The transient simulations have been compared as well against data generated with COBRA-TF and ATHLET. The compared parameters are the coolant average density and the coolant temperature both dependent on time. The results show a good agreement between TWOPORFLOW and ATHLET. In comparison with COBRA-TF larger differences appear.
- ***Laguna Verde nuclear reactor simulation under steady state conditions.*** The steady state simulation with TWOPORFLOW is compared against simulations made with SIMULATE-3 (reference model) and TRACE. The compared parameters are core averaged void fraction, core averaged void fractions dependent on the axial positions and core averaged pressure loss. In this case, the results show many discrepancies, TWOPORFLOW shows a good agreement with SIMULATE-3 in the sub-cooled area, but in saturated boiling there are differences of about 10% of the void fraction. In the comparison TRACE-TWOPORFLOW, the difference is about 14% of the void fraction. In the case of the comparison against TRACE, it is important to mention that the TWOPORFLOW model is a detailed approach (using 444 assemblies), and the TRACE model is simplified (using 29 channels). In any case, it is not possible to state which codes have the better results, because of the lack of measured data.

Summarizing up, progress has been achieved in the development and application of TWOPORFLOW to become a qualified tool to simulate two-phase flow conditions in BWRs.

## 10 Outlook

The future work can be divided into three groups of tasks:

- Revision of the sub-cooled boiling correlations.
- Implementation and validation of post-CHF models.
- Coupling with system thermal hydraulics simulation tools or neutronic simulation codes.

To re-evaluate the sub-cooled boiling models, it is recommended to look for different tests to evaluate these phenomena. It is necessary to analyze whether the deviations are similar to those obtained using the PSBT benchmark. If it is the case, then a review of the implementation and the models existing in TWOPORFLOW is recommended.

TWOPORFLOW can simulate the post-CHF phenomena, but these simulations have not yet been evaluated. First, it is necessary to evaluate the transition boiling, in order to see if it is better to implement a correlation or to continue using the current method. Actually, a heat flux interpolation between the critical and the minimum stable film boiling (MSFB) temperature points is done. Once this evaluation is made, the liquid film, gas, condensation, and mixed boiling heat modes, could be evaluated as well.

The status of TWOPORFLOW already allows the coupling with other codes. It is possible to couple it with system thermal hydraulic simulations tools, like TRACE. This allows simulating the whole plant with more detailed results from the core.

The thermal hydraulic phenomena and the neutron reactions taking place in the core strongly affect the behavior of each other. An important future task is to couple TWOPORFLOW with neutronic simulation codes providing a multi-physics description of the phenomena occurring inside the reactor core.



## 11 References

- [1] International Atomic Energy Agency (IAEA), Power Reactor Information System (PRIS) (2020). PRIS - Reactor status reports - operational & long-term shutdown - by country. <https://pris.iaea.org/PRIS/WorldStatistics/OperationalReactorsByCountry.aspx> (accessed May 4th, 2020).
- [2] International Atomic Energy Agency (IAEA), Power Reactor Information System (PRIS) (2020). Power Reactor Information System (PRIS) - Country details: Mexico. <https://pris.iaea.org/PRIS/CountryStatistics/CountryDetails.aspx?current=MX> (accessed May 4th, 2020).
- [3] D'Auria, Francesco; Aksan, Nusret; Bestion, Dominique; Galassi, Giorgio Maria; Glaeser, Horst; Hassan, Yassin; Jeong, Jae Jun; Kirillov, Pavel Leonidovich; Morel, Christophe; Ninokata, Hisashi; Reventos, Francesc; Rohatgi, Upendra Singh; Schultz, Richard R.; Umminger, Klaus (2017). *Thermal hydraulics in water-cooled nuclear reactors*. 1st edition. Woodhead Publishing. ISBN 978-0-08-100679-5. Pisa, Italy.
- [4] Han Young, Jae Jun Yoon; Jae Ryong, Lee; Hyungrae, Kim; Ik Kyu, Park; Chul-Hwa, Song; Hyoung Kyu, Cho; Jeong (2014). Recent improvements in the CUPID code for a multi-dimensional two-phase flow analysis of nuclear reactor components. *Nuclear Engineering and Technology*. Volume 46, Number 5. Pages 655–666. doi: 10.5516/NET.02.2014.023.
- [5] Takasuo, Eveliina; Hovi, Ville; Ilvonen, Mikko (2012). Applications and development of the PORFLO 3D code in nuclear power plant thermal hydraulics. *International Conference on Nuclear Engineering (ICONE)*. Volume 4. Pages 393–402. doi: 10.1115/ICONE20-POWER2012-54161.
- [6] Alm, B.; Imke, U.; Knitter, R.; Schygulla, U.; Zimmerman, S. (2008). Testing and simulation of ceramic micro heat exchangers. *Chemical Engineering Journal*. Volume 135. Pages 179–184. doi: 10.1016/j.cej.2007.07.005.
- [7] Imke, Uwe (2004). Porous media simplified simulation of single- and two-phase flow heat transfer in micro-channel heat exchangers. *Chemical Engineering Journal*. Volume 101, Number 1–3. Pages 295–302. doi: 10.1016/j.cej.2003.10.012.
- [8] Jauregui Chavez, Veronica; Imke, Uwe; Sanchez-Espinoza, Victor (2018). TWOPORFLOW: A two-phase flow porous media code, main features and validation with BWR-relevant bundle experiments. *Nuclear Engineering and Design*. Volume 338. Pages 181–188. doi: 10.1016/j.nucengdes.2018.08.009.
- [9] Jauregui Chavez, Veronica; Imke, Uwe; Jimenez Escalante, Javier; Sanchez-Espinoza, Victor Hugo (2017). Implementation and Validation of CHF Models in the Two - Phase Flow Porous Media Code Twoporflow. *17th International Topical Meeting on Nuclear Reactor Thermal Hydraulics (NURETH-17)*. Paper ID:20248. Volume 5. Pages 2611–2624.
- [10] Jauregui Chavez, Veronica; Imke, Uwe; Jimenez Escalante, Javier; Sanchez-Espinoza, Victor Hugo (2018). Further Development of a Thermal-Hydraulics Two-Phase Flow Tool. *Atw. Internationale Zeitschrift fuer Kernenergie*. Volume 63(6–7), Number 49076231. Pages 401–404. Available: [https://inis.iaea.org/search/search.aspx?orig\\_q=RN:49076231](https://inis.iaea.org/search/search.aspx?orig_q=RN:49076231).
- [11] Bowring, R.W. (1972). A simple but accurate round tube, uniform heat flux, dryout correlation over the pressure range 0.7 to 17 MPa. Technical report. Penn State University. Report number: AEEW-R 789.
- [12] Biasi, L.; Clerici, G.C.; Garriba, S.; Sala, R.; Tozzi, A. (1967). Studies on burnout Part 3 - A new correlation for round ducts and uniform heating and its comparison with world data. *Energia Nucleare*. Volume 14, Number 9. Pages 530–537.
- [13] Groeneveld, D. C.; Shan, J. Q.; Vasić, A. Z.; Leung, L. K H; Durmayaz, A.; Yang, J.; Cheng, S. C.; Tanase, A. (2007). The 2006 CHF look-up table. *Nuclear Engineering and Design*. Volume 237, Number 15–17. Pages 1909–1922. doi: 10.1016/j.nucengdes.2007.02.014.

- [14] Groeneveld, D. C.; Leung, L. K. H.; Guo, Y.; Vasic, A.; Nakla, M. El; Peng, S. W.; Yang, J.; Cheng, S. C. (2005). Look-Up Tables for Predicting CHF and Film Boiling Heat Transfer: Past, Present and Future. The 10th International Topical Meeting on Nuclear Reactor Thermal Hydraulics (NURETH10). Volume 152, Number 1. Pages 87–104. doi: <https://doi.org/10.13182/NT152-87>.
- [15] Downar, T. J.; Xu, Yunlin; Seker, V.; Hudson, N. (2010). PARCS v3.0 U.S. NRC Core Neutronics Simulator USER MANUAL. Michigan, USA. Report number: UM-NERS-09-0001.
- [16] Todreas, Neil E.; Kazimi, Mujid S. (1990). Nuclear Systems I: Thermal hydraulic fundamentals. 1st edition. Hemisphere Publishing Corporation. ISBN 0-89116-935-0. New York.
- [17] Jimenez Escalante, Javier (2010). Desarrollo e implementación de la descomposición en subdominios del acoplamiento neutrónico-termohidráulico mediante disecciones alternadas con un sistema de cálculo multiescala. Dissertation. Facultad de la Escuela Técnica Superior de Ingenieros Industriales, Universidad Politécnica de Madrid.
- [18] Lerchl, G.; Austregesilo, H.; Schöffel, P.; von der Cron, D.; Weyermann, F. (2012). ATHLET Mod- 3.0 cycle B. User's Manual. Gesellschaft für Anlagen- und Reaktorsicherheit (GRS) mbH.
- [19] USNRC (2009). TRACE V5.0 Field equations, solution methods and physical models. Theory manual. USA. Report number: ML120060218.
- [20] Salko, R.; Avramova, M.; Wysocki, A.; Toptan, A.; Hu, J.; Porter, N.; Blyth, T.; Dances, C.; Gomez, A.; Jernigan, C.; Kelly, J. (2019). CTF Theory Manual. North Carolina. Report number: CASL-U-2018-171500. Available: <https://info.ornl.gov/sites/publications/Files/Pub124657.pdf>.
- [21] Salko, R.; Avramova, M.; Wysocki, A.; Hu, J.; Toptan, A.; Porter, N.; Blyth, T.; Dances, C.; Gomez, A.; Jernigan, C.; Kelly, J. (2020). CTF User's Manual. North Carolina. Report number: CASL-U-2019-1885-002. Available: <https://info.ornl.gov/sites/publications/Files/Pub146928.pdf>.
- [22] IAPWS R7-97 (2013). Revised Release on the IAPWS Industrial Formulation 1997 for the Thermodynamic Properties of Water and Steam. Available: [www.iapws.org](http://www.iapws.org) (accessed September 28th, 2021).
- [23] Imke, Uwe; Sanchez, Victor Hugo (2012). Validation of the subchannel code SUBCHANFLOW using the NUPEC PWR tests (PSBT). Science and Technology of Nuclear Installations. Volume 2012. Pages 465059/1–12. doi: 10.1155/2012/465059.
- [24] Hu, Howard H; Kundu, Pijush K.; Cohen, Ira M.; Dowling, David R. (2012). Fluid Mechanics, Chapter 10 - Computational Fluid Dynamics. 5th Edition. Academic Press. ISBN 978-0-12-382100-3. Boston. Pages 421–472.
- [25] Inc., ANSYS (2009). ANSYS FLUENT 12.0 Theory Guide. [https://www.afs.enea.it/project/neptunius/docs/fluent/html/th/main\\_pre.htm](https://www.afs.enea.it/project/neptunius/docs/fluent/html/th/main_pre.htm) (accessed March 1st, 2021).
- [26] OpenFOAM Foundation (2021). OpenFOAM User Guide. <https://cfd.direct/openfoam/user-guide/> (accessed March 1st, 2021).
- [27] Zhang, Kanglong; Zhang, Xilin; Sanchez-Espinoza, Victor; Stieglitz, Robert (2020). Development of the coupled code – TRACE/TrioCFD based on ICoCo for simulation of nuclear power systems and its validation against the VVER-1000 coolant-mixing benchmark. Nuclear Engineering and Design. Volume 362, Number 110602. doi: 10.1016/j.nucengdes.2020.110602.
- [28] Hovi, Ville; Ilvonen, Mikko (2010). PORFLO Simulations of Loviisa Horizontal Steam Generator. Technical Report. Research Centre of Finland, Finland. Report number: VTT-R-01406-10. Available: <http://www.vtt.fi/inf/julkaisut/muut/2010/VTT-R-01406-10.pdf>.
- [29] Kyu Cho, Hyoung; Cho, Yun Je; Yoon, Han Young (2014). Heat structure coupling of CUPID and MARS for the multi-scale simulation of the passive auxiliary feedwater system. Nuclear



- Engineering and Design. Volume 273. Pages 459–468. doi: 10.1016/j.nucengdes.2014.03.017.
- [30] Cho, Hyoung Kyu; Lee, Seung-Jun; Yoon, Han Young; Kang, Kyoung-Ho; Jeong, Jae Jun (2013). Simulation of single- and two-phase natural circulation in the passive condensate cooling tank using the CUPID code. *Journal of Nuclear Science and Technology*. Volume 50, Number 7. Pages 709–722. doi: 10.1080/00223131.2013.791891.
- [31] Lee, J R; Cho, H K; Jeong, J J (2010). Coupled simulation of component thermal hydraulics and neutron kinetics for a nuclear reactor core with CUPID and MASTER. *Transactions of the Korean Nuclear Society Autumn Meeting*. October 21-22, 2010, Jeju, Korea. Pages 723–724.
- [32] Hovi, Ville; Ilvonen, Mikko; Taivassalo, Veikko (2014). 3D core thermal hydraulics with the PORFLO code: turbulence modeling and porous medium with porosity steps. *International Conference on Nuclear Engineering ICONE22*. July 7-11, 2014, Prage, Czech Republic. Volume 22. Pages 1–11.
- [33] Coindreau, Olivia; Fichot, Florian; Fleurot, Joelle (2013). Nuclear fuel rod fragmentation under accidental conditions. *Nuclear Engineering and Design*. Volume 255. Pages 68–76. doi: 10.1016/j.nucengdes.2012.09.021.
- [34] Hovi, Ville (2008). *Calculations of Boiling Two-Phase Flow Using a Porous Media Model*. Dissertation. Faculty of Technology, Department of Energy and Environmental Technology. Lappeenranta University of Technology.
- [35] Leppänen, Jaakko; Hovi, Ville; Ikonen, Timo; Kurki, Joonas; Pusa, Maria; Valtavirta, Ville; Viitanen, Tuomas (2015). The Numerical Multi-Physics project (NUMPS) at VTT Technical Research Centre of Finland. *Annals of Nuclear Energy*. Volume 84. Pages 55–62. doi: 10.1016/j.anucene.2014.10.014.
- [36] Jeong, J. J.; Yoon, H. Y.; Park, I. K.; Cho, H. K. (2010). The CUPID code development and assessment strategy. *Nuclear Engineering and Technology*. Volume 42, Number 6. Pages 636–655. doi: <https://doi.org/10.5516/NET.2010.42.6.636>.
- [37] Hirt, C. W. (1993). Volume-fraction techniques: powerful tools for wind engineering. *Journal of Wind Engineering and Industrial Aerodynamics*. Volume 46–47. Pages 327–338. doi: 10.1016/0167-6105(93)90298-3.
- [38] Rivard, William C; Torrey, Martin D (1975). Numerical calculation of flashing from long pipes using a two-field model. Technical Report. Los Alamos scientific laboratory, Los Alamos, New Mexico. Report number: LA-6104-MS. doi: <https://doi.org/10.2172/4077425>.
- [39] Thurgood, M. J.; Kelly, J. M.; Guidotti, T. E.; Kohrt, R. J.; Crowell, K. R. (1983). COBRA/TRAC, a Thermal-hydraulics Code for Transient Analysis of Nuclear Reactor Vessels and Primary Coolant Systems. Technical Report. Pacific Northwest Laboratory, USA. Report number: NUREG/CR-3046. Available: <https://ntrl.ntis.gov/NTRL/dashboard/searchResults/titleDetail/NUREGCR3046V1.xhtml>.
- [40] Haar, Lester; Gallagher, John S.; Kell, George S. (1984). *NBS/NRC steam tables*. Hemisphere Publishing Corporation. ISBN 0-89116-353-0; 0-89116-354-9. Washington, D.C.
- [41] Ünal, H.C. (1975). Determination of the initial point of net vapor generation in flow boiling systems. *International Journal of Heat and Mass Transfer*. Volume 18, Number 9. Pages 1095–1099. doi: 10.1016/0017-9310(75)90227-6.
- [42] Collier, John G.; Thome, John R. (1994). *Convective boiling and condensation*. 3rd edition. Clarendon Press. ISBN 0191591262, 9780191591266. Oxford.
- [43] Gnielinski, V. (1976). New Equations for Heat and Mass Transfer in Turbulent Pipe and Channel Flow. *International Chemical Engineering*. Volume 16, Number 2. Pages 359–368.
- [44] Hufschmidt, W.; Burck, E. (1968). Der Einfluss temperaturabhängiger Stoffwerte auf den Wärmeübergang bei turbulenter Strömung von Flüssigkeiten in Rohren bei hohen Wärmestromdichten und Prandtlzahlen. *International Journal of Heat and Mass Transfer*. Volume 11, Number 6. Pages 1041–1048. doi: 10.1016/0017-9310(68)90009-4.
- [45] Holman, J. P. (2010). *Heat Transfer*. 10th edition. Mc Graw Hill. ISBN 978-0-07-352936-3. New York.
- [46] Chen, John C. (1966). Correlation for boiling heat transfer to saturated fluids in convective

- flow. *Industrial & Engineering Chemistry Process Design and development*. Volume 5, Number 3. Pages 322–329. doi: 10.1021/i260019a023.
- [47] Lockhart, R.W.; Martinelli, R.C. (1949). Proposed Correlation of Data for Isothermal Two-Phase, Two-Component Flow in Pipes. *Chemical Engineering Progress*. Volume 45, Number 1. Pages 39–48. doi: [http://dx.doi.org/10.1016/0017-9310\(67\)90047-6](http://dx.doi.org/10.1016/0017-9310(67)90047-6).
- [48] Basu, Nilanjana; Warriar, Gopinath R.; Dhir, Vijay K. (2002). Onset of Nucleate Boiling and Active Nucleation Site Density During Subcooled Flow Boiling. *Journal of Heat Transfer*. Volume 124, Number 4. Page 717. doi: 10.1115/1.1471522.
- [49] Gorenflo, Dieter; Kenning, David (2010). H2 Pool Boiling, VDI Heat Atlas Pages 757-792. Springer. ISBN 978-3-540-77877-6. Berlin, Heidelberg.
- [50] Groeneveld, D. C.; Stewart, J.C. (1982). The minimum film boiling temperature for water during film boiling collapse. *International Heat Transfer Conference*. Volume 7. Pages 393–398. doi: 10.1615/IHTC7.1270.
- [51] Imke, Uwe (2018). Personal Communication. KIT Campus Nord, Leopoldshafen, January 25, 2018.
- [52] Groeneveld, D. C. (1969). An investigation of heat transfer in the liquid deficient regime. Technical report. Atomic Energy of Canada Limited. Report number: AECL-3281. doi: 10.1007/BF00008676.
- [53] Bromley, L. A. (1950). Heat transfer in stable film boiling. *Chemical Engineering Progress*. Volume 46, Number 5. Pages 221–226.
- [54] Shah, M. M. (1979). A general correlation for heat transfer during film condensation inside pipes. *International Journal of Heat and Mass Transfer*. Volume 22, Number 4. Pages 547–556. doi: 10.1016/0017-9310(79)90058-9.
- [55] Kuhn, S.; Schrock, V. P. (1994). Final Report of the U.C. Berkeley Single Tube Condensation Studies. Technical Report. U. C. Berkeley. Report number: UCB-NE-4201.
- [56] Ünal, H.C. (1975). Determination of the initial point of net vapor generation in flow boiling systems. *International Journal of Heat and Mass Transfer*. Volume 18, Number 9. Pages 1095–1099. doi: 10.1016/0017-9310(75)90227-6.
- [57] Lewis, Brent J.; Onder, E. Nihan; Prudil, Andrew A. (2017). *Fundamentals of Nuclear Engineering*. 1st edition. WILEY-VCH. ISBN 978-1-119-27149-9. Chichester, West Sussex, UK.
- [58] Kabelac, Stephan; Kind, Matthias; Martin, Holger; Mewes, Dieter; Schaber, Karlheinz; Stephan, Peter (2013). *VDI-Wärmeatlas*. 11th edition. Springer. ISBN 9783642199806. Düsseldorf.
- [59] Choe, W. G.; Weinberg, L.; Weisman, J. (1978). Observation and Correlation of Flow Pattern Transition in Horizontal, Co- Current Gas-Liquid Flow. *Two-phase Transport and Reactor Safety*, T. N. Veziroğlu, S. Kakaç. Pages 1357-1393. Hemisphere Publishing Corporation. ISBN 0891160523, 9780891160526. Washington.
- [60] Ranz, W E; Marshall, W R (1952). Evaporation from drops. Parts I & II. *Chemical Engineering Progress*. Volume 48, Number 22. Pages 141–146 and 173–180. doi: 10.1016/S0924-7963(01)00032-X.
- [61] Wallis, Graham B. (1974). The terminal speed of single drops or bubbles in an infinite medium. *International Journal of Multiphase Flow*. Volume 1, Number 4. Pages 491–511. doi: 10.1016/0301-9322(74)90003-2.
- [62] Richardson, J.F.; Zaki, W.N. (1997). Sedimentation and fluidisation: Part I. *Chemical Engineering Research and Design*. Volume 75, Number 3. Pages S82–S100. doi: 10.1016/S0263-8762(97)80006-8.
- [63] Ishii, M.; Mishima, K. (1980). Study of Two-fluid Model and Interfacial Area. Technical report. Argonne National Laboratory, NRC, USA. Report number: NUREG/CR-1873; ANL-80-111 ON: TI84017617. Available: <https://books.google.de/books?id=XDVcywAACAAJ>.
- [64] Lahey, Richard; Moody, F J (1993). *The Thermal-Hydraulics of a Boiling Water Nuclear Reactor*. 2nd edition. American Nuclear Society. ISBN 0-89448-037-5. La Grange Park,

Illinois.

- [65] Dittus, F.W.; Boelter, L.M.K. (1985). Heat transfer in automobile radiators of the tubular type. *International Communications in Heat and Mass Transfer*. Volume 12, Number 1. Pages 3–22. doi: 10.1016/0735-1933(85)90003-X.
- [66] Sauter, J. (1928). Die Größenbestimmung der in Gemischnebeln von Verbrennungskraftmaschinen vorhandenen Brennstoffteilchen. VDI-Forschungsheft Nr 312. Verein Deutscher Ingenieure. ISSN 0042-174X.
- [67] Kataoka, Isao; Ishii, Mamoru; Mishima, Kaichiro (1983). Generation and Size Distribution of Droplet in Annular Two-Phase Flow. *Journal of Fluids Engineering*. Volume 105, Number 2. Pages 230–238. doi: <https://doi.org/10.1115/1.3240969>.
- [68] Kronig, R.; Van Der Veen, B.; Ijzerman, Miss P. (1951). On the theory of extraction from falling droplets II. *Applied Scientific Research*. Volume 3, Number 2. Pages 103–110. doi: 10.1007/BF03186653.
- [69] Ryskin, Gregory (1987). Heat or mass transfer from a moving drop - Some approximate relations for the Nusselt number. *International Communications in Heat and Mass Transfer*. Volume 14, Number 6. Pages 741–749. doi: 10.1016/0735-1933(87)90053-4.
- [70] Churchill, Stuart W. (1977). Friction-factor equation spans all fluid-flow regimes. *Chemical Engineering Journal*. Volume 84, Number 24. Pages 91–92.
- [71] Levy, S. (1967). Forced convection subcooled boiling—prediction of vapor volumetric fraction. *International Journal of Heat and Mass Transfer*. Volume 10, Number 7. Pages 951–965. doi: 10.1016/0017-9310(67)90071-3.
- [72] Ferrell, J. K.; Bylund, D. M. (1966). A Study of Convection Boiling Inside Channels: Final Report. USAEC, Division of Technical Information. Report number: 48925836.
- [73] Haaland, S. E. (1983). Simple and explicit formulas for the friction factor in turbulent pipe flow. *Journal of Fluids Engineering*. Volume 105, Number 1. Pages 89–90. doi: <https://doi.org/10.1115/1.3240948>.
- [74] Wallis, G. B. (1970). Annular Two-Phase Flow—Part 1: a simple theory. *Journal of Basic Engineering*. Volume 92, Number 1. Pages 59–72. doi: <https://doi.org/10.1115/1.3424950>.
- [75] Harlow, Francis H.; Amsden, Anthony A. (1971). A numerical fluid dynamics calculation method for all flow speeds. *Journal of Computational Physics*. Volume 8, Number 2. Pages 197–213. doi: 10.1016/0021-9991(71)90002-7.
- [76] Stewart, H. B.; Wendroff, B. (1984). Two-phase flow: Models and methods. *Journal of Computational Physics*. Volume 56, Number 3. Pages 363–409. doi: [https://doi.org/10.1016/0021-9991\(84\)90103-7](https://doi.org/10.1016/0021-9991(84)90103-7).
- [77] Todreas, Neil E.; Kazimi, Mujid S. (2001). *Nuclear Systems II - elements of thermal hydraulic design*. 1st edition. Taylor and Francis publishing. ISBN 0-89116-936-9; 1-56032-079-6. New York.
- [78] Boussinesq, J. (1877). Essai sur la théorie des eaux courantes. Mémoires présentés par divers savants à l'Académie des Sciences. Volume 23. Pages 1–680. Available: [https://www.irphe.fr/~clanet/otherpaperfile/articles/Boussinesq/N0003328\\_PDF\\_1\\_770.pdf](https://www.irphe.fr/~clanet/otherpaperfile/articles/Boussinesq/N0003328_PDF_1_770.pdf).
- [79] Castellana, Frank S.; Adams, Wilton T.; Casterline, Joseph E. (1974). Single-phase subchannel mixing in a simulated nuclear fuel assembly. *Nuclear Engineering and Design*. Volume 26, Number 2. Pages 242–249. doi: 10.1016/0029-5493(74)90059-4.
- [80] Kim, Sung Jin; Jang, Seok Pil (2002). Effects of the Darcy number, the Prandtl number, and the Reynolds number on local thermal non-equilibrium. *International Journal of Heat and Mass Transfer*. Volume 45, Number 19. Pages 3885–3896. doi: 10.1016/S0017-9310(02)00109-6.
- [81] Malhorta, A.; Kang, S. (1984). Turbulent Prandtl number in circular pipes. *International Journal of Heat and Mass Transfer*. Volume 27, Number 11. Pages 2158–2161. doi: [https://doi.org/10.1016/0017-9310\(84\)90203-5](https://doi.org/10.1016/0017-9310(84)90203-5).
- [82] Valette, M. (2012). Analysis of subchannel and rod bundle PSBT experiments with CATHARE 3. *Science and Technology of Nuclear Installations*. Volume 2012. doi: 10.1155/2012/123426.

- [83] Groeneveld, D. C.; Cheng, S. C.; Doan, T. (1986). 1986 AECL-UO critical heat flux lookup table. *Heat Transfer Engineering*. Volume 7, Number 1–2. Pages 46–62. doi: 10.1080/01457638608939644.
- [84] Ahn, Seung Hoon; Jeun, Gyoo Dong (2001). Effect of spacer grids on CHF at PWR operating conditions. *Journal of the Korean Nuclear Society*. Volume 33, Number 3. Pages 283–297. Available: [http://inis.iaea.org/search/search.aspx?orig\\_q=RN:32067195](http://inis.iaea.org/search/search.aspx?orig_q=RN:32067195).
- [85] Rubin, A.; Schoedel, A.; Avramova, M.; Utsuno, H. (2010). OECD/NRC Benchmark based on NUPEC PWR subchannel and bundle tests (PSBT) Volume I: Experimental Database and Final Problem Specifications. US NRC, OECD Nuclear Energy Agency, USA. Report number: Nea/Nsc/Doc(2010)1. Available: [https://www.oecd-nea.org/jcms/pl\\_19106/oecd/nrc-benchmark-based-on-nupec-pressurised-water-reactor-sub-channel-and-bundle-tests-psbt-volume-i-experimental-database-and-final-problem-specifications](https://www.oecd-nea.org/jcms/pl_19106/oecd/nrc-benchmark-based-on-nupec-pressurised-water-reactor-sub-channel-and-bundle-tests-psbt-volume-i-experimental-database-and-final-problem-specifications).
- [86] Avramova, Maria; Cuervo, Diana (2013). Assessment of CTF Boiling Transition and Critical Heat Flux Modeling Capabilities Using the OECD/NRC BFBT and PSBT Benchmark Databases. *Science and Technology of Nuclear Installations*. Volume 2013. Pages 1–12. doi: 10.1155/2013/508485.
- [87] Neykov, B; Aydogan, F; Hochreiter, L; Ivanov, K; Utsuno, H; Fumio, K; Sartori, E (2005). NUPEC BWR Full-size Fine-mesh Bundle Test ( BFBT ) Benchmark. Volume I: Specifications. US NRC, OECD Nuclear Energy Agency, USA. Report number: NEA/NSC/DOC(2005)5. Available: [https://www.oecd-nea.org/jcms/pl\\_14238/nupec-bwr-full-size-fine-mesh-bundle-test-bfbt-benchmark](https://www.oecd-nea.org/jcms/pl_14238/nupec-bwr-full-size-fine-mesh-bundle-test-bfbt-benchmark).
- [88] Glück, M. (2008). Validation of the sub-channel code F-COBRA-TF. Part II. Recalculation of void measurements. *Nuclear Engineering and Design*. Volume 238, Number 9. Pages 2317–2327. doi: 10.1016/j.nucengdes.2008.02.006.
- [89] Jaeger, Wadim; Perez Manes, Jorge; Imke, Uwe; Jimenez Escalante, Javier; Sanchez-Espinoza, Victor (2013). Validation and comparison of two-phase flow modeling capabilities of CFD, sub channel and system codes by means of post-test calculations of BFBT transient tests. *Nuclear Engineering and Design*. Volume 263. Pages 313–326. doi: 10.1016/j.nucengdes.2013.06.002.
- [90] Di Marcello, Valentino; Jimenez Escalante, Javier; Sanchez Espinoza, Victor (2015). Validation of the thermal-hydraulic system code ATHLET based on selected pressure drop and void fraction BFBT tests. *Nuclear Engineering and Design*. Volume 288. Pages 183–194. doi: 10.1016/j.nucengdes.2015.04.003.
- [91] Becker, M., K.; Ling, C. H.; Hedberg, S; Strand, G. (1983). An experimental investigation of post dryout heat transfer. Technical report. Royal Institute of Technology, Stokholm Sweden. Report number: KTH-NEL-33. Available: [https://inis.iaea.org/search/search.aspx?orig\\_q=RN:15049472](https://inis.iaea.org/search/search.aspx?orig_q=RN:15049472).
- [92] International Atomic Energy Agency (IAEA) (2007). Nuclear power plant design characteristics. Structure of nuclear power plant design characteristics in the IAEA power reactor information system (PRIS). Technical report. International Atomic Energy Agency. Report number: IAEA-TECDOC-1544. Available: [https://www-pub.iaea.org/MTCD/Publications/PDF/te\\_1544\\_web.pdf](https://www-pub.iaea.org/MTCD/Publications/PDF/te_1544_web.pdf).
- [93] Jimenez Escalante, Javier; Di Marcello, Valentino; Sanchez Espinoza, Victor; Perin, Yann (2017). Application of the ATHLET/COBRA-TF thermal-hydraulics coupled code to the analysis of BWR ATWS. *Nuclear Engineering and Design*. Volume 321. Pages 318–327. doi: <https://doi.org/10.1016/j.nucengdes.2016.10.001>.
- [94] Kozłowski, Tomasz; Roshan, Sean; Lefvert, Tomas; Netterbrant, Christer; Downar, Thomas; Xu, Yunlin; Wysocki, Aaron; Ivanov, Kostadin; Magedanz, Jeffrey; Hardgrove, Matthew; March-Leuba, Jose (2014). BWR Stability Event Benchmark based on Oskarshamn-2 1999 Feedwater Transient. OECD/NRC. Report number: NEA-1881/01, NEA-1881/03.
- [95] Kozłowski, Tomasz; Wysocki, Aaron; Gajev, Ivan; Xu, Yunlin; Downar, Thomas; Ivanov, Kostadin; Magedanz, Jeffrey; Hardgrove, Matthew; March-Leuba, Jose; Hudson, Nathanael; Ma, Weimin (2014). Analysis of the OECD/NRC Oskarshamn-2 BWR stability benchmark. *Annals of Nuclear Energy*. Volume 67. Pages 4–12. doi: 10.1016/J.ANUCENE.2013.09.028.

- [96] Gonzalez Vargas, Jose Angel (2017). *Advanced Reactor Physics Methods for Transient Analysis of Boiling Water Reactors*. Dissertation. Faculty of Mechanical Engineering, Karlsruhe Institut für Technologie (KIT). doi: 10.5445/IR/1000077121.
- [97] Espinosa-Paredes, Gilberto; Camargo-Camargo, Raúl; Nuñez-Carrera, Alejandro (2012). Severe accident simulation of the laguna verde nuclear power plant. *Science and Technology of Nuclear Installations*. Volume 2012. Pages 1–11. doi: 10.1155/2012/209420.
- [98] Castillo, Rogelio; Alonso, Gustavo; Ramirez, Ramon J. (2013). Validation of SIMULATE-3K for stability analysis of Laguna Verde nuclear plant. *Nuclear Engineering and Design*. Volume 265. Pages 19–24. doi: 10.1016/J.NUCENGDES.2013.08.051.
- [99] DiGiovine, Arthur S.; Rhodes, III, Joel D.; Umbarger, Jerry A. (1995). *SIMULATE-3, Advance Three-Dimensional Two-Group Reactor Analysis Code. User's Manual*. Wilmington, NC. Report number: Studsvik/SOA-95/15.
- [100] Ruzicka, M. C. (2008). On dimensionless numbers. *Chemical Engineering Research and Design*. Volume 86, Number 8. Pages 835–868. doi: 10.1016/j.cherd.2008.03.007.
- [101] Rohsenow, Warren M.; Hartnett, James P.; Ganic, Ejup N. (1973). *Handbook of heat transfer fundamentals*. 2nd edition. Mc Graw Hill. ISBN 0-07-053554-X. New York.
- [102] Gnielinski, V. (2013). On heat transfer in tubes. *International Journal of Heat and Mass Transfer*. Volume 63. Pages 134–140. doi: 10.1016/j.ijheatmasstransfer.2013.04.015.
- [103] Wallis, G. (1968). Letter to the editor on: Phenomena of liquid transfer in two-phase dispersed annular flow. *International Journal of Heat Mass Transfer*. Number 11. Pages 783–785.
- [104] Ishii, M.; Chawla, T. C. (1979). *Local drag laws in dispersed two-phase flow*. Argonne National Laboratory (ANL), USA. Report number: NUREG/CR-1230; ANL-79-105. Available: <https://ntrl.ntis.gov/NTRL/dashboard/searchResults/titleDetail/NUREGCR1230.xhtml>.



## 12 Annexes

### Annex 1 Constitutive models for the closure of the conservation equations

#### a. Dimensionless physical numbers

The correlations used in TWOPORFLOW for the simulation of thermal-hydraulics physical phenomena are dependent on different dimensionless numbers. Those numbers are defined bellow.

**Grashof number:** represents the ratio between the buoyancy force due to spatial variation in fluid density to the restraining force due to the viscosity of the fluid [100]:

$$Gr = \frac{g\gamma|T_w - T_l|D_{Have}^3}{\left(\frac{\mu_l}{\rho_l}\right)^2}, \quad (70)$$

where  $g$  is the acceleration due to gravity,  $\gamma$  the thermal expansion coefficient  $T_w$  and  $T_l$  the temperatures of the wall surface and the liquid correspondingly,  $D_{Have}$  the averaged hydraulic diameter,  $\mu_l$  the viscosity of the liquid and  $\rho_l$  the density of the liquid.

**Nusselt number:** is the ratio of the thermal energy convected to the fluid to the thermal energy conducted within the fluid. In other words it is the dimensionless heat transfer coefficient [100]:

$$Nu = \frac{hL}{\lambda}, \quad (71)$$

where  $h$  is the convective heat transfer coefficient,  $L$  the characteristic length and  $\lambda$  the thermal conductivity.

**Peclet number:** is the ratio of heat transport by motion of a fluid to the heat transport by thermal conduction [101]:

$$Pe = \frac{G_l D_H C p_l}{\lambda_l} = Re Pr = \frac{Nu}{St}, \quad (72)$$

where  $G_l$  is the mass flux of the liquid,  $D_H$  the hydraulic diameter,  $C p_l$  the specific heat of liquid,  $\lambda_l$  the thermal conductivity of the liquid,  $Re$  the Reynolds number,  $Pr$  the Prandtl number,  $Nu$  the Nusselt number,  $St$  the Stanton number.

**Prandtl number:** is the ratio of the momentum diffusivity to the thermal diffusivity [101]:

$$Pr = \frac{\mu C p}{\lambda}, \quad (73)$$

where  $\mu$  is the viscosity,  $C p$  the specific heat of the fluid and  $\lambda$  the thermal conductivity of the fluid.

**Reynolds number:** is the ratio of the inertial forces to the viscous forces and is used to determine whether the fluid flow is laminar or turbulent [101]:

$$Re = \frac{\rho V D_{HAVE}}{\mu}, \quad (74)$$

where  $\rho$  is the density of the fluid,  $V$  the velocity of the fluid,  $D_{Have}$  the averaged hydraulic diameter and  $\mu$  the viscosity of the fluid.

**Stanton number:** ratio of heat transfer coefficient to heat capacity of a fluid [101]:

$$St = \frac{h}{C p \rho V} = \frac{Nu}{Re Pr}, \quad (75)$$

where  $h$  is the heat transfer coefficient,  $Cp$  the specific heat of the fluid,  $\rho$  is the density of the fluid,  $V$  the velocity of the fluid,  $Nu$  the Nusselt number,  $Re$  the Reynolds number and  $Pr$  the Prandtl number.

**Weber number:** is the ratio between the inertial force and the surface tension force and the Weber number indicates whether the kinetic or the surface tension energy is dominant in two phase flow [101]:

$$We = \frac{\rho V^2 L}{\sigma}, \quad (76)$$

where  $\rho_k$  is the density of the fluid,  $V_k$  the relative velocity between the two media,  $L$  the characteristic length,  $\sigma$  the surface tension.

**Froude number:** relates the inertia forces in a system to the effects due to gravity [100]:

$$Fr = \frac{V}{\sqrt{gL}}, \quad (77)$$

where  $V$  is the velocity of the fluid,  $L$  the characteristic length,  $g$  acceleration due to gravity.

## b. Wall heat transfer

### *TPF correlations*

The Chen correlation [46] is used, for nucleate and saturated boiling; the rest of the boiling curve is calculated using different correlations described in the following sections.

### **Single-Phase Liquid/Vapor convective heat transfer**

In the single-phase liquid or gas forced convection regimes the heat transfer coefficient is given in relation to the Nusselt number:

$$h_{fc} = \frac{Nu \lambda_k}{D_{Have}}. \quad (78)$$

Where  $\lambda_k$  represents the conductivity of the fluid (liquid or gas) and the Nusselt number is taken from Gnielinski [43] as:

$$Nu = \left[ \frac{0.5}{(1.58 \log(Re) - 3.28)^2} \right] \left[ \frac{Pr(Re - 1000)}{1 + 12.7 \left( \frac{0.5}{(1.58 \log(Re) - 3.28)^2} \right)^{0.5} (Pr^{2/3} - 1)} \right]. \quad (79)$$

### **Subcooled/Nucleate/Saturated boiling**

The surface heat flux is evaluated as:

$$q'' = h_{l,nb}(T_w - T_{sat}) + h_{l,fc}(T_w - T_l), \quad (80)$$

and the heat transfer coefficient of (sub-cooled) nucleate boiling is given by the correlation of Chen:



$$h_{l,nb} = 0.00122S \frac{\lambda_l^{0.79} C p_l^{0.45} \rho_l^{0.49}}{\sigma^{0.5} \mu_l^{0.29} h_{fg}^{0.24} \rho_v^{0.24}}, \quad (81)$$

where:

$$S = \begin{cases} [1 + 0.12Re^{1.14}]^{-1}, & Re < 32.5 \\ [1 + 0.42Re^{0.78}]^{-1}, & 32.5 \leq Re < 70, \\ 0.1, & Re > 70 \end{cases} \quad (82)$$

and:

$$Re = 10^{-4} (2.35(X_{tt}^{-1} + 0.213)^{0.736})^{1.25} \alpha_l \rho_l V_l \frac{D_{Have}}{\mu_l}. \quad (83)$$

The heat transfer coefficient of forced convection ( $h_{l,fc}$ ) is the maximum of the single-phase liquid coefficient (78) and the Chen heat transfer coefficient, being the latter:

$$h_l = 2.35h_{fc}(X_{tt}^{-1} + 0.213)^{0.736}, \quad (84)$$

and the Martinelli [47] parameter is calculated as:

$$X_{tt}^{-1} = \left[ \frac{x}{(1-x)} \right]^{0.9} \left[ \frac{\rho_l}{\rho_v} \right]^{0.5} \left[ \frac{\mu_l}{\mu_v} \right]^{0.1}. \quad (85)$$

Where  $\mu_k$  are obtained by the IAPWS-97 tables for a given density and temperature.

### Transition boiling

In transition boiling the heat transfer coefficient is given by:

$$h_{l,nb} = \frac{w_{tran}q_c + (1 - w_{tran})h_{film}(T_{msfb} - T_{sat})}{T_w - T_{sat}}, \quad (86)$$

where  $w_{tran}$  is a weighting factor:

$$w_{tran} = \frac{(T_{msfb} - T_w)}{T_{msfb} - T_{cr}}. \quad (87)$$

In this case the minimum stable film boiling temperature ( $T_{msfb}$ ) is computed according to Groeneveld and Stewart [50] using the pressure in MPa and the temperature in K. For  $P \leq 9MPa$ :

$$T_{msfb} = 557.85 + 44.1P - 3.72P^2, \quad (88)$$

and for higher pressures:

$$T_{msfb} = 647.037 + 0.71P. \quad (89)$$

The calculation of  $h_{film}$  is explained below.

### Film boiling

The heat transfer coefficient for film boiling for pressures  $P < 1.33 \times 10^6$  Pa is given by [52] Groeneveld (Dittus Boelter modified):

$$h_{film} = \frac{0.023\lambda_v}{D_{Have}} Re_v^{0.8} Pr_v^{0.4}. \quad (90)$$

For higher pressures:

$$h_{film} = \frac{0.052\lambda_v}{D_{Have}} Re_v^{0.688} Pr_v^{1.26} \left( 1 - 0.1 \left[ (1-x) \left( \frac{\rho_l}{\rho_v} - 1 \right) \right]^{0.4} \right)^{-1.06}, \quad (91)$$

where:

$$Re_v = \frac{D_{Have} G}{\mu_v} \left[ x + \frac{\rho_v}{\rho_l} \right] (1-x). \quad (92)$$

For low or high flow the Bromley correlation plus forced convection [53] is used. In this correlation when the square root of the Froude number is less than 2 ( $\sqrt{Fr} < 2$ ) forced convection is considered to be present. In TWOPORFLOW it is evaluated as:

$$\sqrt{Fr} = \sqrt{\frac{\alpha_v \rho_v V_v}{\sqrt{g D_{Have} \rho_v (\rho_l - \rho_v)}}} + \sqrt{\frac{\alpha_l \rho_l V_l}{\sqrt{g D_{Have} \rho_l (\rho_l - \rho_v)}}}. \quad (93)$$

If  $\sqrt{Fr}$  is lower than 2 then:

$$h_{film} = \frac{0.62 \alpha_l g (\rho_l - \rho_v) \rho_v \lambda_v^3 [h_{fg} + 0.5 C p_v (T_w - T_{sat})]}{2\pi \sqrt{\frac{\sigma}{\rho_l - \rho_v}} \mu_v (T_w - T_{sat})}. \quad (94)$$

### Condensation

The heat transfer coefficient in condensation is given by:

$$h_{l,fc} = w h_{l,sing} + (1-w) h_{film}, \quad (95)$$

where  $w$  is a weighting factor in the range  $0.8 < \alpha_v < 0.9$ . In this case the heat coefficient for film boiling is calculated by the Shah [54] correlation as follow:

$$h_{film} = \frac{0.24 Re_l^{0.8} Pr_v^{0.4} \lambda_l}{D_{Have}} \left[ x^{0.8} + 3.8 \frac{(1-x)^{0.76} x^{0.04}}{\left( \frac{P}{P_{cr}} \right)^{0.38}} \right]. \quad (96)$$

### TPF-TRACE correlations

#### Single-Phase Liquid convective heat transfer

In TWOPORFLOW single-phase liquid convection heat transfer is taken if the wall temperature ( $T_w$ ) is lower than the saturation temperature ( $T_{sat}$ ) and the void fraction  $\alpha_v$  is lower or equal to 0.8. It is calculated using the maximum of the forced convection and natural convection Nusselt numbers. The Nusselt number for forced convection is [102] [44]:

$$Nu_{fc} = \left( \frac{Pr_l}{Pr_w} \right)^{0.11} \frac{h_{fc} D_{Have}}{\lambda_l}. \quad (97)$$

$h_{fc}$  is obtained in equation (78), and the liquid Prandtl number is evaluated at the bulk temperature.

The Nusselt number for natural convection is calculated as [45]:

$$Nu_{nc} = \max\left(0.59(Gr_l Pr_l)^{0.25}, 0.1(Gr_l Pr_l)^{\frac{1}{3}}\right), \quad (98)$$

where the  $Gr$  is the Grashof number. The wall heat transfer coefficient to the liquid  $h_l$  is given by:

$$h_l = h_{fc} = \max(Nu_{fc}, Nu_{nc}) * \frac{\lambda_l}{D_{Have}}. \quad (99)$$

### Onset of nucleate boiling

The wall surface temperature at which nucleate boiling heat transfer begins is denoted as “temperature of the onset of nucleate boiling.” This temperature is considered for the heat transfer regime selection. If the wall temperature is higher than the saturation temperature, but lower than the temperature of onset of nucleate boiling, the heat transfer of liquid is equal to the heat transfer of forced convection. The temperature of the onset of nucleate boiling is calculated as [48]:

$$T_{onb} = \min(T_l, T_{sat}) + \frac{\left[ \sqrt{\left( \frac{2h_{fc}\sigma T_{sat}}{\rho_v h_{fg} k_l (1 - e^{(-\theta^3 - 5\theta)})} \right)} \sqrt{\left( \frac{2h_{fc}\sigma T_{sat}}{\rho_v h_{fg} k_l (1 - e^{(-\theta^3 - 5\theta)})} \right)} + 4\max(0.0, T_{sat} - T_l) \right]^2}{4}. \quad (100)$$

Here the contact angle for water and stainless steel  $\theta = \frac{38\pi}{180}$  is used.

### Condensation

If  $\alpha_v > 0.9$  and  $T_{liq} < T_{sat}$ , the heat flux of the liquid is calculated using the laminar and turbulent Nusselt number as:

$$h_l = \lambda_l \frac{\sqrt{Nu_{lam}^2 + Nu_{turb}^2}}{\max\left(1 \times 10^5, \frac{D_{Have}(1 - \sqrt{\alpha_v})}{2}\right)}, \quad (101)$$

where the laminar Nusselt number is  $Nu_{lam}$  [55] [19] and  $Re_{film}$  is evaluated from the liquid flux  $G_l$ , the averaged hydraulic diameter  $D_{Have}$  and the viscosity of the liquid  $\mu_l$ :

$$Nu_{lam} = 2(1 + 1.83 \times 10^{-4} Re_{film}), \quad (102)$$

and the turbulent Nusselt number is calculated as [43] [19]:

$$Nu_{turb} = \frac{h_{film} D_{Have}}{4\lambda_l}. \quad (103)$$

In this case  $h_{film}$  is calculated with equation (101). If the void fraction is in the range  $0.8 < \alpha_v < 0.9$ , then the heat flux is:

$$h_l = \left( \frac{\alpha_v - 0.8}{0.1} \right) h_{film} + \left( 1 - \frac{\alpha_v - 0.8}{0.1} \right) h_{fc}. \quad (104)$$

### (Sub-cooled) Nucleate boiling

Nucleate boiling begins if the wall temperature is higher than the onset of nucleate boiling temperature. In this case, the liquid heat flux is calculated as:

$$h_l = h_{pb} \frac{T_w - T_{onb}}{T_w - T_{sat}}. \quad (105)$$

In this case heat flux in pool boiling is [49]:

$$h_{pb} = \left( \frac{5600 \left( 1.73 p_r^{0.27} + \left( \frac{0.68}{1 - p_r} \right) p_r^2 \right)}{2000^{(0.9 - 0.3 p_r^{0.15})}} \right)^{\frac{1}{1 - (0.9 - 0.3 p_r^{0.15})}}, \quad (106)$$

where  $p_r$  is the reduced pressure, and the pressure is given in Pa:

$$p_r = \frac{P}{P_{cr}}. \quad (107)$$

### c. Fraction of sub-cooled vapor generation

#### *TPF correlations*

To calculate the fraction of sub-cooled vapor generation the correlation of Ünal [41] is used. This correlation depends only on liquid velocities, wall, saturation, and liquid temperatures. The value for the Ünal coefficient is:

$$\ddot{U} = \begin{cases} 0.11; & |\bar{V}_l| < 0.45 \text{ m/s} \\ 0.24; & |\bar{V}_l| > 0.45 \text{ m/s} \end{cases} \quad (108)$$

The sub-cooling temperature is calculated as:

$$T_{sub} = \ddot{U} \max(T_w - T_l, 0.0). \quad (109)$$

If  $T_{sub}$  is greater than 0 K and the wall temperature is higher or equal than the saturation temperature the vapor generation fraction is:

$$\Gamma_{sub} = \min \left( 1.0, \max \left( 0.0, \frac{T_l - (T_{sat} - T_{sub})}{T_{sub}} \right) \right). \quad (110)$$

If these conditions are not reached  $\Gamma_{sub} = 0.0$ .

#### *TPF-TRACE correlations*

Here a correlation dependent on the Peclet number, saturation temperature, mass flow, hydraulic diameter and conductivity is used. The Peclet number is the ratio of the Nusselt number and the Stanton number. If the Peclet number is below 70000 we have the thermally controlled region, if the local Nusselt number is constant (455); but when the Peclet number is higher than 70000 it is the thermally and hydro-

dynamically controlled region in which the Stanton number is a constant from 0.0065 [57]. The latter case is what is occurring in this case. The liquid temperature at which bubble detachment occurs is calculated as:

$$T_{l,b} = T_{sat} - \frac{G_l D_{Have} \lambda_l}{PeSt}; \quad (111)$$

and the vapor fraction is:

$$\Gamma_{sub} = \min\left(1.0, \max\left(0.0, \frac{T_l - T_{l,b}}{\max(1 \times 10^6, T_{sat} - T_{l,b})}\right)\right). \quad (112)$$

#### d. Liquid-vapor interface heat and mass exchange models

##### *TPF correlations*

##### **Interfacial mass transport**

First the interfacial heat transport is calculated. The heat exchange for direct evaporation from wall is calculated as a heat flux:

$$Q_{Fsl,evap} = \Gamma_{sub} h_{l,nb} (T_w - T_{sat}), \quad (113)$$

where  $A$  is the wall heat transfer area.

The condensation and evaporation heat flux, including sub-cooled boiling. A large coefficient is used to drive sub-cooled vapor and super-heated liquid to saturation with the temperature given in K and is calculated by:

$$Q_{Flv} = 1 \times 10^{12} (T_{sat} - T_v)^2 + h_{v,sat} (T_{sat} - T_v). \quad (114)$$

The first term in equation (114) is used only if  $T_v < T_{sat}$ . In liquid phase, if the saturation temperature is higher than the liquid temperature, and the fraction of liquid is higher than  $1 \times 10^{-8}$  then:

$$Q_{Fl} = -1 \times 10^{12} (T_{sat} - T_l)^2 - Q_{Fsl,evap} + h_{l,sat} (T_{sat} - T_l). \quad (115)$$

The first term in equation (115) is used only if  $T_l > T_{sat}$ . The power density is calculated by multiplying the heat flux by the evaporation-condensation area density. The area density of dispersed bubble flow is calculated as:

$$A'''_{l,db} = 6 \frac{\alpha_v}{d_{db}}. \quad (116)$$

Here, Reynolds and Nusselt number for dispersed bubble flow take the form:

$$Re_{db} = \frac{\rho_l |V_{l,tot} - V_{v,tot}| d_{db}}{\mu_l}, \quad (117)$$

$$Nu_{db} = 2 + 0.6 Re_{db}^{0.5} Pr_l^{0.3}. \quad (118)$$

The diameter of the bubbles in departure boiling and in case of droplets is calculated using the Weber number criteria [58]:

$$d_{db} = \begin{cases} 12 \frac{\sigma}{\rho_l (|V_{l,tot} - V_{v,tot}|)^2}; D_{Have} \leq d_{db} \leq 5 \times 10^{-3} \\ 5 \times 10^{-4}; d_{db} \leq D_{Have} \\ 5 \times 10^{-3}; d_{db} \geq 5 \times 10^{-3} \end{cases}, \quad (119)$$

$$d_{drop} = \begin{cases} 12 \frac{\sigma}{\rho_v (|V_{l,tot} - V_{v,tot}|)^2}; D_{Have} \leq d_{drop} \leq 5 \times 10^{-3} \\ 5 \times 10^{-4}; d_{drop} \leq D_{Have} \\ 5 \times 10^{-3}; d_{drop} \geq 5 \times 10^{-3} \end{cases}. \quad (120)$$

The area of annular flow is:

$$A_{I,annular}''' = 6 \frac{\alpha_l}{d_{drop}}. \quad (121)$$

Then Reynolds and Nusselt annular numbers:

$$Re_{annular} = \frac{\rho_v |V_{l,tot} - V_{v,tot}| d_{drop}}{\mu_v}, \quad (122)$$

and:

$$Nu_{annular} = 2 + 0.6 Re_{annular}^{0.5} Pr_v^{0.3}. \quad (123)$$

The saturation heat transfer coefficients for liquid and vapor are:

$$h_{l,sat} = \frac{(1-w) Nu_{bub} k_l A_{I,db}'''}{d_{db}} + w 1000 A_{I,annular}''', \quad (124)$$

and:

$$h_{v,sat} = \frac{w Nu_{annular} k_v A_{I,annular}'''}{d_{drop}} + (1-w) 1000 A_{I,db}'''. \quad (125)$$

For equations (124) and (125)  $w$  is a weighting factor in the range  $0.3 < \alpha_v < 0.7$ .

If there are fuel rods present, the film diameter is calculated as:

$$d_{film} = \max(1 \times 10^{-5}, 0.5 D_{Have} (1 - \sqrt{\alpha_v})). \quad (126)$$

The area of annular flow is then:

$$A_{I,annular}''' = 4 \frac{\sqrt{\alpha_v}}{D_{Have}}, \quad (127)$$

and the vapor and liquid mass flux:

$$G_v = \alpha_v \rho_v \max(V_{v,tot}, 1 \times 10^{-8}), \quad (128)$$

and:

$$G_l = \alpha_l \rho_l \max(V_{l,tot}, 1 \times 10^{-8}). \quad (129)$$

Here  $Re_{annular}$  is equal to  $Re_v$  multiplied by  $\sqrt{\alpha_v}$  and  $Re_{film}$  to  $Re_l$ . Then the Nusselt number are calculated as:

$$Nu_{annular} = \max(4, 0.023 Re_{annular}^{0.8} Pr_v^{0.4}), \quad (130)$$

and:

$$Nu_{film} = \max(4, 0.023 Re_{film}^{0.8} Pr_v^{0.4}). \quad (131)$$

The saturation enthalpies of liquid and vapor are:

$$h_{l,sat} = \frac{\alpha_v Nu_{bub} k_l A''_{l,db}}{d_{db}} + \frac{\alpha_l Nu_{film} k_l A''_{l,annular}}{d_{film}}, \quad (132)$$

and:

$$h_{v,sat} = \frac{\alpha_l Nu_{annular} k_v \sqrt{\alpha_v} A''_{l,annular}}{D_{Have}} + \alpha_v 1000 A''_{l,db}. \quad (133)$$

In case  $\alpha_v < 1 \times 10^{-4}$  or  $\alpha_l < 1 \times 10^{-8}$  the heat transfer in liquid and vapor in the interface are equal to zero.

### Condensation and evaporation

Once interfacial mass transport and heat transfer are calculated, the condensation and evaporation could be calculated as:

$$Q_I = Q_{Iv} + h_{v,sat} \Gamma. \quad (134)$$

## TPF-TRACE correlations

### Dispersed Bubbly Flow Regime

Dispersed bubbly flow regime is taken up to 30% of void fraction as well as for a specific mass flux, given by the criterion from Choe et al [59]. The transition is implemented by a linear ramp:

$$\alpha_{v,db} = \begin{cases} 0.3 & ; G \leq 2000 \left(\frac{kg}{m^2s}\right) \\ 0.3 + 0.2 \left(\frac{G - 2000}{2700 - 2000}\right) & ; 2000 < G < 2700 \left(\frac{kg}{m^2s}\right) \\ 0.5 & ; G \geq 2700 \left(\frac{kg}{m^2s}\right) \end{cases}. \quad (135)$$

Interfacial area for the dispersed bubble flow regime is computed by equation (116) if  $1 \times 10^{-4}m \leq d_{DB} \leq 0.9D_{Have}$  and  $\alpha_v < \alpha_{v,db}$ . But if  $\alpha_v \geq \alpha_{v,db}$  then it is computed as:

$$A''_{l,db} = \frac{6\alpha_{v,db}}{d_{db}} \left(\frac{1 - \alpha_v}{1 - \alpha_{v,db}}\right). \quad (136)$$

Dispersed bubbles diameter it is approximated by:

$$d_{ab} = 2 \sqrt{\frac{\sigma}{g\Delta\rho}}. \quad (137)$$

Heat transfer coefficient between liquid and bubble interface is computed using the Ranz-Marshall correlation [60]:

$$h_{l,ab} = \frac{k_l}{d_{ab}} Nu_{ab}. \quad (138)$$

The Nusselt number is calculated with equation (118) with Reynolds number as a function of the dispersed bubble relative velocity defined as:

$$Re_{ab} = \frac{\rho_l V_{r,ab} d_{ab}}{\mu_l}, \quad (139)$$

where the dispersed bubble relative velocity is given by:

$$V_{r,ab} = \text{Min}[|V_v - V_l|, V_{db}]; \quad (140)$$

and for a single distorted particle, the Wallis formula [61], applying as well the multi particle correction of Richardson and Zaki [62]:

$$V_{db} = \sqrt{2} \left( \frac{\sigma g \Delta \rho}{\rho_l^2} \right)^{1/4} (1 - \alpha_v)^{1.39}. \quad (141)$$

### Cap Bubble/Slug Flow Regime

For the cap bubble/slug flow regime, the large bubble component is computed and added to the coefficient for dispersed bubbles:

$$h_l A_{l,bs}''' = (h_l A_{l,ab}''') + (h_l A_{l,lb}'''). \quad (142)$$

The interfacial area for the large bubbles regime is computed by the formula of Ishii and Mishima[63]:

$$A_{l,lb}''' = \frac{C^*}{D^*} \left( \frac{\alpha_v - \alpha_{v,db}}{1 - \alpha_{v,db}} \right), \quad (143)$$

where both the coefficient  $C^*$  and the diameter  $D^*$  depend on the flow regime (slug or cap bubble) and the hydraulic diameter of the channel. For channels with a hydraulic diameter less than  $D_{H,cr} = 50\sqrt{\sigma/g\Delta\rho}$  large bubbles are treated as slugs, else they are assumed to be cap bubbles. Then,  $C^*$  and  $D^*$  are computed by:

$$C^* = \begin{cases} 4.5; & D_{Have} < D_{H,cr} \\ 16; & D_{Have} \geq D_{H,cr} \end{cases} \quad (144)$$

$$D^* = \begin{cases} D_{Have} & ; D_{Have} < D_{H,cr} \\ D_{h,cr} & ; D_{Have} \geq D_{H,cr} \end{cases}. \quad (145)$$

The heat transfer coefficient for large bubbles is defined by:



$$h_{l,lb} = \frac{k_l}{D^*} Nu_{lb}, \quad (146)$$

with the Nusselt number given by the Ranz-Marshall correlation [60] and the bubble Reynolds number like:

$$Re_{lb} = \frac{\rho_l V_{r,lb} D^*}{\mu_l}; \quad (147)$$

where:

$$V_{r,lb} = \text{Min}[|V_v - V_l|, V_{lb}], \quad (148)$$

and:

$$V_{lb} = \begin{cases} V_{r,\infty} & ; d_{lb} < 0.125 \\ 1.13 V_{r,\infty} e^{-d_{lb}} & ; 0.125 < d_{lb} < 0.6 \\ 0.496 \frac{V_{r,\infty}}{\sqrt{d_{lb}}} & ; d_{lb} \geq 0.6 \end{cases};$$

with:

$$d_{lb} = \frac{D^*}{D_{Have}}, \quad (149)$$

and:

$$V_{r,\infty} = \frac{\sqrt{2} \sqrt{g \Delta \rho} D^*}{2 \rho_l}. \quad (150)$$

When sub-cooled boiling is present, the liquid interfacial heat transfer is modified for near wall condensation. The model suggested by Lahey and Moody [64] is used in this case with the interfacial heat flux:

$$q''_{cond} = 0.075 \frac{D_{Have}}{4} h_{fg} \frac{\rho_l \rho_v}{\Delta \rho} \alpha_v. \quad (151)$$

Then, the interfacial heat-transfer when sub-cooled boiling is present can be computed by:

$$(h_l A_I''')_{SB} = 0.075 h_{fg} \frac{\rho_l \rho_v}{\Delta \rho} \alpha_v. \quad (152)$$

The sub-cooled boiling heat transfer is added by a simple void fraction ramp between 10% and 20%.

### Annular/Mist Flow Regime

For void fractions of 75% or above, it is assumed to have annular/mist flow regime. Models for annular films as well as entrained droplets are computed separately and combined by:

$$(h_l A_I''')_{am} = (h_l A_I''')_{film} + (h_l A_I''')_{drop}; \quad (153)$$

where the interfacial area is given by the equation (127). For cases where the surface is only partially wetted by the liquid film, this interfacial area is multiplied by the fraction of the surface wetted:

$$f_{wet} = \frac{(1 - \alpha_v)D_{HAVE}}{4\delta}. \quad (154)$$

Where the film thickness take a value of  $\delta = 25 \times 10^{-6} m$  [19].The interfacial heat transfer coefficient for liquid film  $h_{l,film}$  is combined by laminar and turbulent parts, using a power-law weighting as follows:

$$h_{l,film} = [(h_{l,lam})^2 + (h_{l,turb})^2]^{1/2}; \quad (155)$$

where both  $h_{l,lam}$  and  $h_{l,turb}$  are calculated using the next equation, just with either laminar or turbulent Nusselt number:

$$h_{l,lam} = \frac{Nu\lambda_l}{(0.5D_{Have}(1 - \sqrt{\alpha_v}))}. \quad (156)$$

The laminar film is computed by the condensation correlation of Kuhn et al [55] using the Nusselt number based on the film thickness.

$$Nu_{lam} = 2(1 + 1.83 \times 10^{-4}Re_{film}). \quad (157)$$

The turbulent Nusselt number is calculated according to Gnielinski [43] as:

$$Nu_{l,turb} = \frac{0.7(1.58\log(Re_{tur}) - 3.28)^{-2}(Re_{tur} - 1000)Pr_{tur}}{\sqrt{0.5(1.58\log(Re_{tur}) - 3.28)^{-2}(Pr_{tur}^{2/3} - 1)}}; \quad (158)$$

where the turbulent Reynolds is between  $1 \times 10^3$  and  $5 \times 10^6$ , and the turbulent Prandtl between  $5 \times 10^{-1}$  and  $2 \times 10^3$ . Vapor interfacial heat transfer coefficient is computed by:

$$h_{i,v} = \frac{k_v}{D_c} Nu_{i,v}; \quad (159)$$

with the diameter of annular core as:

$$D_c \approx D_{Have}\sqrt{\alpha_v}; \quad (160)$$

and:

$$Nu_{vi} = \text{Max}\{4, 0.23Re_{cr}^{0.8}Pr_v^{0.4}\}. \quad (161)$$

Reynolds' number  $Re_c$  is calculated using  $D_c$ . Those are taken from the Dittus-Boelter correlation [65]. For the heat transfer coming from droplets, the Sauter mean diameter [66] (the drop diameter that has the same ratio of interfacial area/ volume as the entire population) is indirectly used. Due to the fitting parameters that [67] use, the ratio of the Sauter mean to the volume median diameter is  $7.96 \times 10^{-3}$ : Then the droplets diameter is:

$$d_{drop} = \frac{7.96 \times 10^{-3}\sigma}{\rho_v(\alpha_v V_l)^2} Re^{2/3} \left(\frac{\mu_v}{\mu_l}\right)^{2/3} \left(\frac{\rho_v}{\rho_l}\right)^{-1/3}. \quad (162)$$

The drop diameter calculated from (162) has a limit between  $84 \times 10^{-6}m \leq d_{drop} \leq 0.004m$ . Then, the droplet interfacial area dependent on the annular core region occupied by the droplets  $\alpha_{drop}$  is given by:

$$A_{l,drop}''' = \frac{6\alpha\alpha_{drop}}{(1 - \alpha_{drop})d_{drop}}. \quad (163)$$

In the interfacial heat transfer between drops and surface, the asymptotic value given by Kronig and Brink [68] is used:

$$h_{li,drop} = 2\pi^2 \frac{k_l}{d_{drop}}. \quad (164)$$

The vapor side heat transfer coefficient uses the Nusselt number given by Ryskin [69] in both, condensation and evaporation:

$$Nu_{vi,d} = 2 + \sqrt{V_{max}^* Pe}; \quad (165)$$

Where  $V_{max}^*$  is the maximum dimensionless velocity at the surface of the drop:

$$V_{max}^* = \frac{1.5}{1 + \frac{2.8(1 + 2\frac{\rho_l\mu_l}{\rho_v\mu_v})(2 + 3\mu_l/\mu_v)}{(2 + 3\frac{\rho_l\mu_l}{\rho_v\mu_v})\sqrt{Re_d}}}. \quad (166)$$

Finally,  $h_{li,drop} = h_{vi,drop}$ .

### Interpolation between Dispersed/Cap Slug Bubble and Annular/Mist

A simple void-fraction based interpolation is performed, using a weighting factor, resulting in the heat transfer coefficient for all phases k:

$$h_k = \frac{\alpha - 0.5}{0.75 - 0.5} (h_{ki}A_l''')_{am} + \left(1 - \frac{\alpha - 0.5}{0.75 - 0.5}\right) (h_{ki}A_l''')_{bs}. \quad (167)$$

### e. Wall Friction

#### TPF correlations

The wall drag model is the one proposed in [16]. In this case, the wall friction is given by:

$$F_{sv} = \frac{f_{fv}\alpha_v^2\rho_v V_v}{2D_H} + P_{ls,v}, \quad (168)$$

and:

$$F_{sl} = \frac{f_{fl}\alpha_l^2\rho_l V_l}{2D_H} + \frac{C_{LM}\alpha_v\alpha_l\sqrt{f_{fv}f_{fl}\rho_v\rho_l V_v}}{2D_H} + P_{ls,l}; \quad (169)$$

where the local pressure losses by spacers for each phase is given by a friction factor calculated using the pressure loss coefficients ( $\xi$ ) given as input:

$$P_{ls,k} = \frac{\xi\alpha_k\rho_k V_k}{2\Delta x}. \quad (170)$$

$\xi$  is defined as:

$$\xi = \frac{\Delta p}{\frac{\rho}{2}v^2}, \quad (171)$$

where  $\Delta p$  is the pressure difference, in this case between the flux downwards and upwards the spacers,  $\rho$  is the density of the fluid and  $v$  the velocity.

The Lockhart-Martinelli [47] coefficient ( $C_{LM}$ ) take the values:

$$C_{LM} = 15w + 5, \quad (172)$$

where:

$$w = \frac{Re_v + Re_l - 1300}{2000}; \quad (173)$$

being  $w$  a number limited by the code between 0 and 1.

The friction factor is taken from Churchill [70] and when  $Re > 100$ :

$$f_f = 2 \left[ \left( \frac{8}{Re_k} \right)^{12} + \frac{1}{(a+b)^{3/2}} \right]^{1/12}; \quad (174)$$

where:

$$a = \left[ 2.457 \log \left( \frac{1}{\left( \frac{7}{Re} \right)^{0.9} + 0.27 \frac{Ra}{D_{Have}}} \right) \right]^{16}, \quad (175)$$

$$b = \left[ \frac{37530}{Re} \right]^{16}; \quad (176)$$

where  $Ra$  is the surface roughness and in TWOPORFLOW is given by input. If  $Re < 100$ :

$$f_f = \frac{64}{Re}. \quad (177)$$

### ***TPF-TRACE correlations***

The drag wall model for both phases is:

$$F_{sk} = \frac{2f_{fs,reg}\rho_k}{D_H V_k} + P_{ls,k}, \quad (178)$$

where the pressure loss coefficient due to spacers is the same as in the equation (170).

### **Bubbly/Slug Flow Regime**

For two-phase flow with nucleate boiling, the friction coefficient is corrected by a model developed by Levy [71]. This model balances surface tension, drag forces, and states, based on the examination made by Ferrell and Bylund [72]. The bubble diameter used for the model by Levy has to be a function of void fraction. The model is given by:

$$C_{nb} = \min\{2, 155d_b[\alpha_v\alpha_l]^{0.62}\}, \quad (179)$$

where:

$$d_b = 0.015 \sqrt{\frac{\sigma}{\tau_w D_H}}. \quad (180)$$

Then taking the friction coefficient obtained with equation (169) the wall shear stress is:

$$\tau_w = \frac{F_{sl}}{2} \rho_l V_l^2. \quad (181)$$

Finally, the Bubbly/Slug Flow Regime friction coefficient with wall nucleation is:

$$f_{fs,bs} = \frac{F_{sl}}{4} \frac{2\rho_l}{D_H} (1 + C_{nb})^2. \quad (182)$$

### Annular/Mist Flow Regime

The Annular/Mist Flow Regime splits into laminar, turbulent, and single-phase gas flow. While the transition to single-phase gas flow depends on a critical film thickness value, the friction coefficient for laminar and turbulent flow is determined by:

$$f_{fs,film} = (f_{fs,lam}^3 + f_{fs,turb}^3)^{1/3}; \quad (183)$$

when the laminar value is the same as for pipe flows:

$$f_{fs,lam} = \begin{cases} \frac{16}{Re_l'}, & \alpha_v \leq 0.95 \\ \frac{[16 + 8 \left( \frac{\alpha_v - 0.95}{0.99 - 0.95} \right)]}{Re_l}, & \alpha_v > 0.95 \end{cases}; \quad (184)$$

and the turbulent value is given by Haaland's explicit approximation to the Colebrook equation made from [73]:

$$f_{fs,turb} = \frac{1}{\left\{ 1.8 \cdot \log_{10} \left[ \frac{6.9}{Re_l} + \left( \frac{Ra/D_H}{3.7} \right)^{1.11} \right] \right\}^2}. \quad (185)$$

Finally, the wall-liquid drag coefficient is given by:

$$f_{fsl,am} = f_{fs,film} (1 - \alpha_v)^2; \quad (186)$$

and the wall-vapor drag coefficient is:

$$f_{fsv,am} = 0. \quad (187)$$

Film breakdown is assumed to occur when the film thickness becomes less than a critical value of 25 microns.

### Transition Bubbly/Slug to Annular/Mist Flow Regime

The transition from Bubbly/Slug to Annular/Mist uses a weighting factor dependent on the void fraction, and then the wall-drag for liquid and vapor are calculated as:

$$f_{fsl,bs/am} = \left( \frac{0.9 - \alpha_v}{0.9 - 0.8} \right) f_{fsl,bs} + \left( 1 - \left( \frac{0.9 - \alpha_v}{0.9 - 0.8} \right) \right) f_{fsl,am}, \quad (188)$$

and:

$$f_{fsv,bs/am} = \left( 1 - \left( \frac{0.9 - \alpha_v}{0.9 - 0.8} \right) \right) f_{fsv,am}. \quad (189)$$

### f. Liquid-vapor momentum coupling

#### TPF correlations

In TPF correlations the modified correlation of Kazimi [16] is used:

$$F_I = \frac{1 - \alpha_v}{\alpha_v D_H} \left[ \frac{1 - \alpha_v}{\alpha_v D_H} \mu_l + 2\rho_v \Delta V \right]. \quad (190)$$

#### TPF-TRACE correlations

##### Bubbly/Slug Flow Regime

The interfacial drag coefficient for Bubbly/Slug can be computed by:

$$F_{I,bs} = \frac{\alpha_v \alpha_v^3 \vec{g} \Delta \rho}{\bar{v}_{gj}^2} P_S, \quad (191)$$

where the profile slip factor  $P_S$  is:

$$P_S = \max \left( 0.05, \min \left( 1.0, \left[ \frac{1 - \alpha_v \bar{v}_v - \bar{v}_l}{\alpha_l \bar{v}_r} \right]^2 \right) \right). \quad (192)$$

The Bubbly/Slug flow regime is split into three different parts: Dispersed Bubble Phase, Transition Phase, and Slug Flow Phase; and the Dispersed Bubble Phase use the Churn-Turbulent Regime:

$$\bar{v}_{gj} = 0.188 \sqrt{\frac{g \max(1 \times 10^{-5}, \rho_l - \rho_v) D_H}{\rho_v}}. \quad (193)$$

##### Annular/Mist Flow Regime

The Annular/Mist Flow Regime is split into two parts, interfacial drag on a liquid film and on entrained droplets. Therefore, an entrainment model is needed to determine the fraction of liquid flow.

The interfacial friction coefficient for the liquid film can be computed, using the Wallis model [74] for up-flow to compute the friction factor and  $A''_{l,film}$  is computed by equation (127):

$$F_{l,film} = 0.005(1 + 75\alpha_{v,film})A''_{l,film} \frac{1}{2}\rho_v. \quad (194)$$

In order to calculate  $\alpha_{Film}$ :

$$\alpha_{v,film} = 1 - \frac{\alpha_v}{1 - \alpha_{v,drop}}, \quad (195)$$

and:

$$\alpha_{v,drop} = \max\left(1 \times 10^{-5}, \min\left(E_\infty \alpha_l, E_\infty \frac{\max(1 \times 10^{-5}, \alpha_l \bar{V}_l)}{\max(1 \times 10^{-5}, \alpha_v \bar{V}_v)}\right)\right). \quad (196)$$

For the Droplet drag, the Entrainment model is needed to determine the fraction of the liquid flow. For small diameters, the Ishii-Mishima [63] correlation is used, and for large diameters the Steen-Wallis entrainment correlation [103]:

$$E_\infty = \begin{cases} 0.015 + 0.44 \log_{10} \left[ 0.9245 \left( \frac{\max(1 \times 10^{-5}, \alpha_v \bar{V}_v) \mu_v \sqrt{\frac{\rho_v}{\rho_l}}}{\sigma 2.46 \times 10^{-4}} \right)^2 \right], & D_H > 0.032; \\ \tanh[7.25 \times 10^{-7} We_v^{1.25} \min\{6400, Re_l\}^{0.25}], & D_H \leq 0.032 \end{cases} \quad (197)$$

where the Weber number in this case takes the form of the effective Weber number at the entrance like:

$$We_v = \frac{\rho_v |\alpha_v V_v|^2 D_h \left(\frac{\Delta\rho}{\rho_v}\right)^{1/3}}{\sigma}. \quad (198)$$

The drop drag coefficient is computed by a correlation by Ishii and Chawla [104]

$$C_D = \frac{24}{Re_{drop}} (1 + 0.1 Re_{drop}^{0.75}), \quad (199)$$

with the Reynolds number:

$$Re_{drop} = \frac{\rho_v V_{r,drop} d_{drop}}{\mu_{mix}}, \quad (200)$$

the mixture viscosity given by:

$$\mu_{mix} = \frac{\mu_v}{(1 - \alpha_{v,drop})^{2.5}}, \quad (201)$$

and the relative velocity:

$$V_{r,drop} = \max \left( 1 \right. \\ \left. \times 10^{-5}, \min \left( V_r, 1.718 \sqrt{d_{drop}} \sqrt{\frac{g\Delta\rho}{\rho_v}} (1 - \alpha_{v,drop})^{1.5}, \sqrt{2} \left[ \frac{\sigma g \Delta\rho}{\rho_v^2} \right]^{0.25} \right. \right. \\ \left. \left. - \alpha_{v,drop} \right)^{1.5} \right). \quad (202)$$

The interfacial friction coefficient for Droplets can then be computed by:

$$F_{I,drop} = C_D \rho_v \frac{3\alpha_v \alpha_{v,drop}}{4d_{drop}} V_{r,drop}^2, \quad (203)$$

and thus, the Annular/Mist Flow Regime interfacial friction coefficient:

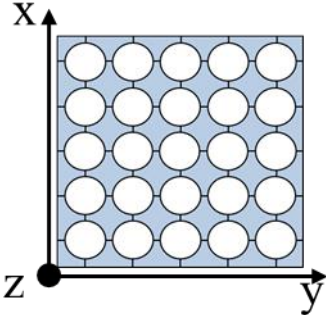
$$F_{I,am} = F_{I,film} + \frac{F_{I,drop}}{V_r^2}. \quad (204)$$



## Annex 2 Boundary and experimental conditions of the steady state experiments used in the evaluations

### a. Boundary and experimental conditions of PSBT Steady state Temperature experiments

**Table 12.1.** Experimental conditions PSBT Steady State Temperature (Turbulent mixing tests)

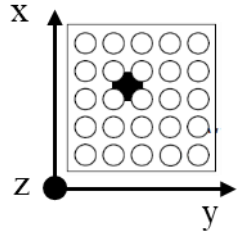
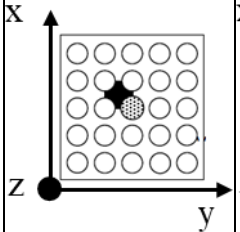
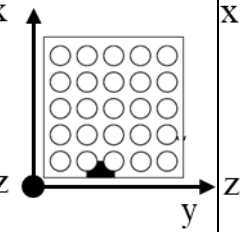
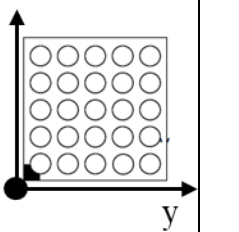
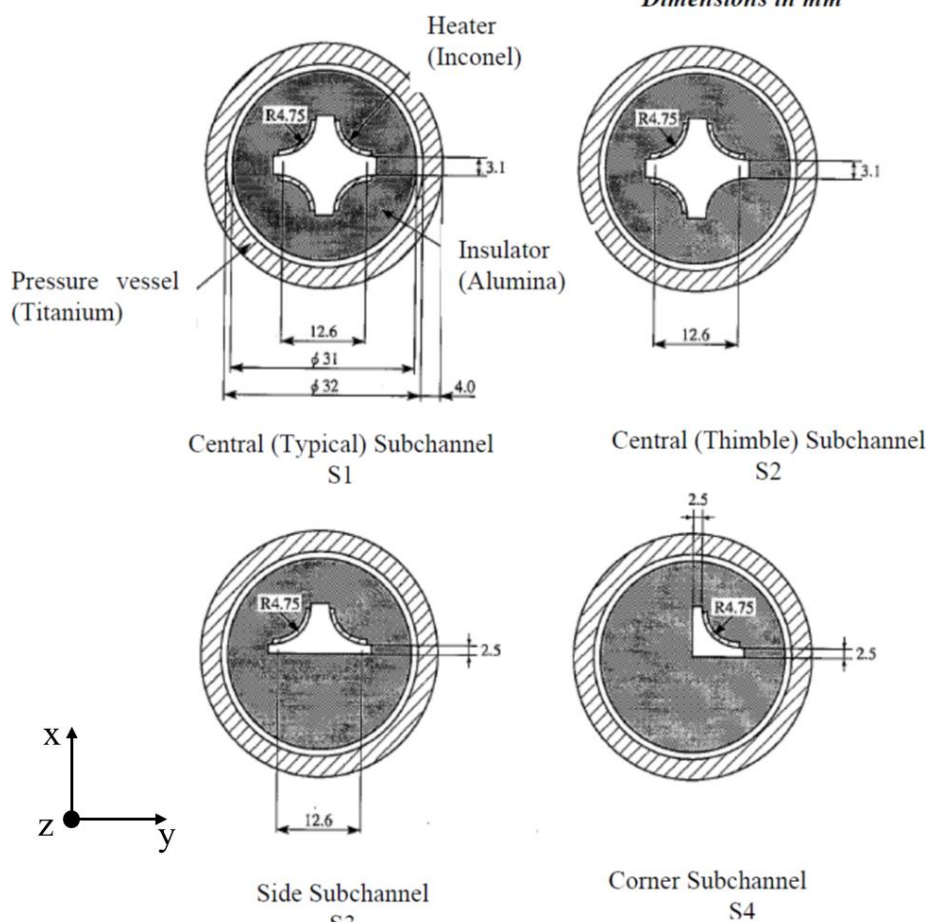


Configuration	
Rods array	5x5
Number of heated rods	25
Heated rod outer diameter (mm)	9.50
Heated rods pitch (mm)	12.60
Axial heated length (mm)	3658
Flow channel inner width (mm)	64.9
Axial power shape	Uniform
Number of spacers:	
Mixing vane spacers (MV)	7
Non-mixing vane spacers (NMV)	2
Simple spacers (SS)	8
Spacer locations:	
MV (mm) z=	457, 914, 1372, 1829, 2286, 2743, 3200
NMV (mm) z=	0, 3658
SS (mm) z=	229, 686, 1143, 1600, 2057, 2515, 2972, 3429

**Table 12.2.** Boundary conditions PSBT Steady State Temperature (Turbulent mixing tests)

Test number	Pressure [MPa]	Flow[kg/m <sup>2</sup> s]	Power [MW]	Inlet temperature [°C]
01-5343	14.74	1397.25	1.25	165.30
01-5342	14.71	533.34	0.52	164.50
01-5215	14.74	3041.72	2.09	282.90
01-5125	14.74	3038.94	1.50	289.20
01-5237	14.72	4708.42	3.23	229.40
01-6232	16.58	583.34	0.42	251.50
01-6233	16.58	1361.14	1.02	254.00
01-1237	4.92	4722.31	3.44	86.00
01-5252	14.71	541.68	0.41	113.90

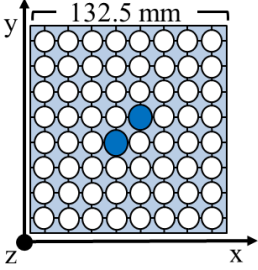
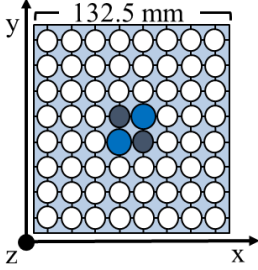
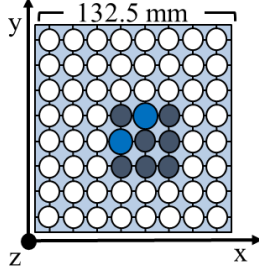
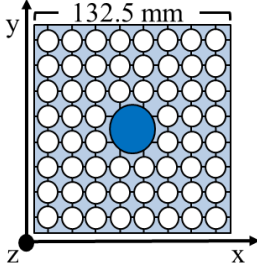
**b. Boundary and experimental conditions of PSBT Single sub-channel experiments**

Table 12.3. Experimental conditions PSBT Single Sub-channel (Sub-cooled boiling)				
Configuration				
	<p><i>Dimensions in mm</i></p> 			
Sub-channel type	S1 Center (Typical)	S2 Center (Thimble)	S3 Side	S4 corner
Number of heaters	4x1/4	3x1/4	2x1/4	1x1/4
Axial heated length (mm)	1555			
Axial power shape	Uniform			
Flow area mm <sup>2</sup>	107.098	107.098	68.464	42.592
Heated perimeter mm	29.845	22.384	14.923	7.461
Wetted perimeter mm	54.645	54.645	44.923	33.161

<b>Table 12.4. Boundary conditions PSBT Single Sub-channel (Sub-cooled boiling)</b>					
Test number	Pressure [Pa]	Flow[kg/s]	Mass flux [ kg/m <sup>2</sup> hr]	Power [W]	Inlet temperature [°C]
1.1222	1.66x10 <sup>7</sup>	0.33	3050.00	5.00x10 <sup>4</sup>	334.70
1.1223	1.66x10 <sup>7</sup>	0.33	3055.56	4.99x10 <sup>4</sup>	339.70
1.2237	1.47x10 <sup>7</sup>	0.33	3036.11	6.00x10 <sup>4</sup>	329.60
1.2422	1.47x10 <sup>7</sup>	0.15	1388.89	6.00x10 <sup>4</sup>	284.10
1.2423	1.47x10 <sup>7</sup>	0.15	1369.44	5.99x10 <sup>4</sup>	299.30
1.4311	9.85x10 <sup>6</sup>	0.15	1391.67	7.99x10 <sup>4</sup>	214.20
1.4312	9.83x10 <sup>6</sup>	0.15	1397.22	7.98x10 <sup>4</sup>	248.90
1.4325	9.84x10 <sup>6</sup>	0.15	1397.22	5.98x10 <sup>4</sup>	253.80
1.4326	9.82x10 <sup>6</sup>	0.15	1394.44	6.01x10 <sup>4</sup>	268.80
1.5221	7.40x10 <sup>6</sup>	0.15	1394.44	4.99x10 <sup>4</sup>	219.20
1.5222	7.35x10 <sup>6</sup>	0.15	1394.44	5.00x10 <sup>4</sup>	243.90
1.6221	4.95x10 <sup>6</sup>	0.15	1391.67	5.00x10 <sup>4</sup>	189.20
1.6222	4.90x10 <sup>6</sup>	0.15	1388.89	4.99x10 <sup>4</sup>	204.20
2.1231	1.66x10 <sup>7</sup>	0.33	3050.00	3.75x10 <sup>4</sup>	335.00
2.1232	1.66x10 <sup>7</sup>	0.33	3055.56	3.75x10 <sup>4</sup>	340.00
2.1233	1.66x10 <sup>7</sup>	0.33	3058.33	3.75x10 <sup>4</sup>	345.00
2.3232	1.23x10 <sup>7</sup>	0.32	3030.56	4.51x10 <sup>4</sup>	309.80
2.3233	1.23x10 <sup>7</sup>	0.32	3030.56	4.51x10 <sup>4</sup>	319.90
2.4421	9.85x10 <sup>6</sup>	0.15	1397.22	6.01x10 <sup>4</sup>	244.00
2.4422	9.86x10 <sup>6</sup>	0.15	1394.44	6.01x10 <sup>4</sup>	279.20
2.4551	9.88x10 <sup>6</sup>	0.05	497.22	1.50x10 <sup>4</sup>	274.00
2.4552	9.88x10 <sup>6</sup>	0.05	494.44	1.51x10 <sup>4</sup>	294.30
2.6431	4.96x10 <sup>6</sup>	0.15	1391.67	3.75x10 <sup>4</sup>	209.20
2.6432	4.96x10 <sup>6</sup>	0.15	1394.44	3.75x10 <sup>4</sup>	224.20
2.6433	4.95x10 <sup>6</sup>	0.15	1397.22	3.76x10 <sup>4</sup>	253.90
3.2231	1.47x10 <sup>7</sup>	0.21	3027.78	4.04x10 <sup>4</sup>	309.40
3.2232	1.47x10 <sup>7</sup>	0.21	3027.78	4.05x10 <sup>4</sup>	314.50
3.2451	1.47x10 <sup>7</sup>	0.09	1377.78	3.02x10 <sup>4</sup>	283.80
3.2452	1.48x10 <sup>7</sup>	0.09	1369.44	3.02x10 <sup>4</sup>	299.00
3.2453	1.47x10 <sup>7</sup>	0.09	1372.22	3.02x10 <sup>4</sup>	314.30
3.6431	4.94x10 <sup>6</sup>	0.09	1377.78	4.02x10 <sup>4</sup>	189.00
3.6432	4.94x10 <sup>6</sup>	0.09	1380.56	4.01x10 <sup>4</sup>	223.90
3.6461	4.96x10 <sup>6</sup>	0.09	1377.78	2.52x10 <sup>4</sup>	203.90
4.2251	1.47x10 <sup>7</sup>	0.13	3072.22	1.52x10 <sup>4</sup>	310.30
4.2253	1.47x10 <sup>7</sup>	0.13	3072.22	1.51x10 <sup>4</sup>	318.40
4.2256	1.47x10 <sup>7</sup>	0.13	3086.11	1.51x10 <sup>4</sup>	330.50
4.2257	1.47x10 <sup>7</sup>	0.13	3088.89	1.51x10 <sup>4</sup>	334.50
4.4455	9.86x10 <sup>6</sup>	0.06	1400.00	1.52x10 <sup>4</sup>	278.80
4.4456	9.86x10 <sup>6</sup>	0.06	1394.44	1.52x10 <sup>4</sup>	289.00
4.6461	4.96x10 <sup>6</sup>	0.06	1397.22	1.25x10 <sup>4</sup>	214.00

**c. Boundary and experimental conditions of BFBT Steady State Sub-channel grade tests.**

**Table 12.5.** Experimental conditions BFBT Steady State Sub-channel grade (Void dispersion tests)

Assembly type 1 and 01 (different axial and lateral power distributions)					
		Assembly type 02	Assembly type 03	Assembly type 4	
					
○ Heated rod		● Water rod		● Non-heated rod	
Assembly	Assembly 1	Assembly 01	Assembly 02	Assembly 03	Assembly 4
Rods array	8x8				
Number of heated rods	62	62	60	55	60
Number of unheated rods	0	0	2	7	0
Heated rod outer diameter (mm)	12.3				
Heated rods pitch (mm)	16.2				
Axial heated length (mm)	3708				
Assembly pitch (mm)	1325				
Number of water rods	2				1
Axial power shape	Cosine	Uniform			
Spacer pressure loss coefficient ( $\xi$ )	1.2				

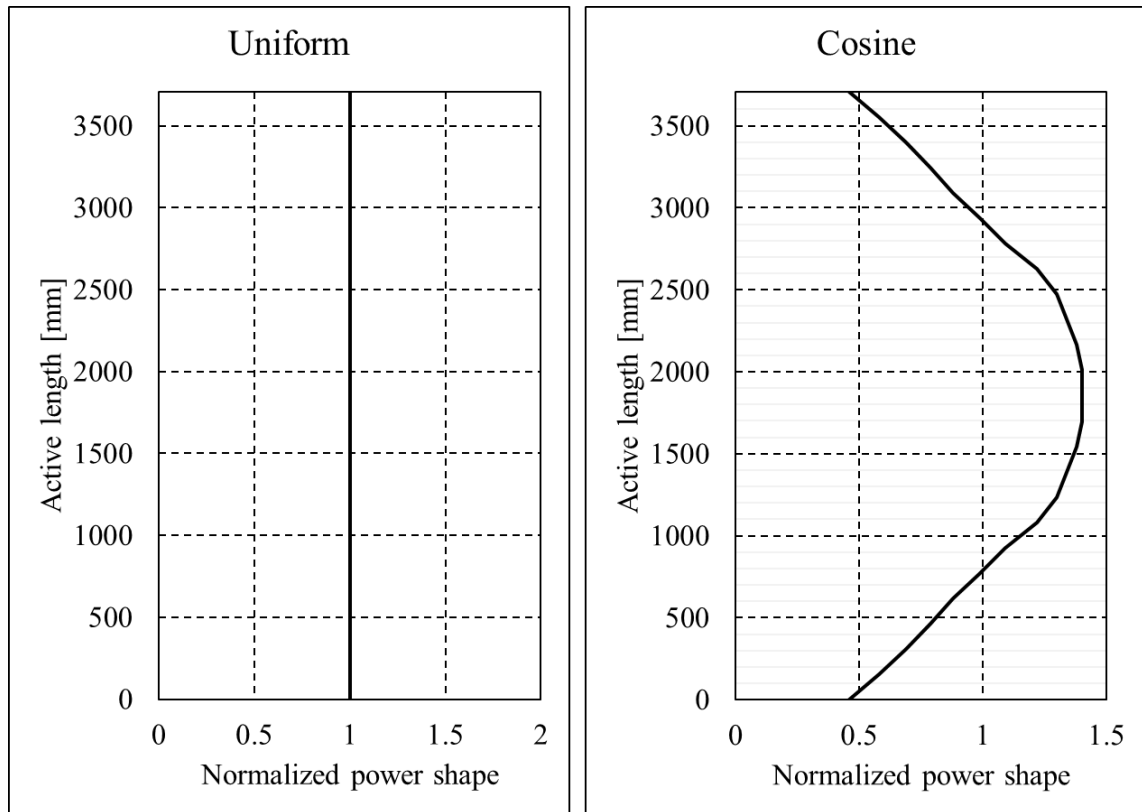


**Figure 12.1.** BFBT axial power distributions used in Sub-channel grade experiments

**Table 12.6.** Boundary conditions BFBT Steady State Sub-channel grade (Void dispersion tests)

Test number	Averaged void fraction	Pressure [MPa]	Flow[kg/m <sup>2</sup> s]	Power [MW]	Inlet temperature [°C]
0011-55	0.4	7.18	734.08	1.9	277.66
0011-58	0.6	7.17	733.05	3.51	277.89
0011-61	0.8	7.21	737.14	6.44	278.28
0021-16	0.4	7.19	735.10	1.91	277.49
0021-18	0.6	7.17	733.05	3.51	276.19
0021-21	0.8	7.18	734.08	6.45	277.88
0031-16	0.4	7.18	734.08	1.92	277.70
0031-18	0.6	7.18	734.08	3.52	278.15
0031-21	0.8	7.17	733.05	6.45	278.19
1071-55	0.5	7.19	735.10	1.92	277.73
1071-58	0.7	7.16	732.03	3.52	277.88
1071-61	0.8	7.2	736.12	6.48	278.01
4101-55	0.4	7.159	756.53	2	277.75
4101-58	0.6	7.2	760.86	1.92	277.77
4101-61	0.8	7.15	755.57	3.52	277.68

**d. Boundary and experimental conditions of CHF Becker tube experiments**

<b>Table 12.7.</b> Experimental conditions Becker tube CHF experiments.		
Hydraulic diameter m	0.01	0.014
Heated length mm	7000	
Inner diameter mm	10	14.9
Outer diameter mm	14	20.8
Axial power shape	Uniform	

<b>Table 12.8.</b> Boundary conditions Becker tube CHF experiments.				
Test number	Pressure [Pa]	Flow[kg/m <sup>2</sup> s]	Power [W]	Inlet temperature [°C]
420	7.02x10 <sup>6</sup>	3034.5	1.86x10 <sup>5</sup>	276.20
424	7.04x10 <sup>6</sup>	2482.4	1.55x10 <sup>5</sup>	275.40
425	7.01x10 <sup>6</sup>	2482.9	1.75x10 <sup>5</sup>	275.60
430	6.99x10 <sup>6</sup>	1997.8	1.41x10 <sup>5</sup>	275.40
431	7.02x10 <sup>6</sup>	1993.6	1.53x10 <sup>5</sup>	275.50
432	6.98x10 <sup>6</sup>	1994.9	1.74x10 <sup>5</sup>	275.40
434	6.99x10 <sup>6</sup>	1501.1	1.31x10 <sup>5</sup>	275.60
435	7.01x10 <sup>6</sup>	1496.4	1.52x10 <sup>5</sup>	276.70
436	7.02x10 <sup>6</sup>	1495.3	1.74x10 <sup>5</sup>	275.90
438	7.00x10 <sup>6</sup>	1008.9	1.10x10 <sup>5</sup>	275.60
439	7.01x10 <sup>6</sup>	1010.6	1.31x10 <sup>5</sup>	275.60
440	7.00x10 <sup>6</sup>	1010.1	1.53x10 <sup>5</sup>	275.30
442	7.00x10 <sup>6</sup>	496.9	6.62x10 <sup>4</sup>	274.80
443	7.01x10 <sup>6</sup>	497.3	7.67x10 <sup>4</sup>	274.60

e. **Boundary and experimental conditions of CHF BFBT Steady State experiments**

**Table 12.9.** Experimental conditions BFBT Steady State CHF experiments.

Test assembly	C2A	C2B	C3
Simulated fuel assembly type	High burn-up 8x8		
Number of heated rods	60		
Heated rods outer diameter (mm)	12.3		
Heated rods pitch (mm)	16.2		
Axial heated length (mm)	3708		
Number of water rods	1		
Water rods outer diameter (mm)	34		
Number of spacers	7		
Spacer pressure loss coefficients ( $\xi$ )	1.2		
Axial power shape	Cosine	Cosine	Inlet-peak

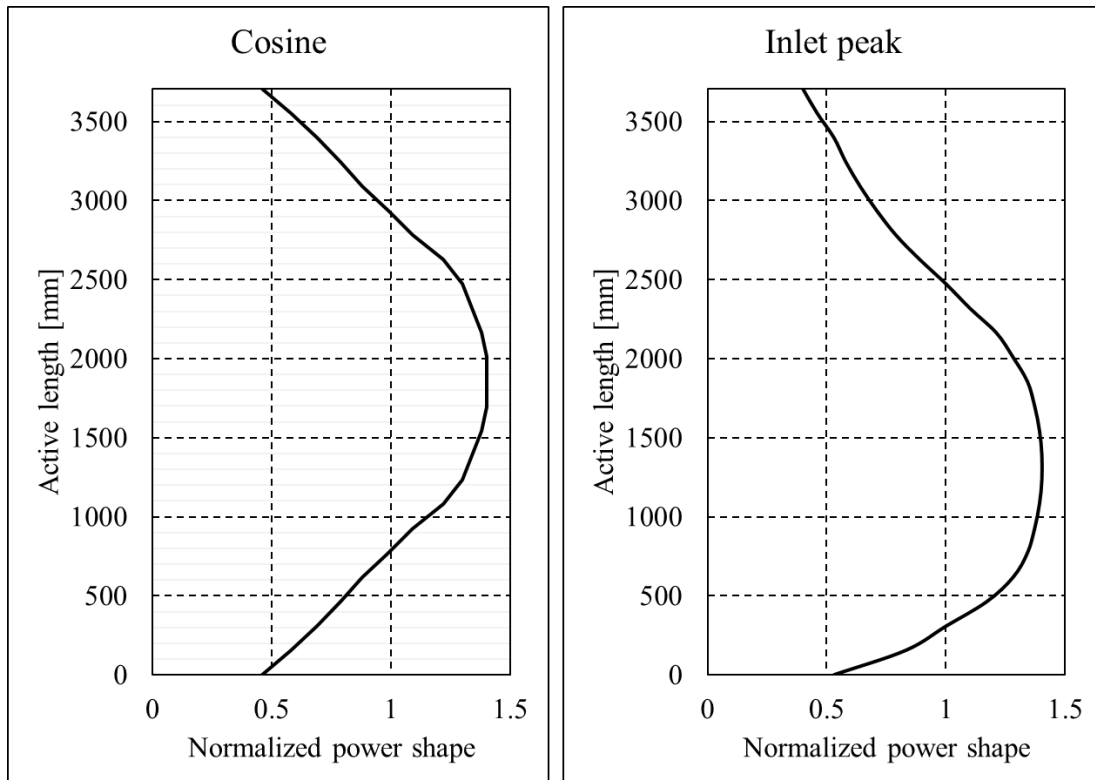


**Figure 12.2.** BFBT axial power distributions used in CHF experiments

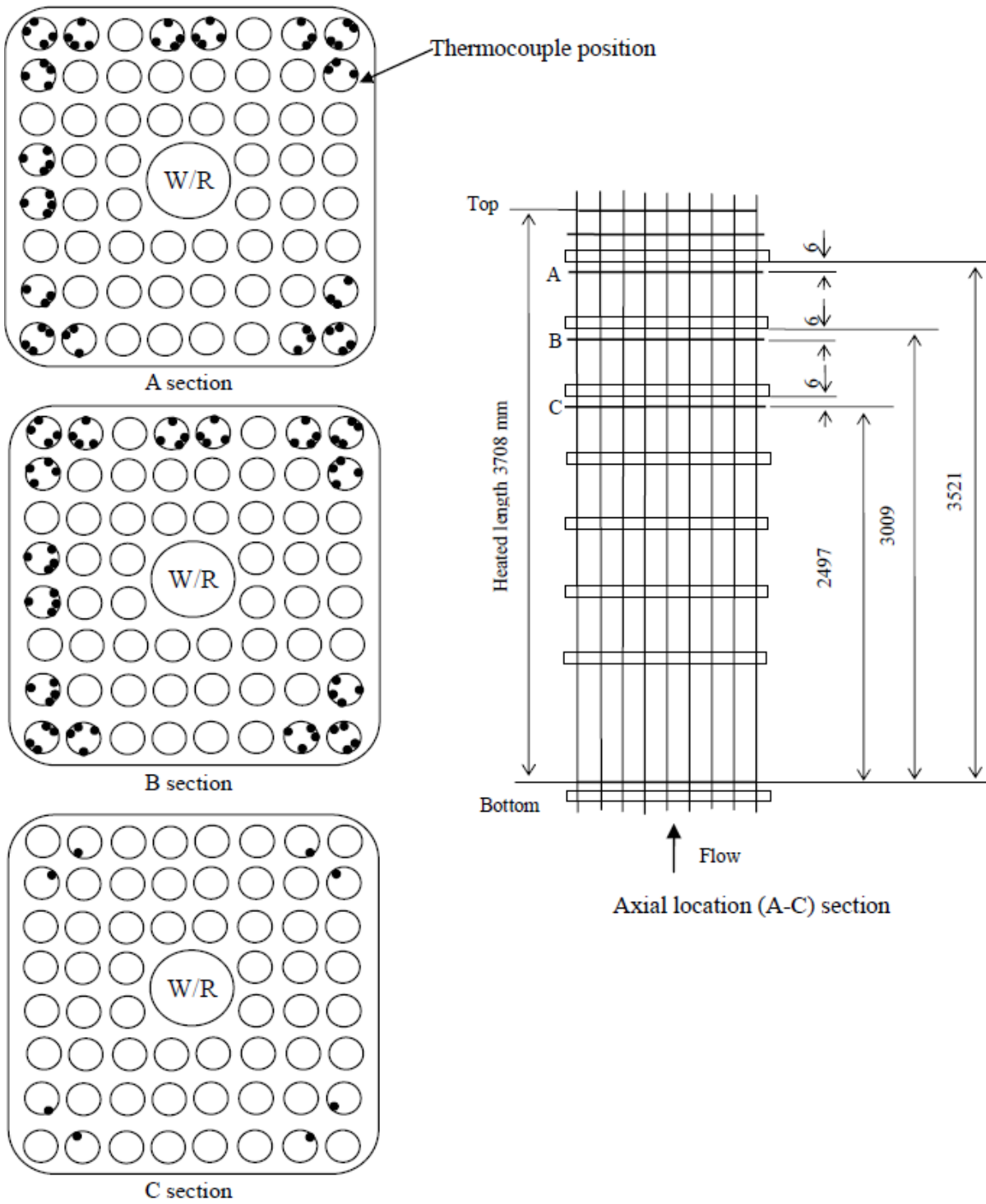


**Figure 12.3.** BFBT location of thermocouples for critical power measurement assembly type C2A [87].



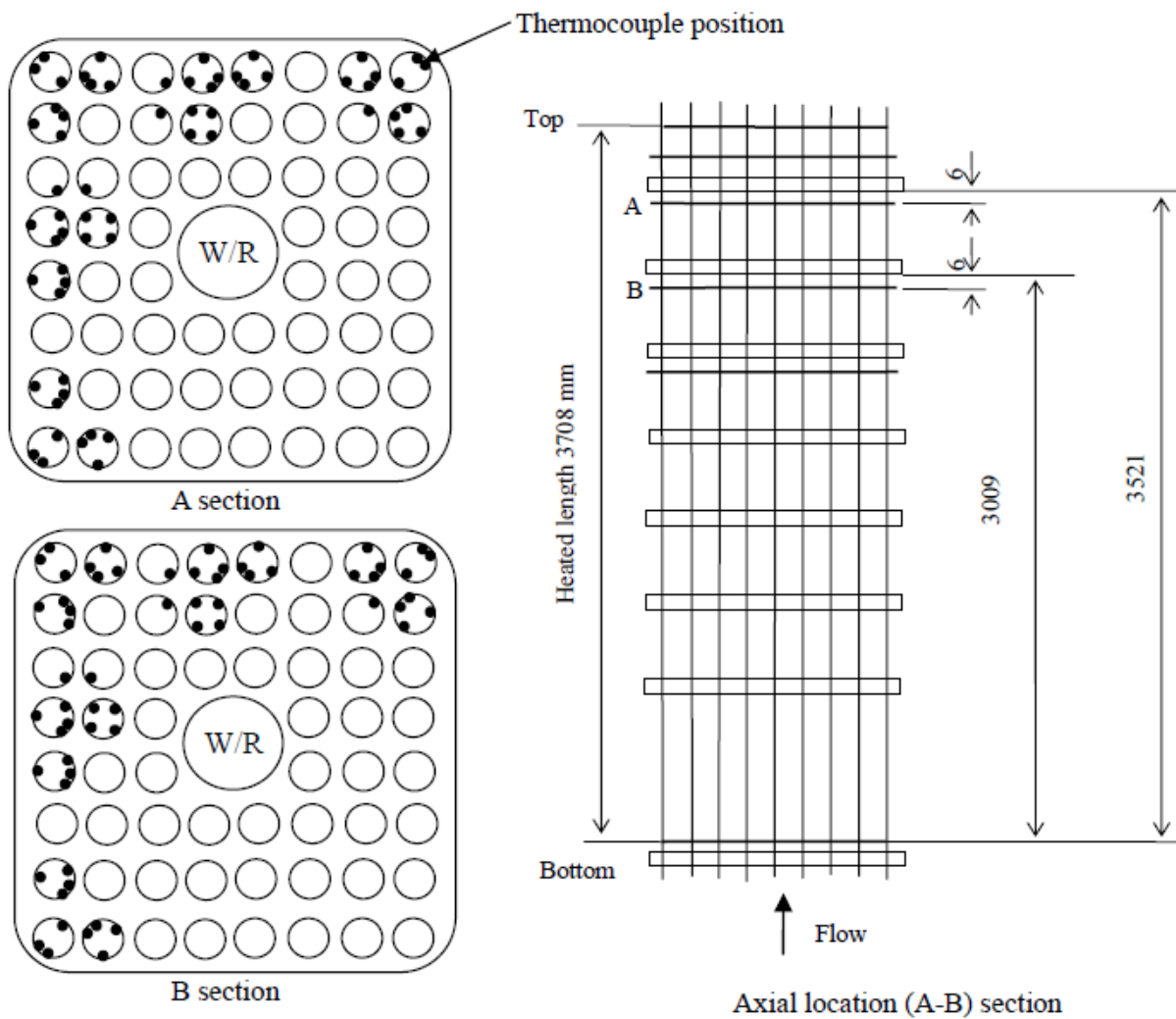


**Figure 12.4.** BFBT location of thermocouples for critical power measurement assembly type C2B [87].

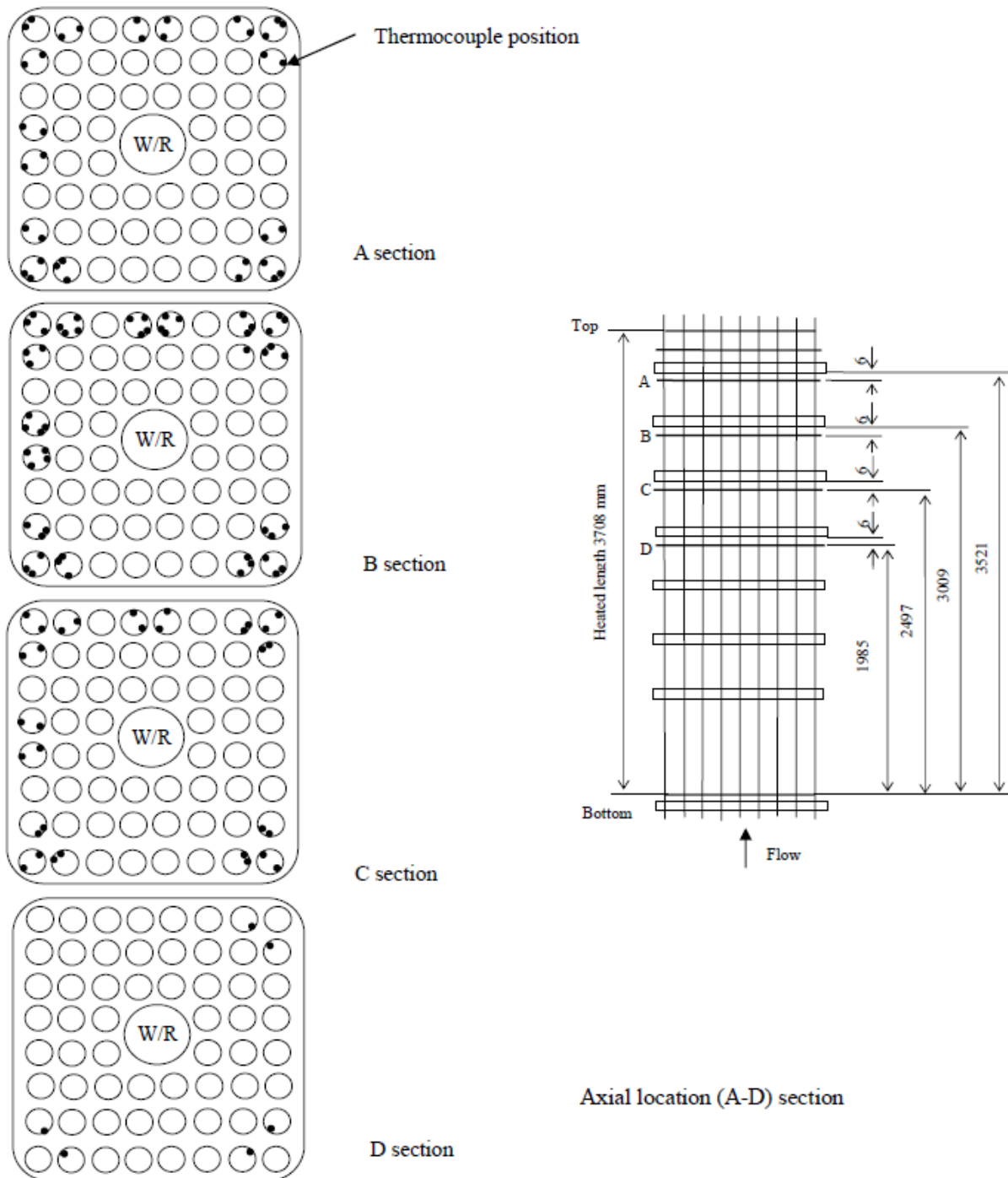


**Figure 12.5.** BFBT location of thermocouples for critical power measurement assembly type C3 [87].

<b>Table 12.10.</b> Boundary conditions BFBT Steady State CHF experiments assembly C2A.				
Test number	Pressure [Pa]	Flow[kg/m <sup>2</sup> s]	Power [W]	Inlet temperature [°C]
SA603500	7.18x10 <sup>6</sup>	295.60	3.25x10 <sup>6</sup>	277.80
SA603600	7.16x10 <sup>6</sup>	295.60	3.39x10 <sup>6</sup>	270.96
SA603700	7.17x10 <sup>6</sup>	292.95	3.39x10 <sup>6</sup>	266.99
SA603800	7.16x10 <sup>6</sup>	293.25	3.46x10 <sup>6</sup>	263.68
SA603901	7.18x10 <sup>6</sup>	293.83	3.20x10 <sup>6</sup>	282.75
SA605500	7.16x10 <sup>6</sup>	589.72	5.77x10 <sup>6</sup>	277.86
SA605502	7.17x10 <sup>6</sup>	589.14	5.73x10 <sup>6</sup>	277.78
SA605600	7.17x10 <sup>6</sup>	592.66	5.88x10 <sup>6</sup>	271.56
SA605700	7.17x10 <sup>6</sup>	594.13	5.98x10 <sup>6</sup>	267.09
SA605801	7.16x10 <sup>6</sup>	593.25	6.09x10 <sup>6</sup>	262.80
SA605900	7.16x10 <sup>6</sup>	593.25	5.62x10 <sup>6</sup>	283.16
SA607500	7.13x10 <sup>6</sup>	881.21	7.04x10 <sup>6</sup>	277.98
SA607600	7.15x10 <sup>6</sup>	887.37	7.24x10 <sup>6</sup>	271.56
SA607700	7.16x10 <sup>6</sup>	880.62	7.37x10 <sup>6</sup>	266.91
SA607800	7.18x10 <sup>6</sup>	884.15	7.51x10 <sup>6</sup>	263.08
SA607900	7.15x10 <sup>6</sup>	887.37	6.87x10 <sup>6</sup>	282.91
SA610503	7.17x10 <sup>6</sup>	1620.35	8.85x10 <sup>6</sup>	276.26
SA610504	7.17x10 <sup>6</sup>	1628.27	8.91x10 <sup>6</sup>	276.51
SA610600	7.18x10 <sup>6</sup>	1615.94	9.20x10 <sup>6</sup>	270.49
SA610700	7.13x10 <sup>6</sup>	1620.35	9.37x10 <sup>6</sup>	266.41
SA610701	7.21x10 <sup>6</sup>	1610.95	9.38x10 <sup>6</sup>	266.09
SA610800	7.24x10 <sup>6</sup>	1623.28	9.52x10 <sup>6</sup>	261.59
SA610900	7.27x10 <sup>6</sup>	1617.41	8.66x10 <sup>6</sup>	281.37
SA610902	7.18x10 <sup>6</sup>	1626.80	8.69x10 <sup>6</sup>	281.40
SA611500	7.13x10 <sup>6</sup>	1768.00	9.10x10 <sup>6</sup>	276.73
SA611600	7.12x10 <sup>6</sup>	1766.53	9.34x10 <sup>6</sup>	269.91
SA611700	7.23x10 <sup>6</sup>	1764.18	9.57x10 <sup>6</sup>	266.09
SA611800	7.15x10 <sup>6</sup>	1763.30	9.72x10 <sup>6</sup>	261.79
SA611900	7.16x10 <sup>6</sup>	1770.05	8.75x10 <sup>6</sup>	281.16
SA612500	7.16x10 <sup>6</sup>	1918.58	9.29x10 <sup>6</sup>	276.88
SA612600	7.17x10 <sup>6</sup>	1907.72	9.61x10 <sup>6</sup>	269.94
SA612700	7.17x10 <sup>6</sup>	1913.59	9.72x10 <sup>6</sup>	266.77
SA612800	7.18x10 <sup>6</sup>	1908.31	1.00x10 <sup>7</sup>	261.87
SA612900	7.16x10 <sup>6</sup>	1929.15	9.12x10 <sup>6</sup>	281.33
SA616500	7.13x10 <sup>6</sup>	1325.92	8.30x10 <sup>6</sup>	276.86
SA616600	7.19x10 <sup>6</sup>	1321.23	8.50x10 <sup>6</sup>	270.75
SA616700	7.23x10 <sup>6</sup>	1324.75	8.65x10 <sup>6</sup>	266.83
SA616800	7.15x10 <sup>6</sup>	1322.99	8.89x10 <sup>6</sup>	262.53
SA616900	7.14x10 <sup>6</sup>	1331.21	8.15x10 <sup>6</sup>	281.46

<b>Table 12.11.</b> Boundary conditions BFBT Steady State CHF experiments assembly C2B.				
Test number	Pressure [Pa]	Flow[kg/m <sup>2</sup> s]	Power [W]	Inlet temperature [°C]
SB603500	7.17x10 <sup>6</sup>	291.49	3.49x10 <sup>6</sup>	277.96
SB603602	7.15x10 <sup>6</sup>	292.37	3.60x10 <sup>6</sup>	271.16
SB603700	7.17x10 <sup>6</sup>	293.25	3.67x10 <sup>6</sup>	267.35
SB603800	7.15x10 <sup>6</sup>	296.18	3.75x10 <sup>6</sup>	262.42
SB603900	7.14x10 <sup>6</sup>	293.83	3.45x10 <sup>6</sup>	282.86
SB605500	7.15x10 <sup>6</sup>	587.96	5.92x10 <sup>6</sup>	277.55
SB605600	7.14x10 <sup>6</sup>	585.03	6.06x10 <sup>6</sup>	271.94
SB605700	7.16x10 <sup>6</sup>	592.37	6.19x10 <sup>6</sup>	267.45
SB605800	7.17x10 <sup>6</sup>	589.14	6.21x10 <sup>6</sup>	263.06
SB605900	7.14x10 <sup>6</sup>	582.39	5.71x10 <sup>6</sup>	283.25
SB607500	7.13x10 <sup>6</sup>	882.09	7.30x10 <sup>6</sup>	277.69
SB607600	7.17x10 <sup>6</sup>	879.16	7.46x10 <sup>6</sup>	271.60
SB607700	7.16x10 <sup>6</sup>	875.63	7.55x10 <sup>6</sup>	267.22
SB607800	7.14x10 <sup>6</sup>	879.74	7.75x10 <sup>6</sup>	262.78
SB607900	7.18x10 <sup>6</sup>	873.58	7.13x10 <sup>6</sup>	282.97
SB610500	7.20x10 <sup>6</sup>	1609.78	9.37x10 <sup>6</sup>	277.53
SB610501	7.19x10 <sup>6</sup>	1611.83	9.34x10 <sup>6</sup>	278.03
SB610600	7.18x10 <sup>6</sup>	1611.83	9.70x10 <sup>6</sup>	271.88
SB610700	7.18x10 <sup>6</sup>	1605.96	9.78x10 <sup>6</sup>	267.37
SB610800	7.14x10 <sup>6</sup>	1611.54	1.00x10 <sup>7</sup>	263.54
SB610900	7.20x10 <sup>6</sup>	1610.95	9.13x10 <sup>6</sup>	282.80
SB611500	7.19x10 <sup>6</sup>	1757.72	9.70x10 <sup>6</sup>	277.48
SB611600	7.19x10 <sup>6</sup>	1759.78	1.00x10 <sup>7</sup>	271.06
SB611700	7.13x10 <sup>6</sup>	1753.61	1.02x10 <sup>7</sup>	267.65
SB611800	7.18x10 <sup>6</sup>	1757.72	1.03x10 <sup>7</sup>	262.99
SB611900	7.13x10 <sup>6</sup>	1756.26	9.45x10 <sup>6</sup>	282.07
SB612500	7.18x10 <sup>6</sup>	1896.27	9.88x10 <sup>6</sup>	278.42
SB612600	7.18x10 <sup>6</sup>	1898.62	1.03x10 <sup>7</sup>	272.07
SB612700	7.21x10 <sup>6</sup>	1880.13	1.06x10 <sup>7</sup>	267.49
SB612800	7.15x10 <sup>6</sup>	1902.73	1.07x10 <sup>7</sup>	263.01
SB612900	7.16x10 <sup>6</sup>	1903.61	9.70x10 <sup>6</sup>	283.42
SB616501	7.14x10 <sup>6</sup>	1315.65	8.63x10 <sup>6</sup>	278.16
SB616600	7.18x10 <sup>6</sup>	1318.29	8.89x10 <sup>6</sup>	271.66
SB616700	7.18x10 <sup>6</sup>	1318.88	9.10x10 <sup>6</sup>	266.96
SB616800	7.16x10 <sup>6</sup>	1321.23	9.25x10 <sup>6</sup>	262.82
SB616900	7.18x10 <sup>6</sup>	1315.65	8.36x10 <sup>6</sup>	282.42

Test number	Pressure [Pa]	Flow[kg/m <sup>2</sup> s]	Power [W]	Inlet temperature [°C]
SC603900	7.14x10 <sup>6</sup>	292.07	3.31x10 <sup>6</sup>	283.13
SC603500	7.15x10 <sup>6</sup>	292.07	3.38x10 <sup>6</sup>	277.70
SC603600	7.16x10 <sup>6</sup>	293.83	3.51x10 <sup>6</sup>	270.48
SC603700	7.17x10 <sup>6</sup>	291.49	3.51x10 <sup>6</sup>	267.22
SC603800	7.16x10 <sup>6</sup>	292.95	3.57x10 <sup>6</sup>	263.17
SC605900	7.12x10 <sup>6</sup>	585.61	5.74x10 <sup>6</sup>	282.86
SC605500	7.16x10 <sup>6</sup>	585.91	5.83x10 <sup>6</sup>	277.89
SC605600	7.15x10 <sup>6</sup>	582.97	5.97x10 <sup>6</sup>	272.02
SC605700	7.13x10 <sup>6</sup>	585.03	6.09x10 <sup>6</sup>	267.43
SC605800	7.15x10 <sup>6</sup>	584.44	6.16x10 <sup>6</sup>	263.10
SC607900	7.17x10 <sup>6</sup>	877.10	6.93x10 <sup>6</sup>	283.06
SC607500	7.15x10 <sup>6</sup>	875.63	7.13x10 <sup>6</sup>	277.65
SC607600	7.15x10 <sup>6</sup>	878.27	7.22x10 <sup>6</sup>	271.51
SC607701	7.15x10 <sup>6</sup>	877.98	7.53x10 <sup>6</sup>	267.01
SC607800	7.10x10 <sup>6</sup>	880.33	7.57x10 <sup>6</sup>	263.06
SC616900	7.13x10 <sup>6</sup>	1318.88	8.50x10 <sup>6</sup>	282.80
SC616500	7.15x10 <sup>6</sup>	1322.11	8.61x10 <sup>6</sup>	277.70
SC616600	7.14x10 <sup>6</sup>	1319.47	8.75x10 <sup>6</sup>	271.41
SC616701	7.12x10 <sup>6</sup>	1318.29	8.91x10 <sup>6</sup>	267.24
SC616800	7.14x10 <sup>6</sup>	1317.71	9.02x10 <sup>6</sup>	263.32
SC610900	7.19x10 <sup>6</sup>	1611.54	8.74x10 <sup>6</sup>	281.80
SC610500	7.19x10 <sup>6</sup>	1611.54	8.98x10 <sup>6</sup>	278.12
SC610502	7.14x10 <sup>6</sup>	1607.43	8.93x10 <sup>6</sup>	277.80
SC610600	7.13x10 <sup>6</sup>	1604.49	9.28x10 <sup>6</sup>	271.48
SC610700	7.15x10 <sup>6</sup>	1609.48	9.47x10 <sup>6</sup>	267.45
SC610800	7.21x10 <sup>6</sup>	1616.24	9.67x10 <sup>6</sup>	263.01
SC611900	7.14x10 <sup>6</sup>	1760.36	9.00x10 <sup>6</sup>	282.46
SC611500	7.19x10 <sup>6</sup>	1753.03	9.22x10 <sup>6</sup>	278.06
SC611600	7.13x10 <sup>6</sup>	1758.60	9.51x10 <sup>6</sup>	271.52
SC611700	7.19x10 <sup>6</sup>	1758.60	9.64x10 <sup>6</sup>	267.54
SC611800	7.15x10 <sup>6</sup>	1754.79	9.87x10 <sup>6</sup>	263.32
SC612900	7.15x10 <sup>6</sup>	1907.72	9.32x10 <sup>6</sup>	282.72
SC612500	7.17x10 <sup>6</sup>	1908.60	9.41x10 <sup>6</sup>	277.62
SC612600	7.17x10 <sup>6</sup>	1904.20	9.77x10 <sup>6</sup>	271.40
SC612700	7.16x10 <sup>6</sup>	1903.91	9.94x10 <sup>6</sup>	267.30
SC612800	7.16x10 <sup>6</sup>	1904.20	1.02x10 <sup>7</sup>	263.09